

DNA NANOTECHNOLOGY TO MAP AND MANIPULATE ADHESION FORCES AT FLUID INTERFACES

A Dissertation
Presented to
The Academic Faculty

by

Roxanne Glazier

In Partial Fulfillment
of the Requirements for the Degree
Doctorate in Biomedical Engineering in the
Wallace H. Coulter Department of Biomedical Engineering

Emory University,
Georgia Institute of Technology
May 2020

COPYRIGHT © 2020 BY ROXANNE GLAZIER

DNA NANOTECHNOLOGY TO MAP AND MANIPULATE ADHESION FORCES AT FLUID INTERFACES

Approved by:

Dr. Khalid Salaita, Advisor
Department of Chemistry
Emory University

Dr. Andrés García
School of Mechanical Engineering
Georgia Institute of Technology

Dr. Jennifer Curtis
School of Physics
Georgia Institute of Technology

Dr. Philip Santangelo
Department of Biomedical Engineering
Georgia Institute of Technology

Dr. Adam Marcus
School of Medicine
Emory University

Date Approved: March 09, 2020

ACKNOWLEDGEMENTS

I would like to thank my advisor, Dr. Khalid Salaita, for his mentorship throughout my PhD. Khalid's creativity, optimism, and technical expertise are inspiring, and I am infinitely grateful for the opportunity to train with him. I would also like to thank my committee members, Drs. Jennifer Curtis, Andrés García, Adam Marcus, and Philip Santangelo, as well as my collaborators, Drs. Olivier Destaing and Alexa Mattheyses, whose scientific insight and mentorship have shaped both my project and my career.

My graduate experience has been enhanced by incredibly talented labmates and friends in the Salaita Lab. It is rewarding to work with such an intelligent, fun, and diverse team, and I appreciate everyone's help and support. Our daily scientific and social conversations have kept me engaged and sane. I look forward to seeing everyone's accomplishments and to future collaborations throughout our careers.

Graduate school would not have been the same without my very close friends. Thank you to my graduate school friends Samantha Boone, Meredith Fay, and Dr. Shannon Rivera for friendship and camaraderie. I am lucky to have found a roommate during BME interviews who is such a compassionate friend and classmate; thank you to Alexandra Atalis for becoming my Atlanta family. Thank you to Rachel Weinstock, Michelle Fox, and Leah Lefkowitz for always there and for many wonderful dinners together.

Lastly, I would like to thank my parents for their undying love and support and to offer a special thank you to my dad, Dr. Arnold Glazier. He has inspired me to challenge myself and to be persistent from a young age.

TABLE OF CONTENTS

ACKNOWLEDGEMENTS	iv
LIST OF TABLES	viii
LIST OF FIGURES	ix
COMMON ABBREVIATIONS	xiii
SUMMARY	xvi
CHAPTER 1. Introduction	1
1.1 Podosome Mechanobiology	1
1.1.1 Podosomes in Cell Biology and Disease	1
1.1.2 Podosome Structure and Mechanics	3
1.2 Biophysical Methods	14
1.2.1 FLIM-FRET and Static Quenching	14
1.3 Dissertation Scope and Outline	16
CHAPTER 2. Supported Lipid Bilayers to Probe Cell Mechanobiology	19
2.1 Abstract	19
2.1.1 Highlights	20
2.2 Introduction	20
2.2.1 Receptor Mechanics	24
2.2.2 Advantages of Supported Lipid Bilayers	25
2.3 Mechanics in Supported Lipid Bilayer Systems	28
2.3.1 Mechanics of Supported Lipid Bilayers	28
2.3.2 Frictional and Mechanical Forces on Membranes and Receptor-Ligand Complexes	31
2.4 Supported Lipid Bilayer Technologies	36
2.4.1 Methods to Perturb Bilayer Mechanics	36
2.4.2 Patterning to Control Receptor Mechanics	44
2.5 Methods to Measure Receptor Forces at Fluid Interfaces	50
2.5.1 Molecular Tension on Supported Lipid Bilayers	50
2.5.2 Tension Measurements on Supported Lipid Bilayers	54
2.6 Mechanobiology of Adhesion Revealed Using Supported Lipid Bilayers	55
2.6.1 Lateral Fluidity Guides Cell Adhesion	55
2.6.2 Mechanobiology of Nascent Integrin Adhesions	60
2.6.3 Mechanobiology of Cadherin-Mediated Adhesion	64
2.7 Conclusions and Future Directions	67
CHAPTER 3. DNA Mechanotechnology Reveals That Integrin Receptors Apply pN Forces in Podosomes on Fluid Substrates	70
3.1 Abstract	70
3.2 Introduction	70

3.3	Results	73
3.3.1	Podosome actin content correlates with RGD-probe depletion	73
3.3.2	MT-FLIM maps pN receptor tension and clustering on SLBs	74
3.3.3	Podosome forces are primarily vertical	80
3.3.4	Integrin forces are actin but not myosin IIa dependent	83
3.3.5	Protrusion and tension engage in a mechanical feedback loop	84
3.3.6	Efficient podosome formation requires integrin tension	87
3.4	Discussion	90
3.5	Methods	94
3.5.1	Sample Preparation, Purification, and Characterization	94
3.5.2	Experimental Methods	98
3.5.3	Molecular Tension – Fluorescence Lifetime Imaging Microscopy Calibration	103
3.5.4	Analysis, Modelling, and Statistics	104
CHAPTER 4.	Evaluation of DNA-Based Probes for Mapping Receptor Forces on Fluid Substrates	108
4.1	Abstract	108
4.2	Introduction	109
4.3	Results	115
4.3.1	Absorbance Spectroscopy of Molecular Tension Probes in Solution	116
4.3.2	Fluorescence Imaging of Tension Probes on SLBs	118
4.3.3	Tension Imaging of Podosome-like Adhesions with Varied Energy Transfer	127
4.4	Discussion	134
4.4.1	Discussion of Probe Design and Spectroscopy	134
4.4.2	Recommendations for Cellular Imaging	136
4.5	Methods	139
4.5.1	Sample preparation	139
4.5.2	Characterization and application of DNA-based tension probes	141
4.5.3	Cell culture	143
4.5.4	Analysis and Statistics	143
CHAPTER 5.	Conclusions	147
5.1	Summary of Advances	147
5.1.1	Discussion of Biological Limitations	148
5.2	Outstanding Questions and Directions in Podosome Mechanobiology	149
5.3	Additional Applications of DNA Nanotechnology at Fluid Interfaces	150
5.4	Novel Applications of DNA-Based Tension Probes and Time-Resolved Fluorescence	151
APPENDIX A.	Supporting Information	153
A.1	DNA Nanotechnology Reveals that Integrin Receptors Apply pN Forces in Podosomes on Fluid Substrates	153
A.1.1	Probe Synthesis and Validation	153
A.1.2	Podosome Model Characterization	159
A.1.3	Molecular Tension – Fluorescence Lifetime Imaging Microscopy	161
A.1.4	Molecular Force Microscopy	176

A.1.5	Mechanisms of Podosome Force Generation	178
A.1.6	Manipulation of Podosome Mechanics	181
A.1.7	Cell Culture	186
A.2	Analysis of DNA Hairpin-Based Tension Probes for Cellular Imaging	187
A.2.1	Probe synthesis and purification	187
A.2.2	Tension Probe Characterization	189
A.2.3	Cellular Imaging	195
APPENDIX B.	Permissions	200
REFERENCES		217

LIST OF TABLES

Table A 1	Oligonucleotide Sequences.	153
Table A 2	Summary of MALDI-TOF Results	158
Table A 3	Summary of TCSPC Settings	161
Table A 4	Percent Open Curve Fit Parameter	167
Table A 5	Photons per Pixel with $\tau < 2.97$ ns	169
Table A 6	Oligonucleotide Sequences	187
Table A 7	Summary of Fluorescence Lifetime, Intensity, and Quenching Efficiencies in Open and Closed Tension Probes	192

LIST OF FIGURES

Figure 1	Podosomes Contain a Core-Ring Organization	4
Figure 2	Electron Micrographs of Micrographs of Membrane Topography and Actin in Podosomes.	6
Figure 3	Superresolution Imaging of Podosome Protein Localization.	7
Figure 4	Graphical Model of Podosome Mechanics and Organization	8
Figure 5	Updated Model of Podosome Actin Networks and Protein Localization	10
Figure 6	Podosome	12
Figure 7	Schematic of FRET versus Static Quenching	15
Figure 8	Schematic of TCSPC and FLIM	16
Figure 9	SLBs Model Cell-Cell Junctions.	20
Figure 10	Supported Lipid Bilayer (SLB) Design and Mechanics.	27
Figure 11	SLB Phase and Diffusion Tuning	44
Figure 12	SLB composition and substrate patterning.	48
Figure 13	MTFM probes to map pN receptor tension at SLB-cell junctions.	53
Figure 14	Cell adhesion on SLBs	56
Figure 15	Mechanotransduction in integrin and cadherin-mediated adhesion assembly.	61
Figure 17	Fibroblasts exert pN integrin tension in podosome rings on SLBs	77
Figure 18	Integrins exert vertical forces in podosome rings	82
Figure 19	Actin polymerization drives integrin tension	84
Figure 20	Loss of integrin ring tension causes local podosome retraction	86

Figure 21	Podosomes maturation requires $F > 12$ pN integrin tension	89
Figure 22	Podosome ring modeling estimates nN tensile forces.	92
Figure 23	DNA-Based Tension Probes Report Receptor Mechanobiology.	110
Figure 24	Summary of DNA Hairpin-Based Tension Probes Evaluated in this Study.	114
Figure 25	Absorption Spectroscopy Reveals Ground-State and Dye-DNA Interactions in Molecular Tension Probes.	117
Figure 26	Fluorescence analysis of Cy3B/BHQ1 probes on an SLB.	121
Figure 27	Fluorescence analysis of A488/Cy3B probes on an SLB.	123
Figure 28	Fluorescence analysis of A488/BHQ1 probes on an SLB.	124
Figure 29	Streptavidin-Immobilized Tension Probes Undergo Intermolecular FRET.	126
Figure 30	Tension Probe Design Impacts the Cellular Read-Out	131
Figure A 1	Chemical structures in oligonucleotide probes.	155
Figure A 2	HPLC chromatograms of modified oligonucleotides.	156
Figure A 3	MALDI-TOF spectra of oligonucleotides	157
Figure A 4	NIH 3T3 fibroblasts form podosomes on fluid RGD-oligonucleotides.	159
Figure A 5	Podosome protrusion does not disrupt the SLB.	160
Figure A 6	Absorption spectra of MTFM and MT-FLIM probes.	161
Figure A 7	MT-FLIM probe calibration.	162
Figure A 8	MT-FLIM probe density slightly reduces fluorescence lifetime.	163
Figure A 9	Podosome rings and integrin clusters contain $\beta 1$ integrin.	164
Figure A 10	Analysis of MT-FLIM photon statistics.	170
Figure A 11	MT-FLIM Analysis Flowchart.	171

Figure A 12	Invadosomes exert pN tension.	172
Figure A 13	Tension probes unfold specifically under integrin-mediated forces.	173
Figure A 14	MT-FLIM dynamics of podosome maturation.	174
Figure A 15	Analysis of clustering and tension dynamics on static quenched tension probes.	175
Figure A 16	MFM set-up and excitation-resolved polarization validation.	176
Figure A 17	Emission resolved fluorescence data does not indicate lateral organization of integrin forces in podosomes.	177
Figure A 18	Actin polymerization and nonconventional myosin regulate podosome mechanics.	178
Figure A 19	Myosin IIa is dispensable in podosome ring force generation.	179
Figure A 20	Kinetics of fluorescence recovery after biotin photostimulation.	181
Figure A 21	Integrin tension is released following PCB photostimulation.	182
Figure A 22	Podosome protrusion is primarily perturbed at the site of photocleavage.	183
Figure A 23	Podosome protrusion is primarily perturbed at the site of photocleavage.	185
Figure A 24	NIH 3T3 Cell Profile	186
Figure A 25	HPLC purification of modified oligonucleotides.	188
Figure A 26	Absorbance spectra of single-dye modified tension probes	189
Figure A 27	Representative TCSPC curve fits.	190
Figure A 28	Analysis of intensity and lifetime derived quenching efficiencies.	191
Figure A 29	Analysis of dual- and single-biotin tension probes on SLBs.	193

Figure A 30	Influence of spacer and overhang sequences on three-way junctions in tension probes.	194
Figure A 31	Analysis Map for Podosome Identification on High QE Probes	195
Figure A 32	Analysis Map for Podosome Identification on Low QE Probes	195
Figure A 33	Analysis Map for Podosome Identification on A_Cy3B/BHQ1- Linear Probes	196
Figure A 34	Analysis of Tension Probe Signal on S_CY3B/BHQ1- (MT-FLIM) and S_Cy3BBHQ1+ Probes.	197
Figure A 35	Analysis of Tension Probe Signal on A_Cy3B/BHQ1- and A_Cy3B/BHQ1+ Probes.	198
Figure A 36	Analysis of Tension Probe Signal on A_A488/BHQ1- and A_A488/BHQ1+ Probes	199

COMMON ABBREVIATIONS

τ	Fluorescence Lifetime
-	Hairpin strand lacking spacer sequences
+	Hairpin strand containing spacer sequences
A	Adjacent Probe
A488	Alexa Fluor 488
AFM	Atomic Force Microscopy
AJs	Adherens junctions
Amp.	Amplitude
ARP2/3	Actin Related Protein 2/3 Complex
AuNPs	Gold nanoparticles
BHQ1	Black Hole Quencher 1
bp	Base pair
BSA	Bovine serum albumin
C	Closed
cRGDFK	Cyclic Arg-Gly-Asp- <i>D</i> -Phe-Lys
D	Dangling Probe
DC	Dendritic cell
DNA	Deoxyribonucleic acid
DOPC	1,2-dioleoyl-sn-glycero-3-phosphocholine
dSTORM	Direct Stochastic Optical Reconstruction Microscopy
ECM	Extracellular matrix
EM	Electron microscopy
EMCCD	Electron Multiplying Charge Coupled Device

$F_{1/2}$	Force at which 50% tension probes unfold
FA	Focal adhesions
FCS	Fluorescence Correlation Spectroscopy
FLIM	Fluorescence Lifetime Imaging Microscopy
FRAP	Fluorescence Recovery After Photobleaching
FRET	Forster Resonance Energy Transfer
GUV	Giant unilamellar vesicle
HPLC	High Performance Liquid Chromatography
Int.	Integrin or Intensity
IRF	Instrument Response Function
LSM	Laser Scanning Microscope
MALDI-TOF	Matrix Assisted Laser Desorption/Ionization- Time of Flight
MFM	Molecular Force Microscopy
MHz	Megahertz, 10^6 Hz
MT-FLIM	Molecular Tension - Fluorescence Lifetime Imaging Microscopy
MTFM	Molecular Tension Fluorescence Microscopy
NA	Nascent adhesions
nN	nanonewton, 10^{-9} newtons
nt	Nucleotide
O	Open
PC	Photocleavable
PFM	Protrusion Force Microscopy
pN	piconewton , 10^{-12} newtons
QE	Quenching efficiency
R	Radius

R_0	Forster radius
ROI	Region of interest
S	Separated Probe
s.e.m.	Standard Error of the Mean.
SD	Standard Deviation
SLB	Supported lipid bilayer
SNR	Signal-to-noise ratio
SUV	Small unilamellar vesicle
TCR	T-cell receptor
TCSPC	Time Correlated Single Photon Counting
TFM	Traction Force Microscopy
TGT	Tension Gauge Tether
TIRF	Total Internal Reflection Microscopy
T_{tol}	Tension Tolerance
TWJ	Three-way junction
WAS	Wiskott-Aldrich Syndrome
WT	Wild type
μM	Micromolar, 10^{-6} Molar
μm	Micron, 10^{-6} m

SUMMARY

Cells transmit piconewton (pN) receptor forces to ligands in the extracellular matrix (ECM) and on the surface of adjacent cells. These forces regulate functions ranging from adhesion to clotting and the immune response. Whereas adhesion mechanics on rigid substrates are well characterized, understanding mechanotransduction at cell-cell junctions remains challenging due to a lack of tools. We develop and apply new classes of DNA-based force probes to map and manipulate receptor forces on supported lipid bilayers (SLBs), planar membranes that mimic an adjacent cell. We use these probes to elucidate force balance in podosomes, which are multipurpose protrusive structures that form at cell-cell and cell-ECM interfaces. Podosomes have a core-ring architecture, and previous works demonstrated that the podosome's actin core generates nanonewton protrusive forces. However, the podosome's contractile landscape remained poorly understood. In Aim 1 (Chapter 3), we develop and apply Molecular Tension- Fluorescence Lifetime Imaging Microscopy to map integrin receptor forces and clustering on SLBs. We demonstrate that integrin receptors apply pN tension in podosome rings. We then introduce photocleavable probes to site-specifically perturb adhesion forces and apply rupturable DNA-based force probes to test the role of receptor tension in podosome formation and maintenance. These studies confirm a local mechanical feedback between podosome core protrusion and integrin receptor tension. In Aim 2 (Chapter 4), we evaluate structure and energy transfer across a library of DNA-based tension probes using spectroscopy and microscopy. We then demonstrate the functional implications of probe design on cellular imaging. This work expands our understanding of receptor forces in podosome mechanobiology and contributes new insight and tools for studying juxtacrine receptor interactions.

CHAPTER 1. INTRODUCTION

Integrin receptors are heterodimeric transmembrane proteins that bind to a variety of ligands on the extracellular matrix and on neighboring cells¹⁸. Integrins form multiple classes of adhesions, and their bonds are strengthened by receptor activation under force^{19, 20}. The best characterized integrin-mediated adhesions are focal adhesions (FA), which serve as the major mechanical linkage between the cell and the ECM. FA exert lateral traction forces²¹ and have a fibrillar, layered architecture²². An additional class of integrin mediated adhesions are invadosomes, which consist of podosomes and invadopodia, podosome-like adhesions in cancer²³. These structures contain many of the same adhesion proteins as FA, but they have a unique columnar architecture and carry out specialized functions (1.1.1)²⁴. These adhesions are most commonly associated with cell-ECM junctions^{25, 26}; however, podosome-like adhesions have also been identified at cell-cell junctions^{27, 28, 29} and on fluid biomimetic membranes called Supported Lipid Bilayers (SLBs)⁹. While many studies have quantified integrin forces in FA^{21, 30, 31, 32}, these forces were not previously characterized in podosomes or on an SLB. To address this gap, we characterized podosome mechanics by quantifying and perturbing integrin receptor forces in podosomes formed on SLBs. To achieve this, we developed, optimized, and applied novel DNA-based force probes³³ to elucidate integrin receptor mechanics with molecular specificity³⁴. These probes have broad applications to the study of mechanobiology.

1.1 Podosome Mechanobiology

1.1.1 *Podosomes in Cell Biology and Disease*

Podosomes are multipurpose, actin-rich adhesions that play a critical role in cell migration, invasion, and mechanosensing^{35, 36, 37}. Podosomes were first discovered in the 1980s, when David-Pfety and Singer demonstrated that Rous Sarcoma Virus-transformed fibroblasts concentrated vinculin and α -actinin in puncta, rather than in focal adhesions³⁸. These structures were later named ‘podosomes,’ because they colocalized with membrane protrusions that resembled cellular feet^{23, 39}. Podosomes have since been shown to play a diverse role in cell biology, forming at both cell-cell and cell-matrix interfaces. Interestingly, podosomes both adhere to the matrix and release metalloproteinases to facilitate its degradation and remodeling^{40, 41}. In osteoclasts, podosomes are required to form the sealing zone for bone resorption^{25, 42}, and in platelets, podosomes support early adhesion to fibrinogen during blood clotting⁴³. Podosomes in the immune system coordinate topography sensing and directional cell migration, diapedesis, and antigen scavenging^{27, 28, 44, 45}. At cell-cell junctions between immature myoblasts or macrophages, podosome formation precedes cell fusion^{29, 46, 47}.

Podosomes play a critical role in disease. Invasive podosomes called invadopodia facilitate cell migration and invasion in cancer by releasing exosomes containing matrix metalloproteinases^{23, 48, 49}, and endothelial cell podosomes promote angiogenesis in tumors. Indeed, several studies are currently investigating anti-metastasis agents that target invadopodia formation^{50, 51}. Podosomes are also indicated in several genetic diseases in which genes encoding actin-binding proteins are mutated. The best-studied case is Wiskott-Aldrich Syndrome, which is caused by mutations in the WAS gene and leads to impaired clotting and frequent infections⁵². This is hypothesized to result from cells’ failure to form podosomes when WAS protein (WASP) is mutant or deficient^{53, 54}. An additional example

is Frank-Ter Haar Syndrome, which is caused by mutations in the gene encoding Tsk4⁵⁵. This protein is required for podosome formation, and patients suffer developmental defects and respiratory infections^{55, 56}. Finally, podosomes can be dysregulated through viral infections. Many HIV patients suffer from reduced bone density, and this is hypothesized to result from enlarged podosomes with enhanced bone resorption capabilities that are found in HIV infected cells⁵⁷. HIV also promotes increased macrophage migration through podosome-dependent migration modes⁵⁸. Thus, given the vast importance of podosomes in cell biology and disease, it is critical to understand the fundamental molecular biology and regulation of these structures.

1.1.2 *Podosome Structure and Mechanics*

Podosomes contain actin-rich puncta, which colocalize with adapter and adhesion proteins including integrin receptors, vinculin, Arp2/3, WASP, and cortactin^{23, 59}. On deformable substrates such as adjacent cells, hydrogels, and ECM, actin puncta are sites of membrane protrusions that extend from the cell^{39, 60}. Podosomes are best characterized at two-dimensional (2D) interfaces, which will be the focus of our work and discussion. In 2D, podosomes have a modular core-ring structure (Figure 1). The podosome's densely crosslinked actin core excludes adhesion proteins, which instead accumulate at the periphery of the core in the podosome ring⁶¹. The ring and core are connected through actin cables^{61, 62} and a capping structure^{63, 64}, though the capping structure remains poorly characterized.

Previous work demonstrated that actin core polymerization exerts pushing forces on the substrate. In our work, we demonstrate that integrin-mediated tensile forces in the

podosome ring oppose core protrusion (Figure 1). While podosomes act primarily as independent mechanosensors⁶⁵, cells typically form multiple podosomes. Throughout their lifecycle, podosomes can split, fuse, and assemble into superstructures that coordinate podosome function^{25, 35, 61, 66, 67, 68}. Individual podosomes within this network are connected by an actin cloud⁶⁹.

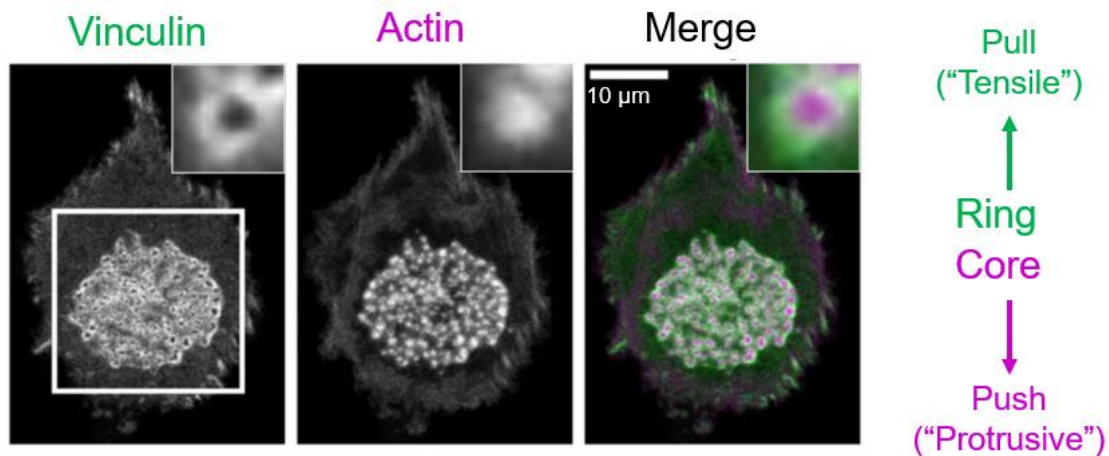


Figure 1 Podosomes Contain a Core-Ring Organization

Confocal imaging of podosomes forming in DCs on glass. Actin puncta correspond to the podosome's protrusive core, which is surrounded by a ring of adhesion proteins, including vinculin. In this dissertation, we demonstrate that the podosome ring applies tensile forces that oppose local actin protrusion. Adapted from Meddens, et. al.⁷⁰ with open access permission from Creative Commons.

1.1.2.1 Advanced Microscopy Reveals Podosome Ultrastructure

Advanced imaging has facilitated podosome structural knowledge, which provides the basis for podosome mechanical models. In this section, we provide a review of these insights. In early structural studies, Transmission Electron Microscopy (TEM) elucidated the cell membrane at podosomes. On rigid substrates, podosomes protruded minimally but exhibited membrane puckering in between individual podosome cores⁶⁰ (Figure 2A). In

contrast, podosomes forming on soft substrates protruded several microns from the cell body (Fig 2B). This behavior was consistent both on gelatin substrates and at cell-cell junctions^{27, 60}, and protrusion depth was myosin II dependent⁶⁰. At the T cell-antigen presenting cell (APC) junction, TEM revealed that the membrane-to-membrane distance was 15 nm at the base of the podosome core compared to 150 nm outside of this region²⁷. Therefore, TEM suggested that podosome cores may exert pushing forces.

By applying Scanning Electron Microscopy (SEM), Luxenburg revealed the actin structure of podosome networks (Figure 2C). This was previously visible as a diffuse network using fluorescence imaging⁶⁹, however SEM allowed visualization of individual actin cables^{62, 71}. Podosomes in osteoclast precursors appeared as dense, ~300 nm cores, which contained multiple actin fibers oriented perpendicular to the cell membrane. An additional population of actin radiated outwards from the core, extending up to 3 μ m in diameter; these cables connected to the actin cloud, which surrounded the individual podosomes⁶². Similar podosome actin structures have since been shown in dendritic cells (DCs) and in smooth muscle cells^{44, 72}. Importantly, podosome connectivity appears to be cell-type specific. While mature osteoclasts and DCs both exhibited actin cables directly linking individual podosome cores, in immature osteoclasts, cables connected to the cloud but not to adjacent podosome cores^{44, 62}, which could impact mechanosensing.

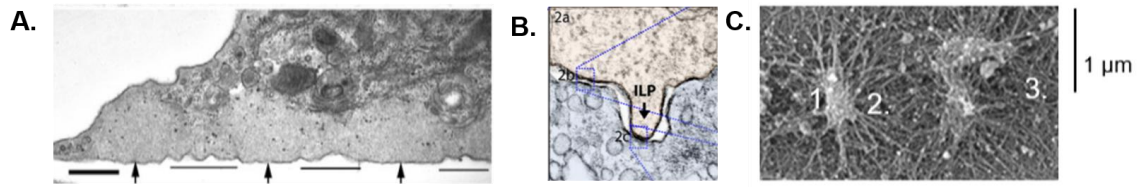


Figure 2 Electron Micrographs of Membrane Topography and Actin in Podosomes.

(A, B) TEM images of podosomes in a DC on glass (A) and in T cell at a T cell-antigen presenting cell junction (B). Arrows indicate podosome cores. In A, lines indicate podosome rings, which experienced membrane ruffling. Scale Bar, 200 nm (A), unavailable (B). C. Scanning electron micrograph of podosomes in an osteoclast precursor cell reveal actin cores (1), actin cables (2), and the actin cloud (3). Adapted from ^{27, 60, 62} with open access permission from Creative Commons and publisher permission.

Podosome's distinct actin populations are also visible in superresolution imaging, which have been useful in mapping podosome protein distribution and geometry^{61, 64, 65, 67}. The first superresolved podosome images used Bayesian Localization Microscopy (3B) to map vinculin in podosome rings⁶⁷. Compared to diffraction-limited images which had suggested a continuous podosome ring, 3B revealed a polygonal structure comprised of 6-60 nm wide vinculin strands that intersected at 116-135 degree angles (Figure 3A)^{67, 73}. In stabilized podosomes, these strands colocalized with talin, however disassembling podosomes lacked talin or showed talin at the podosome core⁷³.

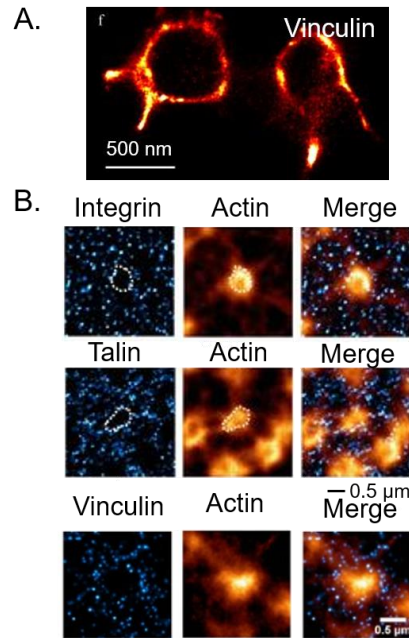


Figure 3 Superresolution Imaging of Podosome Protein Localization.

(A) 3B superresolution images of vinculin in podosome rings. (B) dSTORM maps of integrin receptor, talin, and vinculin localization in podosomes. Integrin receptors and talin are dispersed outside the podosome core. Vinculin is clustered near the podosome core and aligned with actin cables. Adapted from ^{61, 67} with publisher permission and under Creative Commons open access licensing, respectively.

To better understand the distribution of adhesion proteins in relationship to actin, van den Dries and colleagues conducted Dual-color Direct Stochastic Optical Reconstruction Microscopy (dSTORM) on DC podosomes⁶¹. In agreement with SEM data, podosome cores appeared as actin puncta with radiating actin cables. Adhesion proteins were localized to islets that were excluded from podosome actin cores. Interestingly, in these cells, talin and vinculin had differential organizations. $\alpha M\beta 2$ integrin and talin islets were diffusely spread outside of podosome cores (Figure 3B), whereas vinculin islets localized specifically to a confined ring region and were densest near actin cables (Figure 3B)⁶¹. Given this distribution and vinculin's mechanosensitivity⁷⁴, van den Dries and colleagues hypothesized that actin core polymerization may drive tension on actin cables, leading to vinculin ring recruitment⁶¹. Three-dimensional dSTORM of macrophage

podosomes revealed mechanically stretched talin in podosome rings, with the increasing end-to-end distance in regions closer to the podosome core⁶⁵. Vinculin colocalized with stretched talin, and its binding height corresponded with talin stretching. Thus, while there appear to be some cell-type specific determinants of talin localization, these data further support the notion that the podosome core drives tension on the ring, which influences adhesion protein localization and structure (Figure 4).

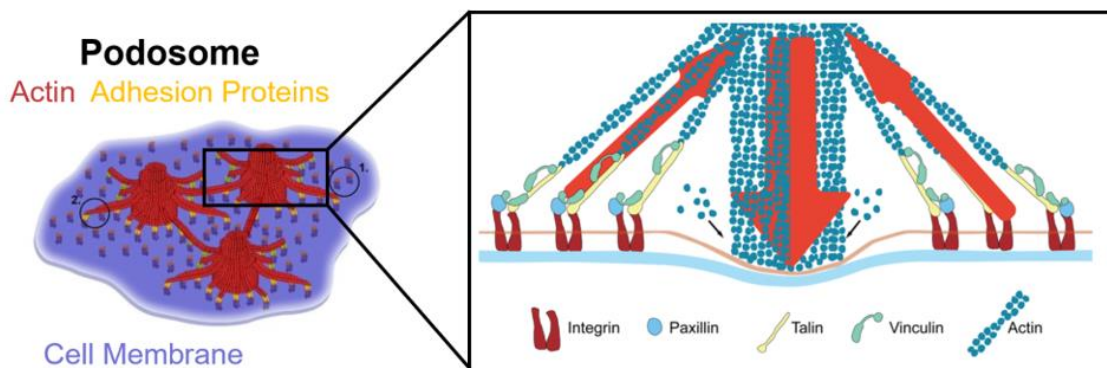


Figure 4 Graphical Model of Podosome Mechanics and Organization

Model of podosome mechanics supported by imaging and mechanical measurements of podosome protrusion (1.1.2). Polymerizing actin cores exclude adhesion proteins and exert pushing forces on the membrane. Talin is stretched near the podosome core, and vinculin is recruited to actin cables under tension. Adapted from ⁶¹ under the Creative Commons Licensing agreement and with permission from and ⁶⁵, Copyright (2017) American Chemical Society.

Since 2018, two new superresolution microscopy papers have challenged the simple model of podosome core-ring structure with actin cables. Joosten and colleagues sequentially imaged podosomes with Airyscan Microscopy and SEM⁴⁴. Their combined fluorescence and SEM data revealed an unexpected protein distribution and actin population. A newly observed actin network bridged nearby neighbors though cables that were sensitive to substrate roughness but not to pharmacological inhibition of actin polymerization. These cables connected individual podosome cores and were zyxin rich,

which was an unexpected observation, because zyxin was previously localized only to the podosome ring⁷⁵.

Following up on this work and concurrent with our manuscript (Chapter 3), van den Dries used superresolution imaging to analyze protein localization in relation to actin networks. Interestingly, this work not only differentiated actin cable subpopulations but also revealed multiple actin structures that overlapped the core and ring. This newest structural model divided podosome actin into four pools: The Protrusion Module (cPM), the peripheral Protrusion Module (pPM), ventral filaments, and dorsal filaments. The cPM and pPM contained branched and fibrillar actin, respectively. Crosslinking proteins that are strongly associated with actin cores, such as WASP and Arp2/3, localized to the cPM. The pPM enclosed the cPM and colocalized with proteins typically found in both podosome cores and rings, including α -actinin, vinculin, and capping proteins which are found over the core⁶³. The protrusion modules connected to radiating actin cables. Ventral filaments surrounded the pPM and dorsal filaments connected actin cores⁴⁴ near the capping region. Whereas adhesion proteins localized primarily to ventral filaments, myosin IIa motor protein localized primarily to the dorsal filaments, indicating a distinct spatial organization. On deformable substrates, actin dorsal filaments shortened, causing vinculin and zyxin to concentrate nearer to the podosome core. Myosin IIa localization was unaltered, suggesting it plays a minor role in mechanosensing⁶⁴. These structural data fit with a model where podosome formation and ring protein recruitment are myosin IIa-independent^{9, 75}. While for the purpose of this dissertation and the present podosome literature, we describe podosomes by their more classical core-ring structure, these new maps of podosome architecture can provide interesting mechanobiological insight. These maps support a

model of protrusion-mediated tension on lateral actin cables, which cause mechanosensitive protein recruitment^{60, 64, 71, 75}. The podosome structure adapts to substrate topography and stiffness, and the response is primarily mediated through the actin cytoskeleton.

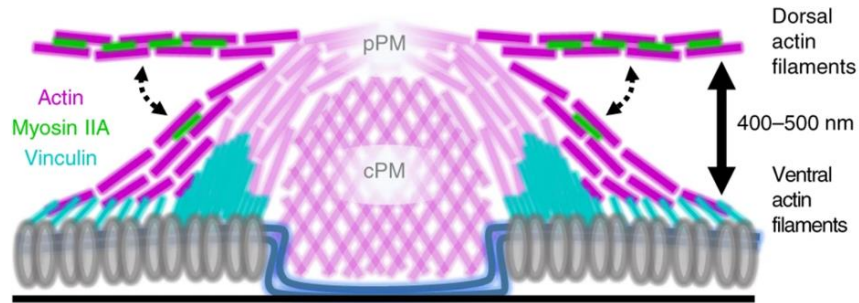


Figure 5 Updated Model of Podosome Actin Networks and Protein Localization

Schematic of the updated podosome structural mechanics. Rather a classical core-ring structure, in this model, the podosome is divided into four actin networks with some overlap between the core and ring. Schematic reprinted from van den Dries, et. al.⁶⁴ with permission under Creative Commons.

1.1.2.2 Podosomes are Dynamic Mechanosensors and Mechanotransducers

Podosomes sense and respond to substrate mechanics, and several studies have aimed to characterize podosome mechanobiology by combining biomaterials-based approaches with mathematical modeling, atomic force microscopy, and genetically encoded tension sensors^{65, 70, 75, 76, 77, 78}. In this section we describe critical advances in this field, which set precedent to our research.

Podosome formation is regulated by substrate properties. Cells tend to form more podosomes on stiffer substrates, and podosome formation on glass is enhanced and aligned on nanoscale scratches^{45, 70, 76, 78}. The podosome's stiffness response corresponds with force generation. In the first demonstration of the podosome as a mechanosensor and a mechanotransducer, fibroblasts were seeded on hydrogels with substrate stiffness from 2

to 6.5 kPa⁷⁹. These cells formed large podosome belts, which exerted increasing traction forces with increased substrate stiffness (Figure 6A-C). When an RGD-coated magnetic bead was used to exert forces on the cell, the tractions measured under the podosome belt increased. While these data do not reveal the molecular basis of mechanotransduction and reveal only the forces exerted by a collection of podosomes, they suggest that podosomes do indeed exert traction forces.

Using a clever Atomic Force Microscopy (AFM)-based method, Labernadie and colleagues later showed that podosomes also exert protrusion forces, which respond similarly to increasing stiffness⁷⁶. In this method, called Protrusion Force Microscopy (PFM), cells form podosomes on deformable FORMVAR membranes (EM grids). The AFM cantilever traces over podosome-induced deformations, which are caused by actin polymerization. This allows mapping of protrusion height and can be used to back-calculate the applied force. PFM reported that individual podosome cores deformed the membrane by up to 20 nm, which corresponded to nN protrusion forces. The magnitude of

force was higher on stiffer FORMVAR substrates (Figure 6D,E).

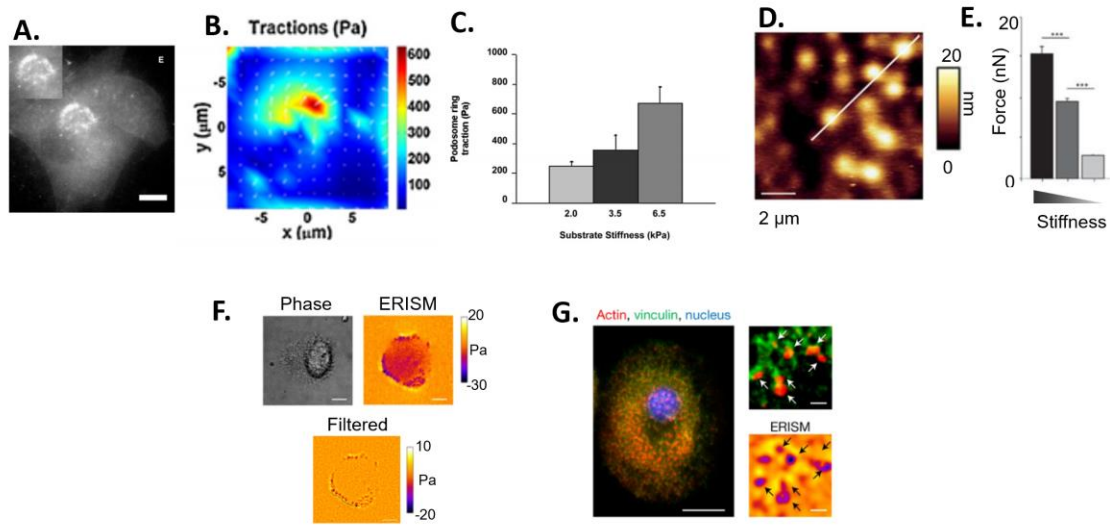


Figure 6 Podosomes are Mechanotransducing Structures.

(A) Podosome belt in a BHK cell labeled with mCherry-actin on a polyacrylamide hydrogel. Scale bar, 20 μm . (B) Traction force map of stress beneath the ring. (C) Quantification of cellular tractions as a function of substrate stiffness. (D) Representative protrusion force microscopy map depicts podosome-induced deformations. (E) Quantification of protrusive forces by PFM as a function of substrate stiffness. Note that the Y axis has been changed following collaborator correspondence with coauthors. (F) Interference-based maps of positive and negative stresses beneath a podosome-forming macrophage. (G) Multiplexed immunostaining and interference-based force measurements of podosomes. Arrows indicate vinculin-rich regions of tension. Figures adapted from literature^{76, 79, 80} with publisher and Creative Commons permission.

Podosomes mechanics are highly dynamic and integrate adhesion, contractility, and polymerization. Individual podosome protrusiveness was reduced in cells treated with pharmacological inhibitors of actin polymerization, Rho Kinase, and myosin II, as well as in talin-, vinculin-, and myosin II- depleted macrophages^{65, 76}. Interestingly, podosome protrusiveness⁷⁶, Young's modulus⁷⁷, and actin content⁶⁶ are all oscillatory. Oscillations are locally correlated and are regulated by myosin II, which, along with actin polymerization, also tunes ring protein recruitment^{66, 71, 75}. These observations lead to a

model in which actin polymerization induces tension on the podosome ring, causing mechanosensory protein recruitment^{71, 75}.

Indeed, given the observation that individual podosomes exert protrusion forces, podosomes must also be under tension in order to achieve force balance⁸¹. Original traction force measurements support this notion but lack the spatial resolution to elucidate the contractile landscape of individual podosomes⁷⁹. Bouissou and colleagues computationally demonstrated that ring tension is required by modeling an array of podosomes exerting pushing forces⁶⁵. Podosomal protrusions were only recovered when opposing tensile forces were distributed in rings surrounding each individual podosome. Tension at the periphery of the cell or spread diffusely across the cell-material interface was unable to support protrusion. This model was further supported by experimental evidence of protein stretching in podosome rings and by insertion of genetically encoded tension sensors in vinculin, which showed a slight increase in tension signal in proteins that were coupled to the cytoskeleton. However, tensions maps of these data were not published, making these results difficult to interpret.

In the most sensitive measurements of podosome tension, Kronenberg, et. al. measured both podosome tension and protrusion in macrophages using interferometry⁸⁰. In these cells, podosomes formed in a belt at the periphery of the cell or throughout the cell. Individual podosomes exerted protrusion forces, and spatial filtering revealed tension signal surrounded podosome cores and colocalized with vinculin (Figure 6F,G). While these data suggest podosome ring tension, they still lack sufficiently high resolution to understand the molecular mechanics of podosome force balance. Quantification of podosome protrusion forces using this method suggested that individual podosomes

applied ~ 10 pN, which is small relative to PFM measurements and to reports of individual actin filaments generating pN forces⁸². Thus, there remains a need for additional podosome force quantification.

Models of podosome mechanics are confounded by the observation of podosomes on fluid interfaces. Yu, et. al. found that cells formed multiple podosomal adhesions on RGD-functionalized supported lipid bilayers (SLBs)^{9, 83}. We review this work and the SLB literature extensively in Chapter 2 and in Figure 15⁸⁴, but briefly, SLBs are planar membranes that are fluid in the XY-plane. When SLBs were patterned with gridlines that supported traction force generation, cells formed fewer podosomes⁹. Given that SLBs cannot support lateral traction forces^{16, 84, 85, 86}, this work was used as evidence that podosomes force balance may be independent of adhesion forces³⁶.

1.2 Biophysical Methods

Our work leverages DNA mechanotechnology, fluorescence imaging, and SLBs. For a thorough introduction to and discussion of SLBs and DNA-based tension probes, we refer the reader to our literature review in Chapter 2, Sections 2, 3, and 5.

1.2.1 FLIM-FRET and Static Quenching

An understanding of our probes requires a basic knowledge of Fluorescence Lifetime Imaging Microscopy (FLIM) and static versus dynamic quenching, including Forster Resonance Energy Transfer (FRET)⁸⁷. Briefly, a fluorophore absorbs an incoming photon of wavelength, λ , and energy $h\nu$, causing the fluorophore to transition to the excited state. The fluorophore remains in the excited state for time, τ , which is defined as the

fluorescence lifetime, before undergoing internal relaxations and returning to the ground state. The transition to the ground state can occur by variety of non-fluorescent mechanisms such as quenching or thermal relaxation or through the emission of a photon the form of fluorescence; the frequency of photon emission is described by the quantum yield.

The fluorescence lifetime is an intrinsic property of a fluorophore, but it can be affected by local chemical environment including energy transfer⁸⁸. In FRET, nonradiative energy transfer occurs between a donor and an acceptor fluorophore, leading to intensity-based quenching and shortening of the fluorescence lifetime (Figure 7, Figure 8). This mechanism contrasts with static quenching. In static quenching, two fluorophores in close contact form a ground state complex that cannot be excited^{89, 90, 91}. Thus, the fluorescence lifetime is constant. It is also possible to observe a combination of contact and FRET quenching⁹².

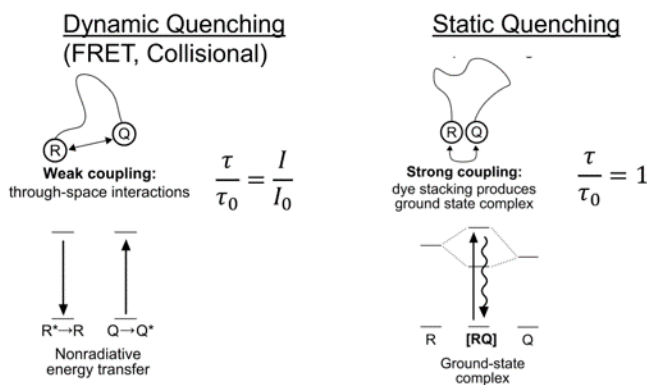


Figure 7 Schematic of FRET versus Static Quenching

Static quenched probes and FRET quenched probes differ in their mechanism of energy transfer and their fluorescence lifetime response to quenching. Note that this FRET relation does not apply in all scenarios⁹². Figure reproduced from ⁹³ with publisher permission.

To measure the fluorescence lifetime, we employ FLIM, which couples Time Correlated Single Photon Counting (TCSPC) with confocal microscopy. In TCSPC, a megahertz (MHz) pulsed laser excites the sample at a sufficiently low frequency to detect

one or fewer photons per pulse. Reconvolution curve fitting of the photon arrival time versus the number of photon counts with the Instrument Response Function (IRF) permits quantification of the individual lifetime components and their relative contributions (Figure 8A). The average intensity- (Int.) and amplitude-weighted (Amp.) fluorescence lifetimes⁹², which are discussed in Chapter 4, are calculated from resulting curve fits. Alternatively, it is possible to estimate τ using a FAST FLIM approach. Here τ is estimated by the center of mass of fluorescence decay per pixel (Figure 8B)⁹⁴.

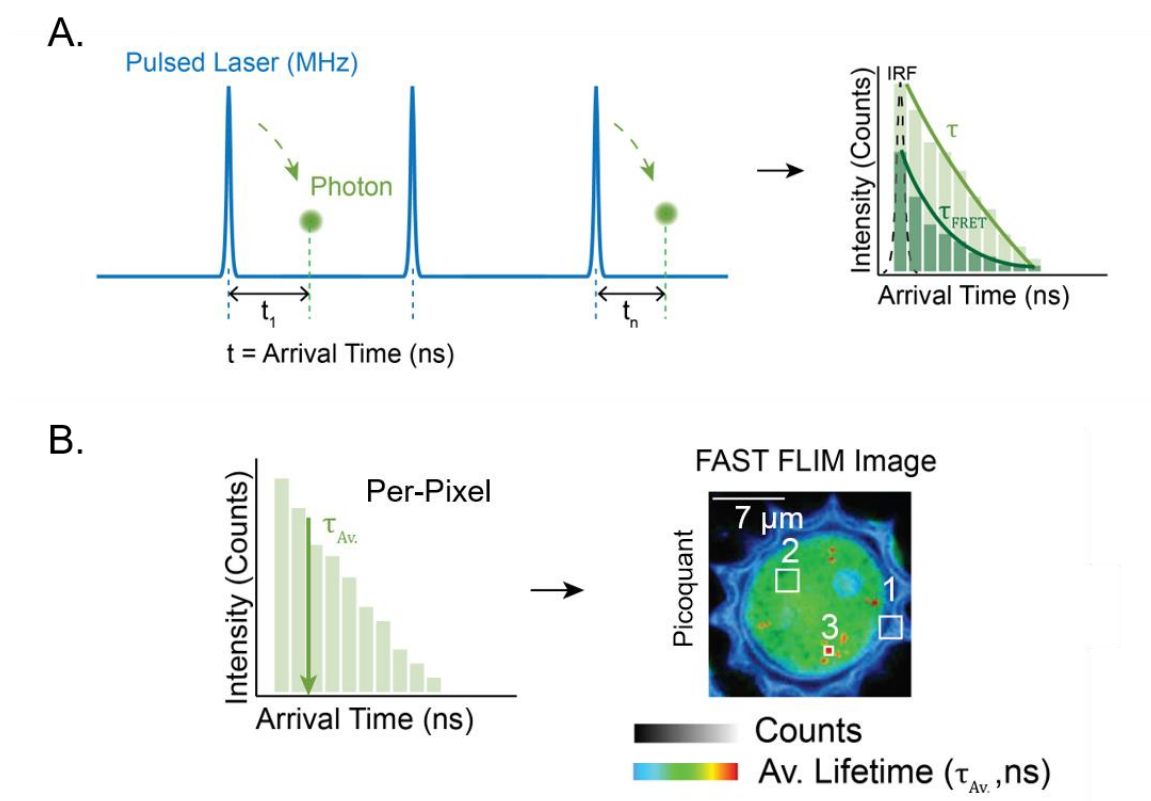


Figure 8 Schematic of TCSPC and FLIM

A. TCSPC reports the arrival time of incoming photons, which is used to determine the fluorescence lifetime. In FRET imaging, the overall brightness and lifetime are reduced.

B. FAST FLIM imaging estimates the fluorescence lifetime per pixel by the barycenter of photon arrival time. FLIM image adapted from the Picoquant website.

1.3 Dissertation Scope and Outline

This dissertation contributes and analyzes new tools for mapping and manipulating receptor forces specifically on fluid interfaces, while addressing key questions in the podosome literature. Whereas previous works have suggested a model of podosome force balance in which actin protrusion is opposed by podosome ring tension, methods to investigate this were indirect or limited in their spatial, mechanical, and molecular resolution^{66, 75, 80}. Furthermore, it seemed that adhesion forces may be unnecessary in this force balance, because of the observation that podosomes form on SLBs^{9, 95}. Indeed, in 2018 it was hypothesized that “regardless of ligand density, cells on DOPC [SLBs] are unable to exert force on the surface”⁸⁵. In this dissertation we challenge this statement and bridge the resolution gap in podosome mechanobiology by combining DNA nanotechnology-based force probes with an SLB-podosome model to investigate force balance.

Chapter 2 contains a detailed literature review⁸⁴ on SLBs and their applications to adhesion mechanobiology. This provides important background information and context to the original research discussed in Chapters 3 and 4. We describe the role of pN forces in cell biology, the mechanics of SLBs, approaches to pattern and manipulate SLBs, and previously developed tools to measure receptor tension in these systems. We then discuss how these surfaces have been applied to study the role of adhesion forces in cell biology, including in nascent integrin adhesions and in podosomes.

Chapter 3 discusses our work integrating DNA nanotechnology with SLBs to study podosome mechanobiology³³. We introduce Molecular Tension – Fluorescence Lifetime Imaging Microscopy (MT-FLIM), which uses the fluorescence lifetime to directly report pN receptor forces on SLBs. We use MT-FLIM combined with Molecular Force

Microscopy²¹ (MFM) to demonstrate that integrin receptors apply pN vertical forces in podosomes on fluid substrates. We then introduce photocleavable probes (PC) to perturb the adhesion forces of podosomes and Tension Gauge Tethers⁹⁶ (TGTs) to test importance of integrin forces in podosome formation. Our work demonstrates that actin polymerization and integrin tension act in a local mechanical feedback within podosomes.

In Chapter 4, we focus on deepening understanding of DNA-based tension probe design. We analyze a library of 19 tension probe variants and characterize them using spectroscopy and imaging. We then apply a selection of these probes to image integrin forces in podosomes to better understand the advantages and disadvantages of design elements. The insights gained from this work will be informative to probe and experimental design for studying receptor mechanics on soft and fluid materials.

In Chapter 5 we conclude with a summary of our advances. This is presented alongside a discussion of questions and future directions for biological investigation and for methodological development.

CHAPTER 2. SUPPORTED LIPID BILAYERS TO PROBE CELL MECHANOBIOLOGY

Adapted from Glazier and Salaita, *BBA – Biomembranes*, 2017.

2.1 Abstract

Mammalian and bacterial cells sense and exert mechanical forces through the process of mechanotransduction, which interconverts biochemical and physical signals. This is especially important in contact-dependent signaling, where ligand-receptor binding occurs at cell-cell or cell-ECM junctions. By virtue of occurring within these specialized junctions, receptors engaged in contact-dependent signaling undergo oligomerization and coupling with the cytoskeleton as part biochemical signaling within cell junctions has advanced over the past decades, physical cues remain difficult to map in space and time. Recently, supported lipid bilayer (SLB) technologies have emerged as a flexible platform to measure and manipulate membrane receptor mechanotransduction, allowing one to mimic cell-cell junctions (Figure 9). Changing the lipid composition and underlying substrate tunes bilayer fluidity, and lipid and ligand micro- and nano-patterning spatially control positioning and clustering of receptors. Patterning metal gridlines within SLBs introduces corrals that confine lipid mobility and introduce mechanical resistance. Here we review fundamental SLB mechanics and how SLBs can be engineered as tunable cell

substrates for mechanotransduction studies. Finally, we highlight the impact of this work in understanding the biophysical mechanisms of cell adhesion.

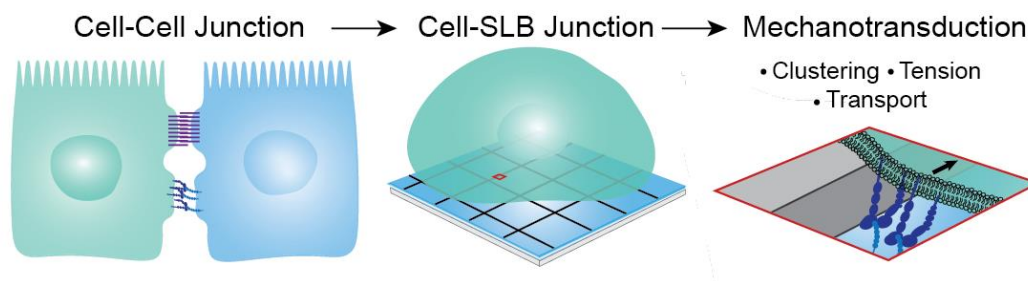


Figure 9 SLBs Model Cell-Cell Junctions.

Cells participate in contact-dependent juxtacrine signaling at cell-cell junctions. These can be modeled on planar SLBs. Diffusion barriers allow the investigation of receptor clustering, tension, and transport in these biomimetic platforms. Reproduced from ⁷ with permission from publisher.

2.1.1 Highlights

- SLBs functionalized with adhesion proteins form artificial junctions with cells.
- Chromium barriers serve as diffusion gates and sites of mechanical resistance.
- Molecular tension probes report pN forces on SLBs.
- Cells adhered to stacked or patterned SLBs exhibit distinct phenotypes.

2.2 Introduction

Sensitivity to mechanical forces is a common feature that is shared by the vast majority of organisms ranging from bacteria to mammals. It is fundamental to developmental processes, disease, and normal physiology. Cells transduce mechanical forces into biochemical signaling events in a bidirectional manner through the process of mechanotransduction. Cell surface receptors and cytoskeletal proteins sense and exert

piconewton forces, which influence downstream biochemical responses through a wide range of processes with different molecular mechanisms. For example, mechanical forces may change the rates of reactions by accelerating or decelerating bond lifetimes⁹⁷. Forces can also confine proteins, thus enhancing local concentration and binding interactions. Alternatively, forces can unfold specific protein domains, which exposes cryptic binding sites or activates functions which is common in stretch sensitive ion channels^{74, 98, 99}. The implications of mechanical forces in cell signaling are vast. Mechanical forces regulate hearing, cell migration and adhesion, embryo development, lineage commitment, heart disease, cancer metastasis, and the immune response^{100, 101, 102, 103, 104}. Even small differences in molecular mechanics can lead to distinct outcomes. In the immune system, for example, piconewton (pN) differences in receptor mechanotransduction have been shown to attenuate downstream cell signaling^{105, 106}. Therefore, to engineer effective cell and material-based therapies, it is critical to understand how cells interact physically with their environment and how mechanical forces contribute to signaling.

The most common model system to study these events is in adhesion, the process of cell-cell and cell-extracellular matrix attachment. In adhesion, cells transmit and sense the mechanical properties of neighboring cells and the extracellular matrix (ECM). Focal adhesions (FAs) structurally and mechanically link the cell and the matrix. These protein-rich assemblies connect the actin cytoskeleton to integrin receptors which physically connect to the underlying matrix²². Integrin receptors are dimeric proteins which can assume a folded low affinity state or an open, high affinity state. Integrins have been shown to pull on their ligands and exert traction forces, forces parallel to the plane of adhesion, on the matrix^{30, 107, 108, 109}. Cell-cell adhesions are more structurally and functionally

diverse, ranging from primarily mechanical linkages such as adherens junctions and desmosomes to tight junctions, which control transport between cells, and immune cell synapses, which bring cells in physical contact for the initiation of an immune response. Integrin receptors including the LFA receptor have also been shown to be key players in cell-cell adhesion, but the primary mediators of cell-cell adhesion are cadherin receptors, which form adherens junctions (AJs). Cadherins are tissue-specific calcium-dependent adhesion proteins that form dimers with adjacent (cis) and opposing (trans) cadherins. Cadherins indirectly link to the actin cytoskeleton, allowing force generation across cell-cell adhesions ^{110, 111}. In both cell-cell and cell-matrix adhesions, forces originate through the cytoskeleton. Actomyosin contractility is the primary mechanism of receptor-mediated forces, but actin also generates dynamic forces through treadmilling, the process of polymerizing and depolymerizing which exerts mechanical forces directly on the cell membrane ^{112, 113}. Actin cytoskeleton remodeling can also drive receptor translocation in clustering, which reinforces adhesion ¹¹⁴.

Adhesion sites are often modeled using ECM or cell-adhesion molecule modified substrates. Geometry and mechanics are adjusted by patterning immobilized ligands on substrates of varying rigidity, from sparsely crosslinked polymers to glass. However, the specific events in mechanotransduction remain fundamentally challenging to study. Whereas biochemical signaling can be manipulated by knock-down assays or by inhibitory drugs, mechanotransduction is linked to substrate rigidity and cannot easily be altered without fundamentally changing the system, including the density of ligands. Thus, despite the advances in scaffolding, the precise role of mechanical forces in adhesion assembly remains poorly understood.

Recently, several studies have attempted to bridge this gap by using supported lipid bilayer (SLB) technologies to spatially control the generation of mechanical forces^{5, 6, 9, 12, 95, 115}. SLBs are biomimetic phospholipid membranes that self-assemble on planar glass substrates (Figure 10A). They initially gained attention for their ability to form hybrid cell-cell interfaces and have been particularly useful in modeling antigen-presenting cells to study immune cell synapse formation during T cell activation^{116, 117}. SLBs can be formed by either vesicle fusion, in which unilamellar vesicles adhere to the substrate, rupture, and fuse into a plane, or by Langmuir deposition, in which individual leaflets of the bilayer are sequentially added^{118, 119, 120}. A thin layer of water separates the glass from the lower leaflet, allowing both leaflets to maintain their fluidity¹²¹ (Figure 10A). Lipids freely diffuse in the XY-plane, and the diffusion coefficient is controlled by the bilayer's phase⁴ (Figure 10B). A high bending modulus confines diffusion to the plane of the substrate. Thus, the physical properties of SLBs closely mimic those of the plasma membrane, and cell-SLB interfaces recapitulate the fluid interface between adjacent cells that physically engage, serving as hybrid cell-cell junctions.

An important advantage of the SLB platform is the ability to manipulate ligand mechanics to study mechanotransduction. Therefore, SLBs have recently emerged as a platform to probe receptor signaling events in both cell-cell and cell-matrix adhesion. Because fluid bilayers cannot support lateral traction forces, signaling pathways proceed in the absence of mechanotransduction in the direction tangential to the membrane. By adjusting the fluidity of the bilayers or by patterning barriers as sites of force generation, resisting forces can be selectively introduced^{16, 122}. In this review, we describe SLB biophysics and various methods to manipulate SLB mechanics and to measure signaling

outcomes. We present this material alongside a discussion of literature that applies this platform to characterize integrin and cadherin mechanotransduction. Note that a number of reviews have fully described the SLB technologies and their use in studying cell biology^{123, 124}. Nevertheless, our focus is to emphasize recent work that pertains to the study of cell mechanobiology.

2.2.1 *Receptor Mechanics*

In adhesion complexes, receptors serve as a mechanical linkage between the cell and the underlying matrix or an adjacent cell. Thus, these sites regulate signaling not only through binding, but also through force transduction. Mechanical forces adjust downstream cell signaling by modulating bond lifetime. For an idealized bond with a single energy barrier, the Bell model states that mechanical forces alter off rate, which reduces bond lifetime⁹⁷. In this scenario, bond lifetime, τ , can be described as:

$$\tau = \tau_0 e^{\frac{E_A}{kT}} \quad (1)$$

in which E_A is the bond energy, τ_0 is bond lifetime at zero external forces, k is the Boltzmann constant, and T is temperature. In the case of applied force, this equation is modified:

$$\tau = \tau_0 e^{\frac{E_A - \gamma f}{kT}} \quad (2)$$

In which γ is a structural parameter and f is the force applied to the bond. Receptor-ligand interactions vary in their response to forces. While most bonds will display a reduced lifetime with the application of pN forces, certain receptors form catch bonds. Catch bonds

are an exception in which mechanical forces strengthen adhesion by lengthening bond lifetime. Many adhesion proteins, most notably the integrin family, have been shown to form catch bonds with their ligands ^{19, 125}. The general form of the Bell model can be applied to understand how forces drive the presentation of cryptic sites or the stabilization of weak interactions

2.2.2 *Advantages of Supported Lipid Bilayers*

Many signaling pathways are contact-dependent and initiated at the cell membrane when a receptor interacts with a ligand presented on an opposing cell surface or ECM. Signaling responses are regulated in part by the biophysical properties of interaction, including bond lifetimes, receptor spatial organization, clustering, and mechanics at these interfaces ^{16, 122, 126, 127, 128, 129, 130}. SLBs provide a convenient model to study and perturb these membrane-mediated interactions and signaling pathways.

SLBs are a reductionist platform. Although the cell membrane includes a rich variety of proteins and lipids that segregate into complex domains, SLBs allow the isolation of a few receptors of interest to study receptor-receptor (cis) and receptor-ligand (trans) interactions. Furthermore, SLBs recapitulate the geometry of juxtacrine interactions, in which ligands and receptors are expressed on adjacent cells and physical contact between the cells is necessary to trigger signaling. Contact-dependent signaling pathways require surface anchoring of ligands and soluble ligand molecules often fail at initiating downstream receptor signaling cascades. For example, surface-bound ligands are required for integrin-mediated cell adhesion ¹³¹. T cell triggering requires surface presentation of antigen and the formation of a physical junction between the T cell and the antigen presenting cell ^{128, 132}. By the incorporation of ligands or transmembrane proteins into an

SLB, the native 2D binding geometry can be sufficiently mimicked to initiate a downstream response.

Although rigid surfaces can also be functionalized to present ligands in a planar geometry, SLBs offer a distinct advantage in their lateral fluidity, which permits clustering and transport ⁶. Super-resolution imaging reveals that many receptors exist in nanoscale clusters on the cell membrane prior to signaling ¹³³. Upon receptor-ligand binding, hundreds to thousands of receptors associate together in microclusters, leading to signal amplification, increased specificity, and response-time coordination ^{134, 135}. Whereas individual receptors typically are not connected with the cytoskeleton, clustered receptors can associate with the cytoskeleton, providing a direct linkage between the extracellular proteins and the cell's force generating machinery. Thus, receptor clustering reinforces cytoskeletal coupling and strengthens the force of adhesion ¹³⁶. In the case of unligated receptor clustering, cluster lifetime is reduced compared to the lifetime of ligand-bound receptor clusters ⁹⁵. In many cases, clusters are actively transported across the membrane, their translocation corresponding to the amplitude of biochemical signaling ^{16, 122, 137}. These mechanisms demonstrate the importance of ligated receptor lateral transport, which can only be captured on fluid substrates.

In addition, SLBs offer several experimental advantages. The bilayer's 2D geometry permits quantitative analysis of receptor diffusion and oligomerization. These can be easily measured with fluorescence recovery after photobleaching (FRAP),

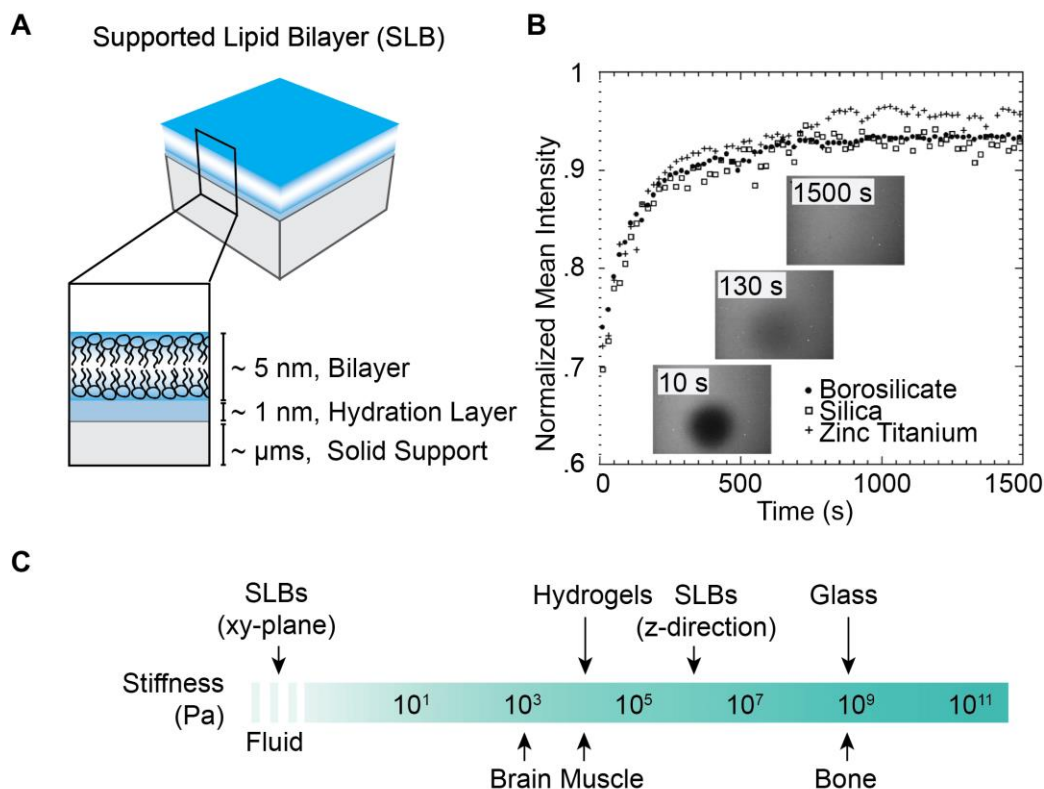


Figure 10 Supported Lipid Bilayer (SLB) Design and Mechanics.

(A) SLBs contain a bilayer separated from a rigid substrate by a thin layer of water. (B) Representative FRAP of labeled lipids illustrating SLB lateral fluidity. Lipids in SLBs freely diffuse within the plane on three representative substrates. Following photobleaching, diffusion causes photobleached lipids to be diluted and the average fluorescence to increase. The disappearance of a visible bleached region indicates total recovery and a fluid bilayer. (Reprinted with permission from ⁴. Copyright 2009, American Chemical Society). (C) SLB stiffness in comparison to tissue, hydrogels, and glass substrates. SLBs are anisotropic, behaving like fluids in the XY-plane, but stiffer than hydrogels in the Z-direction. Inspired by [146]. Reproduced from ⁷ by Author Rights.

fluorescence imaging, and fluorescence correlation spectroscopy (FCS) of tagged lipids or proteins¹²⁰. The planar geometry of cell-SLB interactions can also be easily imaged with total internal reflection microscopy (TIRF). In TIRF, an evanescent wave excites fluorophores in a thin ~150 nm slice at the surface, providing fluorescence images with improved signal-to-noise ratio compared to epifluorescence¹³⁸. Time-lapse TIRM images can be collected on time scales compatible with receptor transport and downstream biochemical signaling.

2.3 Mechanics in Supported Lipid Bilayer Systems

2.3.1 Mechanics of Supported Lipid Bilayers

2.3.1.1 Supported Lipid Bilayer Mechanical Characterization

Bilayer mechanical properties are typically characterized by the compression modulus, K_a , the bending modulus, K_b , and the edge energy, Λ . K_a describes the bilayer's resistance to changing area, whereas K_b measures the energy needed to curve a bilayer. Unilamellar SLBs and SLBs on rigid substrates are tightly confined to XY-plane. In these cases, K_b is not a relevant parameter. However, fluctuations in the z-direction in stacked and cushioned SLBs depend on K_b . For small membrane deformations, K_a and K_b are linearly related, with K_b scaling with bilayer thickness. K_a exhibits phase-dependent behavior. Liquid disordered (l_D) (fluid) SLBs have a low compression modulus of 0.12 N/m. Liquid ordered (l_o) regions of the bilayer behave stiffly for small deformations, with a compression modulus of approximately 1.1 N/m. When further deformed, lipid interactions are disrupted, which causes the SLB to behave as a soft material with a compression modulus of 0.05 N/m¹³⁹. Λ quantifies the bilayer's resistance to pore

formation; it is the energy cost due to exposed fatty acid chains at a pore. Λ contributes to the bilayer's ability to self-heal; positive edge energy indicates that pores will only form under the application of tension. Thus, Λ contributes to the stability of an SLB under receptor mediated forces. For 100 mol% DOPC SLBs, the edge tension, Λ per length, is 27.7 pN¹⁴⁰.

Deforming the SLB over a nanoscale pore using AFM allowed the measurement of an apparent SLB “spring constant”¹⁴¹. In fluid and gel-phase membranes, the apparent “spring constant” was found to be 0.0039 N/m and 0.015 N/m, respectively. For pore sizes below 100 nm, the restoring force decreased with pore radius. For deformations between 4 and 10 nm, the apparent “spring constant” was linearly related to surface tension and K_b ¹⁴¹. The value of the apparent “spring constant” of an SLB is useful for quantifying local membrane deformations, specifically in the case of cell mechanotransduction on cushioned and multilamellar SLBs.

Cell substrate mechanical properties are most commonly characterized by their Young's Modulus, E , which measures the substrate stiffness and is defined as stress (force per area) over strain (deformation). As this parameter is not well defined for membranes, direct comparison of SLB mechanical properties with those of conventional polymer supports is not simple. SLBs are anisotropic materials, rigid in the z-direction and minimally resistive in the lateral direction (2.2.1). The stiffness of SLBs in the z-direction is reflective of the mechanical properties of the underlying support. To obtain the elastic response of an SLB in the z-direction, Picas, et. al. developed a novel AFM-based method, PeakForce-Quantitative Nanomechanics¹⁴². SLBs on mica were oscillated vertically at 2 kHz and allowed to contact an AFM tip. At a loading force of 200 pN, the z-direction

Young's Modulus of SLBs was reported at 19.3 MPa for liquid phase and 28.1 MPa for gel phase SLBs ¹⁴². Gel phase SLBs were effectively stiffer than fluid phase SLBs at all loading forces. These measurements indicate that in the vertical direction, bilayers supported on mica are stiffer than many biological tissues and hydrogels (kPa) but softer than glass (GPa) (Figure 10C). In contrast, polyethylenimine supported DMPC bilayers closely mimicked the stiffness of cells. The underlying polymer swelled to create a ~15 nm cushion between the lower leaflet of the SLB and the underlying mica substrate, leading to an effective Young's Modulus of 32 – 47 kPa ¹⁴³.

2.3.1.2 Lipid Extraction Under Force

In addition to the properties governing the reversible deformation of an SLB under tension, it is important to consider the irreversible destruction of bilayers under mechanical forces. Apart from specialized biological functions such as endocytosis, membranes can only undergo a few percent strain before rupture. In the case of adhesion receptor mechanobiology, the more important parameter is the force of lipid extraction rather than whole membrane rupture. The location of detachment can be determined by the relative energy gradient at the bond.

$$\frac{F_b}{F_m} = \frac{2E_b L_m}{E_m L_b} \quad (3)$$

In this equation, L_m and L_b refer to lipid anchor and bond length, respectively, and E_b and E_m are the energies of bond rupture and membrane failure, respectively. Given the case where the bond energies are similar, the likelihood of failure increases with hydrophobic tail length. Thus, given a constant bond length, the force of lipid extraction decreases with hydrocarbon chain length ¹⁴⁴. Wong, et. al. calculated that pulling a PEG-

lipid from the bilayer into an aqueous environment would require 23 pN¹⁴⁵. Leckband, et. al. measured an adhesion force of 80 pN required to extract a lipid via biotin-streptavidin interaction¹⁴⁴. For mica-supported POPC bilayers, 50 pN was required to extract a single POPE lipid using AFM. Cholesterol extraction in phase-separated SLBs using both AFM and molecular dynamics simulations revealed that extraction requires more force in l_o regions than in l_D regions. Benchmark receptor forces are provided in Section 4.2. SLBs are generally sufficiently stable to withstand short-term applied forces (~ 1 hr) by cells, but lipid extraction is noted at longer time scales. Yu, et. al. reported integrin endocytosis on SLBs and observed internalization 3 hrs following cell-substrate engagement⁸⁶. B cells could extract antigen on viscoelastic plasma membrane sheets, but not on supported lipid bilayers which were more tightly coupled to the substrate¹⁴⁶.

2.3.2 *Frictional and Mechanical Forces on Membranes and Receptor-Ligand Complexes*

2.3.2.1 Diffusion and Viscous Drag in Supported Lipid Bilayers

Diffusion in an SLB is considered in two regimes: diffusion of lipids and similarly small molecules and diffusion of proteins and other large molecules. Lipid diffusion requires sufficiently large free volume and sufficiently high energy to disrupt neighboring tail interactions. In an SLB the diffusion coefficient, D , is determined by phase and substrate-SLB coupling. For larger species, the bilayer is treated as a continuous viscous media. Diffusion is attributed to the net sum of forces due to collisions with lipid molecules and the resisting frictional force, viscous drag that is imparted by the membrane¹⁴⁷. The diffusion coefficient, D , and frictional coefficient, f , are inversely related by the Einstein Relation:

$$D = \frac{kT}{f} \quad (4)$$

in which k is the Boltzmann constant and T is temperature. For an integral membrane protein in an SLB,

$$f = 4\pi\mu hU \left(\log \frac{h\mu}{a\mu'} - \gamma \right)^{-1} \quad (5)$$

This assumes a cylindrical protein with radius a in a bilayer of height h . μ is the viscosity of the bilayer, μ' is the viscosity of the surrounding media ($\mu \gg \mu'$), U is the proteins velocity, and γ is Euler's constant^{147, 148}.

Steric hindrance prevents direct transmembrane protein reconstitution in SLBs, so protein domains or ligands are more commonly tethered to lipid anchors. A useful model to quantify diffusion of tethered protein domains in SLBs is the the pleckstrin homology (PH) domain model, in which each PH domain attaches to single PIP₃. Knight and Falke found that the PH domain protruded further into the surrounding media than into the SLB, but that the diffusion coefficient closely matched that of PIP₃. This indicates that transport is regulated primarily by intra-membrane friction rather than by drag between lipid-tethered proteins and the surrounding media^{149, 150}. These results logically follow from viscosity measurements, which suggest that SLBs are 200x more viscous than their surrounding aqueous environments¹⁴⁹.

In more complex scenarios, the diffusion coefficient depended on protein-lipid interactions. The diffusion coefficient of multimers inversely scaled with the number of

bound lipids, and contributions of lipid binding and protein insertion into the hydrophobic core were additive for membrane penetrating proteins such that:

$$D = \frac{1}{F_{1,Lipid}N + cP} \quad (6)$$

Here, N is the number of bound lipids, F is the frictional contribution of a single lipid, c is a constant, and P is the number of penetrating domains ¹⁵¹.

Typical diffusion coefficients for lipids in fluid and liquid-disorder SLBs are 1-4 $\mu\text{m}^2/\text{s}$ and .1 $\mu\text{m}^2/\text{s}$, respectively ¹⁵². The diffusion coefficient of 17 tethered protein domains with various degrees of lipid penetration ranged from .22 to 2.6 $\mu\text{m}^2/\text{s}$. Corresponding frictional coefficients ranged from .39 for anti-biotin with only one lipid binding domain to 4.6 for a fusion construct with 6 bound lipids ¹⁵¹. Biswas, et. al. estimated that extracellular domains of E-cadherin on a fluid SLB experienced an average of .5 fN viscous drag during lamellipodial retraction ⁵.

Although membrane-bound proteins only attach directly to one or few lipids, protein binding has been observed to alter lipid diffusion within a larger radius. Forstner, et. al. found that near the melting temperature, cholera toxin binding induced the formation of gel-phase islands in DMPC and DMOPC SLBs ¹⁵³. Molecular dynamics simulations of Kv1.2 ion channel in DOPC bilayers suggest that this layer includes approximately 50-100 lipids which diffuse with the protein ¹⁵⁴. At reasonably low concentrations, diffusion coefficients of membrane-bound proteins are concentration independent ¹⁵⁵. This rule breaks down when proteins are added in sufficiently high concentrations to form a monolayer ^{155, 156}.

In cells, receptor-ligand transport is hindered by cytoskeletal barriers imposed on the bilayer. Spectrin forms a geometric mesh that supports the membrane, and actin can limit protein diffusion through the tether model, in which a protein is directly bound to the cytoskeleton, and the fence model, in which proteins diffusion is spatially limited by bulky cytoskeletal barriers ^{157, 158}. Edinin, et. al. demonstrated that these barriers dynamically confine protein diffusion, and that the mechanism of protein attachment to the membrane affects confinement ¹⁵⁹. Transferrin receptors tagged with beads and dragged across an NRK cell membrane using optical tweezers required 0.25 - 0.8 pN trapping force to cross cytoskeletal boundaries. At lower forces, receptors escaped the optical trap, suggesting the cellular barriers winning in a tug-of-war. Barriers behaved elastically with a spring constant of 3pN/ μ m, causing escaped receptors to quickly return to their original position ^{157, 158}. Similarly, E-cadherin dragged across the cell membrane with optical trap velocity of .6 μ m/sec followed the optical trap for .78 μ m, where it began to lag behind the displacement of the trap. The receptor escaped the trap at 1.32 μ m, corresponding to an optical trap force of .8 pN. Homogeneous SLBs cannot impart such forces on ligands and receptors, but several experimental techniques allow the experimenter to controllably pattern corrals (3.2.2), and these phenomena may affect receptor transport in the SLB-adhered cell.

2.3.2.2 Effects of Membrane Tension

Within both cells and cell-free systems, membrane tension has been shown to induce receptor-ligand transport. Smith, et. al. developed parallel fluid and non-fluid cell-free systems to assess adhesion of mobile versus immobile integrins. Giant unilamellar vesicles (GUVs) containing RGD-functionalized lipids equilibrated on SLBs containing mobile or immobile embedded integrin receptors, and a 2-4 pN vertical force was applied

to the membrane using optical tweezers. Whereas immobile bonds stretched and ruptured, mobile linkages clustered beneath the GUV to resist detachment ¹⁶⁰. In the fluid system, which contained more GUV-surface linkages, each bond experienced negligible force (0.2fN), and the remodeling response was attributed to thermodynamic requirements to reduce free energy rather than to mechanics. Nevertheless, this work illustrates the concept that membrane tension can passively drive receptor reorganization at a juxtacrine interface. Accordingly, membrane tension applied by micropipette aspiration was sufficient to cause membrane flattening and passive E-cadherin recruitment in EAhy cells ¹⁶¹.

2.3.2.3 Force Generation by Cytoskeletal and Motor Proteins

Cytoskeletal proteins and motor proteins exert forces on membranes and their associated receptors. The cytoskeleton has two primary mechanisms of active force generation, polymerization and contractility. Actin and microtubules polymerize against the membrane, generating forces through a ratchet model. Thermodynamic fluctuations cause a transient space between the filament and the bilayer, allowing the insertion of a subunit. The extending polymer exerts pushing forces against the membrane. Footer, et. al. demonstrated that 8 parallel actin bundles can exert 1 pN force on a rigid wall, and actin comets have shown persistent polymerization at resisting forces of 4.3 nN ^{162, 163}. In podosomes, crosslinked actin polymerization against the membrane causes the cell to protrude into the substrate. These protrusions have been measured to exert an average of 94 nN or Formvar sheets ^{9, 76}.

Actomyosin contractility directly pulls actin-bound receptors. Motor proteins including myosins walk along actin filaments, generating 3-4 pN per step per myosin head;

this actomyosin contractility is responsible for receptor tension and traction forces in many systems^{164, 165, 166}. A key question in the literature has been whether myosin can generate forces parallel to the membrane or only perpendicular. Long range traction forces are dissipated due to lipid diffusion, but recent work by Pyrpasopoulos, et. al. suggests that myosin motors can act in concert to generate low pN forces at a fluid interface¹⁶⁷. Thus, while motor proteins generate large traction forces on rigid substrates, in-plane force generation and maintenance at fluid interfaces are more transient and require high cooperativity.

2.4 Supported Lipid Bilayer Technologies

2.4.1 Methods to Perturb Bilayer Mechanics

2.4.1.1 Tuning SLB Composition to Control Lateral Diffusion

The simplest way to manipulate SLB mechanics is to adjust lipid composition and packing. This can be accomplished by adjusting the degree of fatty acid unsaturation. Changes in phase are accompanied by changes in transport, both passive diffusion and active transport, due to the altered fluidity. Within an SLB, individual lipids interact via *van der Waals* interactions, and their packing determines SLB phase. Below the melting temperature, SLBs are in gel phase with the lipid hydrocarbon tails rigidly arranged. Above the melting temperature, fatty acids rotate about their C-C bonds and exhibit long range coordinated motion. Lipids with longer hydrocarbon chains exhibit improved packing and reduced free volume, leading to slower diffusion².

In studies of mechanotransduction, adjusting SLB fluidity has two primary consequences. First, the kinetics of the system are altered. In a system with decreased fluidity, ligated receptor transport across the cell-SLB interface is slowed, potentially allowing for nucleation or for additional signaling molecules to bind. In addition, a gel-phase or crowded membrane with low fluidity permits the generation of resisting forces. In a fluid system, lateral forces cannot be applied because there is no resistance ⁵. An additional benefit of phase-controlled bilayers is the ability to better mimic the cell's plasma membrane. SLBs provide a simplistic experimental platform, however they lack the complexity and richness of live cell membranes, which are separated into multiple domains and are comprised of hundreds of lipids and thousands of proteins. Adjusting the phase of a SLB can begin to capture the complexity of the plasma membrane and create a more physiologically relevant model.

Cholesterol biosynthesis is tightly regulated in part to modulate membrane fluidity, thickness, and integral protein activity. This is mediated by cholesterol's rigid ring structure inserting into the membrane. Cholesterol is hypothesized to straighten saturated lipids, allowing them to pack more efficiently. This effect on lipid-lipid interactions likely more directly modulates bilayer fluidity than the introduction of cholesterol-lipid interactions (Figure 11A) ^{2, 168}. Accordingly, cholesterol is a common species used to modulate bilayers *in vitro*. Cholesterol containing membranes exhibit three states, gel phase, liquid ordered (l_o) (at high concentrations of cholesterol and below T_m), and liquid disordered (l_d) (at high temperatures and low cholesterol concentrations). In the l_o phase, lipids exhibit strong tail interactions like in the gel phase, however they retain high fluidity. Cholesterol's effects on bilayers are dependent on lipid composition, temperature, and

cholesterol concentration. For example, DPPC membranes are homogenous at low concentrations of cholesterol and can exist in either the l_o or gel state. At 10 mol% cholesterol, DPPC membranes phase separate into a cholesterol-depleted region and a cholesterol-rich liquid disordered region. However, the addition of 50 mol% cholesterol again gives rise to a homogeneous bilayer ¹⁶⁹. Thus, great care must be taken when doping bilayers with cholesterol to achieve the desired effect. In SLBs, 25 mol% cholesterol in DOPC membranes has been shown to reduce the diffusion coefficient of lipids and anchored proteins 4-5-fold ¹²⁷.

As an alternate approach, SLB phase may be modulated by the addition of lipids with a bulky tail group (Figure 11B). 1,2-dipalmitoyl-sn-glycero-3-phosphocholine (DPPC) labeled with 7-nitrobenz-2-oxa-1,3-diazol-4-yl (NBD) emerged as a popular fluorescent probe in the study of membrane physiology; however differential scanning calorimetry revealed that as low as 1%, NBD-PC altered membrane physical properties ¹⁷⁰. Interestingly, the placement of NBD on the hydrocarbon tail determined the effect on phase. Harnessing the artifacts introduced by NBD-PC, Biswas, et. al. used NBD-PC to generate partially fluid bilayers to study adherens junction formation (Figure 11B) ⁵.

Sterically crowding the membrane with protein alters SLB fluidity without significantly changing the lipid composition. SLB functionalization with streptavidin is achieved by doping in a small amount of biotinylated lipid, typically biotin-DPPE. In kinetics assays, streptavidin binding saturated at 4 mol% biotin-DPPE with two biotinylated lipids binding each streptavidin. At concentrations below 4 mol% biotin-DPPE, streptavidin bound in a dose dependent manner. At 4 mol% biotin-DPPE, bound streptavidin forms a crystal monolayer ^{156, 171}. Whereas SLBs with low streptavidin

coverage retained their fluidity, crowded streptavidin monolayers obstructed long-range diffusion¹²⁶. Thus, the long-range diffusion coefficient is reduced by increasing the density of streptavidin molecules on the SLB. This method is particularly useful for probing the effects of lateral transport on receptors. By comparing Notch activation in cells on fluid, nonfluid, and rigid surfaces, Narui and Salaita identified that the Notch/Delta pathway is mechanosensitive and responds nonlinearly to ligand fluidity¹²⁶. More recently, it was shown that platelets prefer to adhere to crowded membranes¹⁷². A nonfluid interface for cell adhesion was also recently fabricated by covalently linking ECM proteins to fluid lipids¹⁷³.

Selection of lipids with a transition temperature close to physiological conditions allows manipulation of bilayer fluidity without significantly changing SLB chemical composition. For example, 1-myristol-2-palmitoyl-*sn*-glycero-3-phosphocholine (MPPC) has a melting temperature of 35°C, allowing the lipids to be switched between gel phase and liquid phase in a temperature range compatible with live cell imaging. Demonstrating this, Adreasson-Ochsner fabricated micron sized 3-dimensional wells coated with supported MPPC bilayers containing E-cadherin ligands on the walls and base of the well. A single cell could spread in each well, and the differences in adhesion could be observed on chemically identical bilayers different only in their lateral fluidity¹⁷⁴. A key nuance to this work is that the biology itself could be altered by the temperature change between fluid and non-fluid bilayers. However, given the small difference in temperature, these effects are likely minimal. The benefit to this method of adjusting phase is that it is ligand-concentration independent. Whereas membrane crowding with streptavidin also typically affects ligand binding and density, a simple assay with SLBs below and above their melting

temperature avoids convolution with ligand presentation and circumvents the need to add a fluorescent lipid.

2.4.1.2 Stacked and Cushioned Bilayers

The physical properties of SLBs are closely linked with substrate mechanics and topology. SLBs are most often formed on silicon oxide glass, and a thin layer of water separates the lower leaflet from the glass. The exact effects of surface-lipid interactions are highly contested and preparation dependent, but evidence suggests that lipid-substrate coupling can cause uneven leaflet lipid composition, drag between upper and lower leaflets, altered surface tension, and reduced fluidity^{175, 176, 177}. According to the classic model developed by Evans and Sackmann, the frictional coefficient between the membrane and the substrate is inversely related to the thickness of the fluid layer of separation¹⁷⁸. Therefore, increasing the thickness of the fluid supporting the bilayer will increase the mobility of the SLB. This insight has motivated the development of cushioned and stacked bilayers.

From a biomimetic standpoint, the effects of glass cannot be ignored. Whereas glass has a modulus on the order of GPa, atomic force microscopy measurements suggest that stiffness of the cell cortex which supports the cell membrane *in vivo* is one million times softer on the order of kPa¹⁷⁹. Accordingly, creating SLBs on soft cortex-like supports is desirable. Here we discuss two converging approaches using SLB technologies: stacked bilayers in which multiple bilayers are fabricated on top of each other and cushioned bilayers in which the SLB is formed on a polymer support (Figure 11C). These systems physically decouple the SLB from the glass substrate, offering the potential for improved

physiological relevance in cell studies. We anticipate these platforms to be extremely useful in elucidating the role of mechanics in cell signaling and cell differentiation.

Several fabrication methods for stacked SLBs have been attempted with varying levels of success. Covalent linking of lipids by NHS/EDC chemistry generated stacked bilayers, but the upper bilayer exhibited slowed diffusion and only ~75% of the lipids were mobile. This was hypothesized to be the result of nanoscale discontinuities in secondary SLB coverage, which were revealed by AFM ¹⁸⁰. Murray, et al. tethered biotinylated vesicles to streptavidin functionalized SLB and observed secondary bilayer formation at high vesicle concentrations. Diffusion was not significantly altered in the upper membrane compared to single layer SLBs ¹⁸¹. Stacked SLBs stabilized with multiple favorable interactions improved quality, and SLBs connected with two positively charged bilayers with cholesterol functionalized DNA demonstrated high fluidity. However, these membranes remained challenging to characterize ¹⁸².

Recent advances have allowed the formation of homogeneous and heterogeneous SLBs with up to four layers. Zhu, et. al. demonstrated that the incorporation of 10% cationic or anionic lipids allowed the formation of homogeneous or patterned bilayers ¹⁸³. In patterned bilayers, the addition of saturated 1,2-distearoyl-sn-glycero-3-phosphocholine (DSPC) induced charged lipid phase separation. Phase separated domains aligned in each layer but were contingent upon bilayer fluidity. Stacked phase separated domains were also reported in phosphatidylcholine, cholesterol, and sphingomyelin containing membranes ¹⁸⁴. Together these data suggest an underlying physical explanation for aligned phases beyond electrostatic interaction. Kaizuka and Groves suggest the possible role of surface tension in preferentially aligning gel domains ¹⁸⁴. Patterned stacked bilayers require

mechanical characterization but will undoubtedly emerge as a powerful tool to study adhesion.

Polymer “cushioned” and tethered bilayers provide an alternative method to decouple the SLB from the underlying glass¹⁸⁵. These methods were developed with the goal of incorporating integral membrane proteins into SLBs; however they also offer potential for manipulating the mechanical microenvironment. Integral proteins incorporated into SLBs typically fail to maintain their fold and lateral mobility due to adsorption on the glass, steric hindrance to diffusion, and denaturation as proteins are dragged along the surface¹⁸⁶. Polymer cushions or tethers lift the SLB off the glass, not only cushioning the bilayer, but also creating space for diffusing integral proteins. Whereas cytochrome b₅ and annexin V were both immobile in SLBs formed directly on glass, a combination of BSA passivation and polymer tether incorporation raised the highly mobile fraction to 75%^{187, 188}. Tethers must link the bilayer to the glass while not interacting with either the lipids or any incorporated proteins. In addition, the polymer of choice must be hydrophilic to support bilayer formation¹⁸⁷. Therefore, PEG and chitosan have been popular choices for polymer tethers and cushions. Sterling, et. al. also fabricated actin-supported bilayers, in which the actin cushion attempted to better mimic the cortex; the results of this work emphasize that fluidity modulation is polymer specific¹⁸⁹. Alternatively, cushioning the SLB with a thin cellulose cushion has been used to generate homogeneous bilayers with mobile integrins¹⁸⁶.

A major challenge in integral protein orientation is directing protein orientation. When proteins are reconstituted in vesicles for fusion with SLBs, their orientation scrambles. This skews diffusion measurements, because proteins with reversed orientation

can be immobilized or denatured if their large extracellular domain interacts with the support. In mechanotransduction studies, these proteins would fail to interact with their binding partners. Recent work by Richards, et. al. suggested that protein orientation can be controlled by incorporating integral proteins using cell blebs, small, isolated vesicles from mammalian cells. Because these originate from the plasma membrane, proteins were oriented in their natural arrangement. Thermodynamically favorable downwards rupture preserved receptor orientation when vesicles fused during SLB formation ¹⁹⁰.

Although the potential for polymer-cushioned bilayers as a platform to adjust the underlying substrate rigidity in mechanotransduction studies has not yet been explored, stacked and polymer-tethered bilayer technologies have been combined to generate robust surface-decoupled SLBs to study adhesion. Bilayers are linked by maleimide-thiol coupling of lipopolymer linkers ¹⁵. To date, this is the only stacked bilayer system that has been applied as a novel cell substrate. 1-palmitoyl-2-oleyl-sn-glycero-3-phosphocholine (POPC) bilayers were alternately doped with 5 mol% 1,2-dieasteroyl-sn-glycero-3-phosphoethanolamine-N-[maleimide(polyethylene glycol)-200] (ammonium salt) (DSPE-PEG2000-Mal) or 5 mol% 1,2-dipalmitoyl-sn-glycero-3-phosphothioethanol (Sodium Salt) (DPTE). A sucrose gradient promoted the sinking and fusion of giant unilamellar vesicles and maleimide-thiol coupling linked the upper and lower leaflets of adjacent bilayers. In agreement with the Evans-Sackmann model, the diffusion coefficient increased and the viscous drag coefficient decreased for each additional layer¹⁷⁸. Lipopolymer-linked stacked bilayers coated with laminin behaved both viscoelastically and plastically. Individual lipids and attached receptors were laterally mobile but beads containing preclustered receptors became immobilized when attaching to the multi-bilayers ¹⁷. Notably, AFM micrographs

revealed that surface roughness increased with the addition of each layer; these effects were likely the result of decoupling between the upper bilayers and the glass¹⁵.

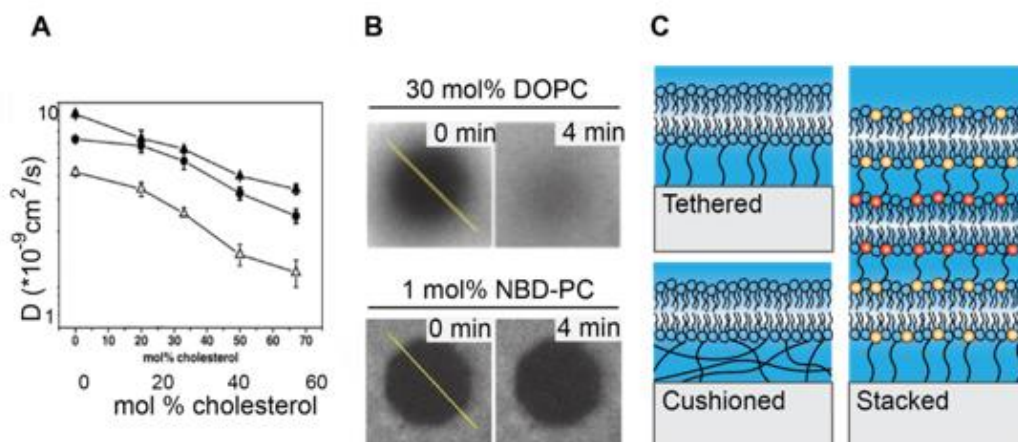


Figure 11 SLB Phase and Diffusion Tuning

(A) Cholesterol reduces SLB fluidity in DMPC (closed triangles), DOPC (circles), DEPC (open triangles) bilayers. Reprinted from² with permission of publisher. (B) Representative FRAP data from fluid and partially fluid DPPC bilayers containing, 30% DOPC and 1% NBD-PC, respectively. In DOPC SLBs, fluorescence almost fully recovers in 4 minutes, but in SLBs containing NBD-PC, the photobleached region persists, indicating low fluidity. (Reprinted from⁵. Copyright 2015, National Academy of Sciences). (C) Schematics of tethered, cushioned, and stacked SLBs. Reproduced from⁷ with permission from publisher.

2.4.2 *Patterning to Control Receptor Mechanics*

2.4.2.1 Lipid and Ligand Patterning

Ligand patterning is a powerful approach that has been widely applied in the study of adhesion and immune cell activation. On glass, block copolymer micelle nanolithography (BCML) allows the deposition of nanoparticles with precise control over particle density, ranging from 50 to 150 nm^{191, 192}. By decorating these particles with ligand, BCML has been used to identify the critical pMHC density required to support T cell spreading, as well as to study the crosstalk between cell migratory behavior and ligand

presentation ¹⁹². To more closely mimic cell-cell interactions and to understand the role of ligand mobility, it is highly desirable to develop similar methods to control ligand geometry and density within supported lipid bilayers.

Until recently, patterning within bilayers has been limited to the ability to pattern blocks of membrane. Several methods have been developed in which lipids are either selectively added or removed in patterns. In one such method, a supported lipid bilayer formed on chromium grids was physically peeled off using a scanning probe tip and then refilled ¹⁹³. Alkaline conditions favored membrane removal. Neutralizing the pH promoted bilayer fusion and allowed these regions to be backfilled with a second lipid composition. SLB micro-voids could also be generated with deep UV illumination ¹⁹⁴. In a widely used method, SLBs are patterned with a polydimethylsiloxane (PDMS) stamp. PDMS stamps are inked with SLBs, which are contact transferred to a glass substrate. Combining this method with BSA barriers, it was possible to form bilayers with a lipid concentration gradient. Following stamping, vesicles with a second composition of lipids were added on top of the printed SLB and allowed to mix within compartments ^{1, 195}. The composition of the resulting membrane patches depended on the size of the stamp applied to each region defined by the BSA grid. Groves, et. al. achieved spatial control over HeLa and fibroblast cell adhesion on patterned SLBs by incorporating phosphatidylserine (PS), which promotes cell adhesion, into individual corrals on an SLB (Figure 12A) ¹. Using these methods, it would also be possible to selectively anchor adhesion ligands within distinct regions of the SLB by controlling which patches contain functionalized lipids or lipid ligands, such as glycolipids, which are commercially available and can support cell adhesion ¹⁹⁶. Examples

include PIP, DNP, reactive lipids such as azide modified lipids and thiol reactive lipid headgroups.

Another more common method to control the spatial arrangement of ligands within the supported lipid bilayer is by membrane protein photolithography. Optogenetic tools including caged and photoactivatable proteins are engineered with naturally occurring photoreceptors such as the LOV domain ¹⁹⁷. By shining the appropriate laser on the engineered proteins, the experimenter can spatiotemporally control protein accessibility and activation. In one approach, these domains can be linked to the protein of interest and then cleaved using photoactivation, therefore allowing the experimenter to control which ligands are accessible and which ligands remain caged. Combining this system with the supported lipid bilayer-T cell synapse model, DeMond, et. al. controlled T cell blast spreading and activation ¹⁹⁸. Membrane-bound MHC molecule IE^K was loaded with MCC peptide fused to a light sensitive 6-nitroveratryloxycarbonyl (NVOC) blocking group. On bilayers with caged pMHC and ICAM-1 to support adhesion, T cell blasts crawled across the surface and failed to form Ts cell synapses. When the NVOC was cleaved with near-UV light, pMHC was exposed, causing T cells to adopt a round shape and to form immunological synapses.

Alternatively, light-sensitive linkers may be used to selectively remove ligands from the surface. Nakayama, et. al. developed a photoeliminative linker that can be used to both site-specifically add and remove proteins on a bilayer ¹⁹⁹. A photoeliminative 4-(4-(1-hydroxyethyl)-2-methoxy-5-nitrobenzyloxy)butanoic acid bridges a biotin group and a farnesyl group, which inserts into the bilayer. Prior to functionalization with streptavidin, biotin can be removed by UV-illumination through a patterned mask. Using a second round

of UV irradiation at later time points, the protein may be released from the bilayer, providing a model to study adhesion and diffusion. To date, photoactivation of ligands has only been applied to continuous bilayers. On corralled bilayers, photobleaching of individual squares allows the generation of detailed patterns and images; the fraction of photobleached species per corral corresponding to the fractional area of the square exposed to light (Figure 12B) ¹¹. One can envision that combining these two methods could yield bilayers with precisely patterned ligands that maintain their lateral mobility but are confined to microscale patches.

Immobilized ligands can be incorporated into an SLB using gold nanoparticles (AuNPs) or nanodots. Lohmüller, et. al. used BCML to disperse AuNPs within the SLB plane. Ephrin A1 ligands were linked to AuNPs with thiolated DNA, and RGD was incorporated into the surrounding bilayer ²⁰⁰. Thus, cells could engage with both laterally mobile and immobile ligands. In an alternate strategy, ligands were attached to size-tunable organic nanodot arrays (STONAs) surrounded by an SLB (Figure 12C) ¹⁴. Beads deposited on a glass surface and coated in an aluminum mask of variable thickness determined STONA lattice spacing, ranging from 100 nm to 1800 nm. Following bead removal, a secondary aluminum-mask determined dot size, and nanodots were modified with biotinylated BSA for functionalization. An SLB was formed surrounding STONAs, giving rise to a ligand-island effect. T cells cultured on STONAs functionalized with anti-CD3 exhibited increased TCR clustering compared to T cells on homogeneous bilayers with equivalent ligand concentrations, and the tightness of adhesion was found to increase with ligand density. An unexplored consequence of ligand immobilization on STONAs is the development of a resisting force, which allows receptors and the cytoskeleton to locally

apply tension. Simultaneous presentation of mobile ligands on the bilayer and immobile ligands on nanodot arrays will allow the relationship between ligand mobility and mechanics in cell signaling to be probed in parallel.

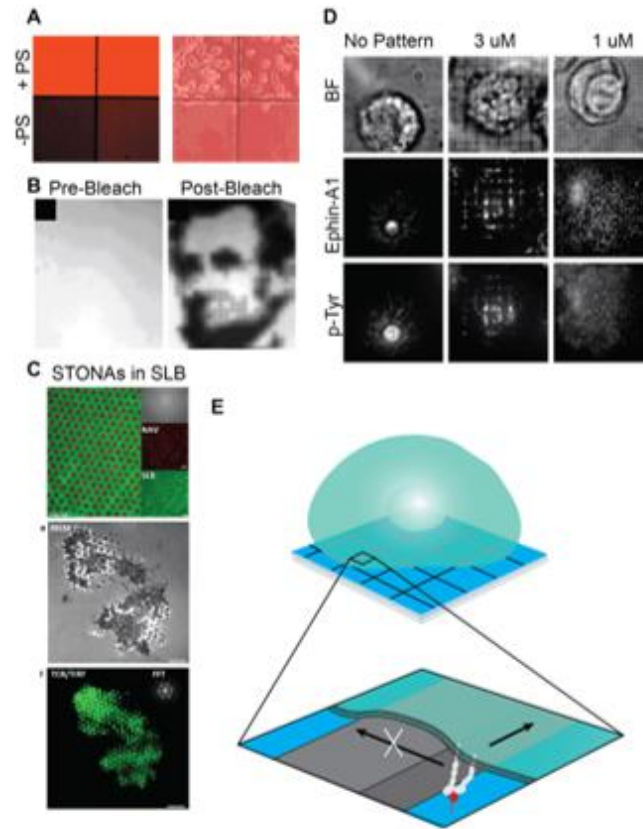


Figure 12 SLB composition and substrate patterning.

(A) SLB composition controls HeLa cell adhesion. PS promotes HeLa cell adhesion, but few cells adhere on PS-free bilayers. Fluorescence image of SLBs (left). Phase contrast image of cell adhesion (right). (Reprinted from ¹ with permission from publisher). (B) Photobleach printing on corrallated bilayers demonstrates the ability to locally control SLBs. (Reprinted from ¹¹ with permission from publisher. (C) STONAs containing nanodot-immobilized ligands embedded in an SLB; Representative image of T cells on a STONA patterned bilayer. Scale bars 4 μ m. (Reprinted from ¹⁴ with permission from publisher). (D) Spatiomechanical mutation of receptor transport and phosphorylation on corrallated bilayers. Levels of tyrosine phosphorylation correlates with ephrin-A1 radial transport. (Reprinted from ¹⁶ with permission of publisher). (E) Diffusion barriers gate receptor transport and serve as sites of local force generation. Reproduced from ⁷ with permission from publisher.

2.4.2.2 Diffusion Barriers

SLBs formed on substrates that are patterned with grids that prevent lipid diffusion separate into non-mixing microdomains. While such partitioned ‘corralled’ bilayers were initially developed for lithographic and electrostatic patterning, they have also become an indispensable tool in mechanobiology^{16, 201, 202, 203}. Each individual region maintains its fluidity, but long-range diffusion is hindered by gridlines or by an energetic barrier to spreading. Thus, cell spreading and signaling on a corralled bilayer will be spatially mutated, and long-range receptor-ligand translocation is diminished (Figure 12D,E). In T cells, when a ligated receptor encounters a physical block, its speed is reduced and its translocation is deflected in an angle-dependent manner²⁰⁴. Grid lines also serve as sites of mechanical resistance. Cells cannot apply traction forces on homogeneous SLBs because the fluid bilayer fails to mount a resisting force; however lateral forces can be applied at barriers^{9, 16}. In molecular mazes, which are similar to corralled SLBs, noncontiguous barriers are patterned onto glass, allowing the resulting bilayer to maintain its long-range fluidity while still presenting mechanical barriers²⁰⁴. These biochemically homogeneous platforms provide a direct method to probe biochemical versus mechanical signaling. A key challenge with diffusion barriers is the convolution of the effects due to blocked receptor transport versus mechanical force generation. Indeed, both clustering and mechanics are altered, resulting in spatiomechanical mutation. The exact forces that diffusion barriers impart are also unknown. Future studies will address this question using ratiometric MTFM on SLBs containing barriers.

Isolated membrane patches can be formed by scratching, blotting, stamping, or microfabrication. In the earliest example, tweezers were used to draw boundaries on a coverslip. Although SLBs in basic conditions remained partitioned at the scratch marks,

bilayers in neutral and acidic conditions healed within hours, making them incompatible for cell imaging ²⁰⁵. Following this work, Kung, et. al. formed BSA barriers by both the application of patterned BSA on a PDMS stamp and by removing lipids in a pattern using a PDMS stamp and then backfilling with BSA to generate walls ²⁰⁶. Surprisingly, distinct membrane patches could also be formed using microcontact printing in the absence of barriers. SLBs applied in blocks with PDMS stamps maintained their shape because of the energetic barrier to spreading on glass and disrupting lipid tail interactions ¹⁹⁵. This method permits regions of ~5 μm to be fabricated. By using polymer-based lift off on silicon supported bilayers, Orth. et. al. were able achieve haptenated SLBs with 1 μm pattern precision ²⁰⁷. SLBs separated by metal grids provide an optimal platform for studying receptor and cytoskeletal mechanotransduction due to their rigidity and ability to support cellular forces. A glass substrate is etched and coated with polymeric photoresist. Electron beam lithography exposes a grid pattern, and metal walls are deposited with electron beam evaporation. Grids are typically composed of chromium but may also be aluminum or gold. The glass regions within the grid are exposed by sonication, and filled with an SLB formed by vesicle fusion ^{16, 201}.

2.5 Methods to Measure Receptor Forces at Fluid Interfaces

2.5.1 Molecular Tension on Supported Lipid Bilayers

2.5.1.1 Ratiometric Tension Probes for Mobile Receptors

Molecular tension fluorescence microscopy (MTFM, previously reviewed by Jurchenko and Salaita ²⁰⁸) is a method to optically image receptor mechanics at the living-nonliving interface. Previously, this method has been applied to map T cell receptor,

epidermal growth factor receptor, and integrin forces with high spatiotemporal resolution 8, 30, 31, 106, 208, 209, 210, 211. In MTFM, an immobilized probe molecule comprised of a flexible linker and flanked by a fluorophore-quencher pair presents a ligand to a receptor of interest. In the resting (dark) state, the flexible linker is in a collapsed state, and the fluorophore and quencher remain in close proximity. When a receptor binds to the ligand and applies pN tension, the linker extends, causing separation of the fluorophore and quencher, which is accompanied by a significant increase in fluorescence. The flexible linker may be made of DNA, polymer, or protein and is selected based on its force-extension relationship. State-of-the-art probes yield greater than 100-fold increase in fluorescent intensity upon opening 106.

In typical MTFM, an increase in donor fluorescence serves as a quantitative reporter of quenching efficiency. This is valid because the immobilized probes have a fixed donor density and fluorescence intensity is directly proportional to quenching efficiency and quantum yield. When probes are attached to a fluid bilayer, the fluorescence intensity is proportional to probe density and quenching efficiency (force). Tension-mediate increases in donor fluorescence are convolved with increases in probe density due to ligated-receptor clustering (Figure 13A). Therefore, the application of MTFM to SLBs requires the separation of the signal contribution due to probe clustering versus probe opening.

To address this problem, Ma, et. al. developed the first ratiometric MTFM probes, which allow the calculation of the contribution of signal due to tension, “tension density.” In this design, AuNPs are decorated with DNA tension probes and is attached to an SLB using biotin/streptavidin interaction. A second fluorophore is non-specifically attached to

the streptavidin, and this “density reporter” fluorophore directly reports probe surface density. An additional benefit to this probe is the high signal-to-noise ratio; donor fluorescence is dual quenched by the molecular quencher and by nanoparticle surface-energy transfer (NSET) with the AuNP⁸ (Figure 134B,C). Nowosad, et. al. published an alternate design in which the traditional MTFM probe is modified with a “density reporter” fluorophore on the hairpin strand. Tension is quantified by the “opening ratio” (Figure 13D,E)¹⁰. It would also be possible to achieve similar measurements by quantifying the “tension density” or FRET efficiency using DNA-FRET probes, which were previously applied to measure single receptor tension on glass³².

2.5.1.2 Genetically Encoded Tension Probes

Although ratiometric MTFM is currently the only method to measure receptor mediated forces on a bilayer, other tension sensors could also be combined with SLBs to elucidate the role of fluidity in modulating the mechanics of accessory adhesome proteins. For example, Grashoff, et. al. introduced a genetically encoded tension sensor in 2014²¹². This sensor contains two fluorescent proteins separated by a spider silk elastic domain, which measures pN tension across a protein. To date this probe has been inserted into a number of proteins including catenin, vinculin, α -actinin, and spectrin^{110, 212, 213}. Combining cells transfected with genetically encoded tension sensors with SLBs and ratiometric MTFM, researchers will gain a more complete understanding of the role of traction forces and lateral fluidity in regulating adhesome mechanics.

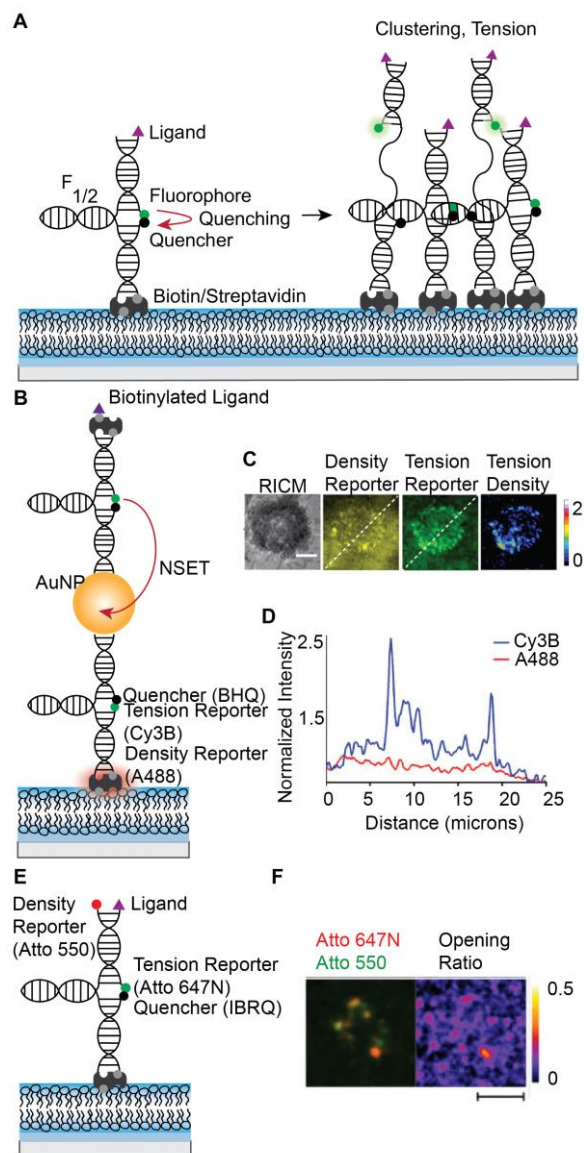


Figure 13 MTFM probes to map pN receptor tension at SLB-cell junctions.

(A) On an SLB, fluorescence increases are attributed to both increased density (clustering) and probe opening (tension). Closed probe fluorescence is quenched. When receptors cluster or pull on probes, intensity increases. At $F_{1/2}$, 50% probes will be open. (B) Nanoparticle-based ratiometric tension probes contain reporters for fluorescence and density. Closed probes are dual quenched by the BHQ molecular quencher and an AuNP and contain a second fluorophore on streptavidin. Labeled streptavidin serves as a probe density reporter. (C) Representative image of T cell tension and clustering. (D) Line scan of density reporter and tension reporter fluorescence. Scale bar 5 μ m. (C,D) reprinted from ⁸ with permission from publisher). (E) Ratiometric DNA tension probes containing a density reporter fluorophore on the hairpin strand. (F) Representative cell image of B cell receptors clustering and pulling on DNA tension probes. Scale bar 5 μ m. (F) reprinted from ¹⁰ with permission from publisher). Reproduced from ⁷ with permission from publisher.

2.5.2 *Tension Measurements on Supported Lipid Bilayers*

Integrin and cadherin molecule force maps have not yet been generated using ratiometric MTFM, but immune-cell receptor forces at the cell-SLB interface have been measured in both B and T cells. Both B and T cell receptors were capable of opening ratiometric tension probes on an SLB, but the measured tension was lower than that generated on glass. Ma et. al. reported T cell receptor tension of 4.7 pN on an SLB ⁸. In contrast, Liu, et. al. demonstrated the ability of potent T cell receptors to unzip a 56 pN tension gauge tether (TGT) on glass ¹⁰⁶. Similarly, primary B cells could unfold a percentage of 7 pN probes on an SLB, but could not open 9 or 14 pN probes ¹⁰. On glass, primary B cells were capable of unzipping 56 pN TGTs ¹⁰⁵. Importantly, MTFM measures the magnitude of tension rather than a force vector, and probe opening reflects net tension. On SLBs, where receptors cannot generate strong traction forces in the parallel to the bilayer, the majority of probe opening must be attributed to vertical forces. Thus, it is not surprising that tension measurements would be lower on an SLB compared to those on glass.

Ratiometric MTFM probes provide a method to characterize the relationship between pN mechanical forces and clustering in a variety of juxtacrine and cell-matrix interactions. Although these measurements have not yet been made, existing measurements on rigid substrates allow us to bound the range of forces. Note that force measurements are dependent on method, loading rate, and specific interaction parameters, so there a great deal of variability. Single molecule techniques report integrin bond strengths ranging 0.1 - 0.65 pN using magnetic tweezers to up to 100 pN using AFM and high loading rate. MTFM on glass suggests that integrins exert >100 pN forces; on 18 kPa elastomer

substrates, the force per focal adhesion was measured to be 5.5 nN/ μm ^{31, 214, 215, 216}. Genetically encoded tension probes suggest that E-cadherin is under 1-2 pN constitutive tension, which increases at stressed cell-cell contacts. The AFM unbinding force for VE-cadherin was 35-55 pN ^{110, 217}.

2.6 Mechanobiology of Adhesion Revealed Using Supported Lipid Bilayers

2.6.1 *Lateral Fluidity Guides Cell Adhesion*

The relationship between cell spreading and substrate stiffness has been well established; substrate stiffness can influence their lineage commitment and morphology ^{218, 219, 220}. In general, cells spread best on stiffer substrates, which support high traction forces that allow the cells to form larger contact areas ^{218, 221}. A related question is how cells respond to ligand mobility and tether flexibility. What are the effects of movable ligands versus rigidly anchored ligands? Many common substrates are limited in their ability to recapitulate the intrinsic flexibility of the ECM; therefore, these effects have been less studied than the stiffness response ²²². Recently, several novel substrates and mathematical models have been developed to probe these effects. SLBs are particularly well-suited for this line of research, because of their easily tunable architecture, fluidity, and functionalization.

Counterintuitively, increased fluidity does not always correspond with poor adhesion. Recall Smith, et. al.'s RGD-containing GUV's that interacted with fluid and nonfluid receptors: receptor mobility increased the GUV's ability to withstand external

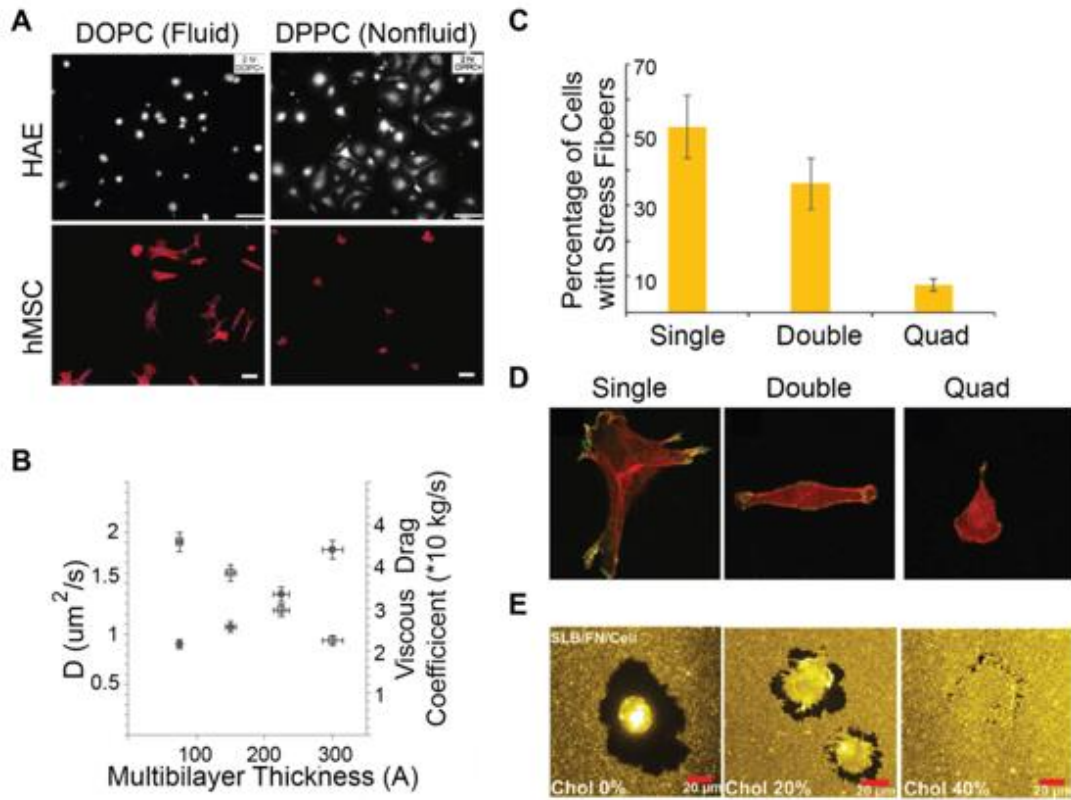


Figure 14: Cell adhesion on SLBs

(A) HAE and hMSCs exhibit opposite adhesion trends on fluid and nonfluid SLBs, demonstrating the cell specificity of the response. Scale Bar 20 μm top, unspecified length, bottom. Reprinted from ³ and ¹³ with permission from publisher. (B) Mechanical characterization of stacked bilayers demonstrates that thicker bilayers are more viscous (Reprinted from ¹⁵ with permission from publisher). (C) Myoblasts on laminin coated lipopolymer-stacked bilayers exhibit fewer stress fibers with increasing SLB stack size. (D) Myoblast morphology is dependent on stack thickness. Cell spreading decreases with multilayer thickness. 50 μm x 50 μm . (C,D reprinted from ¹⁷ with permission from publisher). (E) Depletion zones decrease in size on viscous SLBs. (Reprinted from [91] with permission from publisher). Figure reproduced from ⁷ with permission from publisher.

forces (2.2.1) ¹⁶⁰. Whereas nonmobile bonds stretched under tension, mobile receptor-ligand complexes reorganized under the GUV to distribute the forces ¹⁶⁰. Beyond the special case of catch bonds, nonmobile interaction lifetime would be shortened according to the Bell Model ⁹⁷.

To test the effects of ligand fluidity on adhesion, Garcia, et. al. incorporated three peptides into DOPC and DPPC supported lipid monolayers (SLMs) and monitored the attachment and spreading of HAE amniotic endothelial cells, as well as THP-1 and M07 and hematopoietic progenitor cells. HAE cells and both hematopoietic progenitor cells lines displayed decreased adhesion frequency and spreading on DOPC SLMs compared to DPPC SLMs ²²³. DOPC and DPPC have the same headgroup, but DOPC is fluid at room temperature and DPPC is not, suggesting a preference for nonfluid bilayers. However, in a similar study using human mesenchymal stem cells (hMSCs), Kocer and Jonkheijm obtained opposite results (Figure 14A). On both SLBs, hMSC adhesion frequency increased with ligand density, however, cells always spread better on fluid DOPC SLBs than nonfluid DPPC SLBs. This effect was most pronounced at high ligand densities, where cell area double on DOPC SLBs compared to that on DPPC SLBs. These results suggest that hMSC adhesion is enhanced with increased ligand interaction and binding avidity obtained through ligand clustering on a fluid SLB ²²⁴. Wong, et. al. probed hMSC differentiation substrates containing RGDs tethered to magnetic nanoparticles using PEG. Tethers were flexible at rest, but the application of a magnetic field restricted their flexibility. In contrast to SLB-culture, hMSCs exhibited increased spreading and focal adhesion assembly on less flexible tethers; these differences perpetuated over several days.

These diverging results can likely be attributed to increased mechanotransduction by magnetic actuation and differences in signaling associated with long range versus short range translocation ²²⁵. Attwood, et. al. found that human foreskin fibroblasts attached to RGD ligands on glass also preferred short tethers; increasing adhesion and cell area correlated decreasing tether length ²²⁶.

On lipopolymer-tethered stacked bilayers coated with a laminin network, cells exhibited reduced traction forces by both integrin and cadherin mediated adhesions with the addition of each plane ^{17, 115}. SLB fluidity increased with the number of layers (Figure 14B), and it was unusual that cells on a fluid SLB could generate any traction forces. These forces arose due to slowed cluster diffusion and leaflet coupling by lipopolymer tethers ¹⁷. Cell stiffness, spread size, and adhesion size were all reduced with increasing stack layer and fluidity (Figure 14C,D). This trend was unsurprising given that the addition of each layer reduced substrate stiffness, and compliant substrates cannot develop strong traction forces. However, traction forces associated with rigid substrates are still not incompatible with ligand mobility. Pompe, et. al. propose a model of friction-controlled traction forces, in which focal adhesions are motile, and the friction of adhesion movement generates traction forces ³.

In Vafaei, et. al.'s SLB-ECM hybrid system, Huh-7.5 cells remodeled the local environment through a combination of packing flexible ECM proteins and lipid diffusion. Collagen and fibronectin were covalently coupled to fluid SLBs. Following coupling, lipids remained fluid with a diffusion coefficient of $\sim 1 \text{ } \mu\text{m}^2/\text{s}$, but ECM proteins did not diffuse, so adhered cells could generate traction forces. Huh-7.5 cells spread on the ECM functionalized-SLBs with lower area and rounder morphology than on ECM-

functionalized glass due to reduced effective stiffness of the SLB platform. After 3 hours, cells showed ECM enrichment under the cell and depletion surrounding the cell (Figure 14E). As lipid fluidity was decreased with the addition of cholesterol, ECM depletion zones were also reduced, indicating that adhesion is modulated simultaneously by ligand flexibility and translation ¹⁷³.

Kourouklis, et. al. took a synthetic approach to solving the same problem. Fluid amphiphilic block polymers containing RGD ligands were used to mimic the ECM, and fluidity was adjusted by changing the percent “lubricating” polymer, much like cholesterol composition could tune SLB fluidity ²²². Interestingly, 3T3 cells behaved nonlinearly. Cells on intermediate-fluidity substrates were consistently rounder and smaller with sparser focal adhesions compared to cells on substrates of higher and lower fluidity. Kourouklis, et. al. suggest that at low fluidity, cells generated traction forces on the substrate and adhered primarily through focal adhesions. At high fluidity, traction forces diffused, but receptors reinforced adhesion through clustering ²²². This result and corresponding model, along with Vafaei’s observation of enrichment allude to the cell-free case of adhesion strengthening through mobility.

Altogether these data indicate that the mobility response is specific. We propose that that it is regulated by a complex combination of fluidity and force sensing, molecular friction, adhesion mechanism, and cell and receptor-specific responses; the relationship between these factors is yet to be elucidated. Ligand lateral fluidity and flexibility are convoluted in many attempts to characterize this response. SLBs will be useful in separating the effects of these two parameters through phase tuning, corralling, and altered linker length.

2.6.2 *Mechanobiology of Nascent Integrin Adhesions*

While integrins and mature FAs have been extensively characterized using traction force microscopy (TFM), super resolution imaging, force probes, and single molecule force spectroscopy, nascent adhesions (NA) have been more challenging to study, because few methods have sufficient spatiotemporal and mechanical resolution to map their dynamics^{13, 22, 30, 107, 210}. Recently SLBs have emerged as useful platform to probe NA formation and maturation into FA. Because fluid SLBs are traction force free, comparing the behavior of NAs on SLBs versus glass has allowed identification of the key biochemical and biomechanical signaling events in adhesion formation.

Initial integrin clustering and activation are independent of substrate mechanics and lateral forces; but mechanotransduction is required for the development of mature FAs from NAs. On glass, NAs containing integrins, paxillin, zyxin, and vinculin formed as actin polymerization extended lamellipodia at the leading edge of the cell. These clusters grew to 0.2 μm^2 and the majority rapidly disassembled as actin passed over the NA and further extended the lamellipodia. On average, NA persisted for ~1 minute^{95, 227}. A small fraction of NAs colocalized with actin and α -actinin tracks and matured rather than disassembling²²⁷. Nearly identical clusters formed on SLBs, but these NA persisted through the entire 15 minute observation window. NA size was independent of ligand density and activation state and was consistent on glass and SLBs⁹⁵. NA formation on fluid SLBs and rigid glass indicated that NAs form independent of substrate rigidity. On fluid SLBs, mature adhesions failed to form without traction forces, but NAs stabilized due ligated integrin clustering. Further supporting this, myosin overexpression promoted NA maturation on glass, and

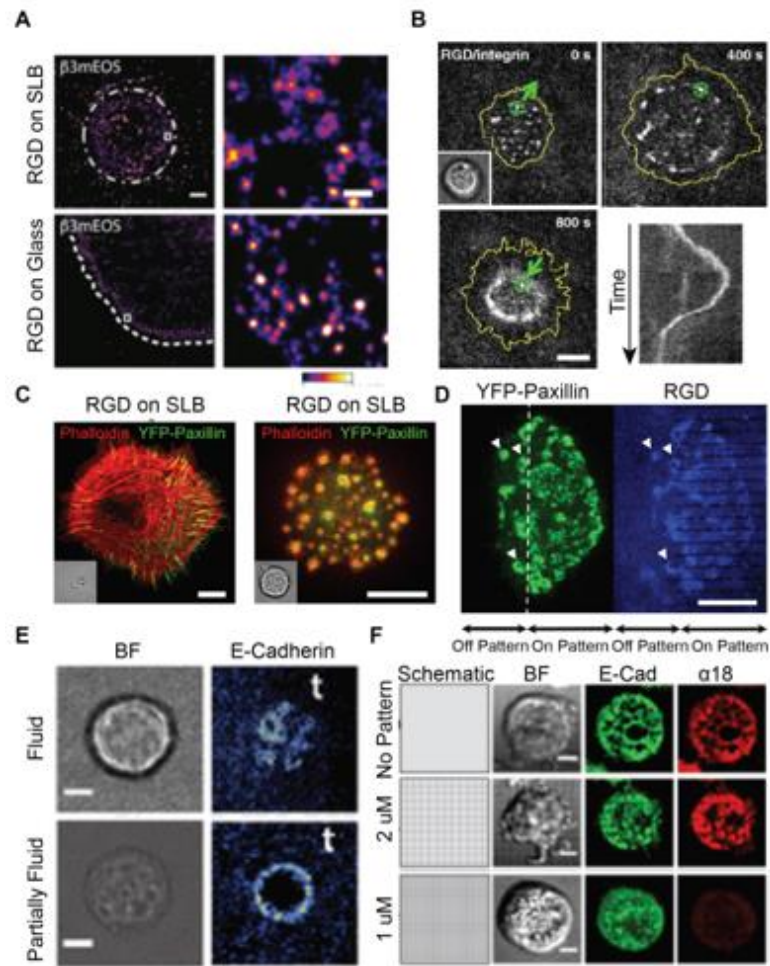


Figure 15 Mechanotransduction in integrin and cadherin-mediated adhesion assembly.

(A) Integrins form uniform-sized clusters on both glass and SLBs, indicating early cluster formation regardless of substrate mechanics. Scale bar 5 μ m. (Reprinted from [24] with permission from publisher). (B) Time-lapse and kymograph (bottom right) of integrin cluster translocation on an SLB. Clusters are transported radially outwards before forming a tight contractile ring. Scale bar 5 μ m. Reprinted from ⁶. Copyright 2011, National Academy of Sciences). (C) Focal adhesion (left) and podosome (right) formation in fibroblasts on glass and SLBs, respectively. Scale bar 10 μ m. (D) Podosomes form in the absence of traction forces on continuous SLBs but not on SLBs patterned with resistive chromium barriers. Scale bar 10 μ m. (C,D reprinted from ⁹ with permission from publisher). (E) Hybrid adherens junctions form on partially fluid bilayers containing NBD-PC but fail to form on fluid bilayers demonstrating the importance of viscous drag. Scale bar 5 μ m. (Reprinted from ⁵. Copyright 2015, National Academy of Sciences). (F) Resistive barriers restrict cadherin transport and serve as sites of mechanotransduction, causing altered α -catenin activation (marked by α 18). Scale bar 5 μ m. (Reprinted from ¹² with permission from publisher). Figure reproduced from ⁷ with permission from publisher.

myosin inhibition inhibited NA maturation but did not interfere with normal assembly or

disassembly⁹⁵.

Cluster stabilization on SLBs allowed observation of previously undetected steps in NA recruitment and migration (Figure 15A,B)⁶. On both continuous and corralled SLBs, integrin-RGD cluster growth coincided with focal adhesion kinase, talin, and paxillin recruitment and promoted actin polymerization over NAs, which caused clusters to initially move inwards in pairs⁶. Several clusters associated with FHOD1, which was activated by Src family kinases to promote actin polymerization driving lamellipodia spreading and cluster outwards translocation^{6, 228}. This was the first observation of outwards cluster motion in adhesion, which is not visible on glass or polymer substrates. On glass, FHOD1 signaling was required for polarized actin polymerization, traction force organization, and NA maturation²²⁸. On SLBS, cells retracted following spreading, and clusters were again translocated inwards, driven by Myosin II. Vinculin associated with clusters, suggesting talin unfolding during retraction^{6, 74}. Cells on gridlines aggregated integrins on the outside of barriers and formed stable adhesions, and cells on continuous substrates clustered integrins in tight rings and became round. Further studies are needed to measure forces generated by Myosin II on an SLB and to investigate whether these forces are sufficient to drive integrin tension, but measurement of very weak and highly cooperative Myo1c forces on an SLB coated bead suggest that this behavior likely also requires many engaged myosins¹⁶⁷.

NA formation and migration required talin. Expression of the talin head domain rescued NA formation and motility, but NAs were slightly smaller than WT. Expression of the rod domain rescued NA formation but with less mobility. Talin rod domains can dimerize, which aided in clustering, but the full protein was required for full and motile

NAs ⁹⁵. These results fit closely with Elosegui-Artola, et. al's recent results that talin expression is required for stiffness-dependent NA maturation on rigid substrates ²²¹. TFM revealed that on low stiffness substrates, fibroblast traction forces increased with rigidity independent of talin expression. On rigid substrates, traction forces increased with rigidity in talin-expressing cells and decrease with rigidity in talin-depleted cells ²²¹. Talin head domain expression activated integrins in talin-depleted cells, but could not recover high traction forces on rigid substrates. The tail-domain alone also failed to rescue the stiffness response, which could only be recovered by expression of the entire protein. Thus, talin binding and unfolding are critical decision-making steps in mechanotransduction. On fluid substrates, talin regulates NA motility, whereas on non-fluid substrates talin regulates the loading-dependent stiffness response.

Traction forces also impact the formation of podosome-like adhesions, mature FAs, and receptor internalization (Figure 15C) ^{9, 76}. NAs in macrophages and fibroblasts on continuous SLBs ultimately transition into podosome-like adhesions in the absence of strong traction forces. NAs initially formed as described above, but adhesion proteins later segregated to a ring surrounding a core of polymerizing actin. These adhesions closely mimicked monocytic podosomes and transformed fibroblast's invadopodia, which are protrusive structures. When fibroblasts spread on 1 μm line pitch corrallated bilayers which could support traction forces, mature adhesions like those observed on glass substrates were recovered ^{9, 76, 95}. Yu, et. al. proposed a mechanotransduction pathway in which traction forces serve as a checkpoint in forming stable FAs and failure to mount traction forces leads to Class 1a phosphatidylinositol 3-kinase (PI3K) recruitment, which initiates a biochemical cascade resulting in podosome formation ⁹. Notably these studies suggest a

model of local rather than global integrin mechanotransduction. The introduction of barriers on SLBs altered local force generation and signaling ^{6, 16}. When cells spanned the boundary of a continuous and corrallated bilayer, they formed traction force stabilized FAs in the patterned region and podosomes in the continuous, fluid region (Figure 15D) ⁹.

A subset of integrins were internalized on SLBs, but not on glass. After initial NA formation, integrin- $\beta 3$ clusters colocalized with Dab2, an adaptor protein in clathrin-mediated endocytosis. These NAs anti-colocalized with talin, indicating that recruitment of endocytosis machinery occurred downstream of mechanosensing. When actomyosin contractility was inhibited on glass, NA also colocalized with Dab2. Thus, failure to generate traction forces and stable FA can lead to integrin internalization ⁸⁶.

2.6.3 *Mechanobiology of Cadherin-Mediated Adhesion*

Cadherin mediated adherens junctions form at the cell-cell interface and are the main junctions responsible for tissue integrity. In adherens junctions, cadherins cluster in cis on the cell surface and bind to cadherins on the opposing cell surface through trans interactions. Several lines of evidence suggest that cadherins both transmit and respond to mechanical forces. AFM studies suggest cadherins can form both slip and catch bonds depending on binding configuration ¹²⁵. Micropillar arrays deflected by cadherin-mediated forces demonstrated that cadherins apply traction forces to their substrate, but the unnatural spatial arrangement of cadherins in these studies obscures the physiological relevance of the results ²²⁹. Borghi, et. al. inserted genetically encoded spider silk tension sensors into the cytoplasmic tails of cadherin, allowing the first measurement of mechanical forces across adherens junctions. Their results revealed that membrane associated E-cadherin is

constitutively under tension and that tension is transmitted across adherens junctions through cadherins¹¹⁰. However, as with FA, AJ formation has been challenging to probe. It was unclear how cadherins associated to form AJs, and how mechanical forces contributed to their assembly. Recently, SLBs have provided a platform to spatiomechanically resolve AJ and cadherin cluster formation, while also offering improved physiological relevance^{5, 17, 86}.

Membrane technologies have been used for more than a decade to study cadherin-mediated adhesion, but only recent works have successfully mimicked AJ formation. The earliest studies characterizing the mechanics of cadherin-mediated adhesion at a fluid interface employed simple cell-free systems^{230, 231}. Giant unilamellar vesicles (GUVs) were decorated with E-cadherin and allowed interaction with bilayers containing E-cadherin. Adhesion was observed by puckering in reflection interference contrast microscopy. Because cadherins bind weakly, vesicle adhesion to the bilayer required high concentrations of surface-presented E-cadherin²³⁰. Adhesions withstood thermal fluctuations but ruptured under shear force, suggesting weak clustering at adhesion sites²³¹.

Inspired by SLB studies using a bilayer to mimic an antigen presenting cell, Perez, et. al. published the first model of cadherin-mediated adhesion at the living-nonliving interface. MCF-7 cells were adhered to an SLB containing glycosylphosphatidyl inositol (GPI)-linked cadherins (hEFG)²³². A small percentage of cells loosely attached and clustered hEFG, but the majority of cells could not spread without anchors. The incorporation of immobile 5 μm fibronectin islands within the bilayers permitted cell spreading and hEGF enhancement under the cell.

In 2015, Biswas, et. al. used phase tuning to develop the first SLB platform to support artificial AJ formation⁵. 1% cells clustered cadherins into an AJs on highly fluid bilayers, but cells on partially fluid bilayers containing NBD-PC readily enriched E-cadherins into AJs (Figure 15E). FCS revealed that cadherins on SLB diffused as monomers, suggesting they only associated during AJ formation. AJ formation was achieved by cluster coalescence during filopodial retraction. In both fluid and partially fluid bilayers, AJs formed in an all-or-nothing fashion; partial junctions were not observed. This observation together with the enhanced AJ formation on low fluidity SLBs suggest that adherens junctions require mechanical forces and kinetic nucleation to form. Very viscous SLBs generated resisting forces that could possibly support catch bonds across bound cadherins which would elongate bond lifetime. Low diffusivity promoted clustering and active nucleation, allowing junction formation to proceed. Within junctions, FRAP revealed that cadherins had low turnover and instead were immobilized within stable junctions¹². Surprisingly, mechanical resistance alone was insufficient to form adherens junctions. Although corralled bilayer gridlines slowed transport and served as sites of force generation, cells on fluid corralled bilayers failed to form AJs. Thus, long range lateral transport of receptors is required (Figure 15F)⁵. This mechanism is in contrast with integrin adhesion, where forces at barriers locally determined the adhesion pathway.

SLBs with reduced fluidity by the addition of high density poly-His E-cadherin ectodomain also supported AJ formation and were used to study α -catenin mechanobiology in cadherin-mediated adhesions¹². Cells spread on these SLBs exhibited two populations of cadherins that clustered during filopodial retraction: AJs at the cell periphery and cadherins loosely clustered in “central adhesions” underneath the cell. AJs and central

adhesions both contained α - and β -catenin, but only AJs colocalized with actin, vinculin, and phosphorylated myosin light chain. Interestingly, the vinculin head domain and $\alpha 18$ could bind both populations of α -catenin; this indicated that α -catenin was active both AJ and central adhesions, which was unexpected because activated α -catenin usually is bound to actin. Cells spread on SLBs with widely spaced chromium grids exhibited normal cluster formation, but spreading and cluster formation by filopodia, along with $\alpha 18$ binding, was reduced on narrow grids (Figure 15F). Thus, α -catenin activation required mechanotransduction during cell spreading and retraction to activate, but sustained forces were not necessary for it to maintain its open conformation in cadherin clusters ¹².

2.7 Conclusions and Future Directions

Major breakthroughs in SLB technologies include the ability to precisely pattern fluid and anchored ligands, to incorporate properly oriented and fluid transmembrane proteins, to generate multiple stacked bilayers, and to measure mechanical forces at the cell-SLB interface using ratiometric tension probes ^{8, 10, 14, 15, 17, 115}. Current studies of integrin and cadherin mediated adhesion using SLBs offer new insight into NA and AJ formation and demonstrate the power of spatiomechanical mutation using SLBs. By combining the techniques described in this review, we envision mechanically tunable cell substrates and sensors to probe specific signaling events in mechanotransduction. Hybrid adhesions consisting of immobilized ligands on STONAs and mobile ligands into the surrounding SLB will reveal the role of ligand mobility and transport in adhesion and cluster formation. Adjusting fluidity and stiffness while maintaining ligand density will deepen our understanding of how cells respond to ligand mobility versus substrate rigidity.

An open topic in the literature remains the dynamics of molecular mechanics: How do forces evolve in time and space across individual proteins, adhesion complexes, and the cell? SLBs provide a useful platform to approach this question, particularly relating to early events in adhesion formation. Ratiometric MTFM will track tension density evolution in spreading and retracting NAs and podosomes. Moving forward, fluorescence lifetime imaging may provide a simpler, concentration independent method to measure forces on an SLB.

SLBs are notable for their reductionist approach to biological interfaces, however further advancements in SLB engineering will focus on the fabrication of more sophisticated and physiologically relevant mechanical niches. Very recently, Vafaei, et. al. introduced ECM functionalized SLBs to mimic very soft neural tissue. This method will allow the probing of mechanotransduction and gene expression in previously inaccessible regimes¹⁷³. The role of the glycocalyx remains poorly understood; decorating SLBs with glycolipids could offer a novel approach to explore its mechanical influence in juxtacrine signaling. Recent literature suggests that the glycocalyx is important regulating receptor clustering and FA assembly in cancer metastasis and in cell recognition in the immune system^{233, 234, 235, 236}. Incorporating ratiometric tension probes into SLBs mimicking the glycocalyx could provide direct evidence of how the glycocalyx influences mechanotransduction independent of cytoskeletal forces²³³.

Although Afensenkau, et. al. succeeded in culturing neurons on an SLB for nearly 3 weeks, SLBs exhibited degradation during this timeframe that would prevent high quality molecular imaging²³⁷. Therefore, SLBs can be used to study initial adhesions, but they cannot yet serve as dual culture and imaging platforms for longer processes such as

synaptogenesis, stem cell differentiation, and embryo development. Further work is needed to optimize SLB stability for long-term studies. One approach has been to chelate calcium following SLB formation, but given the calcium dependence of many adhesion receptors, this unlikely to be a viable strategy for live cell studies²³⁸. In addition, while SLBs capture the planar interface at the cell-cell or cell-ECM junction, cells behave differently in 2D and 3D. Although 3D SLB-coated wells have been developed, these can only contain a single cell, not a cluster of cells that more accurately models tissue. More stable and 3D platforms are needed to understand mechanotransduction during development.

Despite these challenges, SLBs can still offer improved physiological relevance to model cell-cell and cell-matrix interactions. We envisage that SLBs will be widely used as mechanically tunable substrates to spatiomechanically mutate and probe events in adhesion. Beyond adhesion, these techniques will also be useful for studying mechanotransduction pathways in immune cell activation and viral entry. SLB technologies provide a sensitive and controllable toolset to study the link between physics and biology.

Acknowledgements: This work was supported by the NIH (R01-GM097399) and the NSF CAREER Award (1350829) for financial support. This material is based upon work supported by the National Science Foundation Graduate Research Fellowship Program under Grant No. DGE-444932.

Disclaimers: Any opinions, findings, and conclusions or recommendations expressed in this material are those of the author(s) and do not necessarily reflect the views of the National Science Foundation.

CHAPTER 3. DNA MECHANOTECHNOLOGY REVEALS THAT INTEGRIN RECEPTORS APPLY pN FORCES IN PODOSOMES ON FLUID SUBSTRATES

Adapted from Glazier, et. al. *Nature Communications*, 2019.

3.1 Abstract

Podosomes are ubiquitous cellular structures important to diverse processes including cell invasion, migration, bone resorption, and immune surveillance. Structurally, podosomes consist of a protrusive actin core surrounded by adhesion proteins. Although podosome protrusion forces have been quantified, the magnitude, spatial distribution, and orientation of the opposing tensile forces remain poorly characterized. Here we use DNA nanotechnology to create probes that measure and manipulate podosome tensile forces with molecular piconewton (pN) resolution. Specifically, Molecular Tension-Fluorescence Lifetime Imaging Microscopy (MT-FLIM) produces maps of the cellular adhesive landscape, revealing ring-like tensile forces surrounding podosome cores. Photocleavable adhesion ligands, breakable DNA force probes, and pharmacological inhibition demonstrate local mechanical coupling between integrin tension and actin protrusion. Thus, podosomes use pN integrin forces to sense and respond to substrate mechanics. This work transforms our understanding of podosome mechanotransduction and contributes tools that are widely applicable for studying receptor mechanics at dynamic interfaces.

3.2 Introduction

Podosomes are specialized acto-adhesive structures that coordinate a variety of cell-type specific processes ranging from forming the sealing-zone for bone-resorption in osteoclasts to facilitating migration and antigen scavenging in immune cells^{25, 27, 239, 240}. In Wiscott-Aldrich Syndrome, cells fail to form podosomes, and patients experience frequent infections, impaired blood-clotting, and altered bone resorption^{43, 52, 53, 54}. In HIV, however, numerous enlarged podosomes are associated with increased cell migration, macrophage tissue infiltration, and elevated bone degradation^{57, 58}. Invadopodia, which are structurally similar to podosomes, facilitate cancer cell migration during metastasis^{23, 48, 241}. Hence, podosome formation and regulation is critical to disease pathophysiology and homeostasis.

Akin to the widely studied focal adhesions (FA), podosomes have been shown to exert mechanical forces and to respond to ECM stiffness^{24, 36, 76, 80, 242, 243, 244}. Whereas FAs assemble into fibrillar micro-scale structures that apply contractile forces to the substrate^{24, 30, 31, 210, 245, 246}, podosomes assemble into a columnar architecture consisting of an actin core surrounded by a ring complex containing adhesome proteins including integrin receptors⁶¹. The actin core protrudes from the cell body, applying nN compressive forces onto the underlying substrate^{65, 75, 76}. Given that a static cell cannot experience a force imbalance²⁴⁷, it is widely recognized that podosomes apply opposing tensile forces, with some disagreement as to the requirement for integrin adhesion forces^{26, 61, 65, 71, 75, 248, 249}. Mathematical modeling suggests that these tensile forces are localized to the podosome ring⁶⁵, and there are two lines of experiments that support this model. The first comes from biophysical measurements of talin extension²⁴³ and vinculin tension⁷⁵ within podosomes. These measurements are indirect as they fail to map the molecular forces applied by the podosome itself. The second class of measurements reports bulk substrate deformations

using traction force microscopy (TFM). While TFM provides a direct measure of cellular stresses, the spatial and force resolution of the method precludes mapping the forces at the podosome ring complex. A more sensitive variant of TFM that is interferometry-based offers improved force sensitivity but still averages deformations of the substrate²⁵⁰ and thus cannot quantify receptor forces. To the best of our knowledge, no quantitative force maps have been reported validating the role of adhesion receptor mechanics in opposing actin protrusion and mechanically linking the substrate and the cytoskeleton within podosomes.

Further confounding podosome mechanical models, recent results demonstrated the formation of podosome-like adhesions on supported lipid bilayers (SLBs)^{9, 83}. SLBs are phospholipid membranes that self-assemble onto a glass slide. Lipids are confined in the z-direction but are laterally fluid⁸⁴. Thus, on SLBs, podosomes are reported to form even in the absence of traction forces^{9, 85}, which is confounding since podosomes apply compressive forces on the SLB.

In this work, we employ DNA-based mechanotechnology tools to challenge the hypothesis that integrins cannot apply forces on fluid membranes and to investigate the role of integrin tensile forces in podosome mechanosensing. As a material, DNA offers the ability to map and perturb receptor forces with pN force resolution and sub-micron spatial resolution. We first quantify podosome-mediated depletion as a marker of actin core protrusion on SLBs. Next, we introduce Molecular Tension – Fluorescence Lifetime Imaging Microscopy (MT-FLIM), producing pN maps of integrin tension during receptor-ligand clustering at the cell membrane. Previously, Molecular Tension Fluorescence Microscopy (MTFM) imaging on supported bilayers was carried out using ratiometric probes^{8, 10}, but these induced artificial clustering or employed three-way energy transfer,

which hinder quantitative analysis. Moreover, we found that conventional MTFM probes³⁰ are static quenched and poorly suited for FLIM. Thus, we report a re-engineered DNA-based FLIM-FRET probe that circumvents these problems. To better understand podosome tensile forces, we apply a recently developed force-orientation analysis technique to demonstrate that integrin forces are primarily perpendicular to the substrate. Treatment with pharmacological inhibitors showed that podosome tensile forces are a direct consequence of actin polymerization.

Finally, we model pN integrin forces in podosomes and demonstrate that podosomes exert nN vertical forces on an SLB, in agreement with previously measured protrusion forces⁷⁶. Our work offers receptor-level quantitative maps of integrin tension on fluid substrates and provides direct experimental evidence that podosomes are mechanosensors with local pN sensitivity.

3.3 Results

3.3.1 *Podosome actin content correlates with RGD-probe depletion*

Cyclic Arg-Gly-Asp-*D*-Phe-Lys (cRGDfK, RGD) peptides were tethered to the SLB through DNA oligonucleotides (Figure 17a, Table A 1, Table A 2, Figure A 1, Figure A 2, Figure A 3, Figure A 4). RGD-functionalized SLBs displayed a lateral diffusion coefficient of $1.41 \pm 0.07 \mu\text{m}^2 \text{s}^{-1}$ (Figure 16b)⁵. Within tens of minutes of culturing NIH 3T3 fibroblasts onto these substrates, we observed the formation of podosome-like adhesions^{9, 83}. These adhesions were actin rich, excluded the RGD-DNA ligand (Figure 16c) and were surrounded by vinculin and phospho-paxillin (Figure A 4). Since these podosome-like adhesions contained the key elements of podosomes⁹, we refer to these

structures as podosomes throughout this manuscript. The depletion of RGD-DNA was caused by pushing forces generated by the protrusive actin core⁹. Note that these forces exclude RGD-DNA but do not rupture the underlying SLB (Figure A 5), which is largely incompressible^{84, 251, 252}. The f-actin rich core of podosomes was anti-localized with RGD-DNA (Figure 16d), and increased actin content correlated with RGD depletion (Figure 16e). Podosomes that depleted more RGD (measured by % decrease in fluorescence) also had larger depletion radii (Figure 16f). Given these data and the published finding that actin content and protrusion forces display similar behavior^{66, 75}, we reasoned that RGD depletion serves as a suitable proxy for podosome protrusive forces on an SLB.

3.3.2 *MT-FLIM maps pN receptor tension and clustering on SLBs*

To determine whether integrins apply tensile forces in podosomes on an SLB, we developed MT-FLIM to visualize receptor forces applied on fluid membranes. MTFM has permitted mapping of receptor forces on rigid substrates^{21, 30, 31, 106, 208, 210, 211, 253, 254} but is challenging to apply on fluid interfaces such as SLBs, because tension-signal and probe density are convolved as receptors cluster⁸⁴. Two ratiometric approaches have aimed to address this problem. The first used 15 nm particles tagged with MTFM probes and a reference dye,⁸ but this leads to artificial clustering of receptors as they bind to the multivalent ligands presented by the nanoparticle, which may modulate integrin signaling^{255, 256}. A later method leverages DNA-based MTFM probes tagged with three organic dyes¹⁰; however this probe likely experiences difficult to correct through-space energy transfer pathways between the three chromophores.

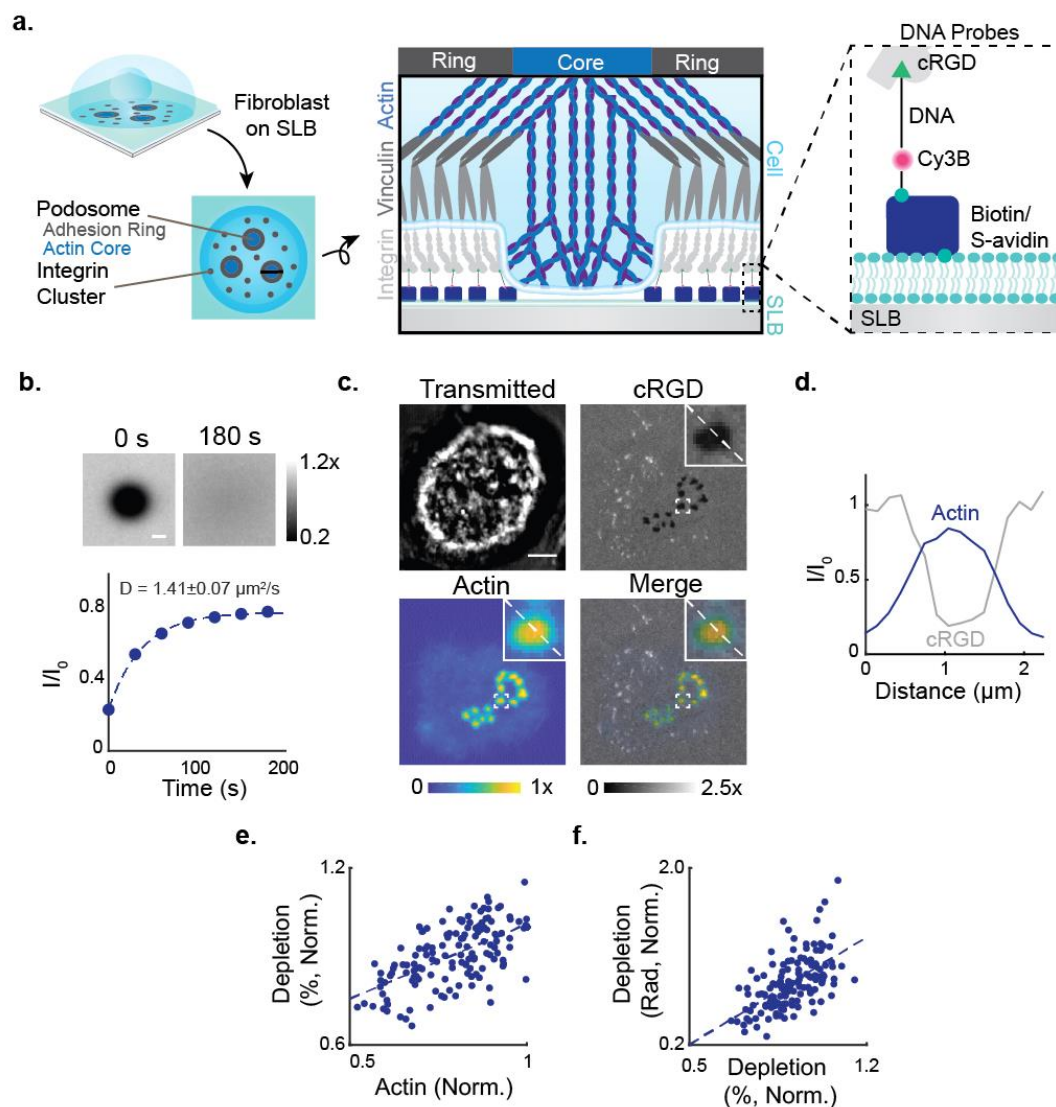


Figure 16 NIH 3T3 Fibroblasts form Protrusive Podosomes on SLBs

(a) (Left) Schematic of the SLB podosome model. (Middle) Schematic of a single podosome at the cell-SLB interface across the black line. Podosomes exclude RGD-probes at their protrusive core. (Right) Zoomed-in schematic of a single DNA probe. (b) Representative images and mean intensity plot of RGD-DNA probes in a fluorescence recovery after photobleaching experiment. Data were normalized to the SLB intensity at $t = 0$ s. DNA probes had a diffusion coefficient of $1.41 \pm 0.07 \mu\text{m}^2/\text{s}$ (Mean + s.e.m., $n = 9$ FRAPs, 3 experiments). (c) Representative podosome-forming cell on an SLB decorated with single-stranded DNA probes. Cells were transfected LifeAct to visualize actin cores. Scale bar, $5 \mu\text{m}$. (d) Linescan analysis across the zoomed-in podosome in c. cRGD and actin intensity are normalized to the SLB background. (e,f) Scatter plots of actin intensity versus depletion (%) and depletion (%) versus depletion radius. All data were normalized by the brightest podosome per cell to account for varying LifeAct expression. ($r = 0.657$, 0.604 , $N = 161$ podosomes, 23 cells, 3 experiments).

We hypothesized that FLIM could be used to map receptor forces on fluid membranes, because fluorescence lifetime is sensitive to energy transfer but is independent of dye concentration⁸⁸. We functionalized SLBs with FRET-based DNA tension probes containing binary DNA hairpins with a tunable $F_{1/2}$ threshold and two linker arms; the $F_{1/2}$ threshold is defined as the force equilibrium at which 50% probes open (Figure 17)³⁰. The bottom arm was hybridized to a biotinylated quencher strand containing an internal deoxythymidine BHQ1 modification. We selected this site for the quencher to ensure that the probe was FRET quenched, as absorbance spectroscopy demonstrated that conventional MTFM probes are static quenched and thus poorly suited for FLIM (Figure A 6). The upper arm of the DNA hairpin was hybridized to a Cy3B ligand strand containing cRGD. At rest, closed probes are FRET quenched, with a low fluorescence intensity and a short fluorescence lifetime. When integrin receptors bind and transport DNA tension probes into nascent integrin adhesions, the probes are clustered, causing an increase in fluorescence intensity. If the applied force equals or exceeds $F_{1/2}$, then the DNA hairpin unfolds, causing an increase in both fluorescence intensity and fluorescence lifetime (Figure 17a).

Because of the limited photon-budget^{257, 258} and the probes' multiexponential fluorescence decay (Table A 3, Figure A 7a-c), we resorted to fit-free FLIM imaging in which the average lifetime is reported as the barycenter of photon arrival time. By this definition of average lifetime, multiexponential decays do not exhibit a linear relationship between average fluorescence lifetime and FRET efficiency^{92, 94}. Therefore, we generated empirical calibration curves to relate the percentage of opened DNA probes to the

measured fluorescence lifetime (Figure 17b). This was achieved by imaging a small library

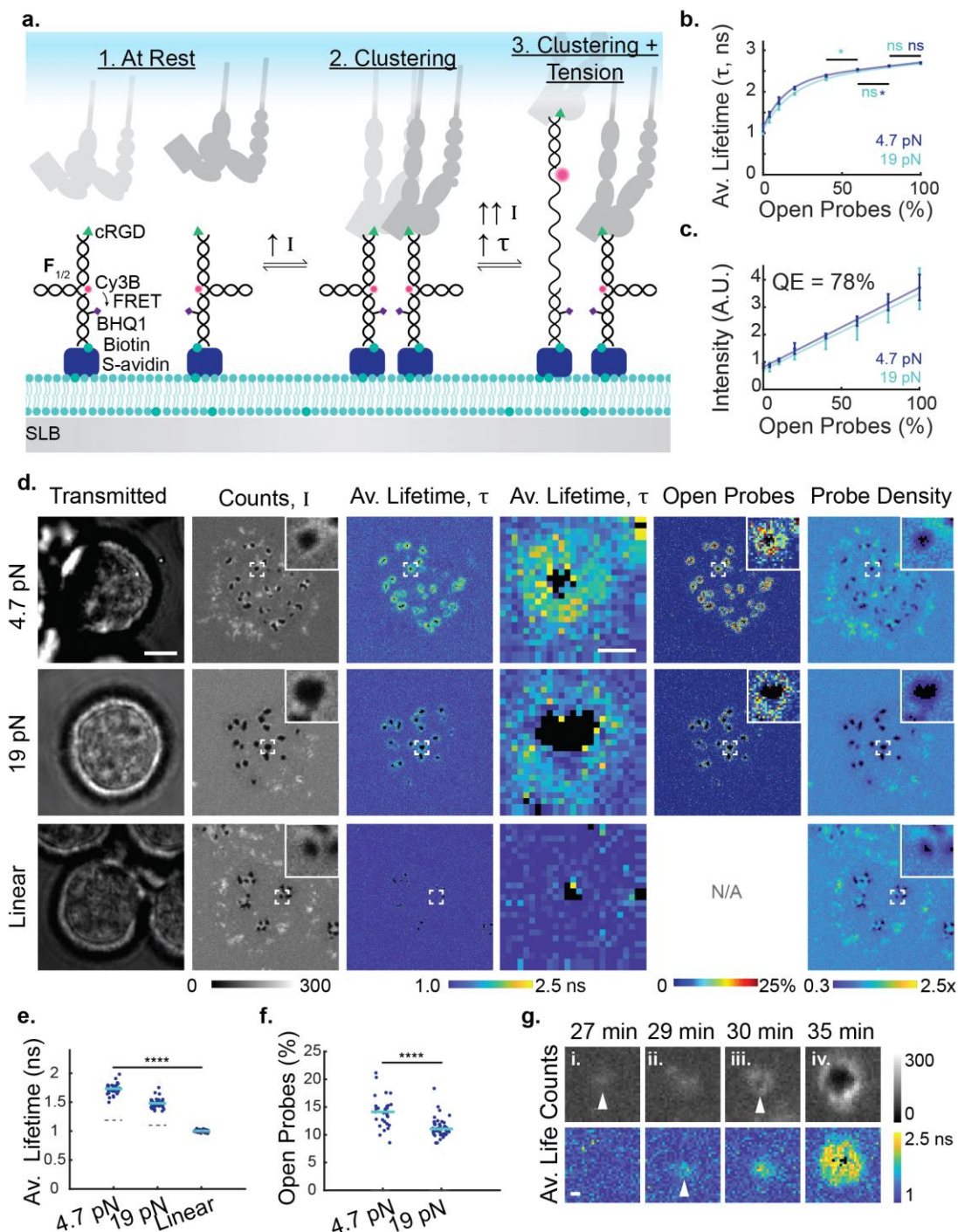
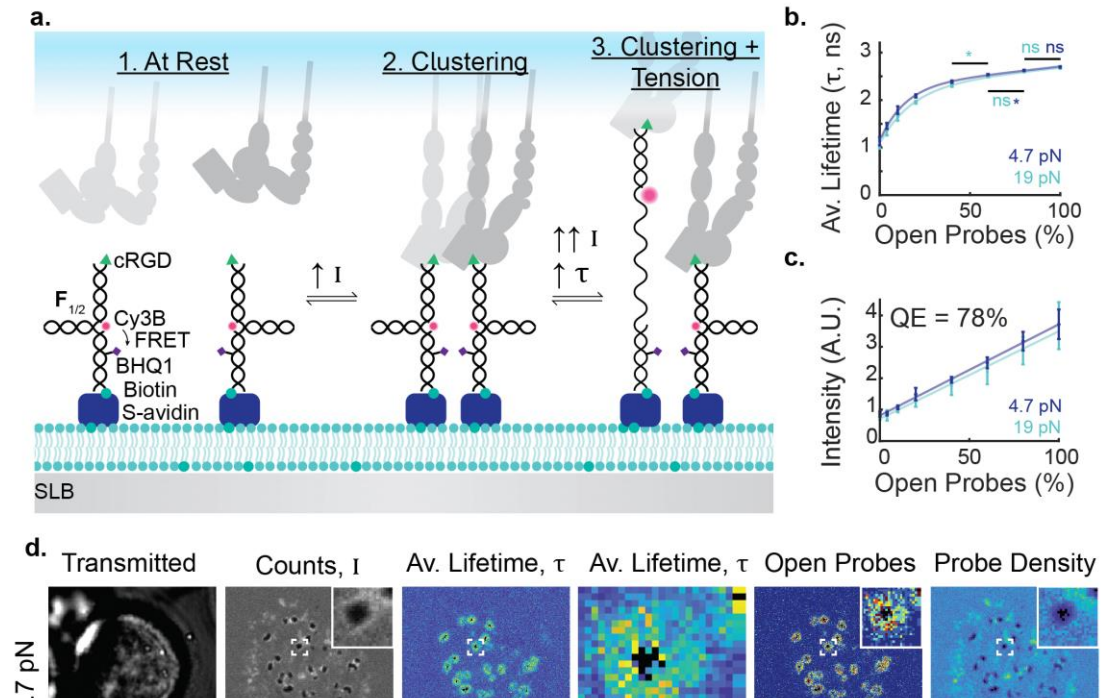


Figure 17 Fibroblasts exert pN integrin tension in podosome rings on SLBs

(a) MT-FLIM probes report clustering and tension. 1. In closed probes, donor fluorescence (Cy3B) is FRET quenched by BHQ1 quencher. 2. Receptor binding and clustering increases probe density and local intensity. 3. When integrin receptors apply tension above $F_{1/2}$, MT-FLIM probes unfold, yielding a massive increase in both fluorescence lifetime and fluorescence intensity. Note that DNA hairpins are binary and thus are either in the open or closed conformation.

Figure**17**

of SLBs presenting a mixture of opened and closed DNA probes (Figure A 7 d,e). We also characterized these SLBs using epifluorescence to determine probe quenching efficiency (Figure 17c) and measured intensity and fluorescence lifetime as a function of probe density (Figure A 8). We found a subtle decrease in probe lifetime with increasing probe density. However, this effect was minor compared to the effect of force-mediated hairpin opening.

To map the podosome tensile landscape, we imaged $F_{1/2} = 4.7$ pN tension probe signal generated by podosome-forming fibroblasts on SLBs (Figure 17d). In the photon counts channel, we observed three populations of signal: negative signal corresponding to actin-mediated depletion at the podosome core, bright rings that surrounded the depletion zones, and bright puncta distributed across the cell-SLB junction, which we termed integrin clusters. Both clusters and podosome rings colocalized with $\beta 1$ integrin, confirming that they were caused by integrin-mediated adhesions (Figure A 9). The fluorescence lifetime increased in podosomes, indicating that integrins mechanically unfolded DNA hairpins

with $F \geq 4.7$ pN. In contrast, the bright puncta outside of podosomes did not show changes in lifetime; thus integrin forces were <4.7 pN in these regions. Using our calibration curves combined with the average lifetime maps, we calculated the percentage of opened probes. By combining these data with a mathematical framework, we also extracted the local probe density (A.1.2.1 Determination and interpretation of percentage of open probes and local probe density). To understand the limits of detection in low density regions, we analyzed MT-FLIM photon statistics (A.1.2.2 Discussion of MT-FLIM Photon Statistics, Figure A 10). Note that low photon count pixels, such as within depletion zones, produce less reliable lifetime values; these pixels were excluded according to lifetime and photon count cutoffs described in A.1.2.2 Discussion of MT-FLIM Photon Statistics (Figure A 11). Images represent the accumulation of signal over one minute, so there is some spatiotemporal averaging. Nevertheless, these images provide the first quantitative maps of integrin forces on an SLB and within podosomes. Moreover, our conclusions are generalizable: MT-FLIM imaging of Src-transformed mouse embryonic fibroblasts indicated that this spatial distribution of forces is also common in invadosomes and invadosome belts (Figure A 12).

We next challenged podosomes using a more stable hairpin with $F_{1/2} = 19$ pN. Fluorescence lifetime increased in podosome rings but corresponded to a lower percentage of open probes. This suggested that a smaller subset of integrins apply $F \geq 19$ pN compared to $F \geq 4.7$ pN (Figure 17e,f). Control experiments employing a linear DNA duplex lacking a hairpin secondary structure exhibited nearly identical photon counts signal as the hairpin probes, showing regions of depletion and bright puncta. These regions did not exhibit significant changes in fluorescence lifetime. In addition, control experiments in which the

fluorophore-quencher pair and ligand were separated onto two independent co-presented DNA probes showed no change in fluorescence lifetime (Figure A 13). Together, these data confirm that changes in lifetime are due to integrin-mediated mechanical unfolding of the hairpin.

To investigate the time-course of podosome mechanical force generation, we next collected timelapse MT-FLIM images of cell spreading and podosome formation (Figure 17g, Figure A 14). Within 20 min of plating, cells formed dynamic integrin clusters which lacked detectable forces. Clustering was followed by tension and podosome-mediated depletion. Depletion was either preceded by tension (as shown) or occurred simultaneously with tension. Note that resolving the order of events with higher time resolution was difficult to achieve because of the 60 s FLIM acquisition time. Nonetheless, we found that integrin tension increased as podosomes became larger and more protrusive. Podosomes tended to move outward toward the cell periphery, and clusters grew by *de-novo* podosome formation at common nucleation sites or by splitting (Figure A 14). These time-resolved tension measurements show tight spatiotemporal coordination between podosome protrusive forces and tensile forces at the single podosome level.

3.3.3 *Podosome forces are primarily vertical*

Given that SLBs cannot support lateral traction forces and that actin cores exert pushing forces on the substrate, we hypothesized that the integrin forces in podosome rings would be primarily oriented in the vertical direction. Alternatively, the protrusive podosome core could serve as a diffusion barrier^{16, 84} to support podosome lateral forces. To test this, we used Molecular Force Microscopy (MFM)²¹, a recently developed

fluorescence polarization-based method to quantify the direction of receptor-forces (Figure 18a-d). Whereas MT-FLIM reports the magnitude of tension, MFM maps force orientation. DNA-based tension probes reorient in the direction of applied integrin forces. In MFM, cyanine fluorophores are rigidly coupled to the DNA duplex²⁵⁹. Thus, integrin forces dictate both the orientation of the DNA tension probe and of its attached fluorophore. MFM utilizes excitation resolved polarization microscopy to measure the orientation of the fluorophore in order to deduce the strained-DNA orientation. MFM leverages mechano-selection, in which only open probes contribute significantly to fluorescence and polarization signal, thereby suppressing the contribution of non-oriented closed probes. Accordingly, we substituted MT-FLIM probes for static quenched tension probes, in which the Cy3B fluorophore and BHQ1 quencher are in direct contact, thus offering mechano-selection of the Cy3B signal (Figure 18a, Figure A 15a-b). Although these probes lack a density reporter, they provide a suitable proxy for integrin forces in this system, because podosome rings tended to show only minor enrichment in the MT-FLIM density channel (Figure 17d). We confirmed that the effects of clustering and dynamics were minor using linear MTFM probes (Figure A 15c-g). MFM fluorophore orientation measurements were validated using a membrane-bead standard as recently described²¹ (Figure A 16).

MFM analysis of podosome rings suggested that forces were primarily vertical or disorganized (Figure 18b-d, Figure A 16g). The average podosome tilt angle per cell was $21^{\circ} \pm 2^{\circ}$ from vertical. In comparison, integrins in fibroblast FAs on glass exert forces with a tilt angle of $40^{\circ} \pm 2^{\circ}$ ²¹. MFM has limited sensitivity to tilt angles less than 20° from the

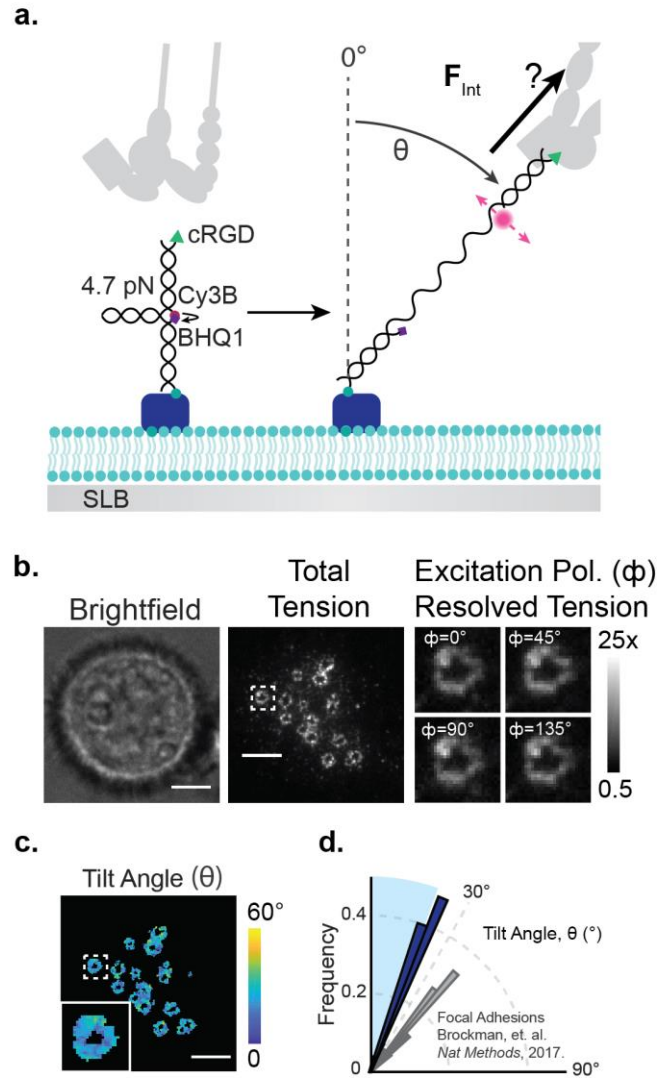


Figure 18 Integrins exert vertical forces in podosome rings

(a) Schematic of MFM on an SLB. When an integrin receptor binds and applies forces above 4.7 pN, the probe unfolds and generates Cy3B fluorescence. Probes orient along the applied force vector, allowing determination of the tilt angle, θ , from the excitation polarization dependent Cy3B fluorescence. (b) Representative podosome MFM data after ~ 90 min cell spreading. Total tension is the maximum tension signal per pixel, which corresponds to the excitation polarization best aligned with the average per pixel Cy3B orientation. Podosome zoom-ins depict the normalized Cy3B fluorescence at four different excitation polarizations. (c) Computed tilt angle map for the cell shown in b. (d) Angular histogram of average podosome tilt angle per cell, θ . Vertical forces are indistinguishable within the $\sim 20^\circ$ cone, represented by the blue region (N = 25, 3 experiments).

normal and becomes more susceptible to noise for these small tilt angles. Therefore, these

MFM results are consistent with podosome tension that is primary oriented normal to the SLB substrate²¹.

To support our MFM result, we performed emission-resolved polarization measurements²¹ (Figure A 17). Here, any global organization in the lateral component of podosome forces within the ring will lead to bright nodes in fluorescence anisotropy. In agreement with a model of vertical force generation, we found no organized pattern in podosome fluorescence anisotropy. This confirms MFM measurements, indicating that podosomes on SLBs lack an organized traction force component in the plane of the SLB.

3.3.4 *Integrin forces are actin but not myosin IIa dependent*

To understand the mechanism of integrin force generation in podosomes, we treated cells with a panel of small-molecule inhibitors and quantified changes in 4.7 pN tension and core depletion size using MT-FLIM. We first treated cells with Y27632 to inhibit Rho kinase and found that integrin forces were not diminished (Figure 19a,b). Surprisingly, we observed an increase in the percentage of open probes and core depletion size (Figure A 18a). To test whether this observation was caused by myosin II inhibition, we treated cells with blebbistatin (Figure A 19a-c). Although it was reported that blebbistatin releases tension on genetically encoded vinculin tension sensors in macrophages on immobile ligands⁶¹, we observed only a slight change in integrin tension ($p = 0.0464$). Podosome core size was not affected ($p = 0.3603$). We further validated this result by knocking down *MYH9*, the myosin IIa head domain. No significant changes in podosome depletion or tension were observed when *MYH9* was knocked down (Figure A 19d-h). Because actomyosin contractility was largely dispensable in generating tension in integrin receptors

on SLBs, we next treated cells with jasplakinolide, which is a potent actin stabilizer and polymerizer that causes reorganization of the cytoskeleton into disorganized aggregates^{77, 260}. Following 500 nM Jasplakinolide treatment for 8 min, core depletion area decreased, and integrin tension in podosome rings was reduced (Figure 19c,d, Figure A 18b). These data support a model in which actin polymerization in the podosome alone is sufficient to support integrin-based tension in the podosome ring complex.

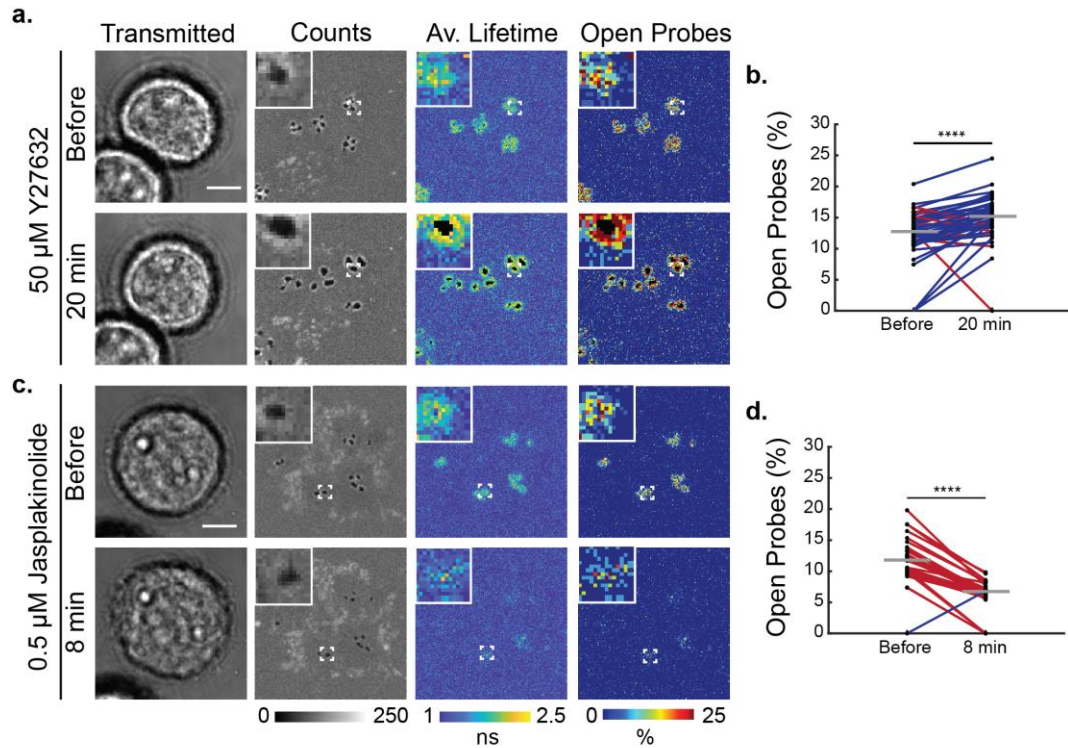


Figure 19 Actin polymerization drives integrin tension

(a,c) Representative before and after MT-FLIM images of NIH-3T3 fibroblasts on 4.7 pN MT-FLIM probes treated with 50 μ M Y27632 or 0.5 μ M Jasplakinolide, respectively. (b,d) Average percent open probes in podosomes per cell before and after drug treatment. Blue and red lines represent an increase or decrease in percent open probes per cell, respectively. Grey horizontal lines represent the median percent open probes. Statistics were performed with a two-tailed Wilcoxon matched-pairs signed rank test. At least 34 cells from 3 experiments were analyzed per condition. **** $P < 0.0001$. All scale bars, 5 μ m.

3.3.5 Protrusion and tension engage in a mechanical feedback loop

We next sought to perturb podosome tension to determine how podosomes respond to external mechanical inputs (Figure 20a). To achieve this goal, we engineered releasable MTFM probes by anchoring probes with a photocleavable (PC) biotin group (Figure 20a-b). This PC modification allows for optical manipulation of integrin tension with high spatial and temporal resolution (Figure A 20). Cells were cultured on SLBs with PC probes for ~ 1 hr. Then, integrin ligands anchoring podosomes were severed with a 405 nm laser (Figure 20c). We anticipated that optical release of DNA probes would terminate integrin tension and cause rapid refolding of the DNA hairpin and re-quenching of tension signal in the podosome ring (Figure A 21). Upon 405 nm illumination of a $7 \mu\text{m}^2$ podosome-containing region, we tracked the changes in tension signal both at the site of photocleavage (proximal) and across the entire cell (distal) (Figure A 22). Although SLBs dissipate long-range forces, we still wondered if it would be possible to observe global changes that were communicated intracellularly, such as through altered diffusion of adhesion proteins⁷⁵. In severed podosomes proximal to photocleavage, we observed a massive loss of tension signal followed by a gradual remounting of tension (Figure A 21), which can be attributed to the replenishing of surface-bound ligands by diffusion. In contrast, podosomes distal to the site of photocleavage exhibited only a small reduction in tension signal.

To quantify the changes in podosome protrusiveness upon loss of integrin tension, we synthesized PC probes lacking the quencher (Figure 20d). Here, Cy3B intensity is insensitive to tension, and changes in signal exclusively report DNA density. Hence, probe depletion radius provided a proxy for the change in protrusive forces applied by the podosome's actin core. We tracked individual podosomes before (-12 s) and after (29 s)

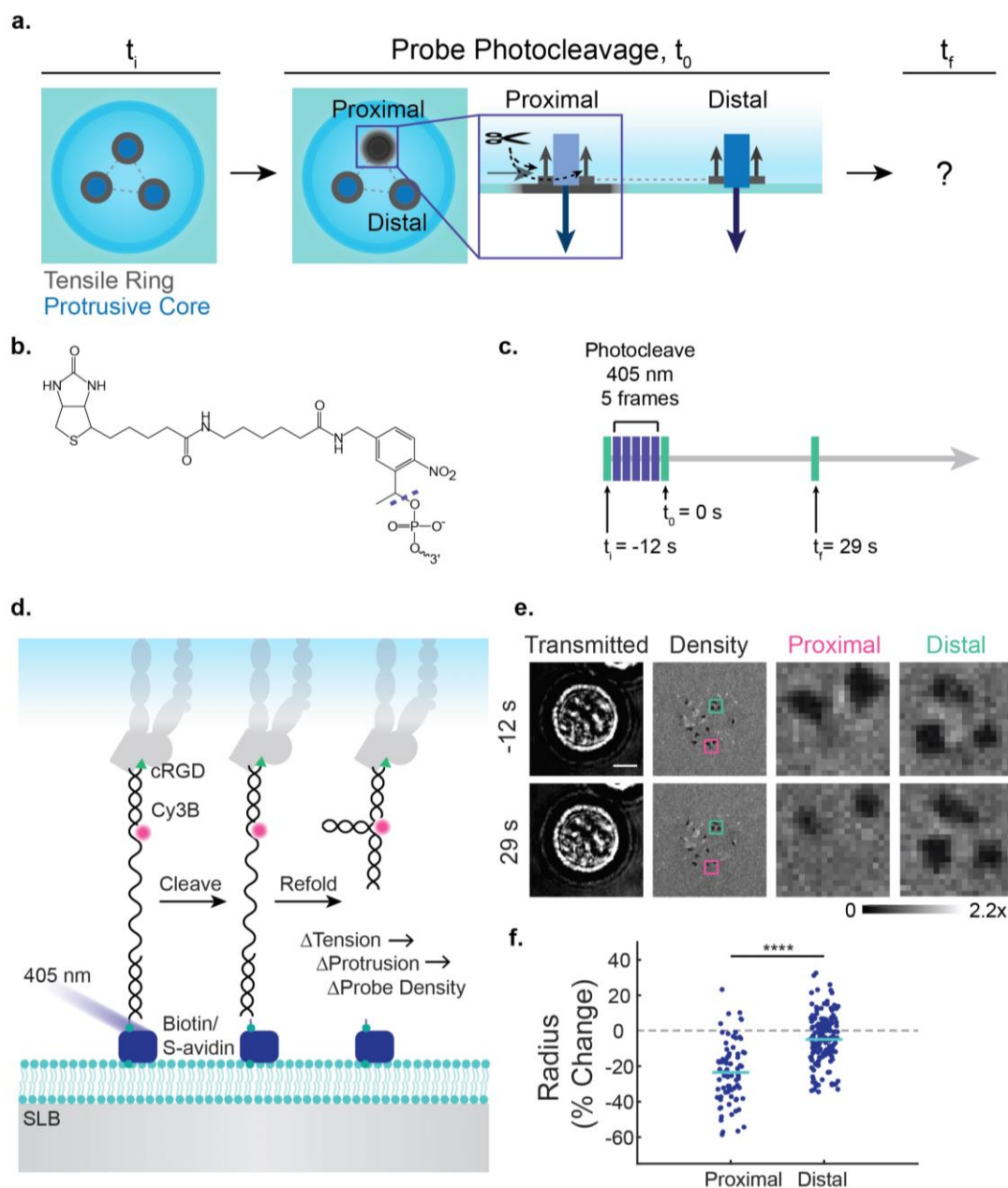


Figure 20 Loss of integrin ring tension causes local podosome retraction

(a) To test how the podosome network responds to perturbations in podosome tension, probes were photocleaved under individual podosomes, and the proximal and distal responses were monitored. (b) Chemical structure of PCB, which was incorporated at the 5' termini of 4.7 pN hairpins. (c) Cells were imaged before and after 5 sequential frames of probe photocleavage with a 405 nm laser. (d) Schematic of photocleavable protrusion probes. When the biotin anchor is cleaved with a 405 nm laser, the probe detaches from the bilayer and refolds, severing the podosome's mechanical connection to the SLB. Cy3B intensity reports probe density, and therefore serves as a marker of core size.

Figure 20 continued. intensity reports probe density, and therefore serves as a marker of core size. (e) Representative images of cells and podosomes before (-12 s) and after (29 s) photocleavage. Proximal pink boxes indicate the entire region of photocleavage. Distal green boxes show a representative region across the cell. (f) Summary statistics showing the percent change in podosome radius as measured by Cy3B depletion in regions cleaved by the 405 nm laser (proximal) and all other regions of the cell (distal)..Statistics were performed using a two-way ANOVA (control groups in Figure A 23). At least 79 podosomes were analyzed per condition, 3. experiments. Outlier podosomes (median \pm 3 median absolute deviations) were excluded. ****P<0.0001. Scale Bar, 5 μ m

photocleavage and found that core depletion radius was reduced proximal to photocleavage ($-23.5 \pm 17.0\%$). Distal to ablation, podosome radius was slightly reduced (mean = $-4.9 \pm 13.8\%$ change) (Figure 20e,f ,Figure A 23). Control experiments confirm that mechanical perturbations were largely responsible for the observed changes in signal, with phototoxicity contributing minimally at the 29 s time point (Figure A 21,Figure A 23). Note that at later time points, some cells do show some light-mediated podosome disassembly. These results confirm local mechanical feedback between integrin tension and actin protrusion as the primary mechanism of force balance in podosomes on SLBs in this 3T3 cell line and suggest that there may be a minor contribution of mechanical coupling across the podosome network. Other podosome-forming cell types such as myeloid cells may display different levels of podosome-podosome coupling.

3.3.6 *Efficient podosome formation requires integrin tension*

Given podosomes' tendency to shrink following loss of tension, we hypothesized that integrin forces are not only important for podosome maintenance but also for podosome initial formation and maturation. To test the hypothesis that integrin tension is required for the efficient formation of podosomes, we employed Tension Gauge Tethers (TGTs), which limit the magnitude of integrin forces⁹⁶ (Figure 21). Here, TGT probes

consist of a Cy3B-labeled DNA duplex that is anchored to the SLB. Upon the application of integrin forces that exceed the tension tolerance (T_{tol} , defined as the threshold force leading to mechanical melting at the 2s time scale) of the probe, the duplex irreversibly ruptures. Thus, TGTs limit the maximum tension per receptor (Figure 21a). The T_{tol} value can be tuned by changing probe geometry. In the Unzipping Mode, the cRGD ligand and biotin are on the same terminus of the duplex, and $T_{\text{tol}} = 12$ pN. In the Shearing Mode the biotin anchor and the cRGD ligand are on opposite sides of the duplex, and $T_{\text{tol}} = 56$ pN (Figure 21b). TGT experiments are unique in that they present chemically identical substrates that differ in their molecular stiffness. Thus, these experiments could also be used to test whether mechanosensory podosomes have piconewton sensitivity. We hypothesized that podosomes would be sensitive to these pN changes in ligand stiffness and that 12 pN TGTs would hinder podosome formation.

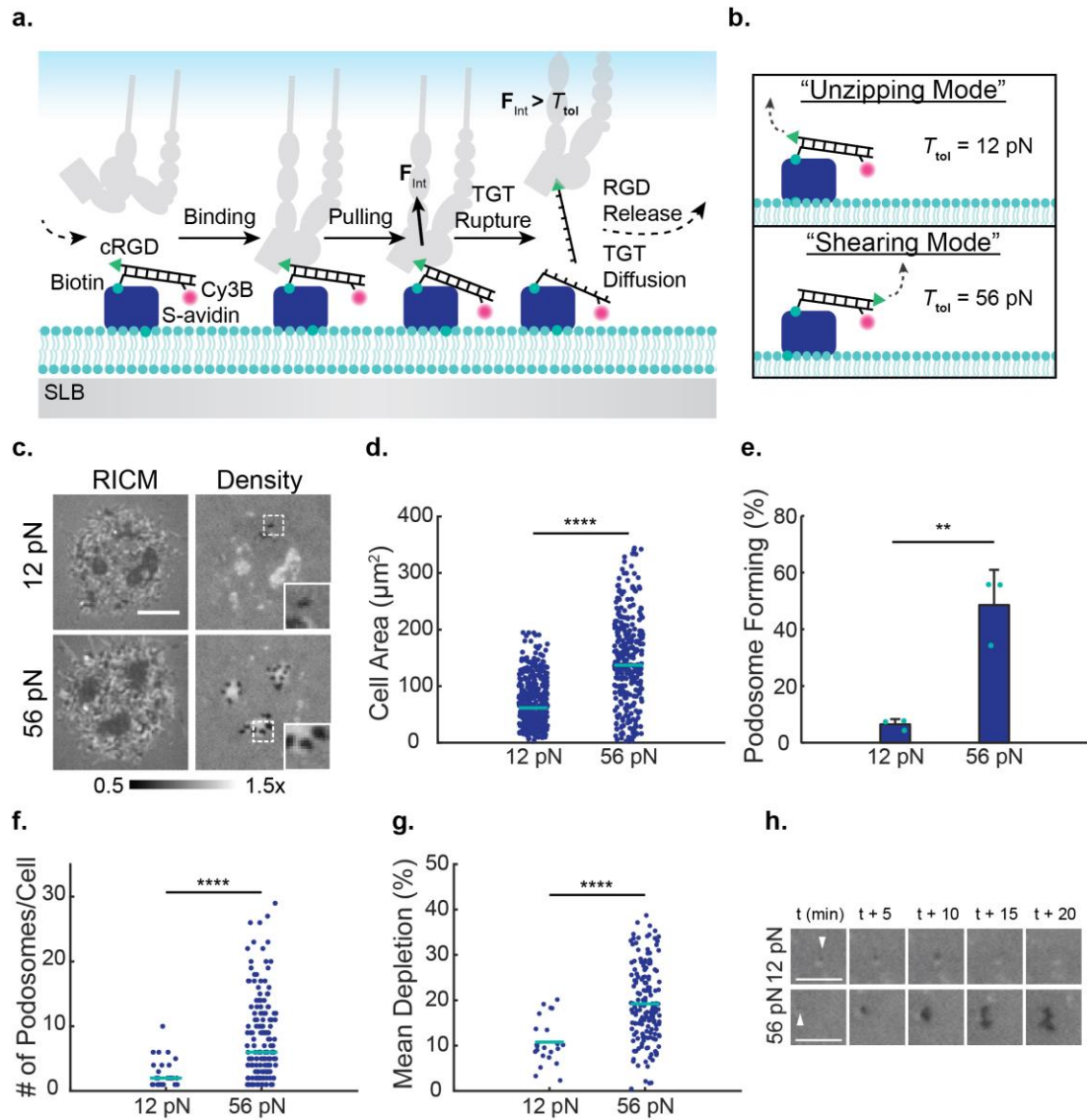


Figure 21 Podosomes maturation requires $F > 12 \text{ pN}$ integrin tension

(a) Schematic depicting integrin-TGT interaction on an SLB. First, an integrin receptor binds to a TGT duplex on the SLB. Upon integrin forces $> T_{tol}$, the TGT irreversibly ruptures, creating a transient local concentration gradient. Probe density is replenished through diffusion, and the cycle repeats. (b) T_{tol} is set by relative orientation of the cRGD ligand and the biotin anchor. (c) Representative images of podosomes on TGTs. Scale bar, 5 μm . (d) Cell area on TGTs. Teal bars represent the median area. Statistics were performed with a Rank Sum Test. At least 332 cells were analyzed per condition, 3 experiments. (e) Percentage of cells forming podosomes on TGTs. Bars represent the mean \pm s.d. (error bars), and teal circles represent individual experiments. Samples were compared using an unpaired two-tailed Students T-Test. At least 76 cells were analyzed per surface, 3 experiments. (f) Scatter plot showing the number of podosomes per cell

Figure 21 continued. in podosome-forming cells on 12 versus 56 pN TGTs. Teal bars represent the median. Statistics were performed using a Rank Sum Test. At least 25 cells were analyzed per condition, 3 experiments. Outliers more than 3 quartiles above the upper quartile were eliminated. (g) Scatter plot showing the mean podosome depletion on 12 versus 56 pN TGTs. Teal bars represent the mean depletion. Statistics were performed using a two-tailed unpaired Students T-Test. At least 25 cells were analyzed per condition, 3 experiments. (h) Time-lapse images of podosome emergence and dissolution (12 pn) or maintenance (56 pN) on TGTs. Cells spread for 2 hours on TGTs prior to imaging for all panels, except in h, in which cells were imaged as they spread on the SLB. **p<0.01, ****p<0.0001. Scale bar, 5 μ m.

On 56 pN TGTs, cells exhibited increased spreading area, and 8-fold more cells formed podosomes compared to SLBs with 12 pN TGTs (Figure 21c-e). Within podosome-forming cells, the number of podosomes per cell and the mean depletion in podosomes were significantly reduced on 12 pN TGTs (Figure 21f,g). This data reveals that limiting integrin tension to a value of 12 pN produces weaker protrusive forces. Time-lapse imaging of cells cultured on TGT substrates revealed that cells formed podosome-mediated depletions regardless of T_{tol} , but podosomes tended to be smaller and more transient on 12 pN TGTs compared to on 56 pN TGTs (Figure 21h). Thus, podosome growth and stability is directly regulated by integrin forces.

3.4 Discussion

Although previous works have suggested that podosomes function as independent mechanosensors, the nature of the mechanical linkage between the substrate and the cytoskeleton was unknown^{36, 65, 76, 79, 248}. Our work demonstrates that podosome integrin receptors apply pN vertical tension to their ligands, and that these tensile forces are required for actin core polymerization. This is a significant departure from past works, which have used the SLB model as evidence that podosome formation occurs in the absence of

adhesion forces and have stated that integrins cannot apply forces to ligands on fluid SLBs^{9, 85, 95}. Instead we observed the formation of integrin clusters⁹⁵, followed by core and ring growth that coincided with at least 19 pN integrin tension in the ring. Clustered integrins not associated with podosomes on SLBs did not apply detectable forces. To contextualize podosome forces on SLBs, we used our data to parameterize a simple adhesion model (Figure 22a,b). Each individual podosome applied nN vertical tensile forces, which was the sum of pN integrin tension and was strikingly similar to the protrusion forces measured for podosomes on FORMVAR, which is non-fluid⁷⁶.

A key question in the podosome literature is whether podosome tensile forces are generated directly from core polymerization or whether actomyosin contractility is required to generate tension in the ring^{26, 65, 71, 75}. Our work validates a model (Figure 22c) of polymerization-induced tension on the ring, as integrin tension was abolished when actin polymerization was perturbed. Few works have reported podosome formation on substrates lacking ligand^{39, 45}, leading to a hypothesis that the podosome architecture can sustain tension without receptor forces³⁶. Our TGT data disagrees with this model, demonstrating that firm integrin adhesion is required to form stable and protrusive podosomes. In contrast to works performed on rigid substrates^{63, 70, 75, 261}, our data support a model of local podosome force balance that is independent of myosin IIa contractility. Cambi, et. al. reported that myosin IIa inhibition led to increased actin core intensity by shifting the feedback between contractility and protrusion⁷⁵. We observed a similar increase in core depletion area and tension signal with Rho kinase inhibitor. It will be important to identify which myosins play a role in this vertical force balance feedback on an SLB. An interesting

candidate is myosin 1, which has been shown to localize to podosome cores and to apply forces when anchored to a fluid membrane^{167, 262, 263}.

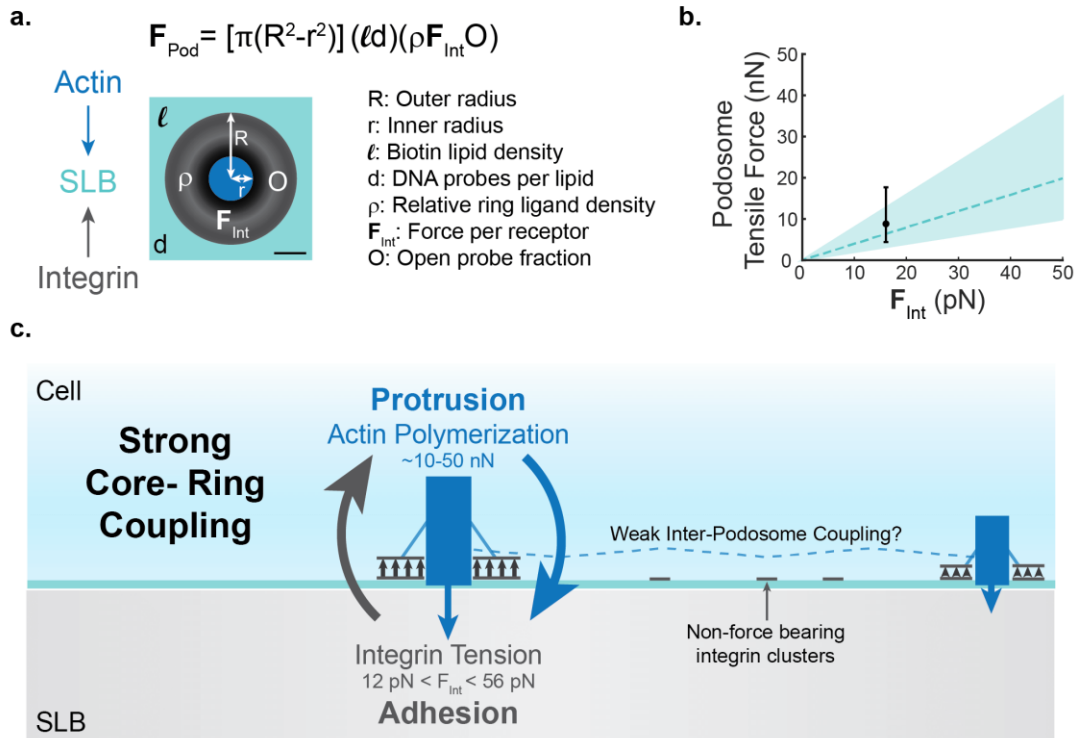


Figure 22 Podosome ring modeling estimates nN tensile forces.

(a) Schematic and equation for modeled podosome tensile forces on an SLB. Modeled podosome consist of a 1 μm outer radius and a 0.3 μm inner radius. The actin core exerts protrusion forces on the SLB, and the integrin receptors in the adhesion ring apply tensile forces. Modeled podosomes were parameterized using data from Figure 17 and Figure A 18. Scale bar, 2.5 μm . (b) Plot of ring tensile forces as a function of the per receptor force, F_{Int} . The dashed line indicates total tensile forces assuming 1 probe per biotinylated lipid, and the black data point represents the minimum force predicted by MT-FLIM. Confidence intervals and error bars correspond to 0.5 to 2 probes per biotinylated lipid. (c) Model of podosome forces on an SLB. Individual podosomes exert protrusion forces on the SLB with the actin core, while integrin receptors tug on RGD ligands in the ring domain. Podosomes experience strong mechanical coupling between protrusive and tensile forces. This coupling is focused within a single podosome and is weak in-between podosomes. This equilibrium can be shifted through myosin or actin inhibition. Podosomes with more actin content have smaller depletion areas and exert less tension. Receptor clusters that are not associated with podosomes do not experience detectable forces.

Our results should be considered in the context of a few important caveats. While fibroblasts provide a robust model to study podosomes *in vitro*, to our knowledge, fibroblasts have not been shown to form podosomes *in vivo*. Another corollary point is that the mechanical properties and the stiffness of the substrate will likely influence podosome dynamics. While MT-FLIM quantitatively maps integrin tension on fluid substrates, this signal is subject to some spatiotemporal convolution, and fast changes in tension will be obscured during the one-minute acquisition. Furthermore, regions of low photon counts such as podosome depletion regions may be disproportionately affected by the diffraction limit. These issues will be addressed as superresolved and faster FLIM electronics become more widely available.

Nevertheless, our work provides valuable mechanobiology tools and insight. SLBs offer a unique landscape to study the minimal mechanical machinery required for podosome formation, and DNA probes provide a powerful method to map and manipulate molecular forces. While RGD ligands on an SLB are more mobile than in physiological ECM, their mobility can recapitulate degraded ECM⁸⁶, which is relevant to podosome and invadosome biology^{25, 48}. During cancer cell invasion, cells alternate between periods of integrin and invadosome-mediated matrix degradation and migration^{248, 264}. Thus, podosome retraction following adhesion photocleavage may provide a model to understand how changes in tension can regulate function. While MT-FLIM has some current limitations in its temporal resolution, this method offers a unique solution to mapping forces at fluid interfaces and is a departure from past methods in its incorporation of a parameter that uniquely reports forces and is not subject to intramolecular fluorescence crosstalk. Photocleavable probes provide a method to perturb individual adhesion

structures with minimal disruption to the cell body and without changing the extracellular environment⁷⁸. Beyond podosome biology, MT-FLIM and photocleavable probes will be useful in studying immune cell interactions, Notch-Delta signaling, and adherens junctions^{5, 126, 265}. Fluorescence lifetime is an improved indicator of density versus tension, and because hairpin probes unfold specifically under receptor tension, all measured forces can be attributed to integrins rather than to the vertical force balance vector that arises at the contact line between a liquid droplet applying pressure on a solid substrate²⁶⁶. In conclusion, we introduce and apply powerful DNA mechanotechnology tools to demonstrate the role and regulation of receptor forces on fluid substrates.

3.5 Methods

3.5.1 Sample Preparation, Purification, and Characterization

3.5.1.1 Probe Synthesis and Purification

All oligonucleotides (Table A 1, Figure A 1) were custom synthesized by Integrated DNA Technologies, except for BHQ-1 modified oligos, which were custom synthesized by Biosearch Technologies. 100 µg cyclo [Arg-Gly-Asp-D-Phe-Lys(PEG-PEG)] (PCI-3696-PI, Peptides International) was sonicated with 50 µg NHS-azide (88902, Thermo-Fisher Scientific) in 10 µL dimethyl sulfoxide (MX1457-7, Millipore-Sigma) for 1 hour. The azide-modified cyclo [Arg-Gly-Asp-D-Phe-Lys(PEG-PEG)] peptide was purified via reverse-phase high performance liquid chromatograph (HPLC) with a Grace Alltech C18 column (0.75 mL min⁻¹ flow rate; Solvent A: Nanopure water + 0.05% trifluoroacetic acid (TFA), Solvent B: acetonitrile (BDH83639.400, VWR) + 0.05% TFA; starting condition 90% A + 10% B, 1% per min gradient B) (Figure A 2a). Following

HPLC purification, products were dried in an Eppendorf Vacufuge plus). Subsequently, the azide-modified peptide was ligated to DNA oligos containing a 5' hexynyl modification using copper-catalyzed azide-alkyne cycloaddition (CuAAC). Briefly, 5 μ L of 1 mM oligonucleotide was reacted for 1 hour with \sim 30 nmol azido-peptide in the presence of 10 mM sodium ascorbate, 1 mM copper sulfate, and 0.8 mM THPTA (1010, Click Chemistry Tools). The reaction was purged under N₂. The product was purified using reverse-phase HPLC with an Agilent Advanced oligo column (0.5 mL min⁻¹ flow rate; Solvent A: 0.1 M TEAA, Solvent B: acetonitrile; starting condition: 90% A + 10% B, 1% per min gradient B). Oligos were conjugated to Cy3B NHS ester (PA63100, GE Healthcare) in a 10 μ L reaction; 50 μ g excess Cy3B-NHS was reacted with 2-5 nmols amine-modified DNA in 1x phosphate buffered saline (PBS) and 0.1 M sodium bicarbonate overnight. The product was purified using a P2 size-exclusion gel to remove excess dye prior to HPLC purification. Reverse phase HPLC was performed with an Agilent Advanced oligo column as described above (Figure A 2b-d). Final products were resuspended in Nanopure water. If significant excess dye remained for MT-FLIM strands, the DNA was repurified with an amicon filter (Amicon Ultra-0.5mL, Centrifugal Filters, Ultracel-3K) or with HPLC. Starting material and final masses were confirmed using MALDI-TOF (Figure A 3, Table A 2).

3.5.1.2 Mass Spectrometry

Oligonucleotides in Nanopure water (18.2 M Ω , Barnstead Nanopure) were plated in a 1:1 vol/vol ratio with saturated 3-hydroxypicolinic acid (56197, Millipore-Sigma) in 50% acetonitrile, 0.1% trifluoroacetic acid, and 5 mg mL⁻¹ ammonium citrate. Dried samples were massed with matrix-assisted laser desorption/ionization-time of flight

(MALDI-TOF) on a Bruker Daltronics ultraflex II TOF/TOF and analyzed using flexAnalysis 3.4.

3.5.1.3 Small Unilamellar Vesicle (SUV) Preparation

SUVs were prepared using a 10 mL LIPEX Extruder (Transferra Nanosciences, Inc.). Lipids were mixed in ~500 μ L chloroform with 1,2-dioleoyl-sn-glycero-3-phosphocholine (DOPC) (850375C, Avanti Polar Lipids) as the base lipid. Biotinylated lipids were incorporated at 0.05-0.2 mol% 1,2-dioleoyl-sn-glycero-3-phosphoethanolamine-N-(biotinyl) (Biotinyl Cap PE) (870282C, Avanti Polar Lipids). To directly tag the membrane in control experiments, N-(Fluorescein-5-Thiocarbamoyl)-1,2-Dihexadecanoyl-sn-Glycero-3-Phosphoethanolamine, Triethylammonium Salt (FITC DHPE) (23304, AAT Bioquest) was incorporated at 0.1 mol%. Lipids were dried first by rotary evaporation and second by ultra-high purity N₂. Lipid cakes were resuspended and sonicated in 3 mL nanopure water (final concentration, 2 mg mL⁻¹) prior to performing three freeze-thaw cycles. SUVs in Nanopure water were then extruded 10x through a 0.08 μ m polycarbonate filter (WHA110604, Whatman) supported by a drain disc (WHA230600, Whatman). SUVs were used within ~2 weeks.

3.5.1.4 Supported Lipid Bilayer Preparation

Planar supported lipid bilayers (SLBs) were prepared on either uncoated glass-bottom 96 well plates (265300, Nunc or 82050-782, Greiner) or glass coverslips (48382 085, VWR). Coverslips were washed and sonicated 3x in nanopure water followed by sonication in ethanol. Coverslips were dried at 90°C overnight and cleaned in piranha solution (3:1 sulfuric acid and 30% hydrogen peroxide; caution, piranha acid is

extremely corrosive and can explode if exposed to organic materials). Cleaned coverslips were washed 3x in nanopure water and were mounted into coverslip chambers in 1x phosphate buffered saline (PBS) for SLB formation. Alternatively, 96-well plates were etched for 1-3 hrs in 2.6 M sodium hydroxide and were washed with 10 mL nanopure water and 5 mL 1x PBS. SLBs were formed by adding SUVs to etched glass for at least 5 minutes and were washed in nanopure water and 1x PBS prior to the ~25 min blocking with 0.1% bovine serum albumin, Fraction V (10 735 078 001, Roche Diagnostics GmbH). Unless otherwise stated, all experiments were carried out with 99.9 mol% DOPC and 0.1 mol% Biotinyl-Cap PE. Blocked SLBs were washed with 5 mL 1x PBS and then saturated in 90-180 nM streptavidin (SA101, Millipore-Sigma) for at least 45 min. Excess streptavidin was removed with 10 mL 1x PBS, and SLBs were incubated with 30 nM DNA for at least 45 min. Functionalized SLBs were washed in 10 mL 1x PBS and then buffer exchanged into hanks balanced salts (Millipore-Sigma) for all imaging. To stain the membrane, SLBs were shaken for 30 min at 240 rpm with 10% (v/v) 250 $\mu\text{g mL}^{-1}$ b-BODIPY FL C₅-HPC (2-(4,4-Difluoro-5,7, Dimethyl-4-Bora-3a,4a-Diaza-*s*-Indacene-3-Pentanoyl)-1-Hexadecaonyl-*sn*-Glycero-3-Phosphocholine (D3803, Thermo Fisher) or were incubated with 10% (v/v) 1.5 $\mu\text{g mL}^{-1}$ 1,1'-dioctadecyl-3,3,3',3'-tetramethylindodicarbocyanine,4-chlorobenzenesulfonate salt (DiD) (D7757, Thermo-Fisher) (DiD). For MFM bead experiments, SLBs were assembled on 5 μm silica beads (SS06N, Bang Laboratories). 100 μL of 1 mg mL^{-1} beads were rocked with 100 μL of DOPC SUVs. SLB- beads were washed in 1x PBS and purified 3x with centrifugation (5 min, 2000 rpm). Purified SLB-beads were incubated with 5 μM 1,1'-dioctadecyl-3,3,3',3'-

tetramethylindocarbocyanine perchlorate (DiI) (468495, Thermo-Fisher) for 15 min. Free dye was removed by washing and pelleting 3x in 1x PBS (5 min, 2000 rpm) ²¹.

3.5.1.5 DNA Hybridization

DNA oligonucleotides in 1x PBS were heated to 90°C for 5 min and cooled at 25°C for 25 min in a 0.2 mL Thermowell tube. The ligand strand was added in 10% molar excess except for in absorbance spectroscopy and photocleavable experiments, in which strands were added in a ratio of 1:1:1. To chemically open tension probes, tension probes were hybridized with 10x molar excess complementary sequence (Figure A 6a).

3.5.2 *Experimental Methods*

3.5.2.1 UV-Vis Spectroscopy

Oligonucleotides (10 μ L of 2.5 μ M hairpin strand) were hybridized as described above to assemble closed tension probes in solution. Following hybridization, thermowell tubes were fit inside microcentrifuge tubes and dried in a vacufuge to <2.5 μ L. The volume was adjusted to ~2.5 μ L using nanopore water, corresponding to a final concentration of ~10 μ M in 4x PBS. Three absorbance spectra per sample were collected with a pathlength of 0.1 cm on a Thermo Scientific Nanodrop 2000c spectrophotometer. This process was repeated in the presence of 10x molar excess of the complimentary strand for each sample.

3.5.2.2 Cell Culture and Transfection

NIH 3T3 fibroblasts and Mouse Embryonic Fibroblasts stably transformed with SrcY527F (MYF) were cultured in Dulbecco's Modification of Eagle's Medium (DMEM) (B003K32,

Corning) with 10% Fetal Bovine Serum (USDAFBS, MidSci), 2.5 mM L-glutamine (G8540, Millipore-Sigma), 1x penicillin streptomycin (97063-708, VWR). Cells were incubated at 37°C in 5% CO₂. Cells were passaged at ~80% confluency. NIH 3T3 fibroblasts were gifted from colleagues at Emory University and were authenticated by IDEXX BioResearch (Figure A 24). Cells were imaged in Hanks Balanced Salts (H1387, Millipore-Sigma), pH 7.4. MYF cells were stably transfected and gifted by Olivier Destaing.

NIH 3T3 fibroblasts were transfected in a 3:1 ratio of Lifeact-mCerulean-7 (#54713, Addgene) and polyethylenimine (23966-1, Polysciences, Inc.) (1 µg mL⁻¹, pH 7) in Optimem for 24 hours prior to confocal imaging with the pinhole fully open. To knockdown *MYH9*, NIH 3T3 fibroblasts were transfected with Lipofectamine RNAiMAX (13778030, Thermo Fisher) and SMARTpool: ON-TARGETplus *MYH9* siRNA (D-040013-00-0005, Horizon Dharmacon) or ON-TARGETplus Non-targeting Pool (D-001810-10-05, Horizon Dharmacon) as a control. Transfection was performed according to the RNAiMAX manufacturers protocol in a 6-well plate. Total volume was 2 mL, and media was changed ~48 hours following transfection. 72 hours following transfection, cells were assayed for podosome formation on SLBs using MT-FLIM and were plated on glass. Knockdown was functionally validated by assessing stress fiber formation in transfected cells ~12 hours after plating.

3.5.2.3 Immunostaining

For staining on an SLB, NIH 3T3 fibroblasts were fixed and stained on 56 pN TGT probes following 2 hours cell spreading. Cells were fixed in 2-4% formaldehyde in 1x PBS

for 8-10 minutes. Cells were permeabilized for 3 min with 0.1% Triton X-100 and were blocked with BSA for 30 min. To characterize the relationship between FRET probe signal and integrin receptors in clusters and podosomes, cells were not permeabilized, and blocking was performed with a low concentration of BSA (0.01 – 0.1% w/v), as this best maintained the membrane and clusters. Staining was performed for 1 hour at room temperature with 1:1000 Alexa 488- Phalloidin (ab176753, Abcam), 1:50 Vinculin Antibody SF9 647 (sc-73614 AF647, Santa Cruz Biotechnology), 1:50 Phospho-Paxillin (Tyr1888) Polyclonal Antibody (PA5-17828, Thermo-Fisher) followed by 1:5500 Alexa Fluor 555 goat anti-rabbit (A21147, Thermo Fisher), or 10 µg/m Anti-Integrin β1 Antibody, clone MB1.2 (MAB1997, Sigma-Aldrich), followed by 1:1000 Alexa Fluor 647 goat anti-mouse IgG_{2b} (γ2b) (Thermo-Fisher) as indicated. Staining on an SLB requires gentle and gradual buffer exchange to avoid disruption of cells and DNA on the membrane. For staining of NIH 3T3 cells on glass, cells were not permeabilized and were stained with Alexa 488-Phalloidin for 30 min. Immunostained cells were imaged using total internal reflection fluorescence microscopy (TIRFM).

3.5.2.4 Drug Treatment

Cells spread and formed podosomes on 4.7 pN MT-FLIM probes for ~1 hour prior to imaging and addition of drug dissolved in DMSO (final DMSO concentration ~0.1%). Cells were either treated with 500 nM Jasplakinolide (J7473, Thermo-Fisher) for 8 min, with 50 µM Y27632 dihydrochloride (Y0503, Millipore Sigma) for 20 min, or with 50 µM (-)-blebbistatin (B0560, Millipore-Sigma) for 30 min. Blebbistatin was first heated to 45°C in hanks balanced salts to improve solubility²⁶⁷.

3.5.2.5 Microscopy

Epifluorescence and TIRFM were performed on a Nikon Eclipse Ti microscopes using the Nikon Elements 4.40.00 or 4.13.05 software and a 1.49 NA CFI Apo 100x objective. To maintain focus during timelapse experiments, a Nikon perfect focus system was used. TIRF images were collected with 80 mW 488, 561, and 647 nm lasers using a Chroma quad cube (ET-405/488/561/640 nm Laser Quad Band) or Chroma quad band C148022 and C-TIRF Cube C125986. RICM images were collected with Nikon cube 97270, and epifluorescence images were collected with Chroma cubes 49004 and C121664. For emission resolved polarization imaging, the emission fluorescence was split into parallel and perpendicular channels using an Andor TuCam system with a wire grid polarizer (Moxtek, Andor: TR-EMFS-F03). Fluorescence was projected two Andor iXon Ultra 897 electron-multiplying charge-coupled devices. The polarization bias of the microscope (G-factor) was computed by taking the ratio of the parallel and perpendicular fluorescence emission of fluorescein in solution. To correct for the polarization scrambling effect of the objective, large numerical aperture corrections were applied to the raw fluorescence data as previously described²⁶⁸. To validate the ability of the microscope to measure systematic spatial variation in anisotropy produced by highly ordered fluorophores, the fluorescence anisotropy of 5 μm silica beads coated with DOPC supported lipid bilayers doped with DiI was measured (Figure A 16)²¹.

Fluorescence lifetime and confocal measurements were performed on a Nikon Ti Eclipse Inverted confocal microscope with a Plan Apo Lambda 60X/1.40 Oil objective and Nikon Elements 4.40.00. Focus was maintained during timelapse imaging via a Nikon perfect focus system. The confocal microscope was equipped with a C2 Laser launch with

405nm and 561nm diode lasers, Nikon Elements software, and a Picoquant Laser Scanning Microscope Time Correlated Single Photon Counting (TCSPC) Upgrade with SymPhoTime 64 2.1.3813. TCSPC settings are summarized in Table A 3. FLIM samples were excited with a 20 MHz pulsed 514 nm laser, and 512 x 512 pixel images were collected at 0.5 frames-per-second with 0.08 or 0.14 $\mu\text{m}/\text{pixel}$ and an average photon count rate of ~4-6% of the laser pulse rate. Light was filtered using a long-pass laser beamsplitter (H560 LPXR, Analysentechnik) and a 582/75 bandpass filter (F37-582, Semrock). Laser light that was reflected by the dichroic was blocked from an additional detector using a 690/35 bandpass filter. Average fluorescence lifetime per pixel was calculated using the Fast FLIM algorithm in SymPhoTime. Only photons contributed by the long-pass detector (582/75) were considered in analysis. Photocleavable biotin experiments were performed on the confocal microscope as illustrated in Figure 20c. Cells were imaged to identify a region of interest (ROI) for photocleavage. Then, time lapse imaging was performed using the Nikon Elements Photostimulation Module. In phase 1, a 561 nm image was collected (~12 s). In phase 2, the ROI was photostimulated for 5 frames using a 405 nm laser (15%). In phase 3, the cell's response was tracked every 30 seconds by imaging in the 561 nm channel (0 – 180 s).

MFM²¹ experiments were performed on a custom-built system (Figure A 17a) consisting of a Nikon-T2 microscope with a 60x 1.49 NA objective (Nikon), a cleanup polarizer, half-wave plate, and a focusing lens (ThorLabs), an Obis 561 nm LS 150 mW laser (Coherent), and an ORCA-Flash 4.0 v3 CMOS camera (Hamamatsu) The half-wave plate was rotated by a motorized mount (PRM1Z8; ThorLabs) driven by the Kinesis software. The half wave plate was set in motion at 25 degrees/s (rotating the excitation

polarization by 50 degrees/s). Once the half wave plate reached maximal rotational velocity, 73 images were taken at 50ms exposure time via Nikon Fast acquisition in Nikon Elements v5.1. Each 50ms exposure image contained the average fluorescence as the laser polarization rotates through 2.5 degrees of arc.

3.5.3 *Molecular Tension – Fluorescence Lifetime Imaging Microscopy Calibration*

3.5.3.1 DNA Probe Fluorescence Calibration

Closed and opened MT-FLIM probes were hybridized as described above and were combined in known ratios in solution immediately prior to incubation with SLBs. For 19 pN probe calibration, a scrambled hairpin was used in opened samples to lower the ΔG of hybridization²¹⁰. SLB fluorescence intensity was measured using epifluorescence, and the background subtracted data were fit using linear regression to determine quenching efficiency (QE). 19 pN and 4.7 pN surfaces did not display statistically significant differences; thus, intensity data were combined for this calculation. For MTFM probes used in MFM and PCB experiments, QE was determined directly from background subtracted opened and closed images using the equation:

$$\text{Quenching Efficiency (QE)} = 100\% \times \frac{I_{\text{Open,BS}} - I_{\text{Closed,BS}}}{I_{\text{Open,BS}}} \quad (7)$$

To determine the average fluorescence lifetime of MT-FLIM probes, surfaces containing 0 – 100% open probes were imaged using the same conditions as in cell experiments. For each image, an average fluorescence lifetime histogram was produced from defect-free regions of interest (ROI) in the image. Histograms were generated in SymPhoTime and contained the default 400 bins across a range of range of 0 to 12.5 ns. The corresponding

ROI fluorescence decay had $\sim 10^5$ photons in the peak. Data were averaged across 2-3 surfaces per condition, and the resulting calibration curves of average fluorescence lifetime versus percent open probes were fit to a biexponential (A.1.2.1) and used to generate look-up tables.

3.5.3.2 Probe Density Determination

Relative probe density (clustering) per pixel was calculated according to the following equation:

$$\rho = \frac{I - D}{\frac{I_o - D}{1 - QE} \mathbf{F}(\tau) + (I_o - D)(1 - \mathbf{F}(\tau))} \quad (8)$$

Here ρ is probe density, I is the illumination profile corrected photon count, D is dark counts, I_o is the illumination profile corrected photon counts on the bilayer in the absence of the cell, Q is the quenching efficiency, and $\mathbf{F}(\tau)$ is the percent of open probes. For SLBs with linear probes lacking a stem-loop structure, the percent open was assumed to be zero.

3.5.4 *Analysis, Modelling, and Statistics*

3.5.4.1 Image Processing

Image processing was performed in MATLAB 2018a (MathWorks) using semi-automated custom scripts unless otherwise stated. Nikon ND2 files were directly transferred into MATLAB using the Bioformats Toolbox. Linescans were generated in MATLAB or ImageJ, and kymographs were generated in FIJI using the MultiKymograph plugin. The diffusion coefficient, D , was calculated according to the following equation:⁸

$$D = w^2/4t_{1/2} \quad (9)$$

n which w is the radius of the bleached region and $t_{1/2}$ is the time of 50% recovery determined by exponential curve fitting. MT-FLIM analysis methods are described in A.1.2.1, A.1.2.2, and Figure A 11. Photocleavable biotin timelapse experiments were processed as shown in Figure A 22. For LifeAct analysis, podosomes were identified by intensity-based thresholding of RGD depletion, and podosomes multiples were separated with a 2-pixel line. Clear single podosomes were selected by hand. For each cell, the data were normalized to the corresponding measurement from the podosome containing the brightest LifeAct signal. For time-lapse image analysis, podosome tracking was performed by hand starting with the final frame and selecting the center of each podosome or corresponding cluster until its emergence or the time-lapse start. To track clusters, images were thresholded based on size and lack of local depletion zone in MATLAB and then tracked using TrackMate in FIJI. Cluster tracking did not allow merging or splitting events. For TGT analysis, because some 12 pN podosomes were challenging to identify computationally, podosomes were counted and identified manually. To determine percent depletion, the centroid of each podosome was selected and dilated by 2 pixels. Fluorescence intensity was then quantified within the dilated region. Semi-automated analysis codes are available on the Salaita Lab GitHub page. MFM imaging was analyzed in MATLAB using published²¹ code that was modified to threshold podosome rings. The XY orientation of the force was given by the phase of the sinusoidal fluorescence variation, while the amplitude of the sinusoidal variation gave information about the Z orientation.

To determine the anisotropy from emission-resolved polarization images, large numerical aperture correction factors were applied in MATLAB²⁶⁸.

3.5.4.2 Podosome Model

To determine the net integrin tensile force exerted per podosome, \mathbf{F}_{Pod} , we modeled a podosome with an outer radius, R , of 1 μm and an inner depletion radius, r , of 0.3 μm (Figure A 18). Using the published value for the DOPC footprint within a membrane²⁶⁹, we calculated the approximate number of biotinylated lipids per square micron, l . Based on our MT-FLIM data and % depletion data, we assumed that probes have a relative oligonucleotide density, d , of 0.5 – 2 probes per biotinylated lipid and that integrin receptors exert \mathbf{F}_{Int} up to 50 pN. Relative probe density, ρ , in the podosome ring was assumed to be equal to that of the SLB background on average. To determine the magnitude of integrin forces in podosomes, we assumed 10% open probes per pixel, O , which was roughly equal to our measured data (Figure 17). Per receptor integrin forces, F_{Int} , were modeled from 0 to 50 pN. Thus,

$$\mathbf{F}_{\text{Pod}} = [\pi(R^2 - r^2)](ld)(\rho\mathbf{F}_{\text{Int}}O) \quad (10)$$

We also plotted an experimental data point parameterized using the percent open data from Figure 17. Because MT-FLIM probes are binary, they can provide the minimum applied force per receptor but not the absolute force per receptor. For this data point we set $\mathbf{F}_{\text{Int}} = \mathbf{F}_{1/2}$ with $F_{1/2}$ equals 19 or 4.7 pN. This data represents the minimum force applied by a podosome on an SLB. For modeling of a hypothetical podosome with isometric tension for emission-resolved polarization measurements, we modeled a 1 μm structure exerting

inwards tensile forces with a tilt angle of 20 degrees (Figure A 17c). Codes are available on the Salaita Lab GitHub page.

3.5.4.3 Statistics and Reproducibility

Statistics were performed in MATLAB 2018a or in GraphPad Prism 7. For biological experiments, each experiment is defined as one flask or well of cells. For surface characterization, each experiment is defined as one SLB. Biological experiments were repeated at least three times, except for emission-resolved polarization imaging and immunostaining of $\beta 1$ integrin with MT-FLIM probes and actin, which were repeated twice. Surface characterization was repeated at least twice per condition. For per-podosome data, only podosomes that were in clear focus easily distinguishable, and that met thresholding criteria were analyzed. P values are reported as ns $P > 0.05$, * $P < 0.05$, ** $P < 0.01$, *** $P < 0.0001$, **** $P < 0.0001$. Detailed information on statistical tests, reproducibility, and outlier omission are listed in each figure caption.

CHAPTER 4. EVALUATION OF DNA-BASED PROBES FOR MAPPING RECEPTOR FORCES ON FLUID SUBSTRATES

4.1 Abstract

DNA-based tension probes offer the highest spatial resolution, force sensitivity, and molecular specificity for cellular tension sensing. Indeed, a number of different classes of DNA tension probes have been developed to measure molecular forces mediated by T cells, platelets, fibroblasts, B-cells, and immortalized cancer cell lines. While the chemical structure of fluorophore-oligonucleotide conjugates and molecular beacons are similar to that of DNA tension sensor, there remains subtle differences in design, surface immobilization as well as the need for cellular integration. Therefore, there remains a need for a more detailed spectroscopic analysis of DNA-based molecular tension probes for cellular imaging. More recent integration of DNA tension probes within hydrogels and phospholipid membranes and the nuances of their design, we conducted a broad analysis of DNA hairpin-based tension probes using absorption spectroscopy, fluorescence intensity and Fluorescence Lifetime Imaging Microscopy (FLIM). We find that tension probes are highly sensitive to their molecular design, including donor and acceptor spatial organization and pairing, DNA backbone structure, and conjugation chemistry. We demonstrate the impact of these design features using a supported lipid bilayer (SLB) model of podosome-like adhesions. Finally, we offer a series of recommendations, describing the pros and cons of FRET-based or static-quenching based probes when making measurements on fluid membranes and glass slides, thus providing a guide for the optimal design and application of DNA hairpin-based molecular tension probes.

4.2 Introduction

Cells transmit piconewton (pN) receptor forces to ligands in the extracellular matrix (ECM) and on the surface of adjacent cells. These forces regulate a variety of biological functions²⁷⁰, including cell migration²¹², blood clotting^{245, 271}, and the immune response^{106, 272}. Understanding the precise role of mechanical forces in cell biology requires quantitative, high-resolution force spectroscopy and imaging. Deformation-based approaches such as traction force microscopy (TFM) and micropillar array devices are commonly used and have allowed for the quantification of cellular forces as a function of material stiffness^{273, 274}. A limitation inherent to TFM and micropillar devices is their μm and nN spatial and mechanical resolution, along with the challenge of measuring the forces transmitted through orthogonal ligand-receptor pairs on the same cell surface. To address these limitations, our lab developed Molecular Tension Fluorescence Microscopy (MTFM)²⁰⁹. MTFM leverages DNA-based tension probes, which offer pN sensitivity and programmability, sub-micron spatial resolution, and molecular specificity^{34, 275, 276}; this sensitivity and specificity have helped elucidate the role of T cell^{106, 253}, B cell¹⁰, and integrin receptor^{30, 33, 245} mechanics in different biological processes.

In our original DNA hairpin design, MTFM probes were comprised of a DNA hairpin (hairpin strand) flanked by a donor/acceptor pair; the probe is anchored to a surface at one terminus through an anchor/acceptor strand, while the second terminus presents a ligand (ligand/donor strand) (Figure 23A)^{30, 277}. Typically, the acceptor is a dark quencher, leading to a high signal-to-noise ratio and facilitating probe and fluorescent protein multiplexing³⁰. At rest, donor fluorescence is quenched. Upon the application of receptor forces above the $F_{1/2}$, which is defined as the equilibrium force that leads to a 50%

probability of probe unfolding, the hairpin opens. This leads to donor and quencher separation, causing a ~20-100-fold increase in donor fluorescence^{30, 106}. Thus, these reversible DNA-based tension probes report mechanics using a real-time optical signal (Figure 23A).

In conventional tension sensing, DNA probes are rigidly anchored to a glass substrate. Therefore, probe density is fixed and changes in fluorescence intensity can be attributed to probe unfolding. In other words, the fluorescence intensity of the donor

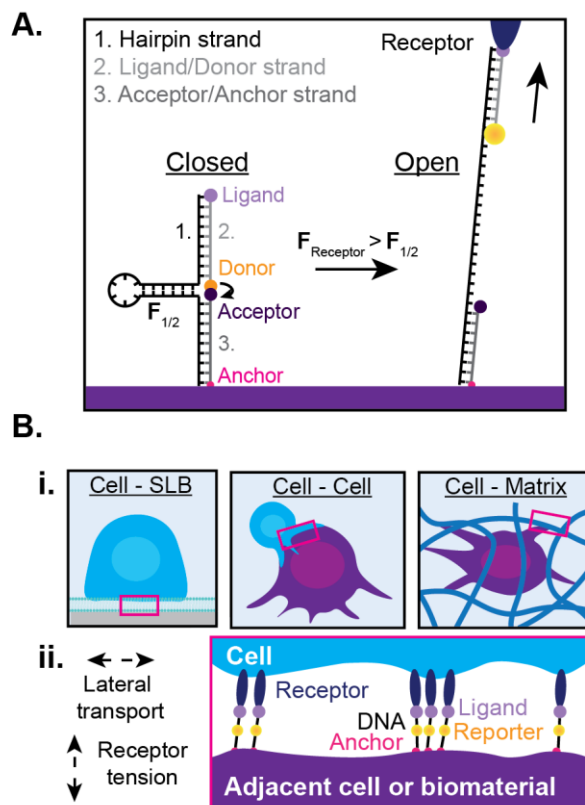


Figure 23 DNA-Based Tension Probes Report Receptor Mechanobiology.

(A) DNA-based tension probes consist of a DNA hairpin hybridized to two-arm sequences each containing a ligand or an anchor moiety. The ligand and anchor strands are labeled with a donor/acceptor pair, respectively. At rest fluorescence is quenched. Receptor forces above the $F_{1/2}$ opening threshold lead to probe unfolding and an increase in donor fluorescence. (B) Advanced applications of molecular tension probes report receptor forces at cell-SLB, cell-cell, and cell-matrix interfaces (i). In these dynamic junctions, receptors can apply tension to DNA probes and can also spatially rearrange probes, through lateral transport (cell, SLB) or viscoelastic deformation (matrix) (ii).

linearly reports the density of probes that are mechanically unfolded experiencing $F > F_{1/2}$.³⁰

While this approach has been useful in mapping the forces applied by immune cell receptors and integrin receptors on glass^{21, 105, 106}, measurements on more physiologically relevant fluid substrates present unique challenges because of ligand remodeling. Receptors can both laterally transport and pull on ligands⁸⁴, leading to spatial reorganization on membranes, including supported lipid bilayers (SLBs), which mimic juxtracrine receptor interactions, and living cell-cell junctions. Furthermore, on viscoelastic hydrogels, receptor tension can cause local material deformations which alter ligand density²⁷⁸ (Figure 23B). Therefore, adapting molecular tension probes to mapping receptor forces and clustering on dynamic biomaterials requires additional fluorescence readouts that can decouple fluorophore density and fluorescence quenching efficiency.

The most common method to measure forces with changing probe density relies on ratiometric intensity-based imaging. This was first demonstrated by Ma, et. al. when mapping T cell receptor forces⁸, and then by Nowosad, et. al. measuring B cell receptor forces on fluid membranes^{8, 10}. In these approaches a third dye is incorporated, which serves as a probe density reporter. A similar approach was also used to measure cadherin tension and density in epithelial cell-cell junctions^{279, 280}. A step toward measuring cellular forces in hydrogels, mechanofluorescent DNA hydrogels were generated by mixing Atto 488-labeled DNA precursors with rupturable DNA duplex crosslinkers containing an Atto 565/Iowa Black donor-acceptor pair. Hydrogel strain in response to externally applied forces was quantified by the ratio of decreasing Atto 488 to increasing Atto 565 fluorescence intensity upon oligonucleotide stretching and duplex rupture, respectively²⁸¹.

While ratiometric intensity-based measurements are advantageous in their accessibility and speed, their quantification and interpretation can be challenging. The need for engineering three dyes in a dynamic DNA structure is complicated because of three-way energy transfer, intermolecular energy transfer, and spectral and autofluorescent bleed-through. Ratiometric measurements are also sensitive to noise and local fluorescence artifacts, and an additional challenge is that measurements require precise detector alignment and pixel registration to ensure suitable quantification^{282, 283}. Furthermore, ratiometric approaches are poorly suited to multiplexing, which is essential in understanding mechanotransduction in context.

Offering a direct readout of energy transfer, we recently developed Molecular Tension-Fluorescence Lifetime Imaging Microscopy (MT-FLIM). MT-FLIM measures receptor tension and clustering on SLBs using Time-Correlated Single Photon Counting (TCSPC)³³. In our original MT-FLIM report, a Cy3B - BHQ1 FRET pair were attached to a DNA hairpin-based tension probe with 9 nucleotide (nt) separation. Changes in fluorescence lifetime, τ , uniquely reported hairpin unfolding under receptor force, and an empirical calibration allowed quantification of the density of mechanically unfolded probes independently from probe clustering.

In the simple case, a donor and acceptor fluorophore pair undergoing FRET have a FRET Efficiency, E described by:

$$E = \frac{1}{1 + \left(\frac{R}{R_0}\right)^6} \quad (11)$$

R is the distance between the donor and acceptor dyes and R_0 is the Forster radius, which is a function of several variables including the dipole orientation factor, κ^2 and the spectral overlap integral, J . For randomly oriented dyes, κ^2 equals $2/3$. In dye-labeled oligonucleotides, this relationship often breaks down due to dye-DNA interactions and linker chemistry, which shift κ^2 away from $2/3$.^{259, 284} In rigidly anchored molecular tension probes, donor/acceptor pairs are typically placed in close proximity to maximize the quenching efficiency (QE) such that only open probes significantly contribute signal^{8, 10, 21, 30, 281}. However, at short distances, organic dyes often undergo additional quenching mechanisms such as Dexter energy transfer and static quenching. Static quenching on three-oligonucleotide complexes has been reported with up to 5 bp separation²⁸⁵. While tension probes are often assumed to be FRET quenched^{10, 106, 208, 281}, this assumption is often incorrect for specific fluorophore-quencher pairs^{93, 286}. Indeed, we recently reported that conventional MTFM probes employing a Cy3B donor and BHQ1 acceptor are static quenched³³. While this is well established in the molecular beacon literature^{89, 93}, its impact on tension imaging is less explored. Static quenched dyes form nonfluorescent ground-state complexes, which offer advantages in intensity-based imaging and assays^{21, 287} but skew fluorescence lifetime data²⁸⁸. Nearby dyes separated by up to 8 bp can also experience short-distance fluorescence fluctuations²⁸⁹. Thus, to advance molecular mechanobiology through MTFM, there is a need for an empirical evaluation of DNA-based probes to understand how fundamental processes impact optimal imaging probe design.

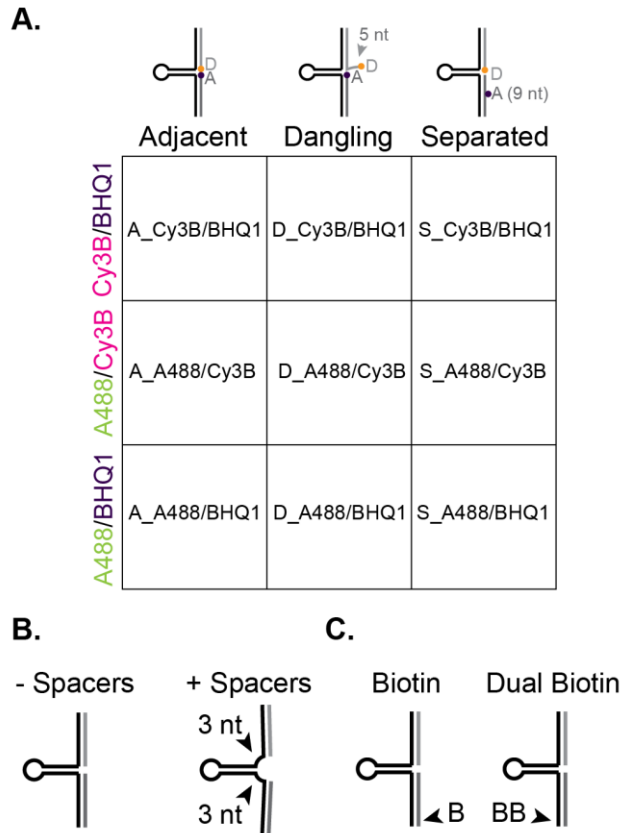


Figure 24 Summary of DNA Hairpin-Based Tension Probes Evaluated in this Study.

(A) Tension probes were evaluated with three Donor/Acceptor pairs and 3 Donor/Acceptor geometries. Abbreviations for each probe are provided in the chart. (B) Hairpins were tested with and without spacers flanking the three-way junction. Each spacer consisted of 3 Ts. (C) Probes were anchored using a single or dual biotin, thus perturbing the local surface concentration.

Herein we characterized the spectral properties of a small library of DNA hairpin-based tension probes. We first considered the impact of donor/acceptor pair and positioning, as well as DNA hairpin structure (Figure 24). We compared the absorption spectra, quenching efficiency (QE), and fluorescence lifetime of closed and open tension probes labeled with three donor/acceptor pairs: Cy3B/BHQ1, Alexa 488 (A488)/Cy3B, and A488/BHQ1. Each pair was assessed in three geometries (Figure 24A). In the adjacent (A)

geometry which is the conventional tension probe design³⁰, the donor and acceptor are conjugated to blunt ends of the probe's arm sequences and are separated by the probe's three-way junction (TWJ). In the dangling (D) geometry, the donor fluorophore is conjugated to a 5 nt overhang. In the separated (S) design, the acceptor is placed 9 nt away from the donor via a deoxythymidine modification. We were also curious to understand the impact of the probe's TWJ structure. Unpaired bps increase TWJ stability²⁹⁰; therefore, in our original MTFM probe design, the DNA hairpin strand's stem-loop was flanked by two spacer sequences containing (3T's) separating it from the arms³⁰. Given that tension probe TWJs contain a nick, we characterized the role of the 3T spacers on probe performance^{33, 291} (Figure 24B). Throughout our manuscript, we adopt a nomenclature as shown in Figure 24A with an added + or – symbol indicating presence or absence of 3T spacers. Thus, a probe containing Cy3B and BHQ1 in the separated geometry with spacers would be called S_Cy3B/BHQ1+ and a probe containing Alexa 488 and BHQ1 in the dangling geometry without spacers would be called D_A488/BHQ1-. We also investigated the impact of intra- versus intermolecular FRET in tension probe signal, by tuning the dimerization of probes using a single or dual biotin anchors (Figure 24C). Finally, we illustrated the impact of FRET probe design by imaging integrin receptor tension and clustering in a podosome model system using three differing probe families. We conclude with a series of recommendations to guide the use of DNA-based tension probes in various experimental settings. This work builds upon our development of MTFM and MT-FLIM and provides important insight into the optimal design of DNA-based tension probes to image molecular forces on soft and fluid materials.

4.3 Results

4.3.1 *Absorbance Spectroscopy of Molecular Tension Probes in Solution*

We first were curious to determine which probes underwent FRET versus static quenching. Dyes undergoing static quenching are excitonically coupled and therefore exhibit distinct ground state energies; this results in perturbation of the absorbance spectra^{89, 91, 292}. Through-space FRET, however, does not impact donor and acceptor fluorophore absorption. We therefore measured the absorption spectra of both closed and open tension probes (Figure 25, Figure A 26). For these experiments, only tension probes lacking spacer sequences were measured. First, closed probes (~2.5 μ M) were annealed, concentrated to ~10 μ M and then the absorption spectra were measured using a microvolume (Nanodrop) instrument in 4x PBS. Probes were then opened by annealing with 10-fold excess of an oligonucleotide complementary to the hairpin's stem-loop, concentrated, and remeasured in the open conformation (Figure 25).

The open and closed Cy3B/BHQ1 probes displayed two overlapping absorption peaks. The open and closed states of the adjacent and dangling probes displayed differing spectra; the relative absorption intensities of the two peaks were inverted. This is in contrast to the separate probe design which showed identical spectra in the open or closed geometry (Figure 25B). These results show that the Cy3B/BHQ1 probes are static quenched when the chromophores are in close proximity (A or D), but undergo FRET when separated by 9 nt. Accordingly, probes exhibited a bathochromic shift in their absorption maximum when opened. This shift was also observed for D_Cy3B/BHQ1- probes, suggesting that static complex formation was largely unaffected by an overhang.

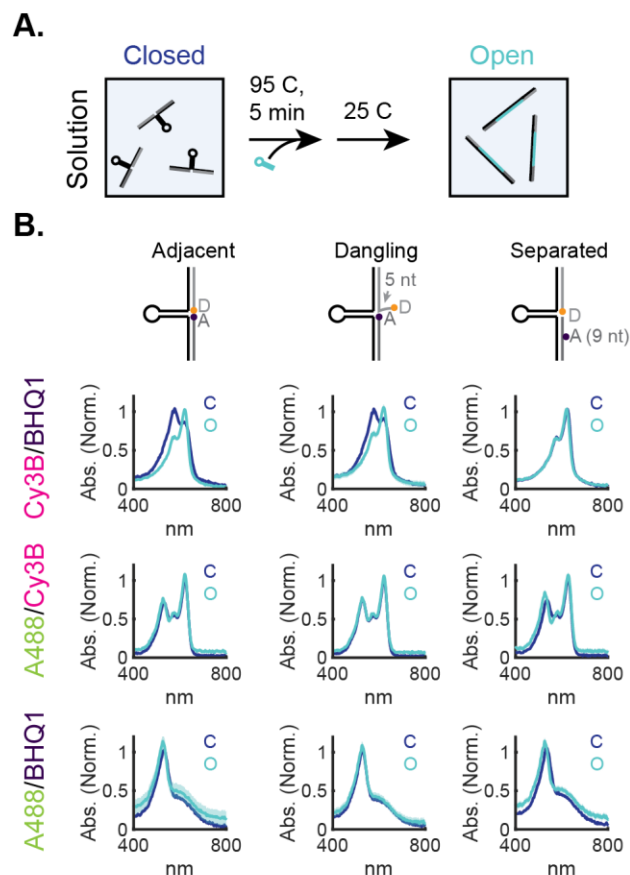


Figure 25 Absorption Spectroscopy Reveals Ground-State and Dye-DNA Interactions in Molecular Tension Probes.

(A) Tension probes were measured in solution in the closed conformation, hybridized at 95 C, and remeasured in the open conformation. (A) Representative absorption spectra of closed and open tension probes with varying donor/acceptor pairs and dye geometries. The representative absorbance spectra of Cy3B/9TBHQ1 is reproduced from ³³. Spectra represent the mean \pm s.e.m. from 3-4 experiments. Outlier spectra (baseline \pm 3 median absolute deviations) were omitted.

Compared to Cy3B/BHQ1 probes, A488/Cy3B probes exhibited minimal chromic shifts in their absorption spectra (Figure 25), and the closed probe absorption spectra of all three donor/acceptor geometries was nearly identical. Both A_A488/Cy3B- and S_A488/Cy3B- probes exhibited a small absorption change at ~500 nm when comparing

their open and closed states. This was accompanied by a slight hypsochromic shift in the A488 absorption peak, which was more notable for S_A488/Cy3B-. Closed and open probe absorption spectra for D_A488/Cy3B- were identical. Because in all three donor/acceptor geometries, the open probe separation between Alexa 488 and Cy3B vastly exceeded reported distances for dye interactions, we determined that the observed shift in A_A488/Cy3B- and S_A488/Cy3B- absorption spectra could not be attributed to the formation of a ground state static complex. We hypothesized that these perturbations were instead caused by an A488-oligonucleotide interaction when A488 was conjugated to the blunt end of a nicked duplex, which was common to A_A488/Cy3B- and S_A488/Cy3B- but not D_A488/Cy3B. To test this hypothesis, we collected absorption spectra for closed and open probes that were labeled only with a donor or only with an acceptor (Figure A 26). The absorbance spectra of tension probes containing A488 but not 5 nt A488 alone exhibited a 6 nm shift ($p = 0.005$) between closed and open probe absorption max, which supported our hypothesis that changes in the A_A488/Cy3B- and S_A488/Cy3B- spectra were caused by dye-DNA interactions that were not present when A488 was attached on an overhang.

A488/BHQ1 probes followed similar trends to A488/Cy3B probes, with the only change in closed and open absorbance spectra being a slight blueshift in the absorption max of A_A488/BHQ1- and S_A488/BHQ1- (Figure 25B). These data indicated that A488/BHQ1 do not undergo static quenching in tension probes and rather suggest that A488 may interact with the complementary strand when chemically opened.

4.3.2 *Fluorescence Imaging of Tension Probes on SLBs*

We next wanted to compare the probes' performance in fluorescence imaging. After annealing, closed and open probes were hybridized and attached to SLBs through biotin/streptavidin interaction and were imaged using both epifluorescence and FLIM. The fluorescence lifetime was measured using TCSPC and was reported using three metrics. The amplitude-weighted and intensity-weighted averages were calculated from fluorescence lifetime decay reconvolution fitting and differentially weight individual lifetime components in multiexponential decays. Typically the amplitude weighted average lifetime is used for FRET studies, because it correlates with the steady state fluorescence intensity; however this breaks down for more complex scenarios including the presence of static quenching and multi-state models^{92, 293}. We also evaluated probes using the average lifetime obtained by curve fitting the FAST-FLIM average lifetime histogram, which approximates the intensity-weighted lifetime. The quenching efficiency (QE), which reports the energy transfer in open versus closed probes, was calculated using both the fluorescence intensity and the amplitude average lifetime. Unless otherwise specified, our manuscript references the intensity-derived QE. These findings are summarized in Figure 26, Figure 27 Figure 28, Figure A 27, Figure A 28, and Table A 7.

Cy3B/BHQ1 probes (Table A 7, Figure 26) were very sensitive to donor/acceptor radius and hairpin-probe geometry. A_Cy3B/BHQ1-, A_Cy3B/BHQ1+, and D_Cy3B/BHQ1- probes exhibited a ~98-99% QE (Figure 25A,D,G). Overhang incorporation in D_Cy3B/BHQ1+ reduced the QE to 95% (Figure 25D). Thus, these probes exhibited a 20- to 100-fold increase in fluorescence intensity upon opening. Across all three definitions of the average fluorescence lifetime, we observed reduction of the fluorescence lifetime in closed static quenched probes compared to open probes (Figure 25B,C,E,F).

During FLIM imaging, we observed that closed static quenched samples lacking a spacer had higher photon count rates at maximal laser power, indicating an increase in brightness. This increase was not statistically significant in our intensity-based data, likely due to the low fluorescence above the Electron Multiplying Charge Coupled Device (EMCCD) background with our imaging settings (Figure 25A,D). The increase in photon counts is reflected in the average lifetime histograms, in which histograms for static quenched probes lacking spacers had high variance compared to the lifetime (Figure 25B,E). Because open and closed probe count rates were held constant, this effect is also observed for this class of open probes despite their 100-fold increase in fluorescence intensity. We therefore conclude that spacers reduced static interactions between Cy3B and BHQ1B. Closed S_Cy3B/BHQ1- (MT-FLIM probes³³), which completely eliminated static quenching were less quenched than static quenched probes (Figure 25G), but exhibited the shortest fluorescence lifetime (Figure 25C,F,I). In contrast to static quenched probes, FRET quenched probes exhibited a decrease in sensitivity and an increase in the closed fluorescence lifetime with the addition of spacer sequences flanking the DNA hairpin (Figure 25G,H,I); this is due to a larger radius between the Cy3B and BHQ1 pair at rest. Thus, S_Cy3B/BHQ1- probes offered the greatest lifetime contrast of Cy3B/BHQ1 probes.

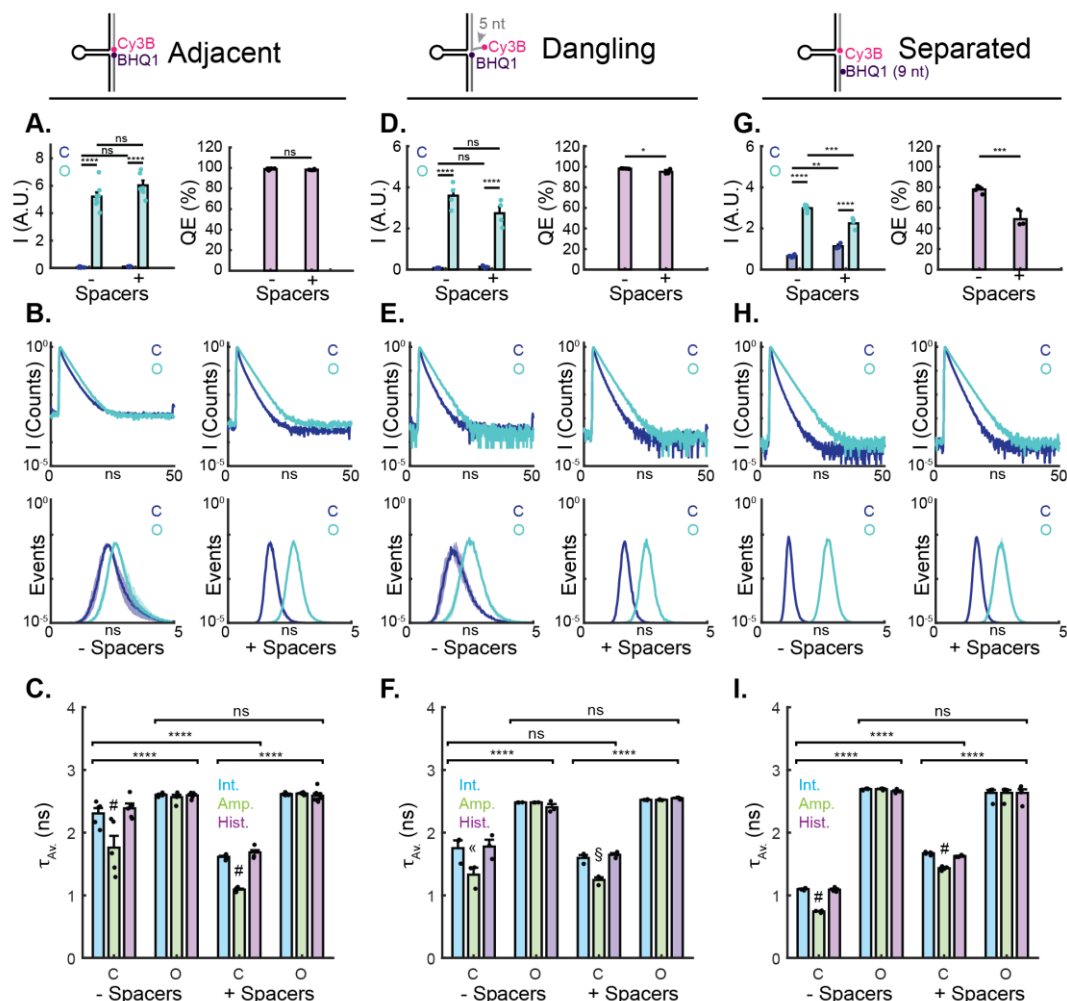


Figure 26 Fluorescence analysis of Cy3B/BHQ1 probes on an SLB.

(A, D, G) Epifluorescence intensities and quenching efficiencies of closed (C) and open (O) probes with (+) and without (-) spacers in the adjacent, dangling, and separated geometries. (B,E,H) FLIM decay curves and FAST FLIM histograms of closed (C) and open (O) probes with (+) and without (-) spacers in the adjacent, dangling, and separated geometries. Intensities were compared using a 2-way grouped ANOVA followed by a multiple comparison test. Quenching efficiencies were compared using an unpaired two-tailed students t-test. (O) probes with (+) and without (-) spacers in the adjacent, dangling, and separated geometries. Representative decay curves are averaged over five time bins. Normalized histograms represent the mean \pm s.e.m. (C,F,I) Quantification of the average intensity-weighted (Int.), amplitude-weighted (Amp.), and FAST FLIM average lifetime (Hist.). The intensity- and amplitude-weighted lifetimes were derived from decay curve fitting. The FAST FLIM average lifetime was defined as the center of FAST FLIM histogram fit to a bi-gaussian. Statistics were performed using a 3-way grouped ANOVA followed by 2 multiple comparison tests to look at differences across all samples or at differences between groups but not fit methods. Experiments were repeated at least 3 times. P values are reported as ns $P > 0.05$, *, § $P < 0.05$, **, « $P < 0.01$, *** $P < 0.0001$, ****, # $P < 0.0001$.

Tension-probe characterization was repeated for Alexa488/Cy3B and A488/BHQ1 probes, which did not static quench. In A_A488/Cy3B, D_A488/Cy3B, S_A488/Cy3B, A_A488/BHQ1, and D_A488/BHQ1 probes, the QE decreased with the introduction of spacer sequences in the hairpin (Figure 27A,D, Figure 28A,D). While this trend was also observed for S_A488/BHQ1 probes, the presence of non-statistical outliers obscured this difference (Figure 28G). For the A488/Cy3B probe family, A_A488/Cy3B- offered the highest QE based on fluorescence intensity measurements. This massive donor quenching was reflected average amplitude-weighted lifetime but was not reflected in the intensity-weighted or FAST-FLIM average lifetimes (Figure 27C). Furthermore, we found that quenched A488/Cy3B probes were extremely sensitive to acceptor photobleaching, making them challenging to image and quantify. To avoid acceptor photobleaching, the laser power was attenuated such that the photon count rate was ~1% of the laser pulse rate, which led to a relatively wide histogram distribution (Figure 27B, Table A 7). Quantified by the amplitude and FAST-FLIM average lifetime and in the context of this artifact, D_A488/Cy3B- probes thus offered the best lifetime sensitivity, despite their intermediate quenching efficiency of 84%. This sensitivity was closely followed by A_A488/Cy3B+ (Figure 27C-F). S_A488/Cy3B- had a shorter FAST-FLIM and amplitude average lifetime than A_A488/Cy3B probes but were ~5-fold less quenched. S_A488/Cy3B+ exhibited the lowest lifetime and intensity sensitivity (Figure 27G-I). A488/BHQ1 probes behaved similarly but were not subject to the bleaching artifact observed for A_A488/Cy3B probes. Thus, A_A488/BHQ1, D_A488/BHQ1, and S_A488/BHQ1 probes exhibited increasing closed fluorescence lifetime and decreasing quenching efficiency (Figure 28), which is the expected trend for a FRET pair separated by increasing radius.

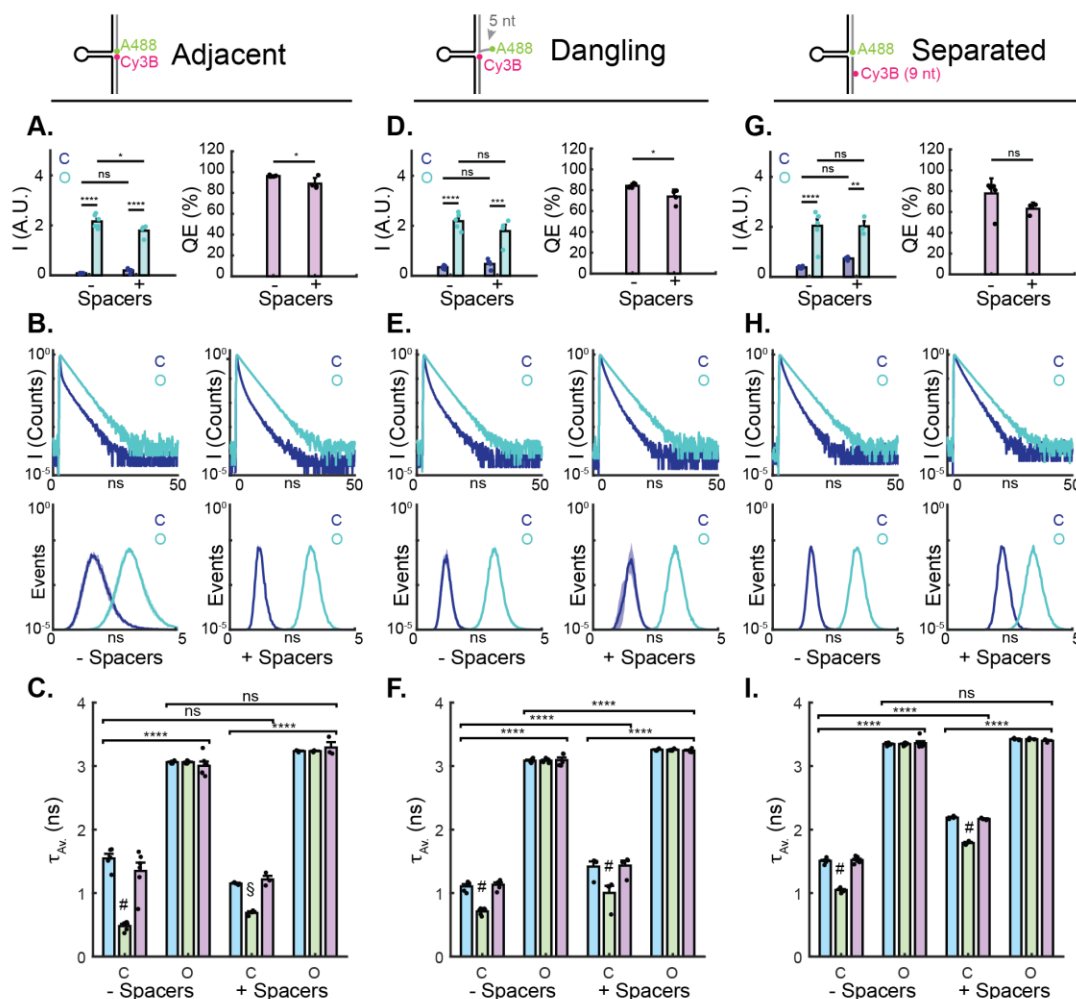


Figure 27 Fluorescence analysis of A488/Cy3B probes on an SLB.

(A, D, G) Epifluorescence intensities and quenching efficiencies of closed (C) and open (O) probes with (+) and without (-) spacers in the adjacent, dangling, and separated geometries. (B,E,H) FLIM decay curves and FAST FLIM histograms of closed (C) and open (O) probes with (+) and without (-) spacers in the adjacent, dangling, and separated geometries. Representative decay curves are averaged over five time bins. Normalized histograms represent the mean \pm s.e.m. (C,F,I) Quantification of the average intensity-weighted (Int.), amplitude-weighted (Amp.), and FAST FLIM average lifetime (Hist.). The intensity- and amplitude-weighted lifetimes were derived from decay curve fitting. The FAST FLIM average lifetime was defined as the center of FAST FLIM histogram fit to a bi-gaussian. Statistics were performed using a 3-way grouped ANOVA followed by 2 multiple comparison tests to look at differences across all samples or at differences between groups but not fit methods. Experiments were repeated at least 3 times. P values are reported as ns $P > 0.05$, *, § $P < 0.05$, **, « $P < 0.01$, *** $P < 0.0001$, ****, # $P < 0.0001$.

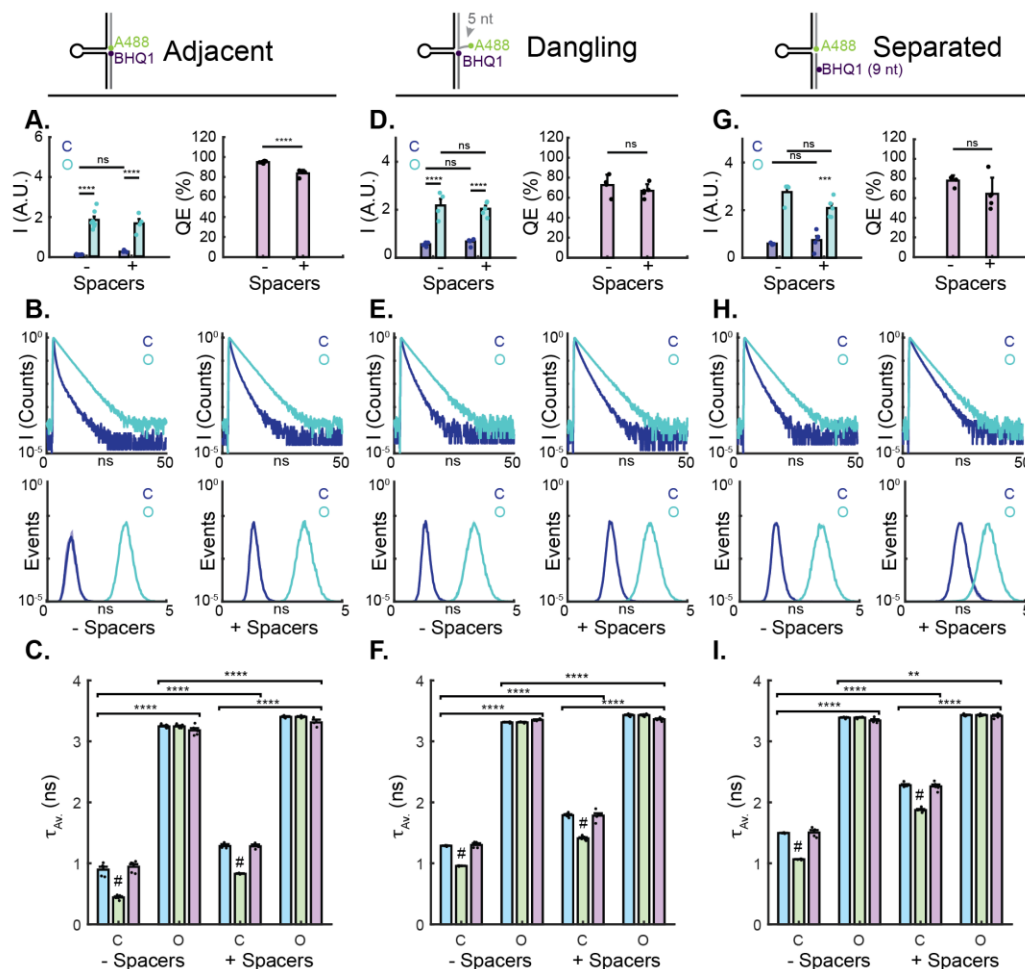


Figure 28 Fluorescence analysis of A488/BHQ1 probes on an SLB.

(A, D, G) Epifluorescence intensities and quenching efficiencies of closed (C) and open (O) probes with (+) and without (-) spacers in the adjacent, dangling, and separated geometries. (B,E,H) FLIM decay curves and FAST FLIM histograms of closed (C) and open (O) probes with (+) and without (-) spacers in the adjacent, dangling, and separated geometries. Representative decay curves are averaged over five time bins. Normalized histograms represent the mean \pm s.e.m. (C,F,I) Quantification of the average intensity-weighted (Int.), amplitude-weighted (Amp.), and FAST FLIM average lifetime (Hist.). The intensity- and amplitude-weighted lifetimes were derived from decay curve fitting. The FAST FLIM average lifetime was defined as the center of FAST FLIM histogram fit to a bi-gaussian. Statistics were performed using a 3-way grouped ANOVA followed by 2 multiple comparison tests to look at differences across all samples or at differences between groups but not fit methods. Experiments were repeated at least 3 times. P values are reported as ns $P > 0.05$, *, § $P < 0.05$, ** , « $P < 0.01$, *** $P < 0.0001$, ****, # $P < 0.0001$.

Given that all closed tension probes in our library exhibited multi-exponential decays (Figure A 27) and that S_Cy3BBHQ1- probes were previously shown to be more sensitive to changes in the percent open probes at low tension densities³³, we hypothesized that probes may experience intermolecular FRET. In this case, Cy3B would not only be quenched by the internal BHQ1 but would also be quenched by dyes on proximal probes. In the absence of dye-dye interactions, FLIM is concentration-independent. However, when conjugated to an SLB through biotin/streptavidin interaction, two tension probes may be clustered on a single streptavidin molecule. To test the hypothesis, that streptavidin clusters probes and leads to intermolecular FRET, we imaged probes that were immobilized either using a single biotin on the 3' terminus of the anchor strand or using a dual biotin attached to the 5' terminus of the hairpin sequence (Figure 29A). Assuming that each streptavidin binds to two biotinylated lipids, streptavidin on a bilayer can bind only one tension probe attached with a dual biotin but can bind up to two tension probes attached with a single biotin. Observed differences in the QE and τ of these samples should reflect the extent of intermolecular quenching. We selected S_Cy3B/BHQ1- probes for analysis, because these probes were free from ground state and dye-DNA interactions, and because we previously characterized these probes on supported lipid bilayers with varying biotin concentration, which showed a slight concentration dependency³³. For each immobilization strategy, we measured the fluorescence intensity and lifetime of bilayers presenting 0, 10, 20, and 100 % open probes.

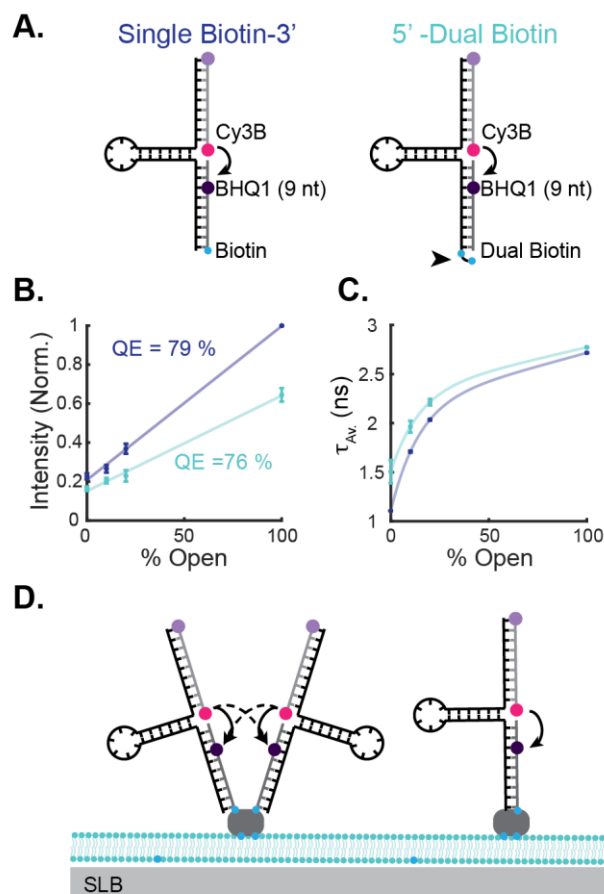


Figure 29 Streptavidin-Immobilized Tension Probes Undergo Intermolecular FRET. (A) Schematic of tension probes containing a single or dual biotin group used in this experiment. (B) Plot of percentage of open probes versus fluorescence intensity normalized to the single biotin 100% open intensity. The QE for each probe was reported as the slope of the corresponding linear curve fit. (C) Percentage of open probes versus FAST-FLIM average lifetime, determined through histogram analysis. (D) Model schematic of tension probes on an SLB during conventional imaging (with 3'-Biotin). ~50% of streptavidin molecules bind to two tension probes, which undergo both intra- and inter- molecular energy transfer.

SLBs presenting probes with a dual biotin were dimmer than SLBs presenting single-biotin labeled probes (Figure 29B). On 100 % open surfaces, single biotin SLBs were 56 ± 15 % brighter than dual biotin SLBs. Despite the lower intensity, QE was not significantly different between probes conjugated using a single or dual biotin anchor. Single and dual biotin were 79 and 76 % quenched based on linear regression; individual replicates were not statically significant. When probes were imaged using FLIM, we

observed that the open probe fluorescence lifetime was only slightly increased in dual biotin probes; however, SLBs presenting closed probes or a mixture of closed and opened probes exhibited an increase in fluorescence lifetime for probes conjugated through a dual biotin, which occupied both free sites on a streptavidin (Figure 29C). In all cases, the fluorescence lifetime fits of samples containing closed probes remained multiexponential, but the average fluorescence lifetime was increased (Figure 29C, Figure A 29). Combining our intensity data, which shows that single biotin SLBs are 56 ± 15 % (Mean \pm SD) brighter than dual biotin SLBs when all probes are opened, with our FLIM data, which suggests that Cy3B on open probes is dequenched and that probes on 100% open surfaces are primarily non-interacting, we estimate that ~50 % of streptavidin molecules are occupied with two tension probes attached via a single biotin (Figure 29D). Despite the unchanged QE, we conclude that probes loaded onto a single streptavidin molecule undergo both intermolecular and intermolecular FRET based on the observed change in τ between single and dual biotin samples.

4.3.3 *Tension Imaging of Podosome-like Adhesions with Varied Energy Transfer*

To demonstrate the impact of design features that affect energy transfer in tension probes, we selected a subset of probes to evaluate in cellular imaging. Probes were selected based on their transfer and structure, which we evaluated using NUPACK (Figure 26, Figure 27, Figure 28, Figure A 30). For this study, we chose to focus on probes without an overhang, which may introduce more degrees of flexibility, making cellular imaging results more challenging to interpret. S_Cy3B/BHQ1- (MT-FLIM) and + probes were selected as a reference and to demonstrate the impact of spacer sequences in FRET probes with large closed donor-acceptor radius. A_Cy3B/BHQ1- and + were selected to demonstrate

imaging using static quenched probes. Finally, we imaged cells using A_A488/BHQ1- and +. These probes both offered high lifetime sensitivity, while demonstrating the impact of QE, as A_A488/BHQ1- exhibits a ~20-fold increase in fluorescence intensity upon opening compared A_A488/BHQ1+, which only displays a ~6-fold increase in intensity.

As a model of receptor mechanobiology with unfixed ligand density, we imaged podosome-like adhesions on an SLB. Podosomes are protrusive structures which consist of an actin core that physically excludes adhesion ligands and an adhesion ring, which surrounds the podosome core^{36, 61}. Fibroblasts on SLBs form multiple podosome-like adhesions within ~1 hour spreading, which have been previously validated and characterized with immunostaining and MT-FLIM^{9, 33, 83}. Integrin receptors on fibroblasts bind to cRGD-ligands on tension probes. Bound probes can be laterally transported, leading to a change in probe density and intensity, which is measured by photon counts. At forces above the $F_{1/2}$ threshold, probes mechanically unfold, leading to an increase in fluorescence intensity that is coupled to an increase in the τ (Figure 30A). In podosome-forming cells, regions of low intensity correspond to regions where a podosome core exerts pushing forces on the SLB and physically excludes probes. This is accompanied by the application of pN tension in the podosome ring, which causes an increase in fluorescence lifetime. Integrin receptors can also cluster ligands outside of podosome regions, leading to bright puncta without a measurable change in fluorescence lifetime³³.

For each sub-class of tension probe, we imaged cells on 4.7 pN probes with and without spacer sequences and linear control probes which lacked a stem-loop sequence but contained spacers as indicated (Figure 30B, C). For these experiments, it is important to consider that spacer sequences not only affect the TWJ but also may act as a small entropic

spring, which could affect the probe signal. Curve fitting and calculation of the amplitude average lifetime exhibited the largest shift in fluorescence lifetime, but we used the FAST FLIM average lifetime to analyze cell data. Compared to most genetically encoded tension sensors²⁹⁴, our probes offered a massive change in fluorescence lifetime. Furthermore, this approach could be easily integrated with quantitative intensity-based thresholding workflows to identify podosome regions in MATLAB (Figure A 34, Figure A 35, Figure A 36). $\tau_{Int.}$ is typically the best parameter for FLIM-FRET because it reports the steady state lifetime. Here we found that it was poorly correlated with intensity-based imaging (Figure A 28), such that there was little advantage to its use. While our main figures report the change in fluorescence lifetime in podosome regions, note that for DNA-based tension probes, the relationship between probe opening and fluorescence lifetime is not linear (Figure 29, Figure A 29)³³.

On 4.7 pN S_Cy3B/BHQ1- (MT-FLIM) and S_Cy3B/BHQ1+ probes (Figure 30C,D, Figure A 34), cells exhibited an increase in fluorescence lifetime surrounding podosome core depletion regions. This change in fluorescence lifetime was accompanied by an increase in photon counts on S_Cy3B/BHQ1-. On S_Cy3B/BHQ1+ probes, the change in fluorescence lifetime was 0.51 ± 0.06 smaller than on S_Cy3B/BHQ1- probes, and there was only a slight increase in the fluorescence intensity in podosome rings. The small change in intensity can be attributed to the combined effects of changing probe density and lower quenching efficiency in these probes. Receptor clusters at the cell periphery were clearly observable in the photon counts channel on both S_Cy3B/BHQ1- and S_Cy3B/BHQ1+ probes; these clusters did not experience an increase in lifetime. On linear probes we observed some clustering surrounding podosomes. This signal was

dimmer than the bright rings typically observed in samples with unfolded 4.7 pN S_Cy3B/BHQ1- tension probes. Podosome regions displayed only a slight increase in fluorescence lifetime on linear probes, validating that changes in fluorescence lifetime were caused by mechanical unfolding of the stem-loop sequence. The incorporation of a spacer sequence in linear probes was statistically significant but effectively negligible.

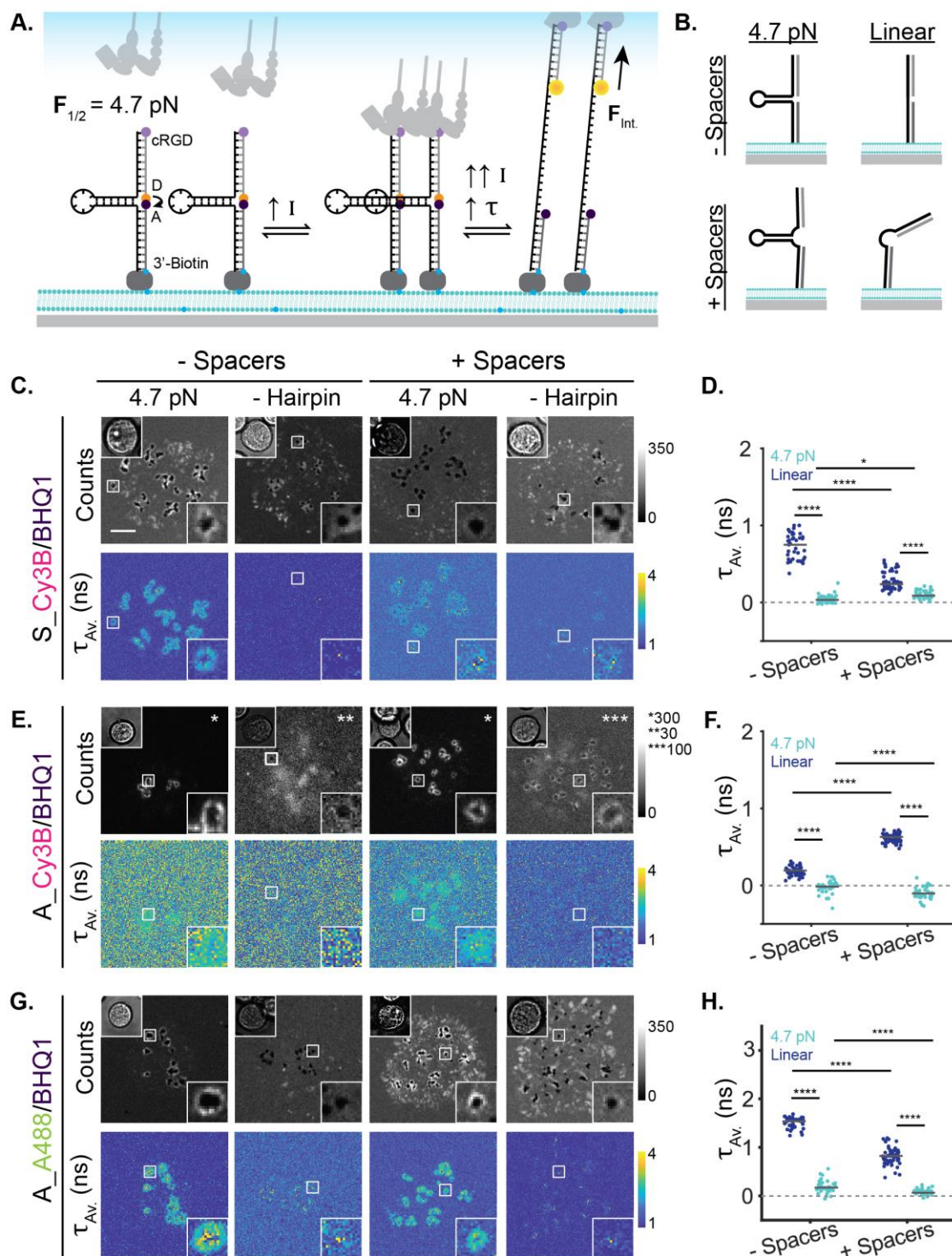


Figure 30 Tension Probe Design Impacts the Cellular Read-Out

(A) Schematic of integrin receptor and tension probe interactions on an SLB. Unbound probes are closed and undergo quenching. Integrin receptor binding and clustering leads to an increase in density and intensity (I). Alternatively, probes can be depleted, leading to a

loss of fluorescence (not shown). Upon integrin receptor forces above $F_{1/2}$, the hairpin unfolds leading to an increase in intensity (I) and fluorescence lifetime (τ). **(B)** Cells were imaged on 4.7 pN tension probes with (+) or without (-) spacer sequences. As a control, cells were imaged on corresponding Linear probes, which lacked a stem-loop. **(C, E, G)** Representative images of NIH 3T3 cells imaged on SLBs containing the indicated tension probes. Statistics were performed using a 2-way grouped ANOVA followed by a multiple comparison test. Experiments were repeated at least 3 times. P values are reported as * < 0.05, ****P < 0.0001. Scale bar, 5 μ m

Cells on A_Cy3B/BHQ1 (Figure 30E,F, Figure A 35) probes exhibited different tension probe signatures, due to static quenching. On A_Cy3B/BHQ1- and +, podosomes appeared as bright rings in the photon counts channel, which were accompanied by a smaller but significant increase in the fluorescence lifetime channel (0.19 ± 0.05 ns and 0.62 ± 0.06 ns, respectively). A_Cy3B/BHQ1+ had a larger shift in lifetime compared to A_Cy3B/BHQ1-, because of the reduced contribution of static quenching, which made these probes more sensitive. Nevertheless, with both static quenched probes, while the average fluorescence lifetime increased over the background, the large variance in background lifetime still led to poor separation of signal and noise (Figure A 35). On both hairpins, clustering and probe exclusion in the podosome's actin core were visibly suppressed, because of the nonfluorescent ground-state complex present in closed probes. The fluorescence intensity signal from linear probes was largely dominated by autofluorescence. Podosomes on linear A_Cy3B/BHQ1+ probes exhibited a characteristic ring pattern, but these rings were much dimmer than on surfaces presenting DNA hairpin probes. On linear A_Cy3B/BHQ1+ probes, rings exhibited a decrease in fluorescence lifetime compared to the background. This could be attributed to mechanical rupturing of static quenched complexes and a subsequent transition to a FRET quenching.

Finally, we imaged podosome-forming cells on A488/BHQ1 probes. These probes provided an example of tension signal on both highly and intermediate quenched FRET probes (Figure 28G,H, Figure A 28). On 4.7 pN A_A488/BHQ1- probes, the photon counts channel showed bright rings corresponding to adhesion rings. Podosomal depletion and receptor clustering were less obscured than on static quenched probes, but were still largely suppressed, due to the probes' ~95% QE. With the highest lifetime sensitivity, resulting from the combination high FRET efficiency and a long A488 intrinsic lifetime, these probes offered the largest increase in fluorescence lifetime in podosome rings. With the incorporation of a spacer sequence, A_A488/BHQ1+ probes had a lower quenching efficiency, which allowed clear visualization of clustered and depleted probes in podosome-forming cells and still maintained a large dynamic range for tension mapping and quantification. In comparison to 4.7 pN probes, linear A488/BHQ1 probes had very little change in the photon counts signal surrounding podosomes. Note that we do not attribute this to meaningful change in probe behavior compared to S_Cy3B/BHQ1 probe signal but rather hypothesize this is caused by a slight difference in the sample specific length of incubation on the SLB. Meanwhile, although the change in podosome fluorescence lifetime on 4.7 pN probes was significantly higher than on linear probes, the change in podosome fluorescence lifetime on A_A488/BHQ1- was the largest in our data set for linear probes. This may be attributed to an increased sensitivity to rotational freedom and twisting in highly quenched FRET probes. The effect of entropic spring spacer sequences in A_A488/BHQ1+ linear probes was larger than that in S_Cy3B/BHQ1+ probes but was still small in comparison. Although linear A_A488/BHQ1- probes were

highly quenched, probe background was sufficient to obscure autofluorescence contribution observed in static quenched linear samples (Figure 30E,F).

4.4 Discussion

4.4.1 Discussion of Probe Design and Spectroscopy

Whereas several studies have focused on sm-FRET and dye-DNA interactions, few studies perform side-by-side spectroscopic and imaging measurements to understand the practical impact of molecular probe design for cellular imaging. Indeed, our lab has found that different biological systems require slightly different tension probe schematics to maximize signal^{30, 33, 106, 253}. Our library here focused on DNA hairpin structure and energy transfer specifically in the context of DNA-based MTFM probes. Cy3B, A488, and BHQ1 are commonly used in DNA-based tension probes, with Cy3B selected as the tension reporter for its photostability and quantum yield. Because Cy3B and BHQ1 are hydrophobic dyes and dye interactions are governed by a combination *van der Waals* and hydrophobic interactions^{91, 295}. In this study we selected A488 to represent the more hydrophilic dyes. A488 offers excellent imaging properties and minimally stacks with DNA^{21, 296}. Interestingly, in our absorption spectroscopy data (Figure 25), we did observe some dye-DNA interaction in open Alexa 488 probes lacking a 5T overhang. Since A488 has a low anisotropy on DNA^{21, 296}, we hypothesize that interaction is caused by proximal guanosine quenching by the 5' end of the complementary sequence, which can alter absorbance in some cases²⁹⁷.

Our three donor/acceptor spatial arrangements offered sequential perturbation of conventional tension probes. In the separated geometry, all tension probes were FRET

quenched. When the donor and acceptor dyes were separated only by the width of the DNA hairpin duplex in the adjacent geometry, Cy3B/BHQ1 probes were static quenched and A488/BHQ1 probes were FRET quenched. This observation was in agreement with our previous report that A_Cy3B/BHQ1+ probes are static quenched but S_Cy3B/BHQ1- probes are FRET quenched³³. As expected, this observation was maintained for A_Cy3B/BHQ1- probes, which further reduce the donor/acceptor radius. Dexter quenching may also play a role in this geometry, but our methods were not able to distinguish these two mechanisms. Marras and colleagues reported that a 5 nt overhang maximized FRET while significantly decreasing static quenching between a donor-acceptor pair at the terminus of a DNA duplex⁸⁹. We therefore hypothesized that separation of the Cy3B and BHQ through a short overhang may reduce dye interactions. However, our results indicated that 5 nt was insufficient to remove ground state interactions in D_Cy3B/BHQ1- probes.

The interpretation of our static quenched FLIM data required is counterintuitive. Static quenched samples do not typically display a change in fluorescence lifetime compared to the donor only sample, because only dequenched free dyes contribute to the fluorescence decay. We observed a slight decrease in the fluorescence lifetime of static quenched samples. This is especially confounding, because probe anchoring to the SLB requires hybridization to the quencher-modified strand. We explain these results through thermal fluctuations and hydrophobic interactions. Although the majority of closed probes are folded, quenched, and spectroscopically silent, a small fraction of probes will thermally breathe and generate fluorescence²⁹⁸. During hairpin breathing, the fluorophore and quencher are separated and contribute long-lifetime photons. When static quenched

complexes breathe, either due to bp breathing at the TWJ or due to the static complex' intrinsic off rate, the static complex dissociates, but the Cy3B and BHQ1 remain in sufficiently close proximity to undergo FRET or Dexter Energy Transfer, leading to the contribution of a short fluorescence lifetime photons. A second contribution to long-lifetime impurities is due to a small amount of free Cy3B in the sample, which intercalates into the SLB⁹⁰ and is not removed by wash steps. Finally, with few photon counts, quantification of dark, static-quenched samples may be influenced by the contribution of long-lifetime noise. Although fully dequenched probes and Cy3B molecules are rare, because dequenched Cy3B has a much higher quantum yield than FRET quenched Cy3B at this radius, long-lived fluorophores dominate the fluorescence decay, and only a small reduction in fluorescence lifetime is observed. This is in agreement with Sillen and Engelbourns, who argue that the average fluorescence lifetime can change in a heterogeneous population with partial static quenching ⁹².

It is notable that even for our purely FRET probes, the quenching efficiency calculated using fluorescence intensity versus the amplitude-weighted average fluorescence lifetime did not necessarily agree (Table A 7, Figure A 28). Even in cases where the quenching efficiencies did match, we caution against using these data without proper calibration and controls. Whether or not a amplitude-weighted lifetime and percent open probes are linearly related in our system requires additional investigation (Figure 29, Figure A 29). This discrepancy could arise from uncertainty τ_{Amp} ,²⁹⁹ nonradiative contributions to energy transfer³⁰⁰, or inconsistencies between the timescale of probe dynamics and the fluorescence lifetime³⁰¹.

4.4.2 *Recommendations for Cellular Imaging*

While our previously reported MT-FLIM probes (S_Cy3B/BHQ1-) provided a suitable option to image receptor clustering and tension, A488/BHQ1 probes offer improved lifetime sensitivity due to A488's long intrinsic lifetime. We also tested A488 and Cy3B in combination as an example of a potential dual-labeled FLIM-FRET and ratiometric measurements. Although our probe A488/Cy3B probes were sensitive to photobleaching rendering them poor choices for FLIM with these conditions, these probes may be useful ratiometric intensity probes. With appropriate density optimization to maximize the SNR while minimizing photobleaching, these probes may offer potential for side-by-side intensity-based imaging and FLIM.

Given the complexity of the dangling TWJ and the potential for geometric uncertainty, we more strongly recommend probes that lack this overhang. For donor/acceptor pairs that tend to form static complexes and undergo dye interactions, we recommend probes where the donor and acceptor are in the separated geometry. For ensemble measurements with FRET pairs that do not static quench, maximal lifetime sensitivity may be achieved by attaching the dyes adjacent on the on the duplex. It is notable that this can lead to short-range dye-dye interactions. We did not explicitly test these effects in our system, but they should be carefully considered in the context of the specific experiment at hand and are particularly important if transitioning to tension-sm-FRET experiments^{289, 302}. For a more extensive discussion on FRET probe design and troubleshooting, we refer the reader to the recent review by Algar and colleagues²⁸⁶

While modeling suggests that tension probes are slightly more stable with the incorporation of spacer sequences flanking the DNA hairpin (NUPACK Package, Figure A 30), the practical impact of this stability is likely minor. Estimated from previously

reported $F_{1/2}$ measurements and calibrations^{30, 276}, we hypothesize that tension probe ensembles may experience slight (~ 2 pN) broadening of the $F_{1/2}$ transition. However, given the discrepancies that are observed between estimated and experimentally measured $F_{1/2}$ thresholds, this difference may be negligible^{30, 276}. In static quenched probes, this effect would likely be further countered by the stabilizing effect of static complex formation between the donor and acceptor at the junction⁸⁹. Therefore, the impact of spacer sequences can be evaluated from an SNR perspective.

For intensity-based imaging with static-quenched probes, we argue that spacers are largely negligible. It is possible that with optimized gain settings, the QE of these probes may be distinguishable, but we did not measure a significant difference in quenching efficiency, and neither probe was well-suited for FLIM (Figure A 33A-C). For FRET-based probes, the incorporation of spacer sequences should be decided based on the specific biological sample. For samples such as the podosome model applied here, it is desirable to maximize both positive and negative signal-to-noise ratio while maximizing lifetime sensitivity. For these cases, A488/BHQ1 probes with spacers offer the best imaging features. These probes are also optimal for samples in which receptor translocation and microclustering plays a critical role, such as the study of immune receptors³⁰³, because higher quenching efficiencies may reduce the ability to visualize spatial signaling in the absence of tension. In contrast, A488/BHQ1- may be useful for visualizing weak or transient forces, such as the forces applied by the PD-1 receptor^{106, 253}. These highly quenched probes may also be advantageous for imaging forces applied to DNA-loaded hydrogels, in which volumetric tension probes may contribute high background.

Overall, our work highlights the significant impact of photophysics and nanoscale design on DNA-based tension probes. While previous works have provided a more quantitative framework of energy transfer and 3WJ structure in oligonucleotides on the single-molecule level, our results bridge the gap from single-molecule analysis to cellular and molecular imaging. Our data offer important insight for the future development and application of tension probes to image receptor tension on soft materials and fluid interfaces. This work is broadly applicable to FRET sensor design and may be useful in the optimization of nucleic acid-based probes for computing and light harvesting^{304, 305, 306}.

4.5 Methods

4.5.1 *Sample preparation*

4.5.1.1 Probe synthesis and purification

Oligonucleotides (Table A 6) were custom synthesized by Integrated DNA Technologies or Biosearch Technologies (BHQ1-modified oligonucleotides). Synthesis and purification were performed as previously described (Figure A 25)^{30, 33}. 100 µg cyclo [Arg-Gly-Asp-D-Phe-Lys(PEG-PEG)] (PCI-3696-PI, Peptides International) was reacted with NHS-azide (88902, Thermo-Fisher Scientific) in 10 µL dimethyl sulfoxide (MX1457-7, Millipore-Sigma) for 1 hour. The reaction was performed in a bath sonicator and was purified using reverse-phase high performance liquid chromatography (HPLC) on a Grace Alltech C18 column (0.75 mL min⁻¹ flow rate; Solvent A: Nanopure water + 0.05% trifluoroacetic acid (TFA), Solvent B: acetonitrile (BDH83639.400, VWR) + 0.05% TFA; starting condition 90% A + 10% B, 1% per min gradient B). To generate cRGD ligand strands, alkyne modified oligonucleotides were

conjugated to the purified cRGD-azide performed with 10 mM sodium ascorbate, 1 mM copper sulfate, and 0.8 mM THPTA (1010, Click Chemistry Tools) under N₂ for ~1 hour. Amine-labeled oligonucleotides were conjugated to Cy3B-NHS ester (PA631000, GE Healthcare) in a 10 uL reaction containing 10% 10x PBS, 0.1 M sodium bicarbonate, and ~8x excess dye prior to initial purification on a P2 size-exclusion gel. Peptide and dye-labeled oligonucleotides were purified using HPLC on an Agilent Advanced oligo column (0.5 mL min⁻¹ flow rate; Solvent A: 0.1 M TEAA, Solvent B: acetonitrile; starting condition: 90% A + 10% B, 1% per min gradient B). Alexa 488-labeled oligonucleotides were purchased pre-labeled. HPLC products were dried in an Eppendorf Vacufuge Plus and were experimentally validated. Labeled oligonucleotides with significant excess dye were repurified using HPLC or Amicon filtration (3kDA cutoff).

4.5.1.2 Probe hybridization

DNA in 1x PBS was heated to 90 C for 5 min and cooled to 25 C for 25 min in a 0.2 mL Thermowell Tube to assemble tension probes. For surface experiments, the donor strand was added in 10% excess. To unfold tension probes, the complimentary strand was added at 10x excess. For absorption spectroscopy, which was performed in-solution, BHQ1 samples lacked biotin. For SLB characterization, donor strands did not contain ligands.

4.5.1.3 Supported lipid bilayer formation and functionalization

Small unilamellar vesicles (SUVs) were prepared by mixing 1,2-dioleoyl-sn-glycero-3-phosphocholine (DOPC) (850375C, Avanti Polar Lipids) and 1,2-dioleoyl-sn-glycero-3-phosphoethanolamine-N-(biotinyl) (Biotinyl Cap PE) (870282C, Avanti Polar

Lipids) in known ratios in chloroform. Chloroform was removed using rotary evaporation followed by drying under ultra high purity N₂. Lipids were resuspended in Nanopure water (2 mg/mL), sonicated, and freeze-thawed (3 cycles). Liposomes were extruded 10x through a 0.08 or 0.2 micron filter and drain disk. To prepare SLBs using SUVs, uncoated glass-bottom 96 well plates (265300, Nunc) were base etched for ~1 hr in ~2.6 M NaOH and were washed with excess nanopure water and 1x PBS. 100 uL of 0.5 mg/mL liposomes in PBS were added for ~10 min to form an SLB. SLBs were washed with excess water and PBS and were stored for up to 24 hours in water at 4 C. SLBs were passivated with 0.01% bovine serum albumin, Fraction V (10 735 078 001, Roche Diagnostics GmbH) prior to incubation with ~180 nM streptavidin (SA101, Millipore-Sigma) for at least 45 min. SLBs were washed with excess 1x PBS and incubated in ~30nM DNA for at least 45 min prior to imaging. Imaging was conducted in 1x PBS (cell-free assays) or Hanks Balanced Salts (cell assays).

4.5.2 *Characterization and application of DNA-based tension probes*

4.5.2.1 NUPACK modelling

Base pair probabilities were using the freely available NUPACK package³⁰⁷ with dangle treatment applied. Probes were computationally hybridized at 0.5 μ M (1x) and were analyzed at 25 C in 137 mM Na⁺, corresponding to 1x PBS. These conditions matched the conditions used to hybridize DNA prior to SBL functionalization.

4.5.2.2 UV-Vis Spectroscopy

Tension probes were hybridized at 2.5 μM and concentrated to $\sim 10 \mu\text{M}$ prior to measuring on a Thermo Scientific Nanodrop 2000c spectrophotometer with a 0.1 cm pathlength. Closed samples were rehybridized, concentrated, and measured with the complimentary sequence to obtain the open spectra.

4.5.2.3 Microscopy

Epifluorescence imaging was carried out on a using the Nikon Elements 4.40.00 or 4.13.05 software and a 1.49 NA CFI Apo 100x objective equip with perfect focus. Insert cubes. Fluorescence lifetime imaging was performed on a Nikon Ti Eclipse Inverted confocal microscope with a Plan Apo Lambda 60X/1.40 Oil objective, Nikon Elements 4.40.00, perfect focus, and a C2 laser launch. The microscope was updated with a Picoquant Laser Scanning Microscope Time Correlated Photon Counting (TCSPC) Upgrade with SymPhoTime 64 2.1.3813 software. FLIM samples were excited with a 20 MHz pulsed 514 nm or 485 nm laser, and images were collected at 0.5 frames-per-second. Samples were imaged at 20 MHz with a photon count rate of $\sim 5\%$ of the laser pulse rate, except for highly quenched samples which were imaged at the maximum achievable photon count rate (Cy3B probes) or the maximum photon count rate that did not bleach the sample (A_A488/Cy3B-). Light was filtered using a long-pass laser beamsplitter (H560 LPXR, Analysentechnik) or Insert 488 dichroic and a 582/75 bandpass filter (F37-582, Semrock) or insert 488 bandpass. Laser light that was reflected by the dichroic was blocked from an additional detector using a 690/35 bandpass filter. Surface characterization was performed with the pinhole fully opened. For cellular imaging, A_Cy3B/BHQ1 were imaged with an open pinhole to maximize light collection; all other samples were imaged with the pinhole optimized to 1.2 Airy Units.

4.5.3 *Cell culture*

NIH 3T3 fibroblasts were cultured in Dulbecco's Modification of Eagle's Medium (DMEM) (B003K32, Corning). Media contained 10% Fetal Bovine Serum (USDAFBS, MidSci), 2.5 mM L-glutamine (G8540, Millipore-Sigma), and 1x penicillin streptomycin (97063-708, VWR). Cells were incubated at 37°C in 5% CO₂. Cells were authenticated by IDEXX BioResearch. Note that while these surpassed the criteria for cell line validation³⁰⁸, they did show small genetic deviation. Nevertheless, we find these cells to be a robust mechanical model.

4.5.4 *Analysis and Statistics*

Fluorescence lifetime decay traces were fit using reconvolution in SymPhoTime 64 according to the equation:

$$I(t) = \sum_{n=1}^m A_n e^{-t/\tau_n} \quad (12)$$

Goodness of fit was evaluated by the chi-squared parameter. All curve fits had chi-squared > 2. Curves were fit with the minimum number of lifetimes to reduce sinusoidal residuals, while minimizing chi-squared. If additional lifetime components only corrected deviations near the IRF region, the lower lifetime fit was selected. All open probes were fit to monoexponential decays. Closed probes were fit to bi- or triexponential decays. Lifetime fits were performed on regions-of-interest (ROIs) containing $\sim 10^3$ - 10^4 photons in the decay peak. We found that this intensity was optimal to minimize the contribution of detector nonlinearities, which had prevented curve fitting of our MT-FLIM data in its

original report³³. Curve-fit data were used to calculate the intensity and amplitude weighted average fluorescence lifetimes according to the following equations:

$$\langle \tau \rangle_{Int.} = \frac{\sum A_n \tau_n^2}{\sum A_n} \quad (13)$$

$$\langle \tau \rangle_{Amp.} = \frac{\sum A_n \tau_n}{\sum A_n} \quad (14)$$

The amplitude average lifetime was used to calculate the lifetime-based quenching efficiency:

$$E = 100 \times \left(1 - \frac{\langle \tau \rangle_{Amp., Closed}}{\langle \tau \rangle_{Amp., Open}} \right) \quad (15)$$

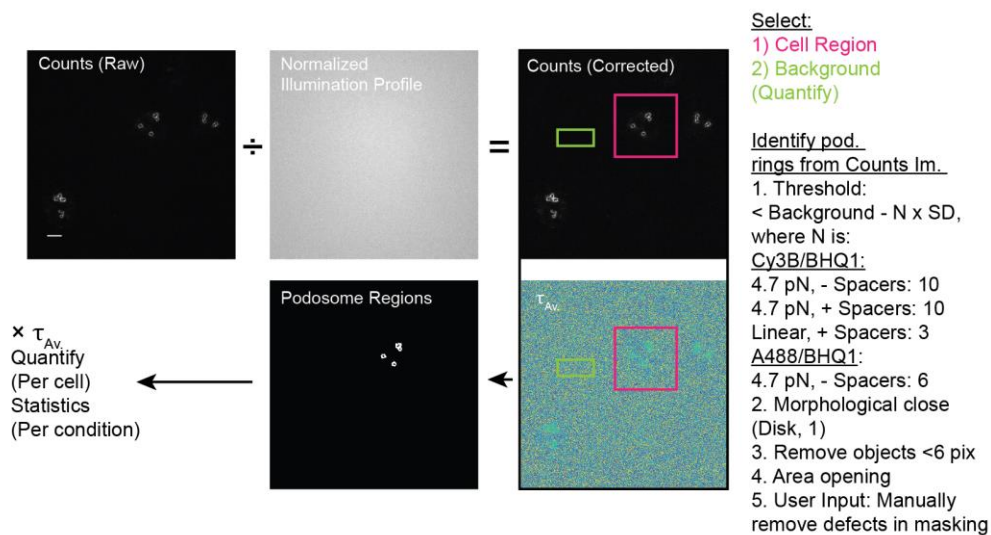
Note that this value poorly agreed with the quenching efficiency calculated from epifluorescence images, which can be expected for a system with mixed static quenching and probe dynamics^{92, 293}. Statistical analysis and plotting were performed in MATLAB. Curve-fit ROIs were also used to generate FAST FLIM average fluorescence lifetime histograms, which represent the center-of-mass fluorescence lifetime weighted by the number of events. To obtain the average fluorescence lifetime from these data, histograms were fit to a curve in MATLAB according to the equation:

$$y = \sum_{n=1}^2 a_n e^{-\left(\frac{x-b_n}{c_n}\right)^2} \quad (16)$$

B1 was used for the Average Fluorescence Lifetime, and C1 was used as a measure of the peak width. Fluorescence intensity data was processed in MATLAB. Aggregates and holes in the SLB were omitted by standard-deviation based thresholding, and the average fluorescence intensity was calculated from the central region of the SLB. The quenching efficiency was calculated by the following equation:

$$E = 100 \times \left(1 - \frac{I, \text{Closed}}{I, \text{Open}} \right) \quad (17)$$

Absorbance data was processed in MATLAB. Curves were background corrected using the baseline absorbance between 720 and 750 nm and were normalized to the absorption at 490 or 559 nm for probes containing A488 or Cy3B as the donor, respectively. Cell image analysis was performed as illustrated in



Figure

A

31,

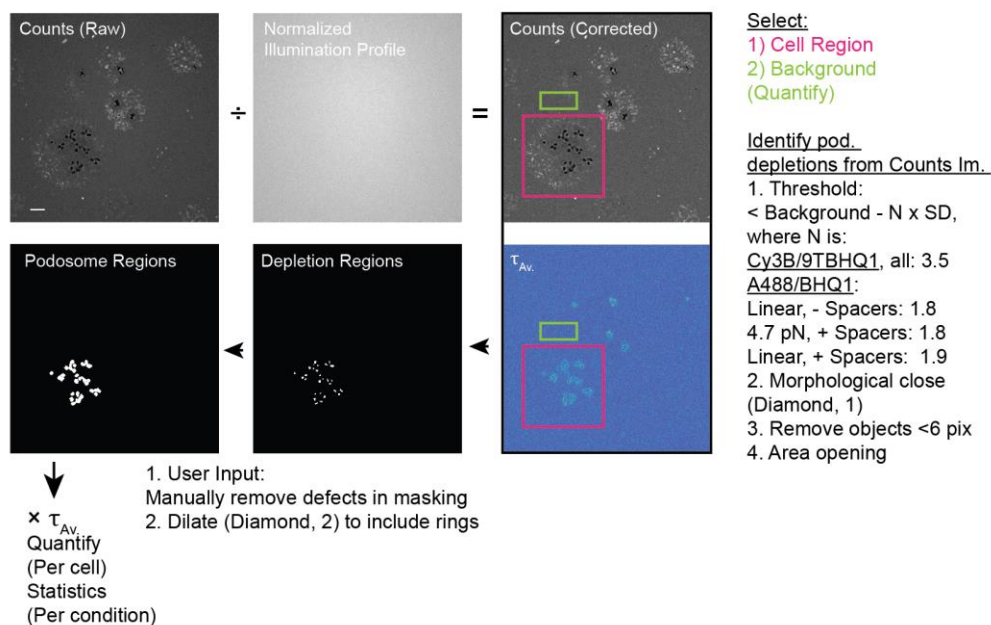


Figure A 32, and Figure A 33. The FAST FLIM average lifetime per pixel was used to calculate statistics on masked regions. At least three technical replicates were collected per experiment and at least three independent experiments were performed. Statistical tests and outlier testing were performed as described in figure captions.

CHAPTER 5. CONCLUSIONS

5.1 Summary of Advances

In this work, we developed, analyzed, and applied a novel approach to map forces on fluid interfaces and to perturb adhesion mechanics on a membrane. In our literature review in Chapter 2⁸⁴, we described the major mechanical parameters influencing SLBs and summarized state-of-the art approaches to adjust their properties. Our review contributed a new perspective through its side-by-side presentation of SLB mechanics and mechanobiology. Chapter 3 expanded the tools available to map and manipulate receptor forces on a membrane and applied these tools to elucidating the mechanism of force balance in podosomes³³. Whereas previous approaches to measure forces on SLBs applied ratiometric imaging^{8, 10}, MT-FLIM contributed a novel and direct approach to mapping receptor clustering and tension using FLIM. FLIM was previously used to report forces across adhesion proteins using genetically-encoded sensors²¹², but our binary DNA hairpin-based FLIM-FRET tension probes were a departure in their direct quantification forces exerted by single receptors and the tension density (reported by percent open probes)³³. Whereas previous studies applied patterning to spatially mutate cell and receptor mechanotransduction^{9, 16, 122, 309, 310}, photocleavable probes and TGTs allowed us to dynamically perturb forces on the SLB. Photocleavable probes offered an approach for experimental perturbation of stable adhesions; TGTs served as responsive materials that ruptured under high cellular forces³³. Through this work³³ we demonstrated that integrin receptors not only apply pN forces on mobile ligands, which was previously unknown^{6, 85, 86}, and we expanded upon the model of the podosome as an independent mechanosensor⁶⁵.

Our work experimentally demonstrates that podosomes apply pN integrin receptor tension to counter nN protrusion forces applied by the podosome core⁷⁶, which was previously suggested through mathematical modeling, analysis of material deformations, and protein stretching^{61, 65, 75, 80} but lacked molecular resolution. The modular design of DNA-based force probes makes them adaptable for imaging forces in a variety of systems. To facilitate future applications of molecular tension probes, Chapter 4 explored the biophysical properties of DNA-based tension probes and evaluated the impact of probe design in a podosome model system. This work will be useful in informing future experiments, which apply DNA mechanotechnology²⁷⁵ to reveal the role of mechanical forces in a variety of receptor-ligand interactions at both cell-cell, cell-SLB, and cell-matrix interfaces.

5.1.1 *Discussion of Biological Limitations*

While our work provides novel approaches to map and manipulate adhesion forces on an SLB, it is notable that these biological systems have some limitations. SLBs represent a reductionist platform to study cellular interactions, and our biological models consider only a subset of the many receptor-ligand interactions at play within these cellular junctions. Specifically, the use of cRGD ligands bias our findings toward the $\beta 3$ class of integrin receptors³¹¹. In addition, while the SLB offers fluidity, the actual membrane is much more biophysically complex, and can undergo dynamic changes in stiffness in response to mechanical forces; these changes are mediated by the actin cytoskeleton³¹². Finally, while fibroblasts provide a facile model of podosome-like adhesions⁶, it is notable that these cells have not been observed to form podosomes *in vivo*. In future work, it will be important to also map receptor forces in podosome-forming immune cells.

5.2 Outstanding Questions and Directions in Podosome Mechanobiology

Although the integration of biophysical probes, materials, and imaging have helped elucidate many features of podosome mechanosensing, there are several outstanding questions that require further investigation. The mapping of integrin receptor clustering and tension on fluid SLBs is interesting from a fundamental biophysics perspective and may provide insight into the mechanoregulation of podosomes formed at cell-cell junctions^{27, 28, 29}. However, many podosomes form on stiff substrates⁶², and it has been shown that cells on stiffer substrates tend to form more podosomes with increased protrusiveness⁷⁶. How is integrin receptor tension regulated in podosome rings on non-fluid materials? Future studies will measure podosome forces on glass and ultimately on hydrogels. Does receptor tension contribute to podosome coupling on materials that are permissive to lateral forces? How are forces regulated in 3D, and how are podosomes and invadopodia similar and different in their mechanisms of force balance? Notably, concurrent with our work which showed podosome retraction when integrin adhesion was photocleaved on a supported lipid bilayer, Ferrari and colleagues demonstrated that invadopodia mechanically bend collagen fibers in 3D³¹³. Although this work suggested a mechanism of actin protrusion rather than tension, the authors similarly found that forces were dependent on actin but not myosin II.

Protein stretching and superresolution imaging suggest that podosome ring tension may vary function of podosome radius⁶⁵. Using newly developed Structured Illumination Microscopy – Molecular Tension Fluorescence Microscopy³¹⁴, it will be interesting to directly test this hypothesis. Super-resolved tension imaging will also provide a new

approach to directly correlate podosome structure and force. These features will be important to distinguish in both podosomes and in related invadopodia.

An additional area of investigation will be in understanding tension oscillations in podosomes. Podosomes on non-fluid substrates have been shown to undergo force and stiffness oscillations^{66, 70, 75, 77, 243}; this remains unexplored on fluid materials and for receptor. Do integrin receptor forces oscillate in podosomes and do podosomes undergo force oscillations on SLBs and at cell-cell junctions? Future studies will apply multiplexed fluorescence imaging and MTFM to answer these questions. A current limitation of MT-FLIM lies in its spatiotemporal resolution. Therefore, to study oscillations on fluid substrates, it will be necessary to apply ratiometric FRET probes or FLIM detectors with faster electronics, which are becoming increasingly commercially available.

Podosome function is facilitated by structure, mechanics, and spatial organization, but current studies still only hint at how these relate. There is a need to develop new biomaterials and imaging probes to study the relationship between podosome mechanics and function, such as diapedesis, migration, bone resorption, in which environmental cues and mechanical cues could influence podosome structure and in turn tune mechanical force generation and the outcome. It is well known that podosomes and invadopodia release MMPs and that integrin adhesion and substrate stiffness modulate degradation in both invadopodia and podosomes^{49, 315, 316}. Therefore, a major open question in the literature focuses on the role of receptor forces both in regulating MMP release and in responding to changes in the local matrix structure and adhesion²⁴⁸.

5.3 Additional Applications of DNA Mechanotechnology at Fluid Interfaces

Beyond podosome mechanobiology, our work has applications at a variety of cell-cell interfaces. We expect these proteins to be integrated with cadherins and ICAM-1. With growing interest in immunotherapy, there are vast applications of immune-modulating biomaterials and cell therapies. Therefore, it will be important to understand the fundamental mechanics of immune cell receptors and their ligands. We anticipate that MT-FLIM and photocleavable probes will be useful in revealing the mechanobiology of receptors such as the TCR and PD1. SLBs were recently applied to studying chimeric antigen receptors³¹⁷, DNA mechanotechnology may be useful in evaluating these engineered receptors. Future platforms will integrate our probes with surface patterning and diffusion tuning to further map, manipulate, and reveal cell forces. In addition, our FRET probes can be applied to measuring forces at cell-cell junctions and in hydrogels. Ratiometric DNA probes were recently used to quantify forces in epithelial sheets²⁷⁹; we hope to use our probes to study the forces between individual immune cells and within platelet clots.

5.4 Novel Applications of DNA-Based Tension Probes and Time-Resolved Fluorescence

Time-resolved fluorescence measurements of DNA-based force probes may allow for quantification of currently inaccessible parameters. Although podosome receptor forces have been shown to oscillate over tens of seconds⁷⁶, it is currently unknown whether receptor forces oscillate or sample on short time scales. Ma, et. al. recently demonstrated that immune cells exert weak and short-lived forces²⁵³, but the temporal limit is unknown. Scanning Fluorescence Correlation Spectroscopy and smFRET measurements may be useful in revealing whether receptors experience transient force fluctuations. In addition, fluorescence lifetime imaging may ultimately help bring molecular mechanobiology *in*

vivo, since FLIM is concentration independent and is compatible with two-photon imaging, which increases tissue penetration³¹⁸.

APPENDIX A. SUPPORTING INFORMATION

A.1 DNA Nanotechnology Reveals that Integrin Receptors Apply pN Forces in Podosomes on Fluid Substrates

A.1.1 Probe Synthesis and Validation

Table A 1 Oligonucleotide Sequences.

Summary of oligonucleotides used in this study. Oligo ID is used to denote sequence in MALDI-TOF IDT = Integrated DNA Technologies, BT = Biosearch Technologies.

Oligo	Purpose	Sequence	Source
1	Hairpin Ligand Strand	5'-/5Hexynyl TTT GCT GGG CTA CGT GGC GCT CTT /3/AmMO-3'	IDT
2	4.7 pN Hairpin	5'-GTG AAA TAC CGC ACA GAT GCG GTA TAA ATG TTT TTT TCA TTT ATA C AAG AGC GCC ACG TAG CCC AGC-3'	IDT
3	19 pN Hairpin	5'-GTG AAA TAC CGC ACA GAT GCG CGC CGC GGG CCG GCG CGC GGT TTT CCG CGC GCC GGC CCG CGG CGA AGA GCG CCA CGT AGC CCA GC-3'	IDT
4	Linear (No Hairpin)	5'-GTG AAA TAC CGC ACA GAT GCG AAG AGC GCC ACG TAG CCC AGC -3'	IDT
5	4.7 pN Hairpin (Photocleavable)	5'-/5PCBio/TT TGT GAA ATA CCG CAC AGA TGC GGT ATA AAT GTT TTT TTC ATT TAT ACA AGA GCG CCA CGT AGC CCA GC-3'	IDT
6	4.7 Complementary	5'-GTA TAA ATG AAA AAA ACA TTT ATA C-3'	IDT
7	19pN Scramble	5'-GTG AAA TAC CGC ACA GAT GCG TTT ATC GTC AAT ATA TAC GAT ATT TTT TAG AAT CTA GAT GTT AAC TTT TTA AGA GCG CCA CGT AGC CCA GC-3'	IDT
8	Scramble Complementary	5'-AAG TTA ACA TCT AGA TTC TAA AAA ATA TCG TAT ATA TTG ACG AT-3'	IDT
9	MT-FLIM Anchor/Quencher Strand	5'-CGC ATC TG(I-TBHQ1) GCG GTA TTT CAC TTT/3Bio/-3'	BT
10	Unlabeled Bottom Strand	5'-CGC ATC TGT GCG GTA TTT CAC TTT-3'	IDT
11	MTFM Anchor/Quencher Strand	5'-/5BHQ1/CGC ATC TGT GCG GTA TTT CAC TTT/3Bio/-3'	BT
12	MTFM Quencher Strand	5'-/5BHQ1/CGC ATC TGT GCG GTA TTT CAC TTT-3'	BT
13	Alkyne-Amine-Biotin	5'-/Hexynyl/CG CAT CTG TGC GGT ATT TCA C/iAmMC6T/TTT/3Bio/-3'	IDT
14	TGT Ligand Strand*	5'-/5Hexynyl/GTG AAA TAG CGC ACA GAT GCG/3AmMo/-3'	IDT

15	12 pN TGT Anchor Strand	5'-/CGC ATC TGT GCG GTA TTT CAC /iAmMC6T/ TT T /3Bio/-3'	IDT
16	56 pN TGT Anchor Strand	5'-/5Biosg/TTT/AmMC6T/CGC ATC TGT GCG GTA TTT CAC-3'	IDT
17	4.7 (TTT) pN Hairpin**	5'-GTG AAA TAC CGC ACA GAT GCG TTT GTA TAA ATG TTT TTT TCA TTT ATA C TTT AAG AGC GCC ACG TAG CCC AGC-3'	IDT
18	4.7 (TTT) Complementary**	5'-AAA GTA TAA ATG AAA AAA ACA TTT ATA C AAA-3'	IDT

* Note: TGT sequences in this work contain a single base pair mismatch (bolded) in the TGT Ligand strand (Oligo 14). Sequences used here are as written, however, for future studies, this mismatch should be corrected: **G**→**C**. Despite this mismatch, we proceeded with the interpretation of our data. Although to our knowledge, there is no model describing the impact of a mismatch on the tension tolerance, T_{tol} , single molecule force spectroscopy suggests that only the termini of the duplex are critical to defining T_{tol} . According to the deGennes model³¹⁹, T_{tol} is sequence independent and follows the equation:

$$T_{tol} = 2f_c \left[\chi^{-1} \tanh\left(\chi \frac{L}{2}\right) + 1 \right] \quad (18)$$

$2f_c$ is the tension tolerance per bond, L is the sequence length (bp), and χ^{-1} is the number of force-bearing base-pairs at the end of a duplex. Measuring the T_{tol} of DNA duplexes using magnetic tweezers revealed that χ^{-1} equals 6.8 base-pairs³²⁰. Therefore, although a mismatch at bp 9 will slightly reduce the duplex's thermal stability, it will not significantly impact T_{tol} .

**Note: These oligos were used only in absorbance spectroscopy of static quenched probes, in accordance with Zhang, et. al³⁰. All other experiments using 4.7 pN tension probes used Oligo 2.

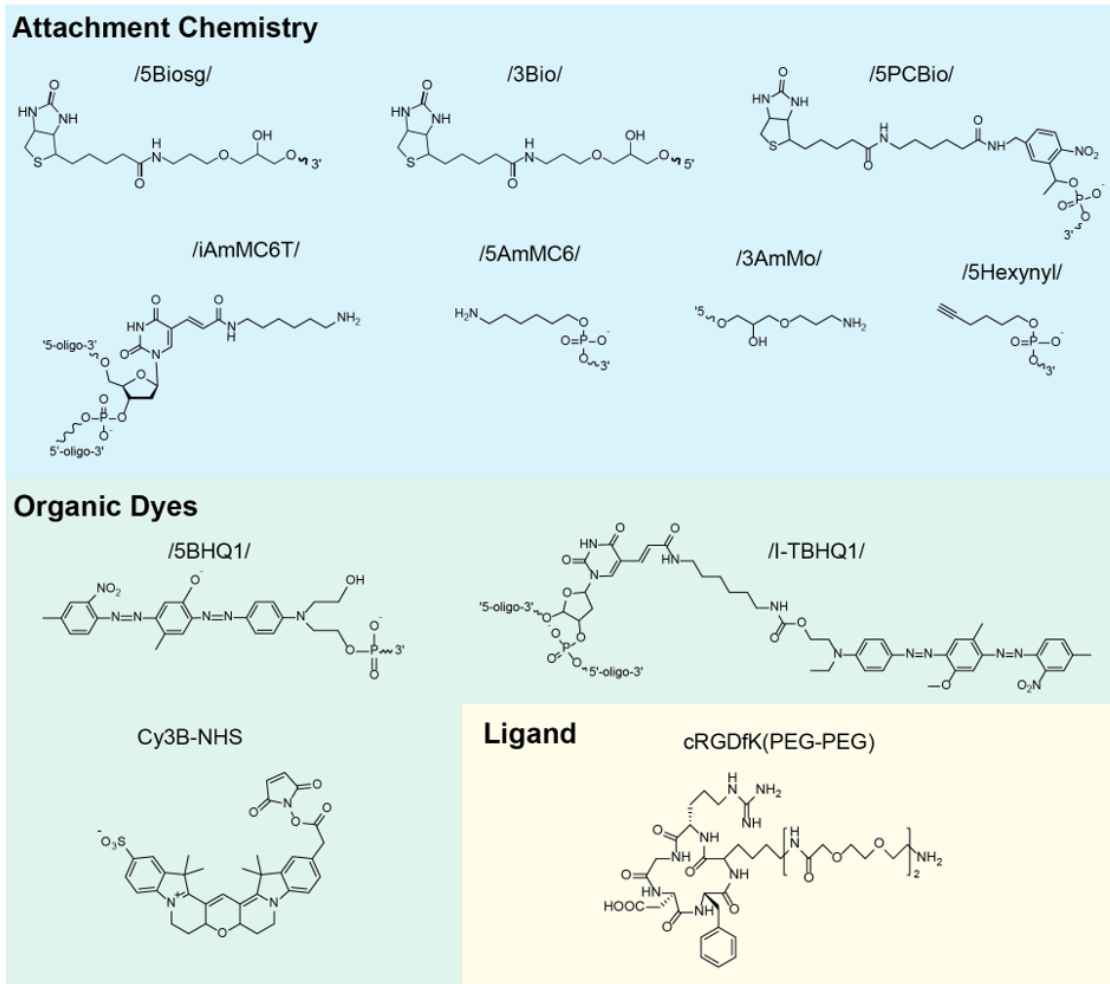


Figure A 1 Chemical structures in oligonucleotide probes.

Chemical structures for relevant DNA modifications. Cy3B and cRGDfK(Peg-PEG) were conjugated as described.

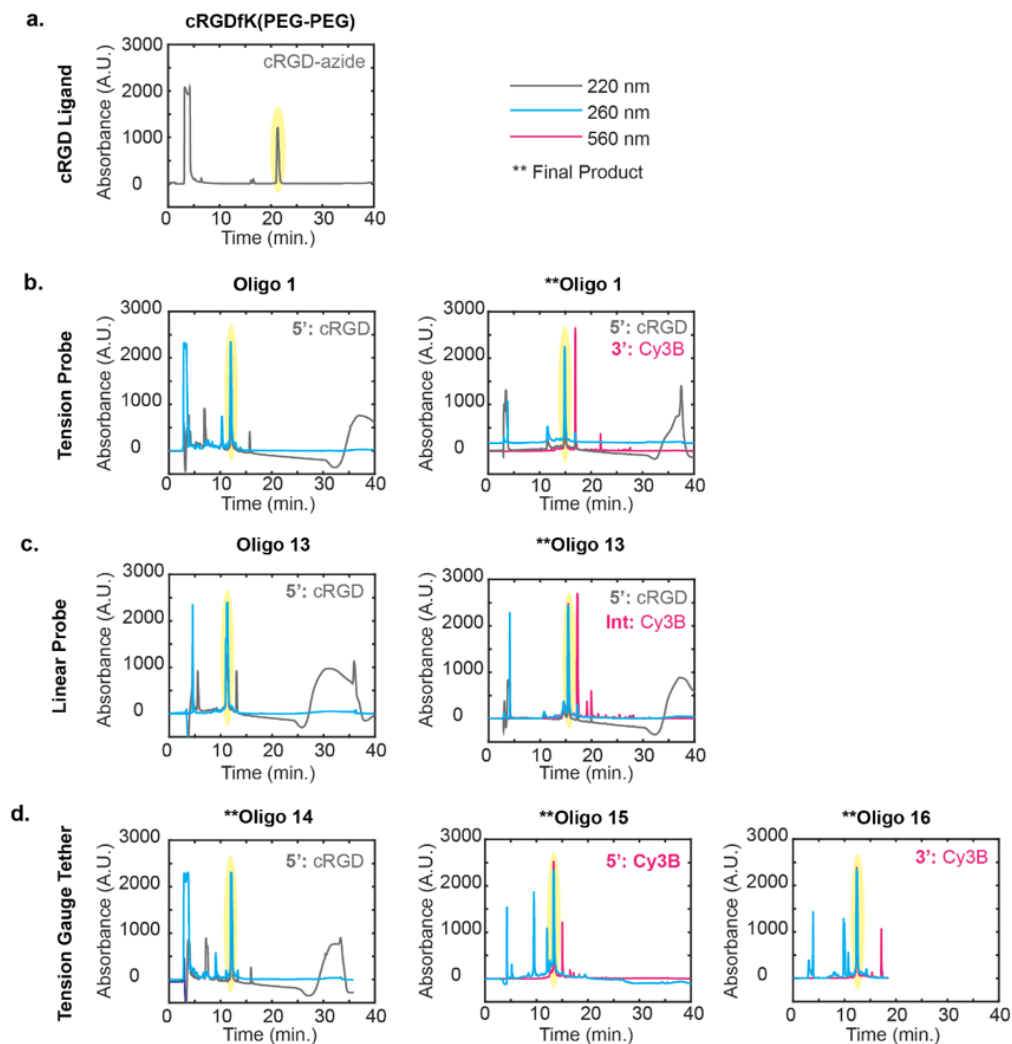


Figure A 2 HPLC chromatograms of modified oligonucleotides.

(a-d) Chromatograms of cRGD and DNA probes. Oligos sequences are as shown in Table A 1. Grey, blue, and pink lines are for cRGD, DNA, and Cy3B, respectively. Product peaks are highlighted in yellow, and HPLC spectra for final products are marked **. Final products were validated by MALDI-TOF. The locations of the cRGD and Cy3B are indicated as 5', 3', or Int for internal modifications.

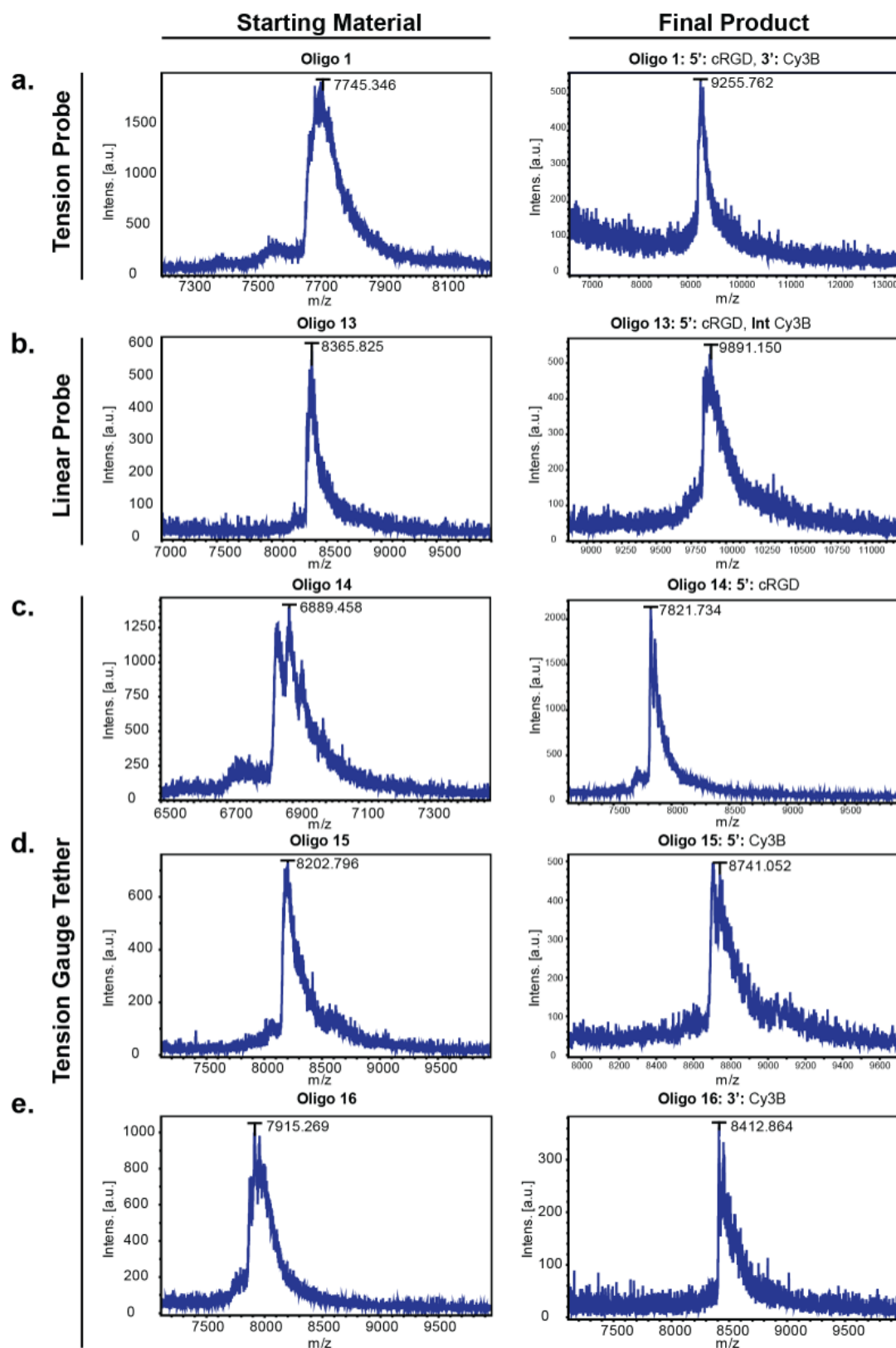


Figure A 3 MALDI-TOF spectra of oligonucleotides
(a-e) Mass spectra of starting materials and final probe products

Table A 2 Summary of MALDI-TOF Results

MALDI	Sequence	Starting or Product	Calculated MW	Difference (%)
a.	1	Starting	7729.0	0.211
a.	1	Product	9361.96	-1.134
b.	13	Starting	8356.7	0.001
b.	13	Product	9989.66	-0.986
c.	14	Starting	6875.5	0.203
c.	14	Product	7852.6	-0.392
d.	15	Starting	7903.3	0.203
d.	15	Product	8559.21	-0.392

A.1.2 Podosome Model Characterization

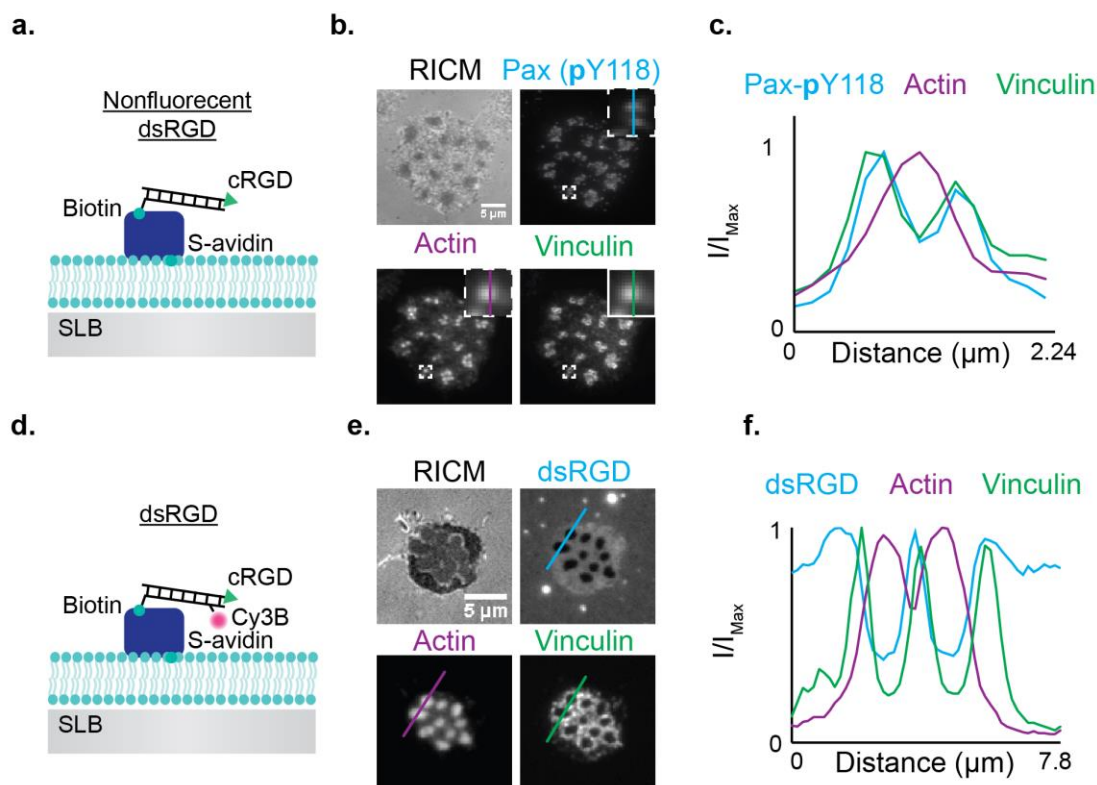


Figure A 4 NIH 3T3 fibroblasts form podosomes on fluid RGD-oligonucleotides.

(a) Schematic of unlabeled cRGD-functionalized DNA probes tethered to an SLB. (b) Immunostaining of podosome-forming NIH-3T3 cell stained with Phospho-Paxillin Tyr 118 Polyclonal Antibody, Phalloidin-iFluor 488, and Vinculin Antibody SF647. (N=85 cells, 3 experiments.) (c) Normalized linescan analysis of podosome in **b**. Blue, green, and purple lines represent pY118, vinculin, and actin, respectively. (d) Schematic of fluorescently-tagged DNA probes presenting cRGD ligands on and SLB. (e) Immunostaining of podosome-forming NIH 3T3 cells (n=97, 4 experiments). Cells were stained with Phalloidin-iFluor 488 and Vinculin Antibody SF 647. (f) Normalized linescan analysis of podosomes in **e**. Blue, green, and purple lines represent dsRGD, vinculin, and actin, respectively.

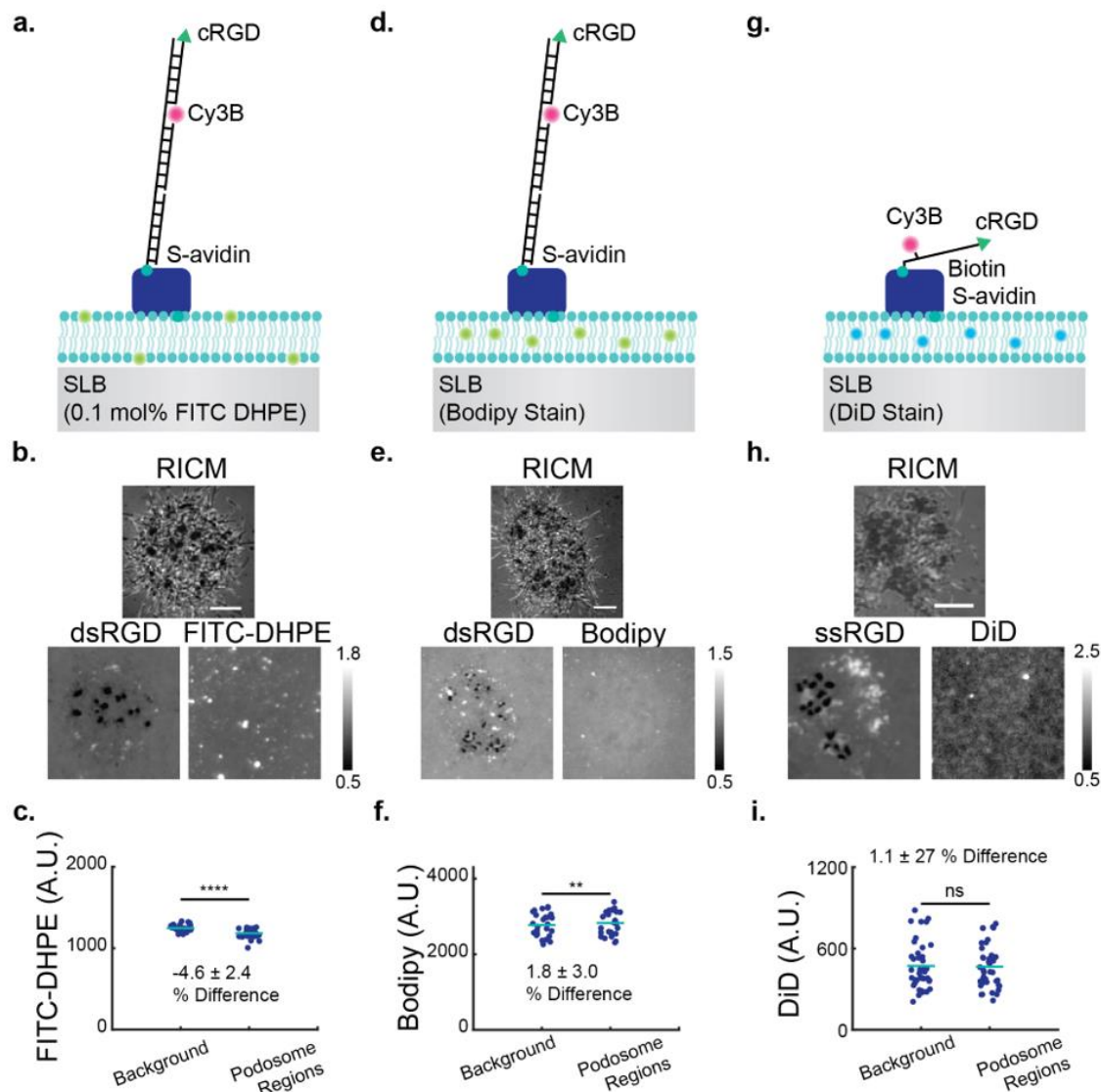


Figure A 5 Podosome protrusion does not disrupt the SLB.

(a,d,g) Schematic of oligonucleotide probes and membrane labels used in b and c, e and f, and h and i, respectively. (b,e,h) Representative epifluorescence images of podosomal depletion as indicated by Cy3B-DNA depletion. The SLB beneath was labeled with FITC-labeled lipids or stained with membrane intercalating dyes, as indicated. Fluorescence images are displayed normalized to the SLB background. (c,f,i) Average membrane fluorescence beneath podosome depletion regions versus the SLB background. Statistics were performed with a two-tailed Wilcoxon matched-pairs signed rank test (c,f) or a two-tailed, paired Students T-Test (i). Teal bars represent the median (c,f) and the mean (i). $P > 0.05$, ** $P < 0.01$, **** $P < 0.0001$. Statistics were calculated on at least 26 cells, 3 experiments. Outliers were excluded (median \pm 3 scaled median absolute deviations).

A.1.3 Molecular Tension – Fluorescence Lifetime Imaging Microscopy

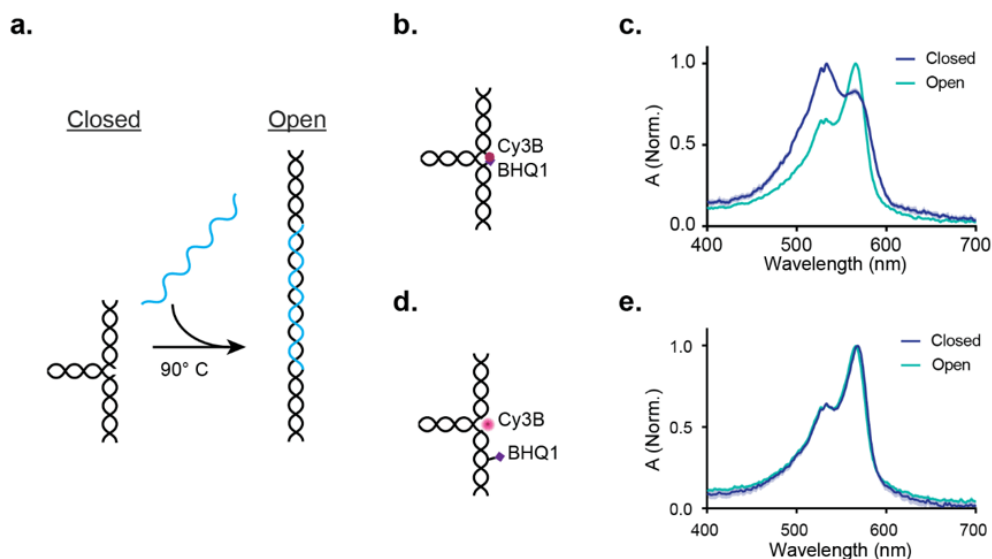


Figure A 6 Absorption spectra of MTFM and MT-FLIM probes.

(a) Tension probes were chemically unfolded by annealing with a strand complimentary to the stem-loop sequence (blue). (b,d) Schematic of conventional and MT-FLIM probes, respectively, in solution. (c,e) Absorbance spectra of closed (dark blue lines) and open (teal lines) conventional and MT-FLIM probes, respectively. Conventional MTFM probes exhibited a shift indicative of static quenching. Data represent the mean \pm s.e.m. N = 3 experiments.

Table A 3 Summary of TCSPC Settings

Setting	Parameter
TCSPC Resolution	25.0 ps
TCSPC Mode	T3
Sync CFD Level	-150 mV
Sync Zero Cross	-10 mV
Sync Divider	8
Detector CFD Level	-45 mV
Detector Zero Cross	-10 mV
Detector Offset	530 ps

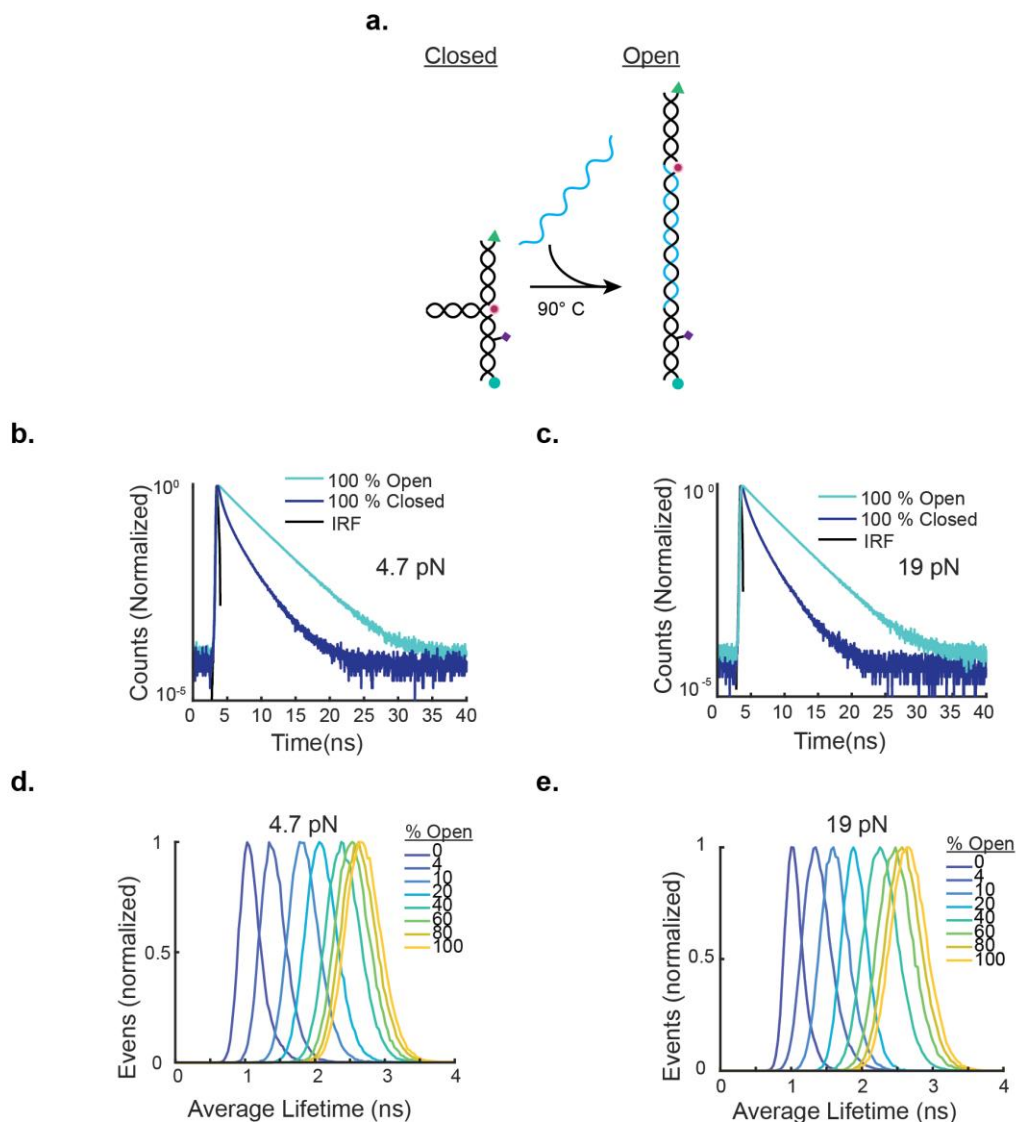


Figure A 7 MT-FLIM probe calibration.

(a) To open probes, hairpins were thermally annealed to a sequence complimentary to the stem-loop. (b,c) Representative fluorescence decay histograms for opened and closed 4.7 and 19 pN tension probes, respectively. Closed probes exhibit a multiexponential decay (3 experiments). The instrument response function (IRF, calculated in software) is shown in black. Photon counts are displayed on a logarithmic scale. (d,e) Representative average fluorescence lifetime histograms for SLBs with increasing percent open 4.7 and 19 pN tension probes, respectively. (2-3 experiments per condition).

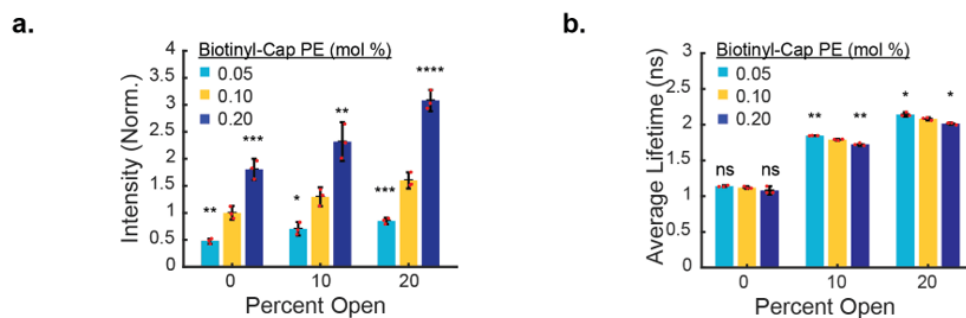


Figure A 8 MT-FLIM probe density slightly reduces fluorescence lifetime.

(a) Normalized fluorescence intensity of SLBs containing 0-20% open probes on SLBs with 0.05 – 0.2 mol% Biotinyl-Cap PE. **(b)** Average fluorescence lifetime on SLBs containing 0-20 % open probes on SLBs with 0.05-0.2 mol% Biotinyl-Cap PE. Light blue, yellow, and dark blue bars represent 0.05, 0.1, and 0.2 mol% Biotinyl-Cap PE, respectively. Red circles represent the means of individual experiments. Data points represent the mean of individual experiments. Bars represent the mean \pm s.e.m (error bars), 3 experiments. Statistics were performed with an ANOVA followed by a multicomparison test comparing each data point to the corresponding 0.1 mol% Biotinyl-Cap PE data (yellow bars). ns $P > 0.05$, * $P < 0.05$, ** $P < 0.01$, **** $P < 0.0001$.

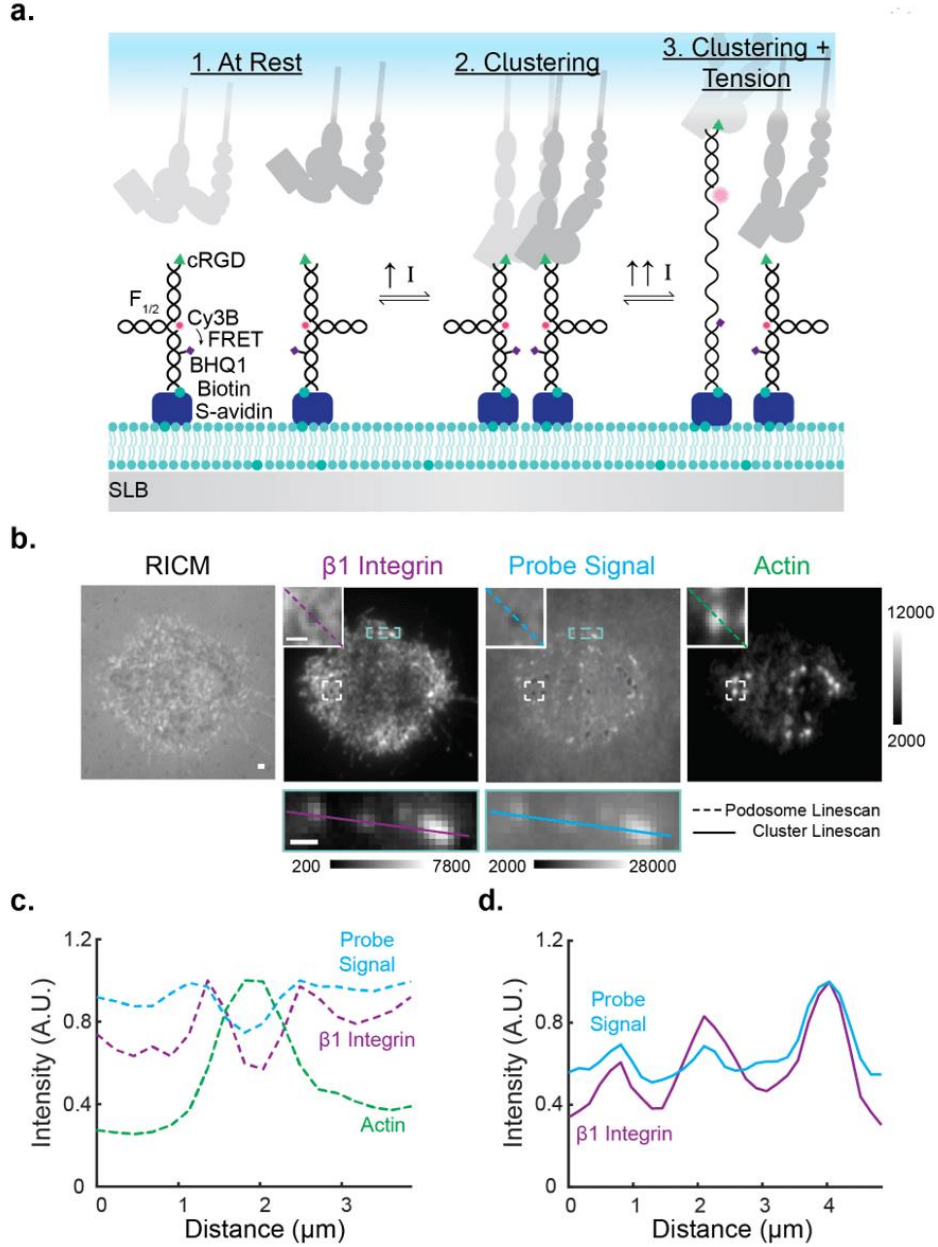


Figure A 9 Podosome rings and integrin clusters contain $\beta 1$ integrin.

(a) MT-FLIM probes were used with intensity-based imaging, such that both clustering and opening events could cause an increase in fluorescence signal. **(b)** Representative images of podosome-forming cells show colocalization of $\beta 1$ integrins with RGD clusters (solid lines) and podosome rings (dashed lines) in the probe channel. $\beta 1$ integrins and actin were detected by Anti-Integrin $\beta 1$ Antibody, clone MB1.2 followed by Alexa Fluor 647 goat anti-mouse IgG_{2b} ($\gamma 2b$) and Alexa 488- Phalloidin, respectively. **(c,d)** Linescan analysis of podosomes **(c)** and clusters **(d)** shows good colocalization of $\beta 1$ integrin and probe signal. Linescan locations are indicated in **b**. Green, blue, and purple lines represent actin, probe signal, and $\beta 1$ integrin, respectively. $N = 16$ cells, 2 experiments. Scale Bars, 5 μm .

A.1.2.1 Determination and interpretation of percentage of open probes and local probe density

The intensity of tension probe signal, I , measured as the number of photon counts per pixel, is a function of the local probe density, ρ , the fraction of open and closed probes, O and C , their per-probe photon count contributions, m and n , and the dark counts, D .

$$I(O, C, \rho) = \rho(m(O) + n(C)) + D \quad (19)$$

Because probe opening is binary (probes are either open or closed), O and C are related such that:

$$O + C = 1 \quad (20)$$

Assuming that in the SLB background, all probes are closed and the relative probe density is 1, we find that:

$$QE = \frac{m - n}{m} \quad (21)$$

$$m = \frac{n}{1 - QE} \quad (22)$$

Rearranging (2) and substituting with (3)-(6), we find that probe density,

$$\rho = \frac{I(O, C, \rho) - D}{(\frac{I_0 - D}{1 - QE}(O) + (I_0 - D)(1 - O))} \quad (23)$$

We obtained QE from the slope of the linear curve-fit epifluorescence images of titrated open and closed probes (Figure 2c). To determine D , we calculated the average number of photons per pixel on the second detector blocked with a 690 nm band-pass filter during calibration image acquisition. Since the average number of photons was less than 1 per pixel, we determined dark counts to be negligible. To determine O , the fraction of open probes per pixel, we used a 5%-open-interval look-up-table (LUT) generated from the

empirical calibration curve of percent open probes versus average fluorescence lifetime per pixel, τ , (Figure 18b, Figure A 7d,e), which fit to the biexponential equation:

$$\tau = ae^{b\phi} - ce^{d\phi} \quad (24)$$

Here τ is the mean photon arrival time determined by the Fast FLIM algorithm in SymPhoTime 64. This metric provides the distance between the rise of the IRF and the center-of-mass of photon arrivals in a decay and does not require curve-fitting. This method has some disadvantages such as uncertainty due to uncertainty of time-zero and contribution of background photons; therefore, it is not typically the most quantitative metric to characterize a system and is typically used to give an initial real-time FLIM image. However, it has still proven useful as an estimate of the fluorescence lifetime in a variety of FLIM applications^{321, 322, 323}. For our purposes, we found it to be a robust measure of the fluorescence lifetime of our tension-probe surfaces, in which empirically measured lifetimes were much more important than the physical processes giving rise to these exact lifetimes. When used with our calibration curve to convert the average fluorescence lifetime per pixel to the percentage of open probes per pixel, the precision is related to the number of photons in the calibration curve image, which we held at constant of approximately 10^5 photons in the peak of the fluorescence lifetime decay curve, as well as with the number of photon counts in the pixel of interest. The major sources of uncertainty in this metric comes from the width of the histogram used to generate the percentage of open probes look-up-table and uncertainty due to the computed IRF. Because we were concerned that dwell time could cause some probe melting and affect the fluorescence lifetime, we performed these measurements for all imaging conditions (0.14 and 0.08), but this effect was negligible. The constants $a - d$ were as follows:

Table A 4 Percent Open Curve Fit Parameter

Probe (pN)	a	b	c	d	r ²
4.7	2.306	0.001	-1.166	-0.072	0.9996
19	2.295	0.002	-1.21	-0.056	0.9992

While we found the average fluorescence lifetime of probes on our SLBs to be consistent, it was important to minimize the free dye in solution, which could shift the lifetimes. We recommend that anyone using this method generate a calibration curve on their own instrument prior to data quantification.

A.1.2.2 Discussion of MT-FLIM Photon Statistics

A challenge in MT-FLIM interpretation was determining the cutoff between signal and noise. In our raw average fluorescence lifetime images, we observed an increase in fluorescence lifetime even in regions inside the podosome core depletion zone, where integrin receptors are excluded⁶¹. In very static podosomes in MT-FLIM (60x objective, 1 min acquisition) and on conventional tension probes (100x objective, 500 ms exposure time) (Figure A 15), it was apparent that signal was contributed primarily by the adhesion ring. We attributed this effect to three factors: (1) Podosomes are micron-sized structures and are subject to the diffraction limit. Thus, high fluorescence lifetime photons from the ring could be collected in depletion regions. (2) Podosomes are dynamic structures. Any movement of the ring could cause slight blurring of signal. (3) Depletion regions have low signal-to-noise ratio (SNR) and are subject to influence by noise (detector shot noise and otherwise). We hypothesize that these three features together give rise to the appearance of tension in the podosome core. Considering a primarily depleted (dark) podosome core, some photon contribution from the ring will increase the photon count, but it will still be

much darker than the surrounding regions. However, assuming that most of these photons have a long fluorescence lifetime, then it will appear that the core region has a high percentage of open probes. This effect would be magnified by any movement or changes of the podosome ring or core structure during imaging.

To determine which pixels were the most reliable, we performed an extensive analysis of MT-FLIM photon statistics. It is desirable to maximize photon counts, because the SNR equals \sqrt{n} , where n is the number of photons. Since each photon in a FLIM image is time-tagged, FLIM images can be subdivided into different frame widths. Images in Figure 17 were collected for 3 min, but we empirically selected an acquisition time of 60 s for analysis as a compromise between podosome dynamics and the need for a maximal photon count. To demonstrate this effect, we have subdivided a podosome image acquisition into time-bins (Figure A 10a,b). To determine the tolerable minimum SNR, or photon count, we analyzed τ versus photons counts per pixel. From these data, we observed that some low photon pixels contributed long fluorescence lifetimes that were inconsistent with Cy3B's fluorescence lifetime (data not shown). Using our calibration curves, we defined the maximum reasonable fluorescence lifetime per pixel to be 2.97 ± 0.04 ns (mean \pm s.e.m., 6 surfaces), which corresponds to one standard deviation above the average fluorescence lifetime of an SLB containing 100% open probes. Note that here the standard deviation describes the width of the histogram data rather than the variation of mean lifetime across experiments. 19 and 4.7 pN surfaces did not have a statistically significantly different fluorescence lifetime for open probes, so this 2.97 ± 0.04 ns lifetime applied to both data sets. To determine a photon count cutoff, we identified regions associated with the SLB background, clusters, and podosomes and plotted histograms of fluorescence

lifetime and photon counts per pixel for each of our hairpins (Figure A 10c,d). Since the average number of photons per pixel with $\tau > 2.97$ in podosomes was 23 ± 12 photons (mean \pm s.d.), we set the minimum SNR tolerance to 1:5. Therefore, in all MT-FLIM analysis, only pixels with $\tau < 2.97$ ns and photon counts > 25 were considered.

Table A 5 Photons per Pixel with $\tau < 2.97$ ns

	Linear	4.7 pN	19 pN
SLB	n/a	73 ± 14	n/a
Background			
Clusters	n/a	n/a	n/a
Podosomes	16 ± 6	30 ± 18	22 ± 11

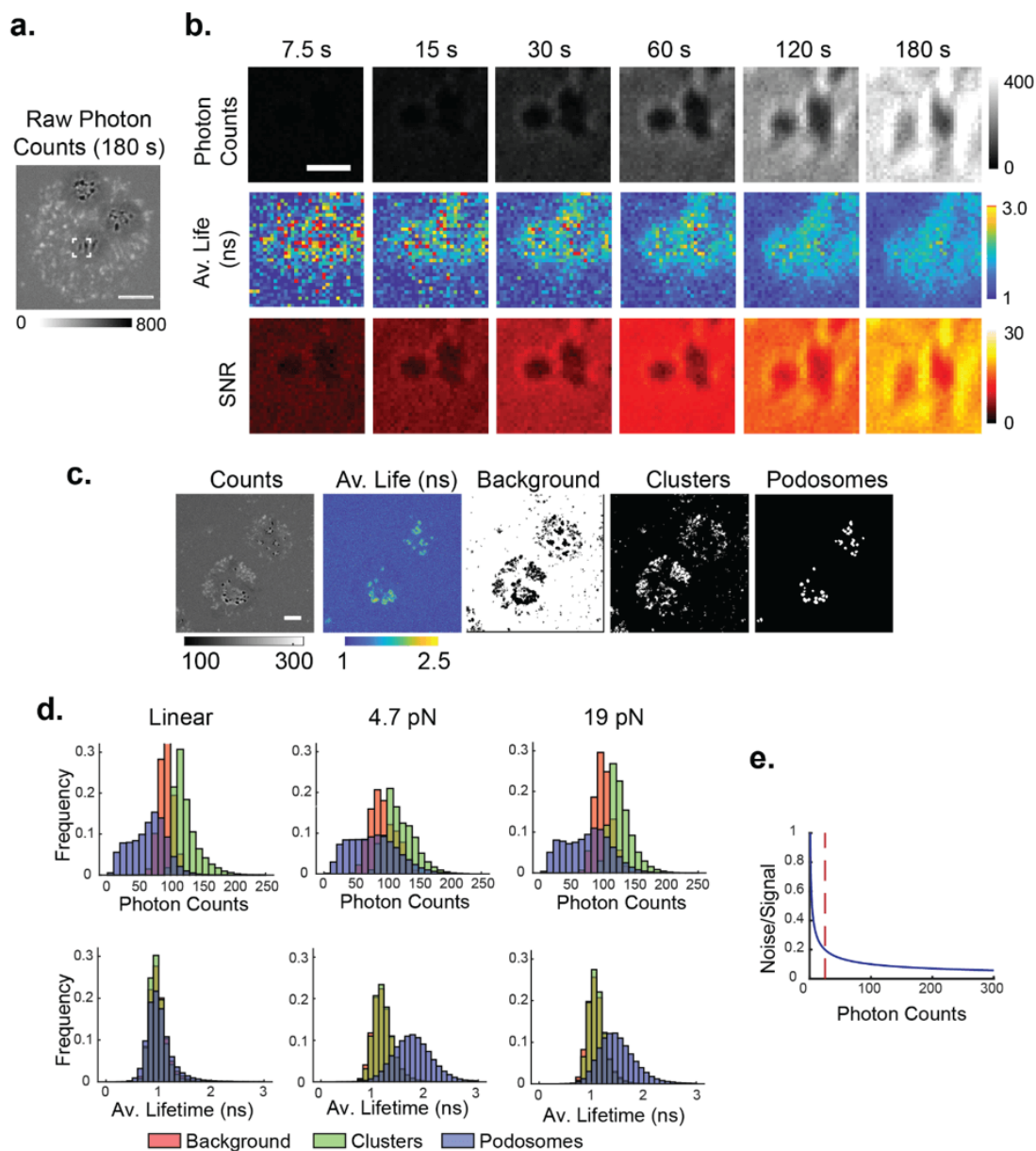


Figure A 10 Analysis of MT-FLIM photon statistics.

(a) Representative 3-minute photon counts image of podosomes on 4.7 MT-FLIM probes. Scale bar, 5 μm . (b) Podosome zoom-in of white box in a subdivided into 7.5 - 180 s bins. For MT-FLIM analysis, 60 s image bins were used to maximize SNR while minimizing temporal blurring. Scale bar, 1 μm . (c) Representative 4.7 pN MT-FLIM image and maps of the background, clusters, and podosomes. Features were identified by intensity-based-thresholding. Scale bar, 5 μm . (d) Histogram analysis of the average photon counts and fluorescence lifetime per pixel on MT-FLIM probes. Red, green, and blue histograms represent background, cluster, and podosome photons, respectively. (N = 48 Images, 3 experiments). (e) Plot showing the noise-to-signal ratio versus photon counts. The red dashed line represents the 25-photon cutoff.

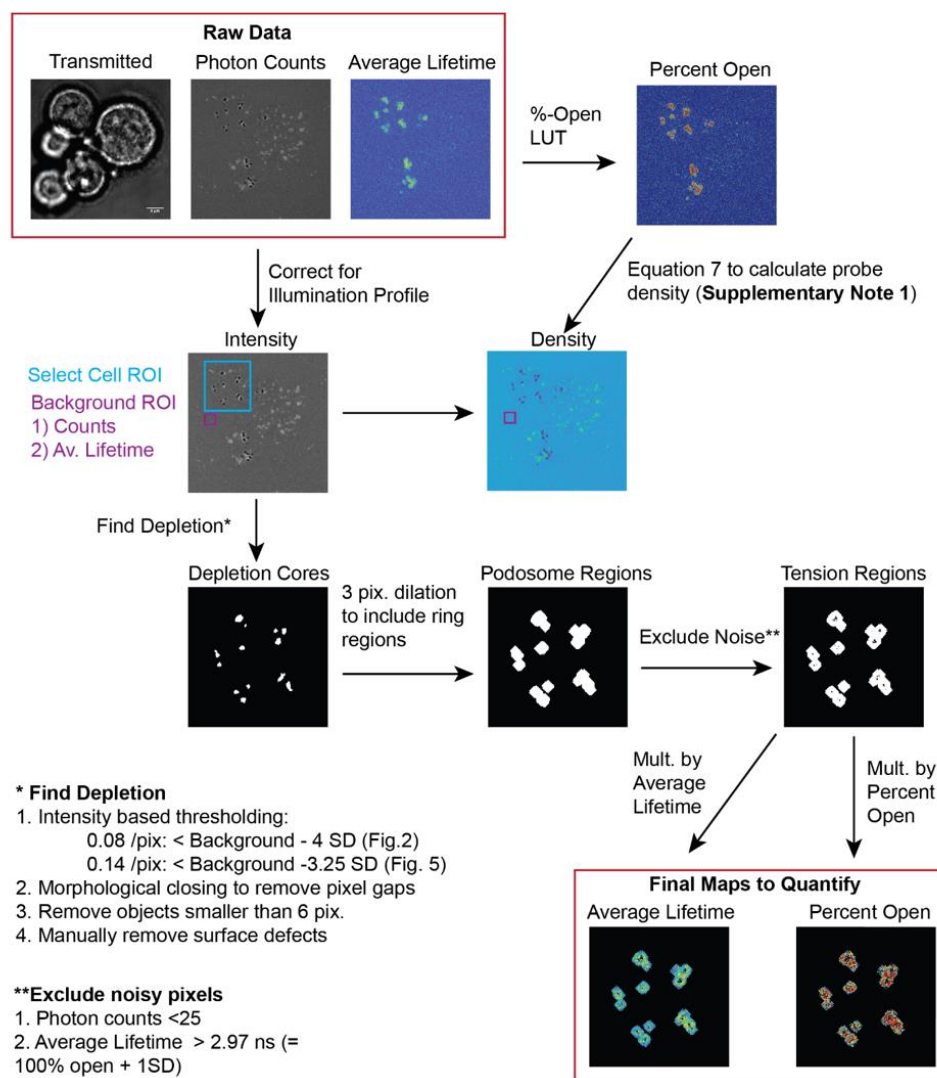


Figure A 11 MT-FLIM Analysis Flowchart.

MT-FLIM images were read into MatLab using the BioFormats plugin. To account for the uneven confocal illumination profile, the raw photon counts data was corrected using an average illumination profile generated from SLBs lacking cells. For each cell, we selected an ROI containing the cell and a local background ROI, which was used to define the background photon counts and fluorescence lifetime. To identify podosomes, we first identified podosome cores as described in steps 1-4, above (*). Surface defects, such as holes in the SLB, were manually removed. To include the podosome ring region, we performed a 3-pixel dilation on podosome cores. Noisy pixels as determined in A.2.1.2. were excluded in the final masks (**). To determine the percentage of open probes and the relative probe density, we applied our empirical look-up table and Equation 8, which are described in detail and derived in A.2.1.1. Percent open and average fluorescence lifetime maps were multiplied by the final podosome mask, and statistics were performed on a per cell-level, unless otherwise stated. Scale bar, 5 μm .

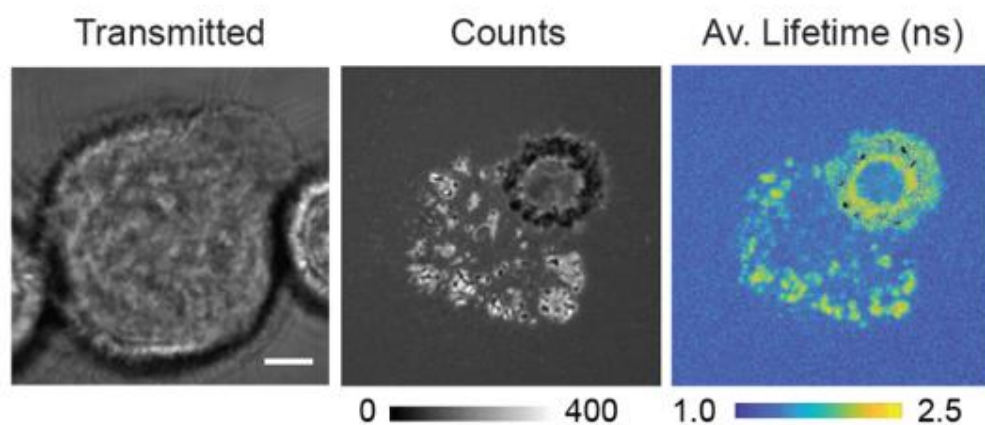


Figure A 12 Invadosomes exert pN tension.

Myf cells were seeded on SLBs presenting 4.7 pN (shown here) or 19 pN tension probes and imaged following ~1 hour cells spreading. Image depicts a full three-minute acquisition. Scale Bar, 5 μ m. (N = 61 cells, 3 experiments).

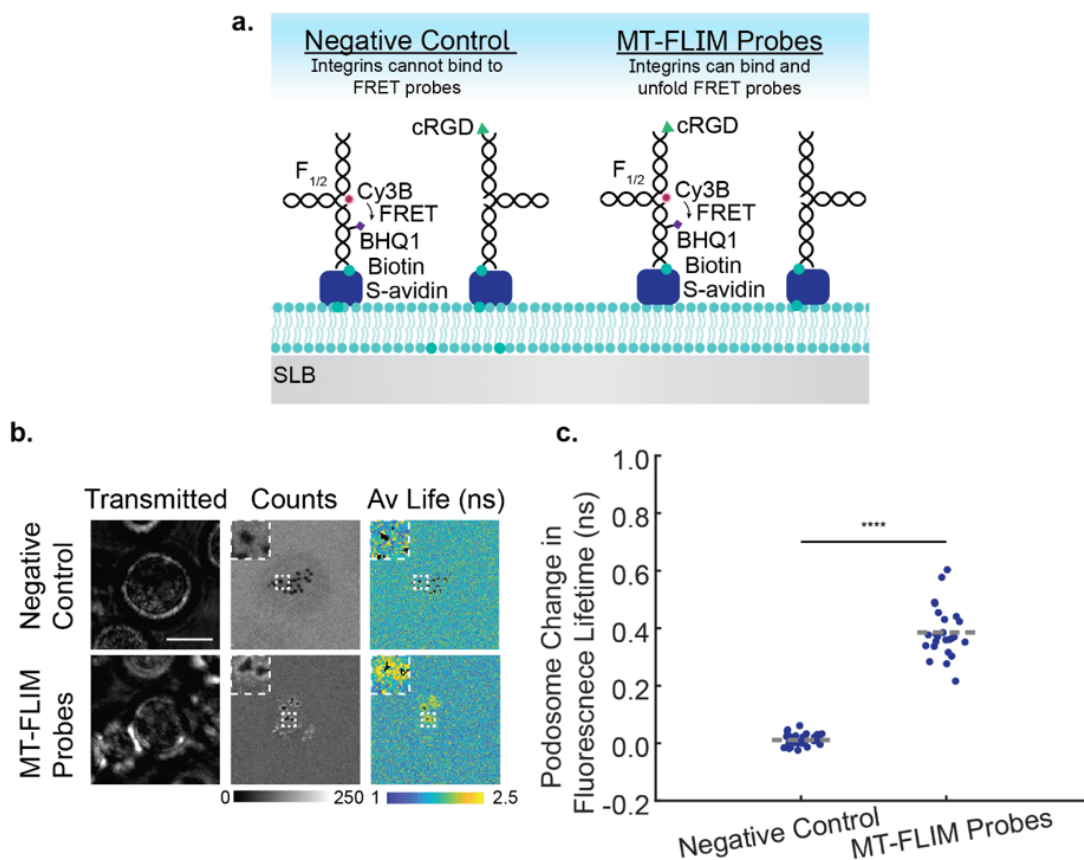


Figure A 13 Tension probes unfold specifically under integrin-mediated forces.

(a) DNA probes were co-presented on an SLB such that the ligand and FRET pair were either separated or presented on the same probe. To maintain ligand density, SLBs contained 0.2% biotinyl cap PE. (b) Representative images of podosomes on co-presented DNA probes. Note that the fluorescence lifetime was higher than in other experiments, likely due to probe co-presentation. Scale bar, 5 μ m. (c) Average change in fluorescence lifetime in podosome-regions per cell. Dashed grey lines represent the mean. Statistics were performed with a two-tailed paired Students T-Test. Each group contained at least 25 cells, 3 experiments. ****P<0.0001.

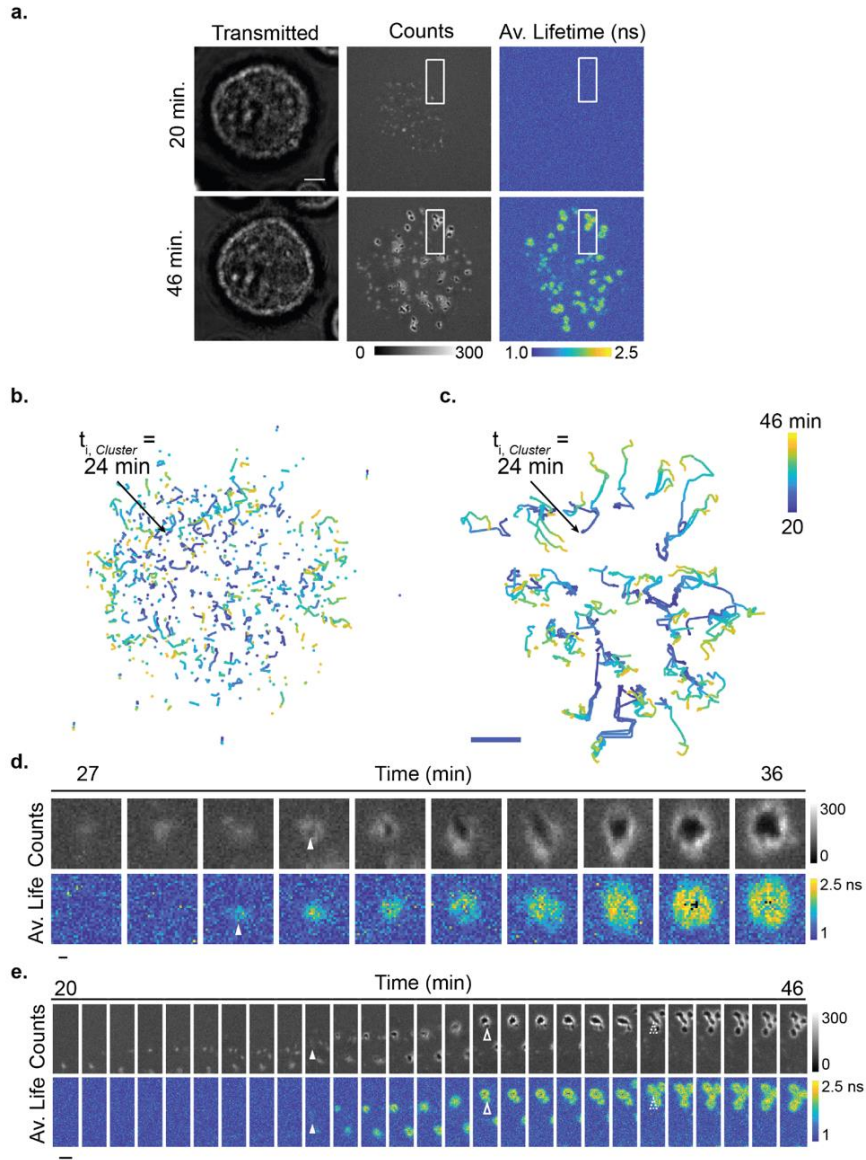


Figure A 14 MT-FLIM dynamics of podosome maturation.

(a) MT-FLIM image of the NIH 3T3 cell from Figure 17g at 20 and 46 minutes (N=6 cells, 3 experiments). Scale bar, 5 μm . (b,c) Cluster and podosome trajectories from 20 to 46 min. Filled circles represent the emergence of a new cluster (b) or podosome/ podosome-preceding cluster (c). Scale bar, 5 μm (d) Representative kymograph of podosome formation with each frame centered on the centroid of the podosome or cluster noted with the arrow in b. White triangles indicate the emergence of tension and depletion. Select frames are reproduced in Figure 17g. Scale bar, 0.3 μm . (e) Kymograph of the white boxed region in a showing the emergence and maturation of podosomes from clusters (filled white arrows). Podosomes spread outwards over several minutes, and new podosomes emerge by splitting (unfilled white arrows) and *de-novo* formation (dotted white arrows). Scale bar, 0.2 μm .

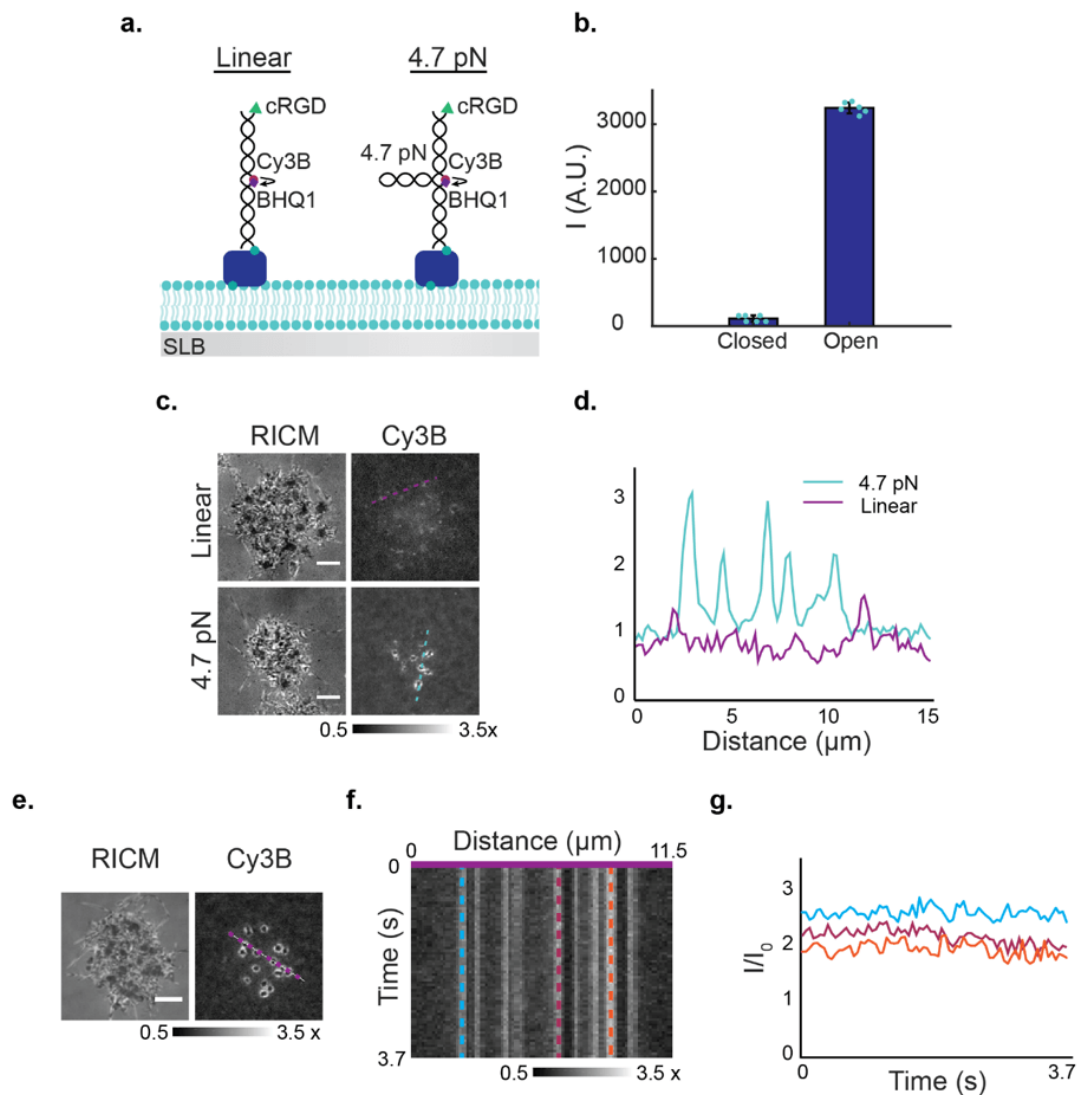


Figure A 15 Analysis of clustering and tension dynamics on static quenched tension probes.

(a) Schematic of conventional MTFM probes with a linear scaffold and 4.7 pN hairpin. (b) Determination of MTFM probe quenching efficiency on an SLB. Teal circles represent the mean intensity from 6 individual measurements. Bars represent the mean \pm s.d. (error bars), 2 experiments. (c,d) Representative images and linescan analysis of NIH 3T3 cells forming podosomes one hour after addition to MTFM probes on an SLB. To minimize the contribution of autofluorescence, Cy3B images are normalized to the non-podosome signal underneath the cell. (N = 42 cells, 3 experiments) (e) Representative first frame of a 3.7 s MTFM epifluorescence timelapse with 73 frames to mimic an MFM experiment. (f) Kymograph of linescan in (e). (g) Linescan analysis of 3 representative podosomes in f show only small noise-dominated fluctuations in MTFM ring signal (N = 35 cells, 3 experiments). All scale bars, 5 μm .

A.1.4 Molecular Force Microscopy

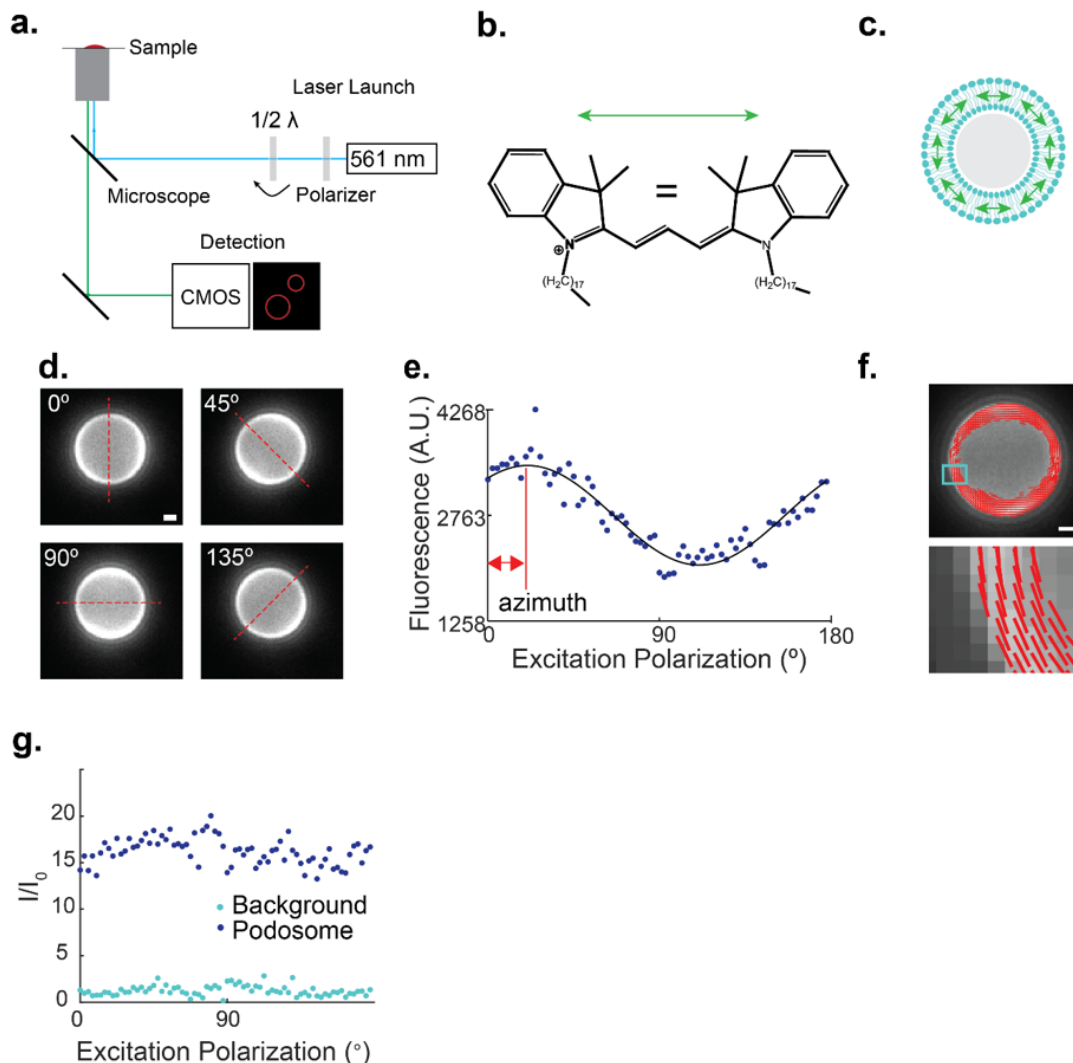


Figure A 16 MFM set-up and excitation-resolved polarization validation.

(a) Optical configuration for MFM. The excitation polarization was varied using a $1/2$ wave plate and a rotating polarizer. (b,c) To validate our MFM set-up, we imaged SLB-coated silica beads loaded with DiI. DiI is known to align parallel to the membrane³²⁴. The green arrow indicates the direction of the fluorophore's dipole. (d) Representative images of DiI loaded beads at varying excitation polarization angles ($N=3$). (e) Representative per-pixel plot of fluorescence intensity as a function of excitation polarization. The phase of the sinusoid (indicated by the red arrow) corresponds to the azimuthal angle, which is the measured orientation of the fluorophore's transition dipole moment. (f) Map of DiI orientation on an SLB-coated bead reveals that DiI is parallel to the SLB surface. (g) Representative per-pixel plot of normalized and bleach-corrected fluorescence intensity in podosome shown in Figure 18b as a function of excitation polarization does not reveal significant variation in fluorescence intensity with varying excitation polarization

orientation. Teal circles correspond to background fluorescence, and dark blue circles correspond to podosome fluorescence. Scale bars, 1 μm .

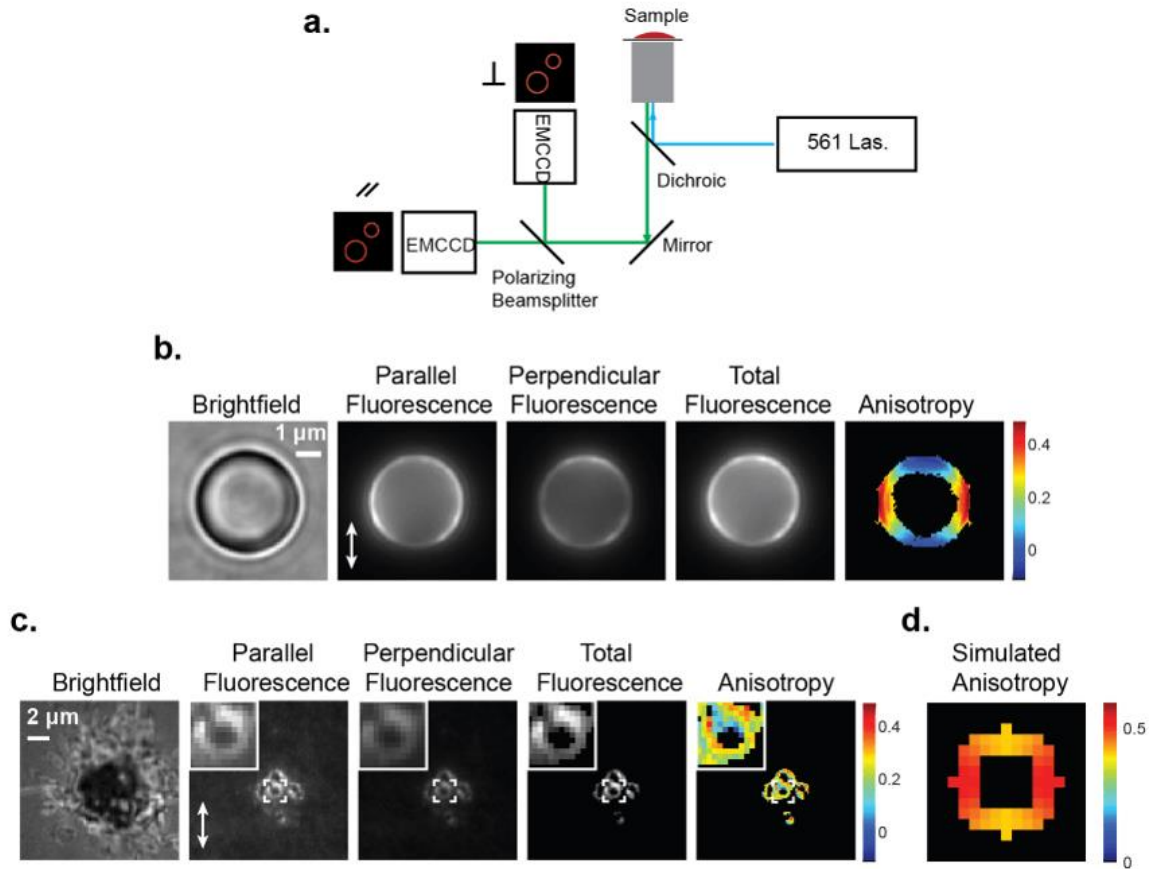


Figure A 17 Emission resolved fluorescence data does not indicate lateral organization of integrin forces in podosomes.

(a) Optical configuration for emission resolved fluorescence polarization imaging. Tension probe fluorescence emission was split into parallel and perpendicular channels using a polarizing beamsplitter. (b) Representative DiI-loaded SLBs on 5 μm silica beads exhibit systematic variations in anisotropy around the bead perimeter (consistent with DiI alignment parallel to the SLB on the bead surface), validating emission resolved polarization imaging (N = 23 beads, 3 experiments). (c) Representative emission resolved polarization imaging of a podosome-forming cell (N=29 cells, 2 experiments). (d) Simulated podosome (radius = 1 μm) with a contractile ring of 20° (selected to approximate MFM data). In contrast with the anisotropy of DiI-doped SLBs on 5 μm beads, podosome integrin tension does not exhibit systematic spatial variations in anisotropy. White arrows indicate laser polarization.

A.1.5 Mechanisms of Podosome Force Generation

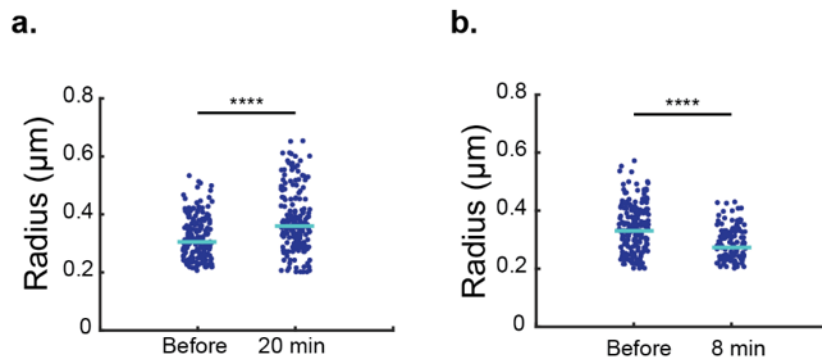


Figure A 18 Actin polymerization and nonconventional myosin regulate podosome mechanics.

(a, b) Podosome depletion radius before and after drug treatment with 50 μM Y27632 or 0.5 μM Jasplakinolide, respectively. Statistics were performed with a two-tailed Mann-Whitney test. Teal lines represent the median. Outliers were excluded (median \pm 3 scaled median absolute deviations). Each condition contains data from at least 91 individual podosomes with an eccentricity of <0.7 from at least 30 cells, 3 experiments.

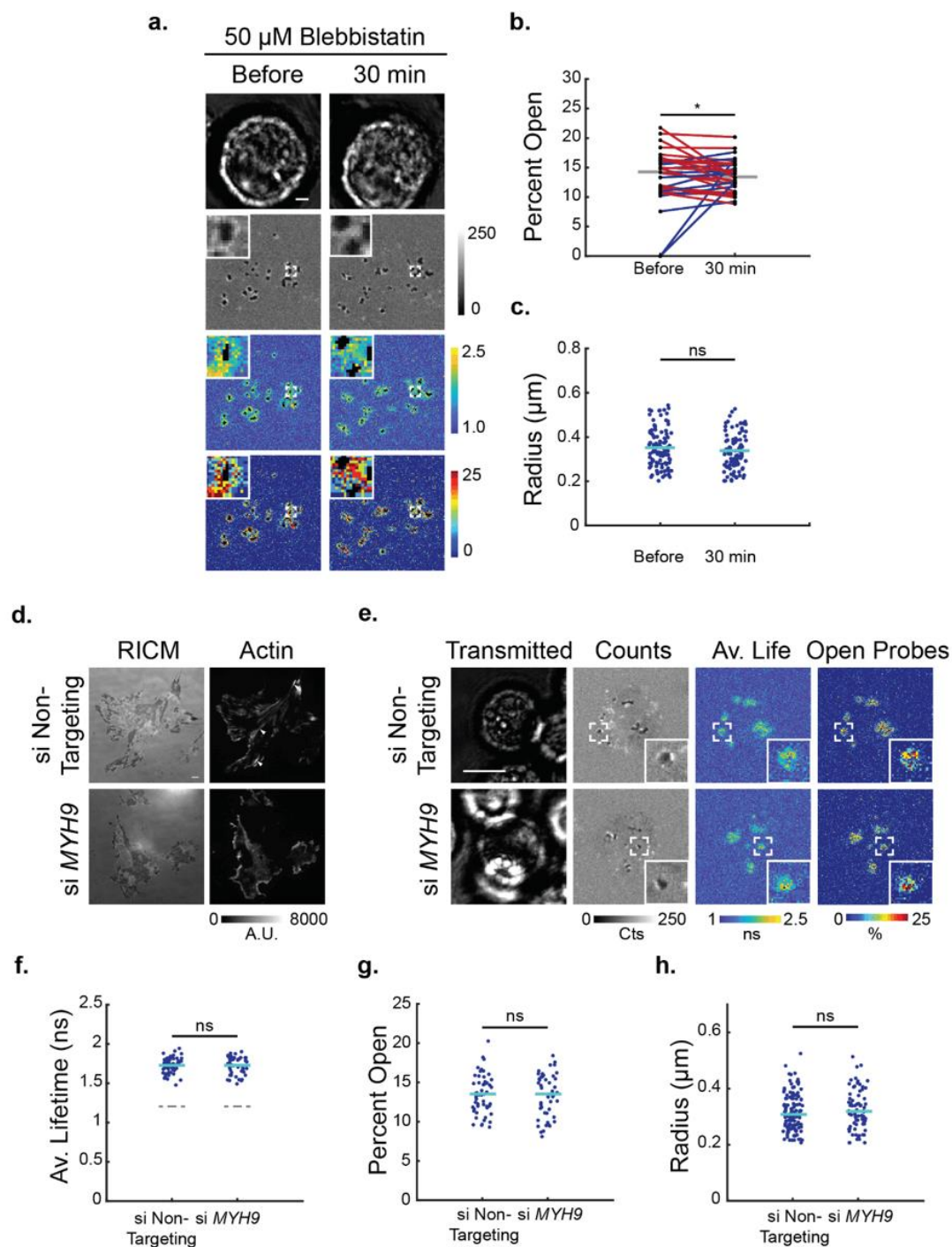


Figure A 19 Myosin IIa is dispensable in podosome ring force generation.

(a) Representative images of a podosome-forming cell before and after treatment with 50 μ M blebbistatin. (b) Average percent open probes in podosomes per cell before and after blebbistatin treatment. Blue and red lines represent an increase or decrease in percent open probes per cell, respectively. Grey horizontal lines represent the mean percent open probes. Statistics were performed with a two-tailed paired Students t-test. 31 cells, 4 experiments.

Scale Bar, 2.5 μm . **(c)** Podosome depletion radius before and after drug treatment with 50 μM Blebbistatin. Statistics were performed with a two-tailed unpaired t-test. Teal bars represent the mean. Outliers were excluded (Median \pm 3 scaled median absolute deviations). Each graph contains data from at least 69 individual podosomes with an eccentricity of <0.7 , 4 experiments. **(d)** Representative images of actin staining of cells treated with nontargeting siRNA or si*MYH9* after ~12 hours on glass. *MYH9* knockdown cells had impaired focal adhesion formation. Representative focal adhesions are marked by white arrows. Scale Bar, 5 μm . **(e)** Representative MT-FLIM images of podosome-forming transfected cells on an SLB. Scale Bar, 5 μm . **(f)** Average fluorescence lifetime in podosome regions of control and si*MYH9* cells. Teal bars represent the mean, and grey bars represent the mean SLB fluorescence lifetime. At least 47 cells per condition were analyzed, 3 experiments. Statistics were performed with a two-tailed unpaired t test. **(g)** Average percent open in podosome regions of control and si*MYH9* cells. Teal bars represent the median. At least 47 cells per condition were analyzed, 3 experiments. Statistics were performed with a two-tailed Mann-Whitney Test. **(h)** Podosome depletion radius in siNT and si*MYH9* cells. Statistics were performed with a two-tailed, Mann-Whitney Test. Outliers were excluded (median \pm 3 scaled median absolute deviations). Teal bars represent the median. Each condition contains data from at least 74 individual podosomes with an eccentricity of <0.7 , 3 experiments. ns, $P>0.05$, * $P<0.05$.

A.1.6 Manipulation of Podosome Mechanics

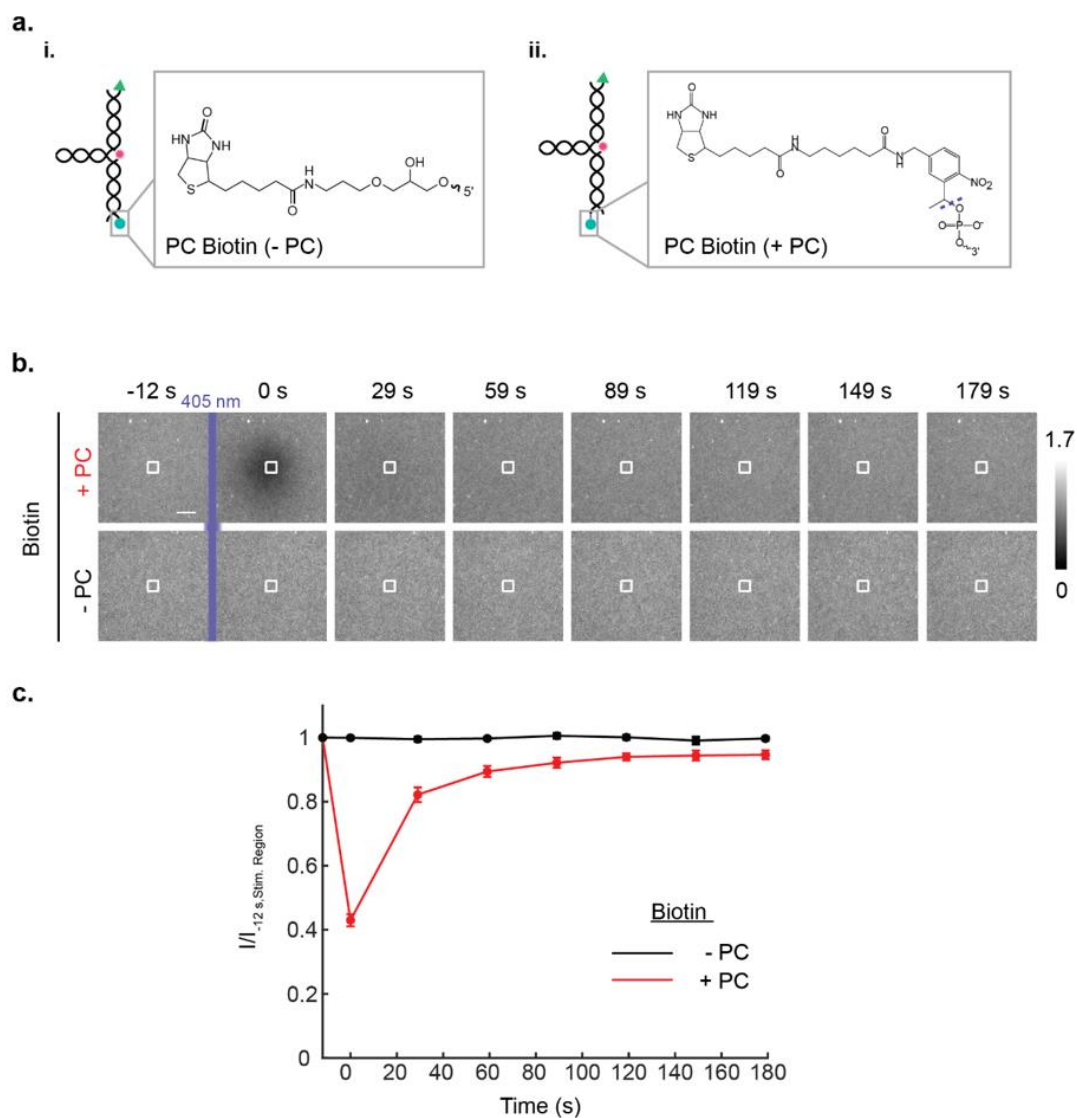


Figure A 20 Kinetics of fluorescence recovery after biotin photostimulation.

(a) Representative images of SLBs with DNA probes attached to the SLB with either regular or photocleavable biotin. (b) SLBs were photostimulated in the red box as described in Figure 20c. Scale bar, 5 μ m. (c) Quantification of fluorescence in the photostimulation region indicated in (a). DNA with a photocleavable biotin was ~60% released. SLBs recovered by lateral diffusion. Red lines represent SLBs with photocleavable biotin (+PC); black lines represent control SLBs with regular biotin (-PC). SLBs lacking a photocleavable biotin group were not released or photobleached under these illumination conditions. Data represent the mean \pm s.e.m. (error bars), 3 experiments.

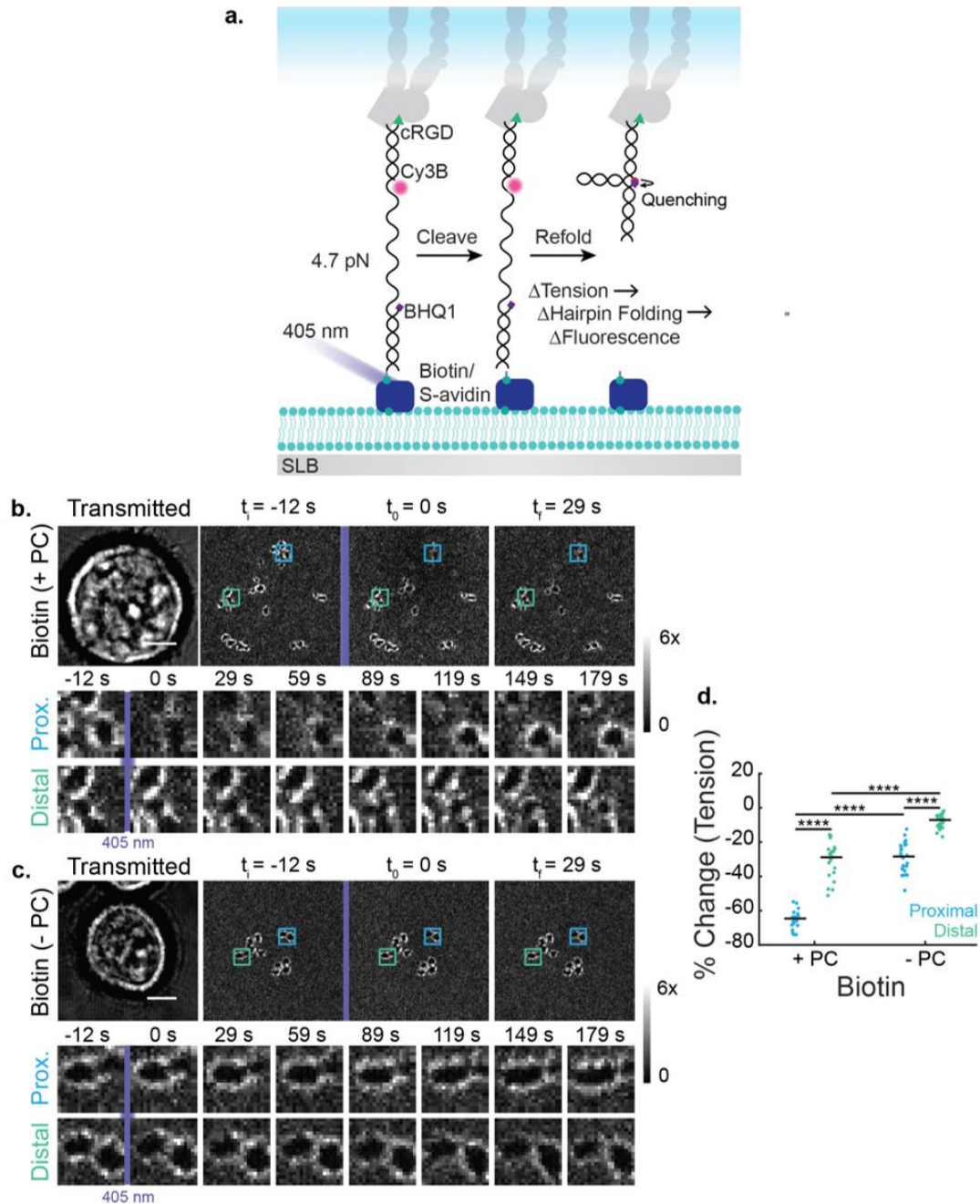


Figure A 21 Integrin tension is released following PCB photostimulation.

(a) Schematic of photocleavable tension probes. When the biotin anchor is cleaved with a 405 nm laser, the probe detaches from the bilayer and refolds, severing the podosome's mechanical connection to the SLB and quenching Cy3B fluorescence. (b,c) Representative time-lapse acquisitions of podosome tension proximal and distal to the site of photostimulation on substrates with a photocleavable biotin group and with a regular biotin anchor. (d) Percent change in tension proximal (blue) and distal (green) to photocleavage on probes containing regular biotin and PCB. Statistics were performed with a 2-way ANOVA. Each group contained at least 23 cells, 3 experiments. ****P<0.0001. All scale bars, 5 μ m.

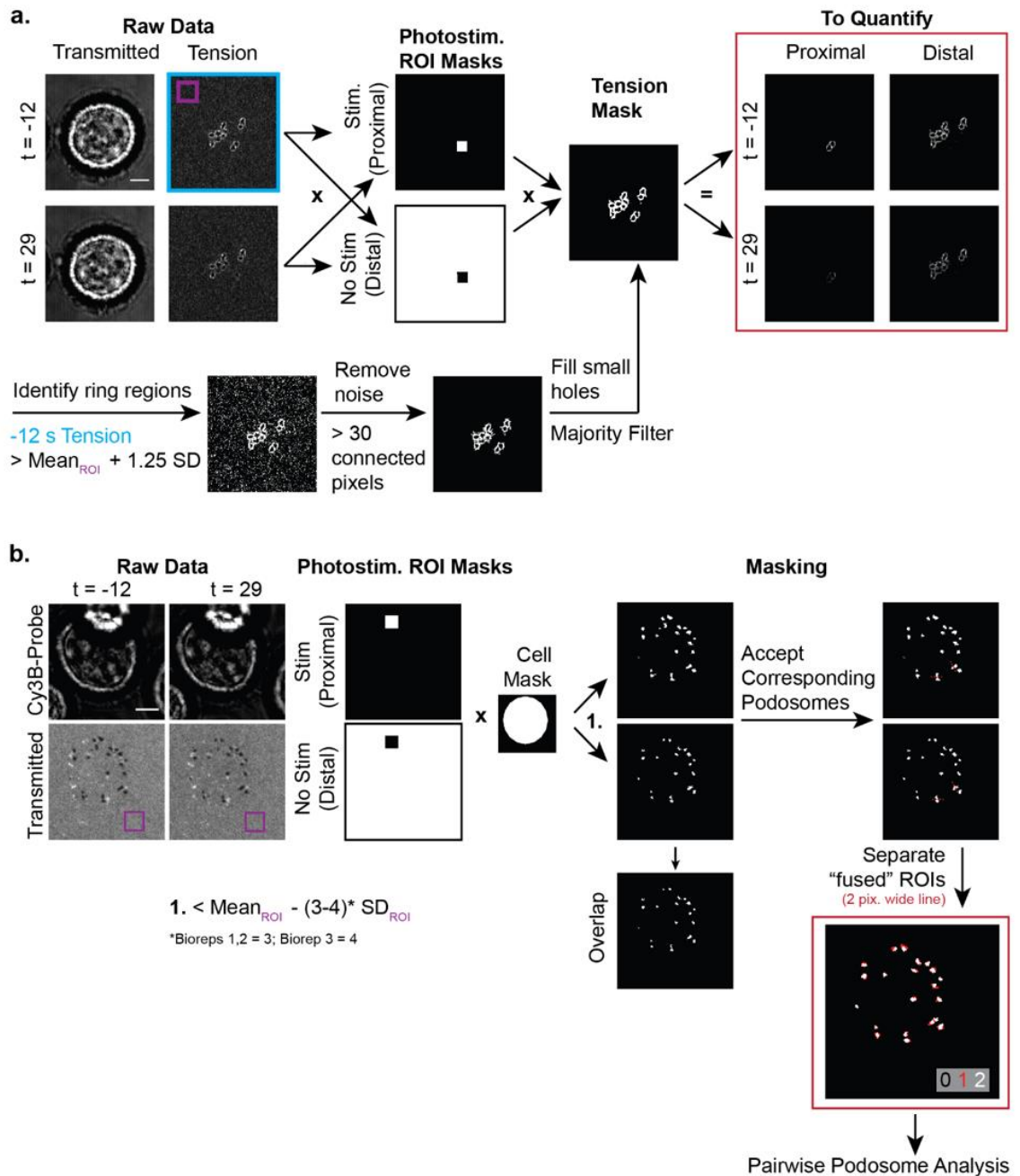


Figure A 22 Analysis protocol for photocleavable biotin experiments

(a) Flowchart for PCB tension analysis. Masks were generated from the -12 s image, because the signal-to-noise ratio was not sufficiently high to reliably identify photo-stimulated podosomes at later time points. First, tension regions were identified by intensity thresholding of the -12 s pre-stimulation image. Then, small objects in the background were removed, and a majority filter was used to fill any single pixel holes in rings. The tension mask was multiplied by both the raw tension signal and by the photostimulation masks exported from Nikon Elements to produce quantifiable tension maps for proximal and distal regions of the cell. Proximal regions corresponded to the 7

μm^2 region that was photocleaved. **(b)** Analysis flowchart for PCB protrusion experiments. To generate masks of podosome depletion, the fluorescence images at -12 s and 29 s were intensity thresholded and multiplied by masks of the cell area, determined by the transmitted light, and by the photostimulation mask, which was exported from Nikon Elements. The cell area mask served to remove any holes in SLB in the field of view. Podosome masks were overlapped, and any podosomes in the original mask that aligned with the overlap mask were accepted. Clear podosome doublets were split in two using a 2-pixel line. Single podosomes were processed. A small percentage of podosomes could not be clearly distinguished from their neighbors or were double-counted in the overlap criteria; these data were excluded.

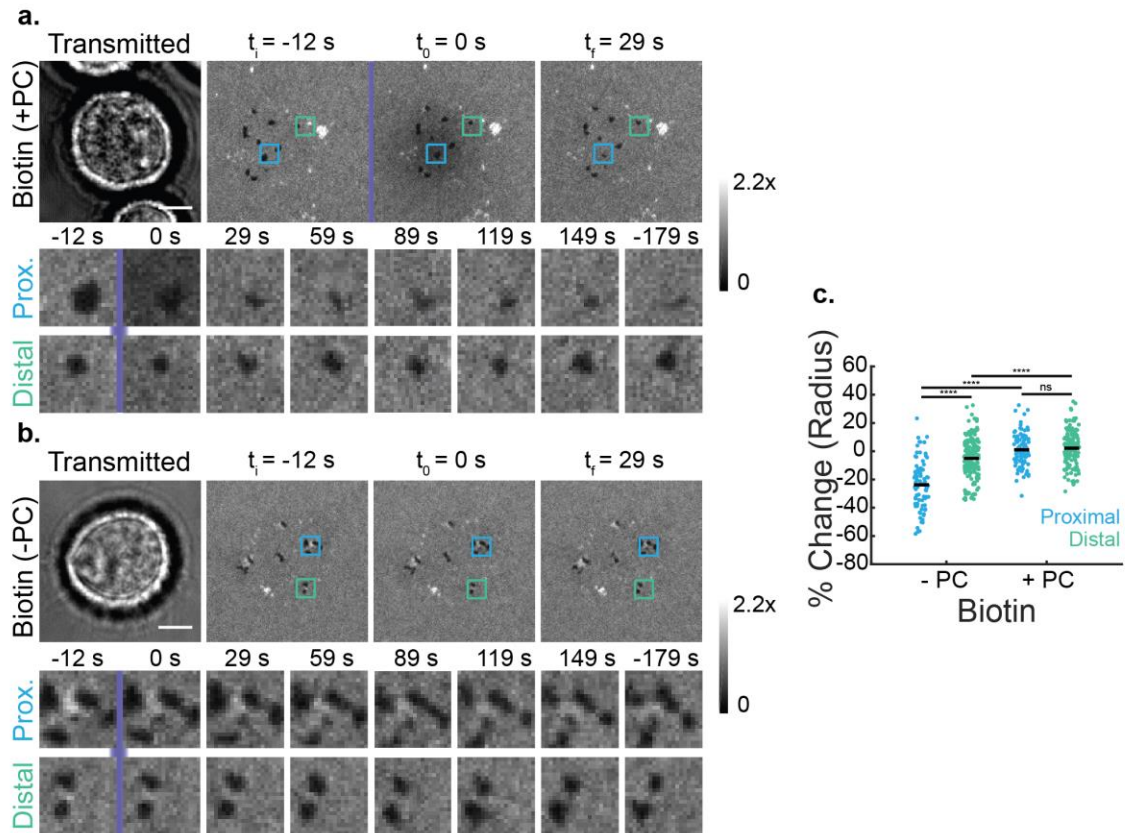


Figure A 23 Podosome protrusion is primarily perturbed at the site of photocleavage.

(a,b) Representative time-lapse acquisitions of probe density proximal and distal to the site of photostimulation on substrates with a photocleavable biotin group and with a regular biotin anchor. (c) Percent change depletion radius proximal (blue) and distal (green) to photocleavage on probes containing regular biotin and PCB at $t = 29$ s. Statistics were performed with a 2-way ANOVA. Each group contained at least 79 podosomes across 3 experiments. Outliers were excluded (median \pm 3 scaled median absolute deviations). ns $P > 0.05$, **** $P < 0.0001$. Scale Bar, 5 μ m.

A.1.7 Cell Culture

CELL CHECK

Species-specific PCR Evaluation

Species	1
mouse	+
rat	-
human	-
Chinese hamster	-
African green monkey	-

Marker Analysis

Marker Name	1	
	Sample Results	NIH/3T3 (CRL-1658)
MCA-4-2	19.3	19.3, 20.3
MCA-5-5	14, 15	14, 15
MCA-6-4	14.3	14.3
MCA-6-7	12	12
MCA-9-2	15, 16	15, 16
MCA-12-1	20	20
MCA-15-3	20.3	20.3
MCA-18-3	17, 18, 19	17, 19
MCA-X-1	25	25

Sample ID	Remarks
1	<p>The sample was confirmed to be of mouse origin and no mammalian interspecies contamination was detected. A genetic profile was generated for the sample by using a panel of STR markers for genotyping.</p> <p>The sample profile has minor genetic changes (loss of an allele at marker MCA-4-2 and an addition of an allele at marker MCA-18-3), but is otherwise identical to the genetic profile established for this cell line.</p>

Figure A 24 NIH 3T3 Cell Profile

Cell profile by IDEXX Bioanalytics. Short tandem repeat analysis of NIH-3T3 cells reveals an 85% match to the standard, confirming cell line identity³⁰⁸.

A.2 Analysis of DNA Hairpin-Based Tension Probes for Cellular Imaging

A.2.1 Probe synthesis and purification

Table A 6 Oligonucleotide Sequences

Summary of oligonucleotides used in this study. IDT = Integrated DNA Technologies, BT = Biosearch Technologies.

Purpose	Sequence	Source
4.7 pN (+ Spacers)	GTG AAA TAC CGC ACA GAT GCG TTT GTA TAA ATG TTT TTT TCA TTT ATA C TTT AAG AGC GCC ACG TAG CCC AGC	IDT
4.7 pN (- Spacers)	GTG AAA TAC CGC ACA GAT GCG GTA TAA ATG TTT TTT TCA TTT ATA C AAG AGC GCC ACG TAG CCC AGC	IDT
4.7 pN (+ Spacers) Complementary Strand	AAA GTA TAA ATG AAA AAA ACA TTT ATA CAA A	IDT
4.7 pN (- Spacers) Complementary	GTA TAA ATG AAA AAA ACA TTT ATA C	IDT
5'-Alk-3'-Amine	/5Hexynyl/ TTT GCT GGG CTA CGT GGC GCT CTT /3AmMO/	IDT
5'-Alk-5T-3'- Amine	/5Hexynyl/ TTT GCT GGG CTA CGT GGC GCT CTT TTT TT /3AmMO/	IDT
5'-Amine-3'-Biotin	/5AmMC6/CG CAT CTG TGC GGT ATT TCA CTT T/3Bio	IDT
5'-BHQ1-3'-Biotin	BHQ-1-CGCATCTGTGCGGTATTTCACTT-Biotin	BT
5'-BHQ1-3'	BHQ-1-CGCATCTGTGCGGTATTTCACTT	BT
5'-9TBHQ1-3'- Biotin	CGCATCTG-T(BHQ-1)-GCGGTATTTTAC-Biotin	BT
5'-9TBHQ1-3'	CGCATCTG-T(BHQ-1)-GCGGTATTTTAC	BT
5'-9Tamine-3'	CGC ATC TG/iAmMC6T/ CGG TAT TTC ACT TT/3Bio/	IDT
5'-Dual Biotin- 4.7pN (-Spacers)- 3'	/52-Bio/GT GAA ATA CCG CAC AGA TGC GGT ATA AAT GTT TTT TTC ATT TAT ACA AGA GCG CCA CGT AGC CCA GC	IDT
Linear (- Spacers)	GTG AAA TAC CGC ACA GAT GCG AAG AGC GCC ACG TAG CCC AGC	IDT
Linear (+ Spacers)	GTG AAA TAC CGC ACA GAT GCG TTT TTT AAG AGC GCC ACG TAG CCC AGC	IDT

* Note that the biotin location was swapped between single and dual biotin experiments due to limitations in commercial availability; we expect this effect to be negligible.

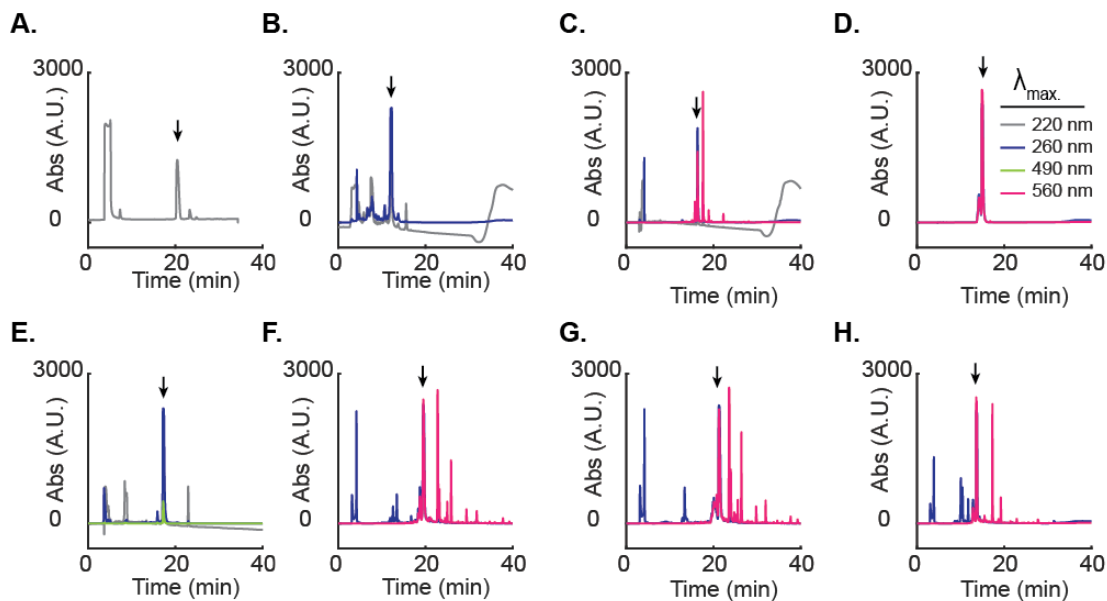


Figure A 25 HPLC purification of modified oligonucleotides.

HPLC chromatograms of **A.** cRGDfk(PEG-PEG)-Azide. **B.** 5'-cRGDfk(PEG-PEG)- 3'-Amine (intermediate), **C.** 5'-cRGDfk(PEG-PEG)-3'-Cy3B, **D.** 5'-Alk-3'-Cy3B, **E.** 5'-cRGDfk(PEG-PEG) -3'-A488, **F.** 5'-9TCy3B-3'-Bio, **G.** 5'-Alk-5T-3'-Cy3B, **H.** 5'-Cy3B-3'-Bio. Arrows indicate the product peak. **D** shows a repurified oligonucleotide, due instrument/input error.

A.2.2 Tension Probe Characterization

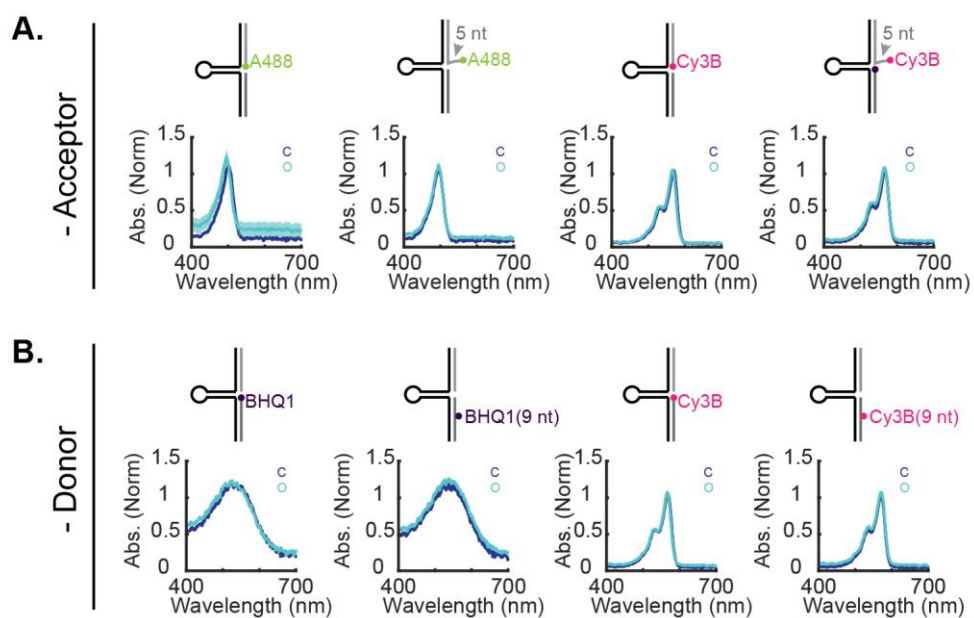


Figure A 26 Absorbance spectra of single-dye modified tension probes.

Schematics and absorbance spectra of tension probes labeled only with the donor (A) or acceptor (B). Spectra represent the mean \pm s.e.m. for 3 experiments. Outlier spectra (Baseline \pm 3 median absolute deviations) were omitted.

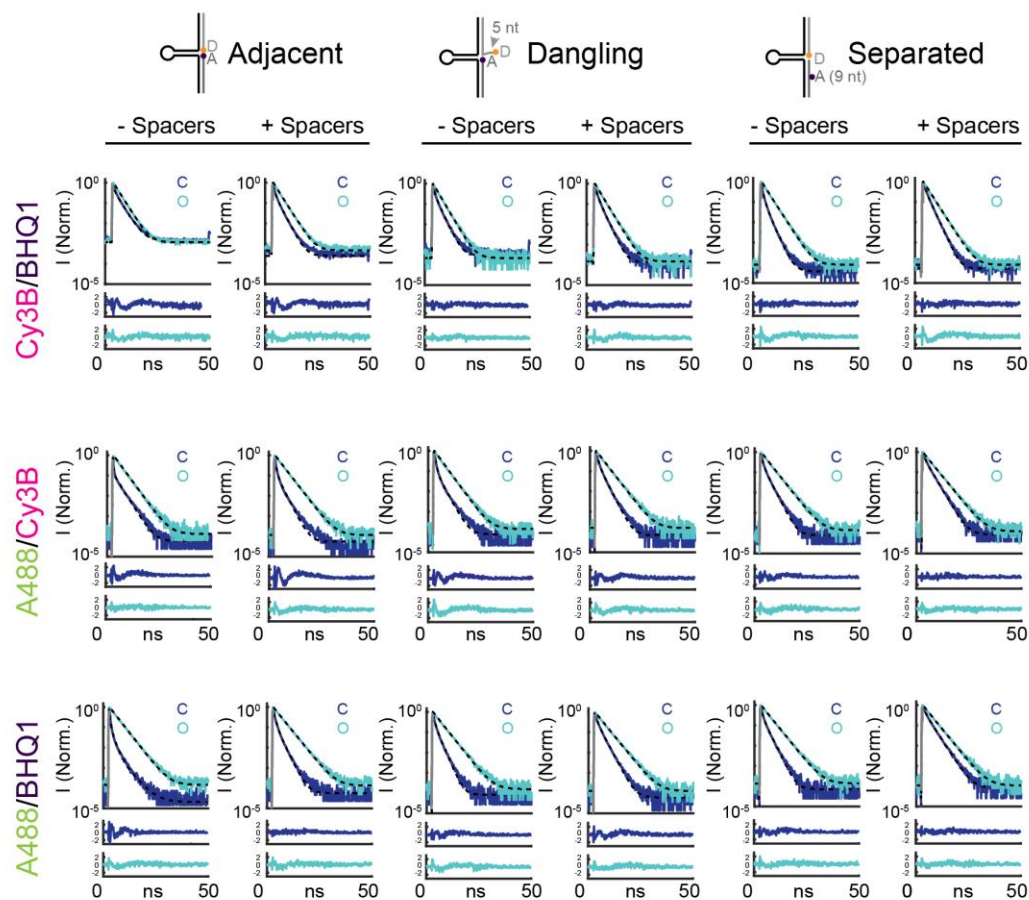


Figure A 27 Representative TCSPC curve fits.

Representative TCSPC decay curves and curve fits (dashed black lines) and residuals for close and open tension probes on SLBs. Probes were fit in SymPhoTime as described in the Methods section using the system IRF (grey). For visualization, curves are averaged over 5 time-bin window. Open probes fit to a monoexponential decay. Closed probes were fit to a bi- or triexponential decay. For all curves, chi-squared < 2.

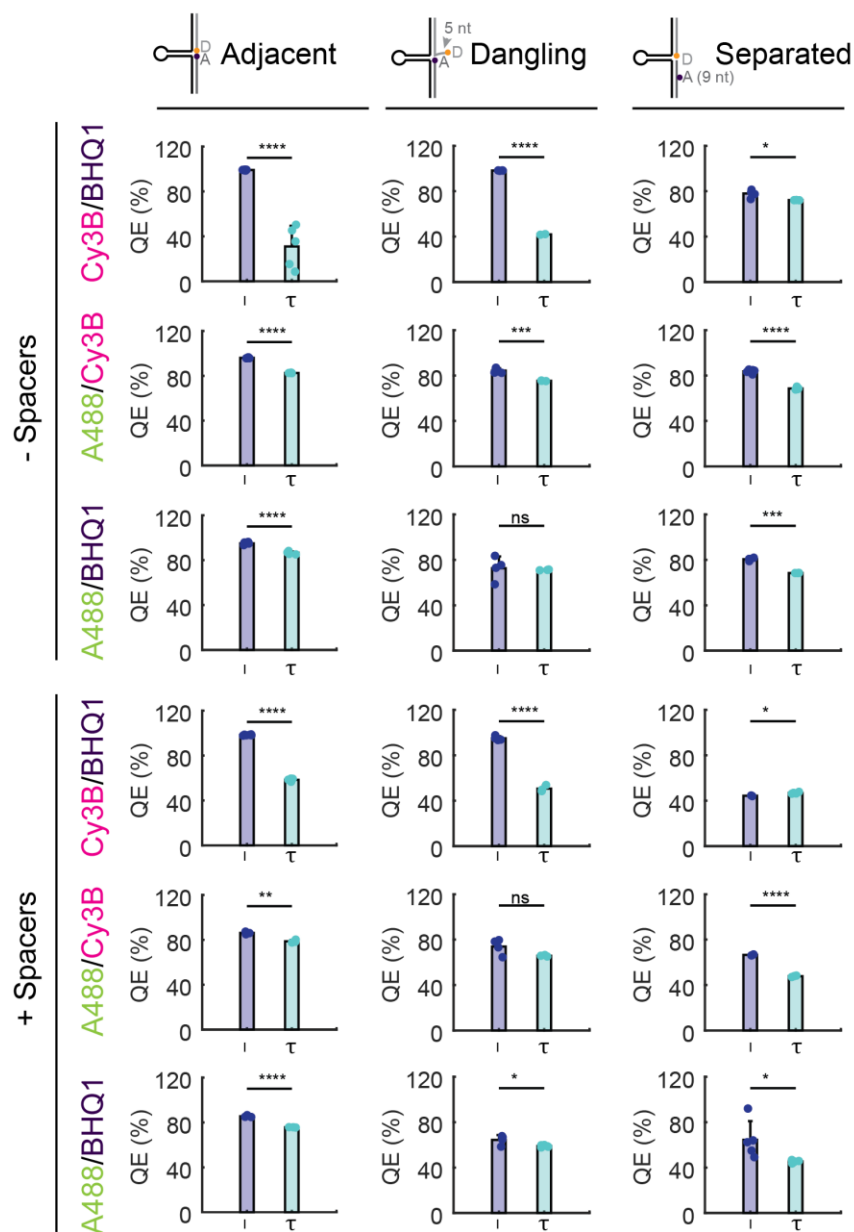


Figure A 28 Analysis of intensity and lifetime derived quenching efficiencies.

Scatter plots of quenching efficiencies calculated using the fluorescence intensity (I) versus the amplitude-average lifetime (τ). Bars and error bars represent the mean \pm SD for at least 3 experiments. Outliers beyond 3 median absolute deviations were omitted. Statistics were performed using a two-tailed unpaired T-test. P values are reported as ns $P > 0.05$, * $P < 0.05$, ** $P < 0.01$, *** $P < 0.0001$, **** $P < 0.0001$.

Table A 7 Summary of Fluorescence Lifetime, Intensity, and Quenching Efficiencies in Open and Closed Tension Probes

Measurements represent the mean of at least 3 experiments per sample. Error represents the standard error of the mean (Amplitude-Weighted Lifetime, Intensity) or standard deviation (QE). For the FAST-FLIM Average Lifetime, error reflects the histogram width. The standard error of the mean is shown in parentheses.

	τ_{Av} . (FAST-FLIM) (ns)		τ_{Av} . (Amplitude) (ns)		Intensity (A.U.)		QE (%)	
	Closed	Open	Closed	Open	Closed	Open	Intensity	Lifetime
A_Cy3B/BHQ1-	2.388 \pm 0.428 (0.076)	2.592 \pm 0.325 (0.220)	1.760 \pm 0.188	2.566 \pm 0.037	56 \pm 11	5210 \pm 307	99 \pm 1	31 \pm 18
A_Cy3B/BHQ1+	1.685 \pm 0.251 (0.036)	2.589 \pm 0.296 (0.037)	1.092 \pm 0.015	2.621 \pm 0.009	102 \pm 10	6030 \pm 351	98 \pm 0	58 \pm 2
D_Cy3B/BHQ1-	1.777 \pm 0.500 (0.110)	2.405 \pm 0.554 (0.051)	1.328 \pm 0.112	2.481 \pm 0.000	66 \pm 8	3594 \pm 298	98 \pm 0	46 \pm 7
D_Cy3B/BHQ1+	1.654 \pm 0.199 (0.028)	2.574 \pm 0.279 (0.010)	1.245 \pm 0.042	2.523 \pm 0.004	132 \pm 24	2736 \pm 311	94 \pm 2	51 \pm 3
S_Cy3B/BHQ1-	1.089 \pm 0.149 (0.017)	2.659 \pm 0.319 (0.014)	0.743 \pm 0.008	2.693 \pm 0.007	655 \pm 25	2988 \pm 71	78 \pm 3	72 \pm 1
S_Cy3B/BHQ1+	1.626 \pm 0.208 (0.006)	2.625 \pm 0.324 (0.056)	1.432 \pm 0.012	2.634 \pm 0.044	1135 \pm 78	2249 \pm 170	49 \pm 8	46 \pm 3
A_A488/Cy3B-	1.349 \pm 0.465 (0.132)	3.003 \pm 0.712 (0.067)	0.418 \pm 0.034	3.061 \pm 0.009	80 \pm 4	2153 \pm 107	96 \pm 1	84 \pm 2
A_A488/Cy3B+	1.214 \pm 0.164 (0.059)	3.292 \pm 0.332 (0.085)	0.688 \pm 0.026	3.233 \pm 0.009	195 \pm 49	1785 \pm 122	89 \pm 5	78 \pm 1
D_A488/Cy3B-	1.132 \pm 0.170 (0.035)	3.093 \pm 0.372 (0.042)	0.713 \pm 0.026	3.084 \pm 0.015	344 \pm 31	2186 \pm 147	84 \pm 7	77 \pm 2
D_A488/Cy3B+	1.434 \pm 0.262 (0.077)	3.243 \pm 0.406 (0.014)	1.002 \pm 0.113	3.255 \pm 0.008	475 \pm 97	1788 \pm 258	74 \pm 7	69 \pm 7
S_A488/Cy3B-	1.520 \pm 0.207 (0.021)	3.361 \pm 0.307 (0.032)	1.005 \pm 0.013	3.345 \pm 0.009	379 \pm 15	2046 \pm 268	78 \pm 14	69 \pm 1
S_A488/Cy3B+	2.166 \pm 0.208 (0.011)	3.396 \pm 0.288 (0.014)	1.788 \pm 0.018	3.423 \pm 0.010	735 \pm 43	2021 \pm 205	48 \pm 1	48 \pm 1
A_A488/BHQ1-	0.943 \pm 0.181 (0.043)	3.180 \pm 0.343 (0.037)	0.440 \pm 0.016	3.244 \pm 0.015	92 \pm 8	1847 \pm 171	95 \pm 1	86 \pm 1
A_A488/BHQ1+	1.278 \pm 0.187 (0.030)	3.31 \pm 0.365 (0.047)	0.828 \pm 0.007	3.400 \pm 0.014	262 \pm 25	1668 \pm 228	84 \pm 4	76 \pm 0
D_A488/BHQ1-	1.300 \pm 0.200 (0.026)	3.349 \pm 0.389 (0.011)	0.956 \pm 0.003	3.311 \pm 0.008	557 \pm 44	2177 \pm 274	73 \pm 10	71 \pm 0
D_A488/BHQ1+	1.781 \pm 0.239 (0.038)	3.361 \pm 0.390 (0.013)	1.410 \pm 0.016	3.429 \pm 0.009	671 \pm 62	2038 \pm 130	67 \pm 7	59 \pm 1
S_A488/BHQ1-	1.503 \pm 0.263 (0.040)	3.3340 \pm 0.356 (0.022)	1.064 \pm 0.005	3.388 \pm 0.007	592 \pm 21	2757 \pm 220	78 \pm 5	69 \pm 0
S_A488/BHQ1+	2.261 \pm 0.386 (0.031)	3.418 \pm 0.475 (0.016)	1.874 \pm 0.016	3.429 \pm 0.007	740 \pm 169	2087 \pm 177	65 \pm 5	45 \pm 1

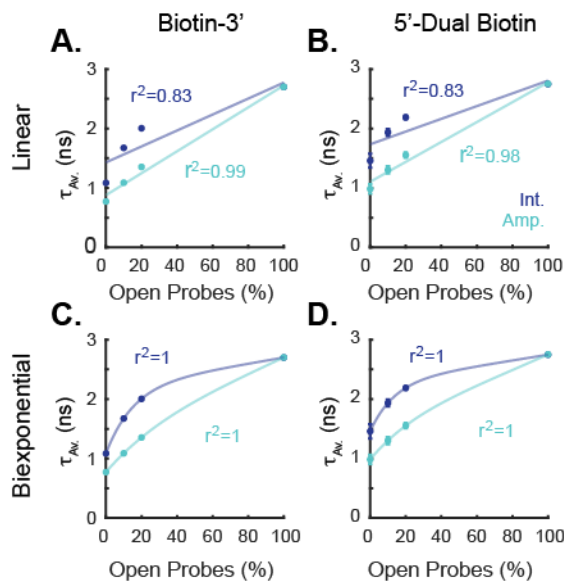


Figure A 29 Analysis of dual- and single-biotin tension probes on SLBs.

Scatters plots of the intensity and amplitude-weighted average fluorescence lifetimes of 0 to 100% open probes on SLBs. Data represent the mean \pm s.e.m. for three experiments. Data are curve fit using a linear model (A-B) or a biexponential model as used for MT-FLIM histogram calibration³³ (C-D). While nonlinear curve fits better represent the data, for this small data set, these curves are likely overfit. Therefore, understanding this relationship will require further investigation.

A.1.1.1 NUPACK Structural Modeling of DNA-based Tension Probes

For a course-grain view of tension probe structure, we used freely available NUPACK software to model open and closed tension probes with and without spacers and a 5nt overhang on the donor strand (Figure A 30, A.1.1.1). While this cannot provide the atomistic detail provided by smFRET combined with MD simulations, this allowed us to understand the broad structural features. NUPACK estimates and illustrates the equilibrium pair probabilities. When the probes were opened with a complementary strand, probes lacking an overhang had a relatively linear structure. Probes containing a 5nt overhang were bent in the open conformation, but the interpretation of these results is limited. Even with tension probe's knicked structure at the TWJ, probes with spacers separating the stem-loop structure from the arm sequences were the most

thermodynamically stable. Nevertheless, NUPACK modeling suggested that most probes lacking spacers still folded, with a fraction of probes exhibiting some peeling of the upper arm sequence or the terminal two base-pairs in the step-loop sequence

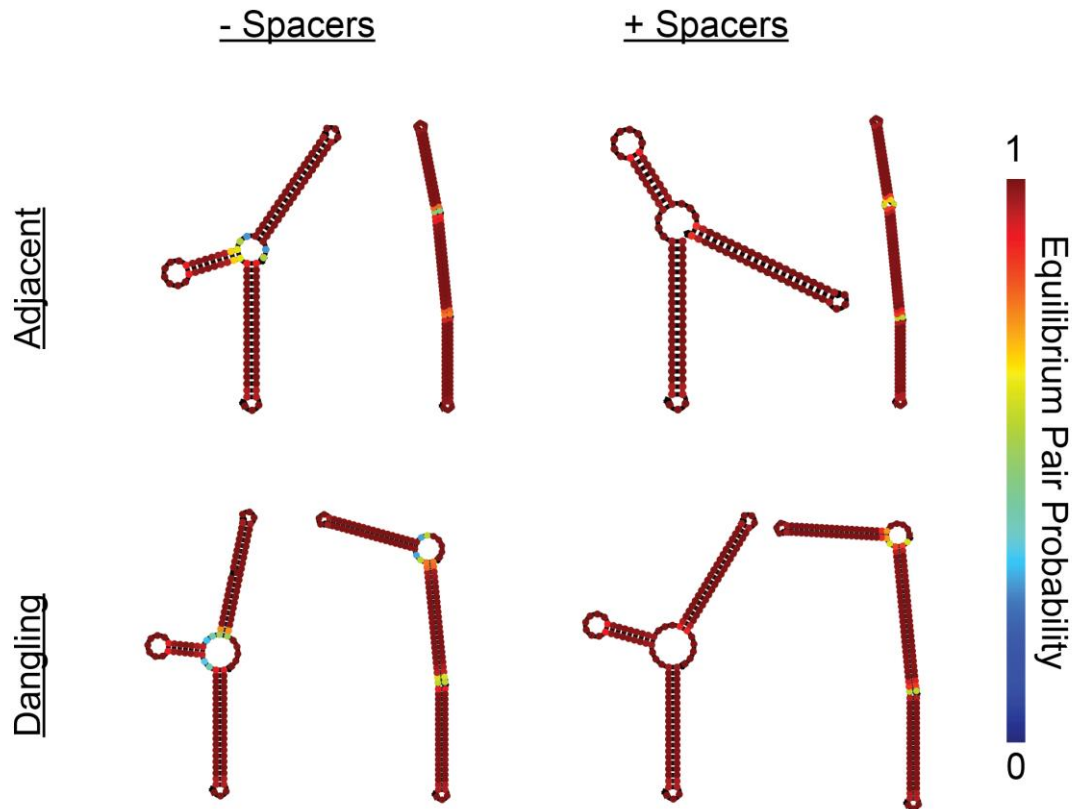


Figure A 30 Influence of spacer and overhang sequences on three-way junctions in tension probes.

NUPACK equilibrium pair probability analysis of DNA tension probes in the closed and open conformations. Probes were modeled at identical temperature, DNA, and salt concentrations as experimental analysis. Pair probability is the probability that a given base will be paired or unpaired as shown. Thus, unpaired blue bases are equivalent to orange paired bases and vice versa.

A.2.3 Cellular Imaging

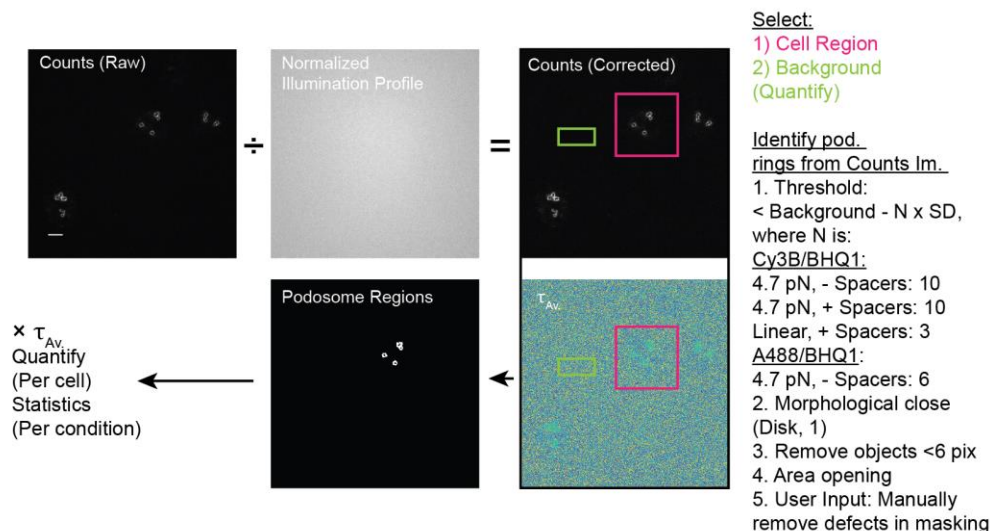


Figure A 31 Analysis Map for Podosome Identification on High QE Probes

The FLIM photon counts image was illumination profile corrected and used to select regions of interest containing a podosome-forming cell and the SLB background. Podosomes were detected by the presence of bright rings in the photon counts image. Scale bar, 5 μm .

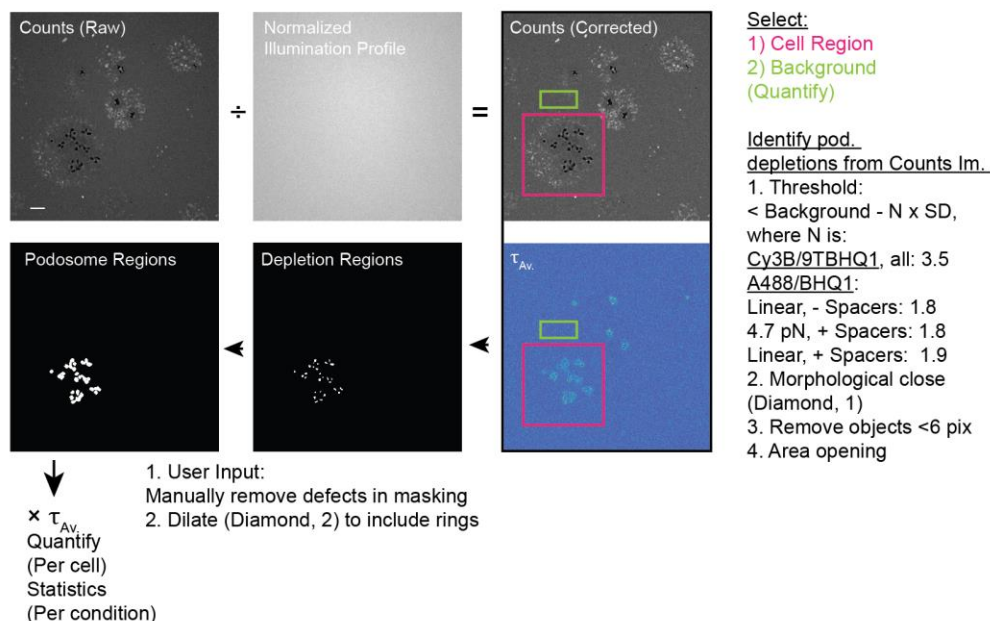


Figure A 32 Analysis Map for Podosome Identification on Low QE Probes

The FLIM photon counts image was illumination profile corrected and used to select regions of interest containing a podosome-forming cell and the SLB background. Podosomes were detected based on the decrease in fluorescence intensity at the podosome cores and rings were included through mask dilation. Scale bar, 5 μm .

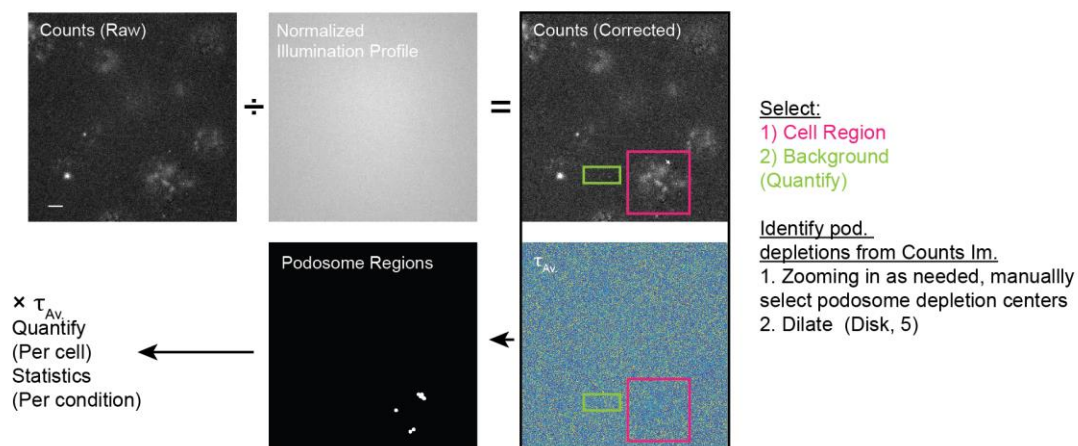


Figure A 33 Analysis Map for Podosome Identification on A_Cy3B/BHQ1- Linear Probes

The FLIM photon counts image was illumination profile corrected and used to select regions of interest containing a podosome-forming cell and the SLB background. Individual podosome depletion regions were hand-selected and pixels were dilated to include the entire podosome region. Scale bar, 5 μm .

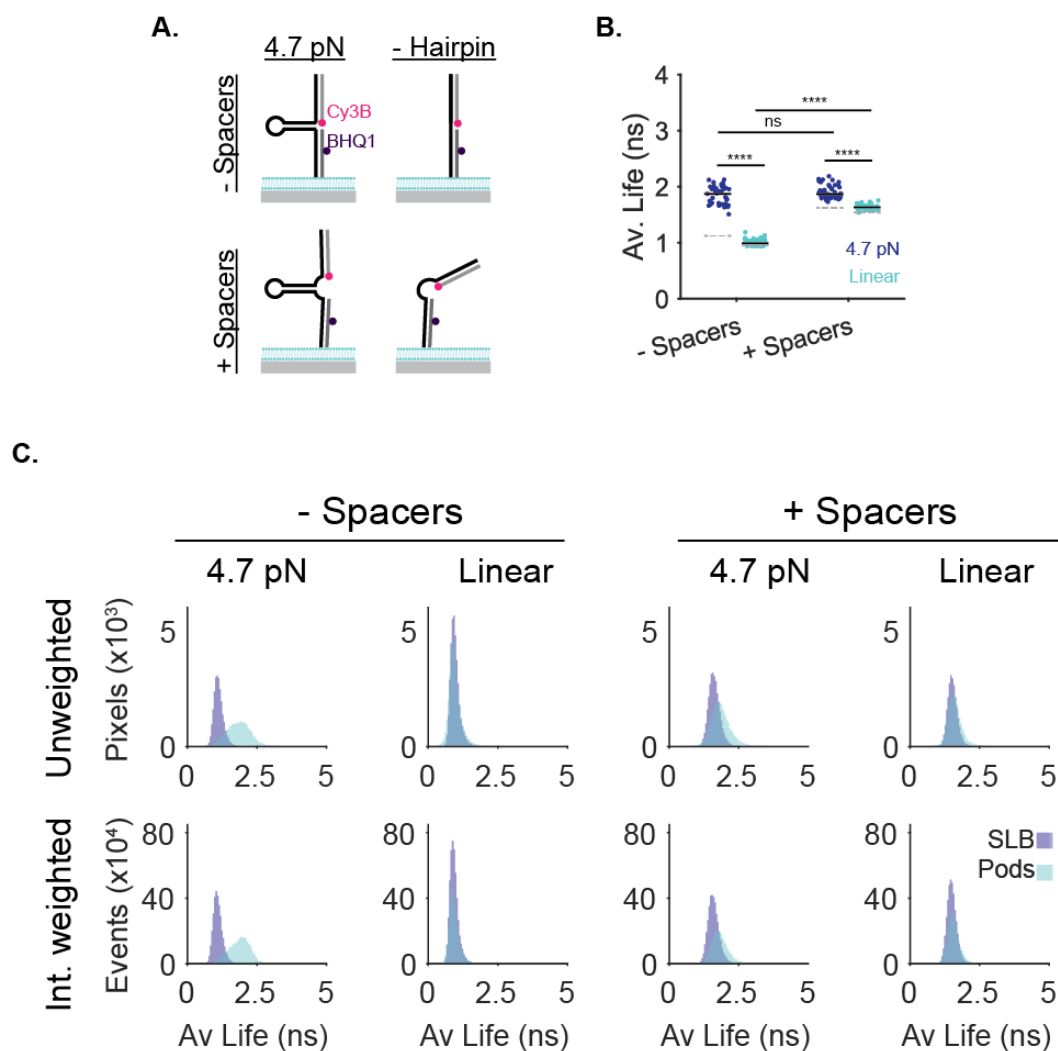


Figure A 34 Analysis of Tension Probe Signal on S_CY3B/BHQ1- (MT-FLIM) and S_Cy3BBHQ1+ Probes.

(A) Schematic of S_Cy3B/BHQ1- and S_Cy3B/BHQ1+ 4.7 pN and linear probes. (B) Quantification of the raw fluorescence lifetime in podosome-regions per cell. Grey lines indicate the background average fluorescence lifetime. At least 41 cells from 3 experiments were analyzed per sample. Statistics were performed with a grouped 2-way ANOVA followed by a multicomparison test. (C) Histograms showing the average fluorescence lifetime of podosome regions (teal) versus the SLB background (blue) in 35 cells. Here, intensity weighted refers to weighting by the number of photon counts per pixel, not the intensity-weighted average lifetime. P values are reported as ns $P > 0.05$, **** $P < 0.0001$.

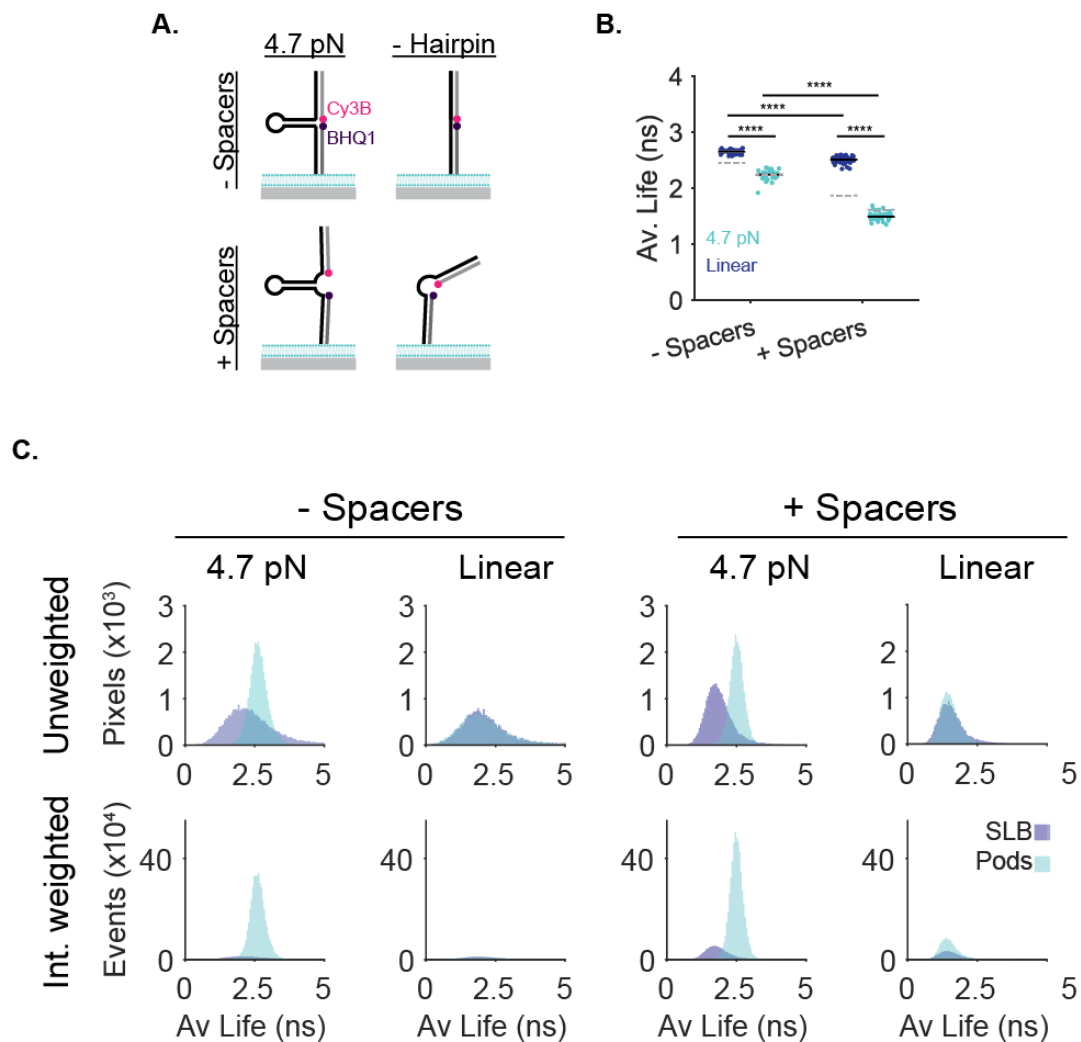


Figure A 35 Analysis of Tension Probe Signal on A_Cy3B/BHQ1- and A_Cy3B/BHQ1+ Probes.

(A). Schematic of A_Cy3B/BHQ1- and A_Cy3B/BHQ1+ 4.7 pN and linear probes. (B) Quantification of the raw fluorescence lifetime in podosome-regions per cell. Grey lines indicate the background average fluorescence lifetime. At least 35 cells from 3 experiments were analyzed per sample. Statistics were performed with a grouped 2-way ANOVA followed by a multiple comparison test. (C) Histograms showing the average fluorescence lifetime of podosome regions (teal) versus the SLB background (blue) in 35 cells. Here, intensity weighted refers to weighting by the number of photon counts per pixel, not the intensity-weighted average lifetime. P values are reported as **** P < 0.0001.

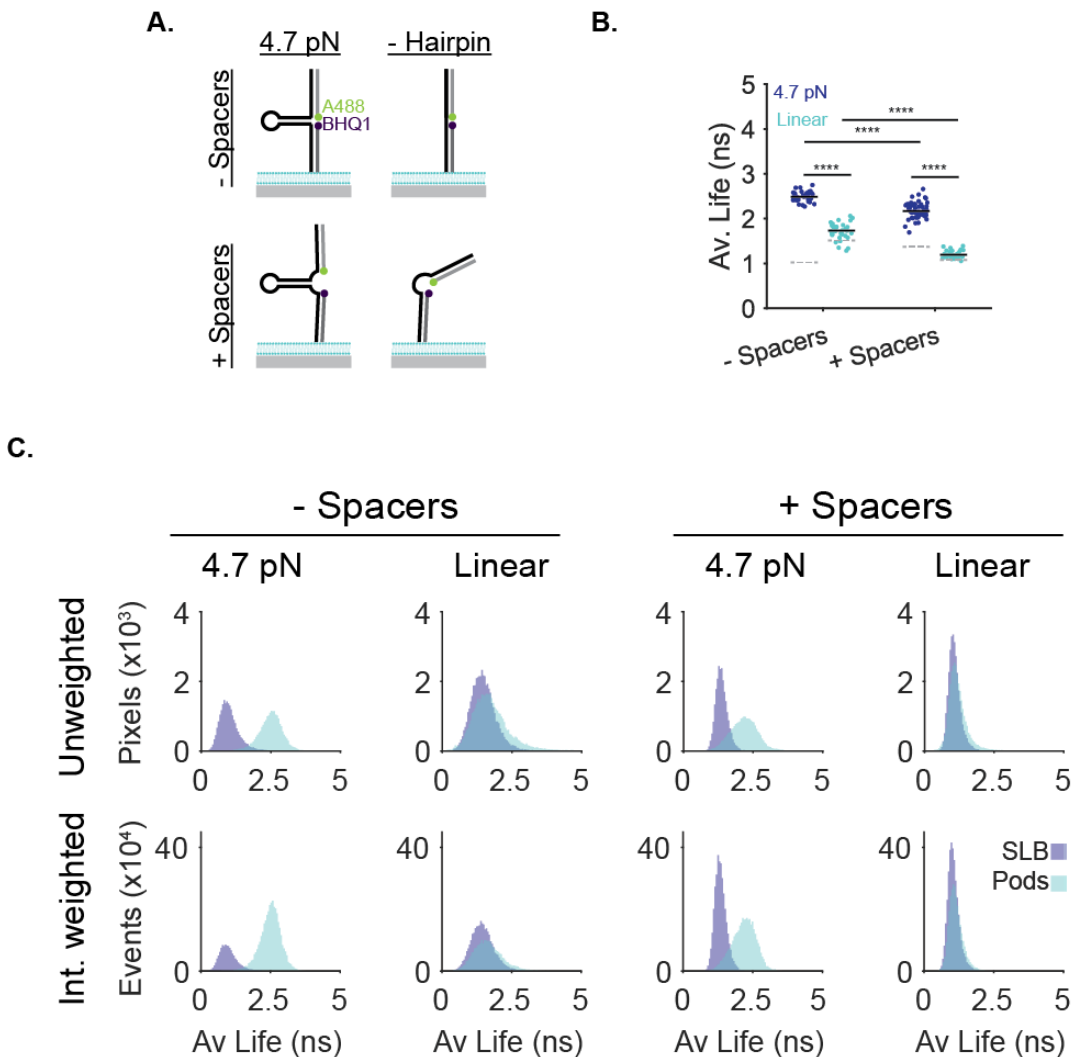


Figure A 36 Analysis of Tension Probe Signal on A_A488/BHQ1- and A_A488/BHQ1+ Probes

(A). Schematic of A_A488/BHQ1- and A_A488/BHQ1+ 4.7 pN and linear probes. (B) Quantification of the raw fluorescence lifetime in podosome-regions per cell. Grey lines indicate the background average fluorescence lifetime. At least 33 cells from 3 experiments were analyzed per sample. Statistics were performed with a grouped 2-way ANOVA followed by a multiple comparison test. (C) Histograms showing the average fluorescence lifetime of podosome regions (teal) versus the SLB background (blue) in 35 cells. Here, intensity weighted refers to weighting by the number of photon counts per pixel, not the intensity-weighted average lifetime. P values are reported as **** P < 0.0001

APPENDIX B. PERMISSIONS

[External] Glazier **Permission** Request

Catherine Wattenberg
Director of Publications
[The Journal of Immunology](#) and [ImmunoHorizons](#)
The American Association of Immunologists
1451 Rockville Pike, Suite 650
Rockville, MD 20852
Phone: 301-634-7835
www.aai.org

From: Web Email <noreply@aai.org>
Sent: Monday, March 2, 2020 11:11 AM
To: Copyright Requests <copyright@aai.org>
Subject: **Permission** Request

Name	Roxanne Glazier
* Institution	Georgia Institute of Technology, Emory University
* Address	1515 Dickey Drive
* City, State, and Postal Code	Atlanta, GA. 30309
* Country	USA
* Phone	6178759132
Fax	
* E-mail	roxanne.glazier@emory.edu
* Title of Article	Antigen Recognition is Facilitated by Invadosome-Like Protrusions Formed by Memory/Effector T Cells
* Volume Number	188
* Page Range	3686-3699
* Year	2012
DOI Number	
* Will figure be reproduced without changes from the original?	Yes
* Will figure be modified from the original?	No
* Figure or Table Number(s)	Fig 9.2
Other Reproduction (please describe)	
* Are you the author of the requested material?	Yes
* Is this for your Ph.D. thesis?	Yes
* Title of Publication (not article title)	Dissertation
* Publisher	Dissertation
Date of Publication (optional)	
* Provide a brief explanation of how the material will be used	Dissertation Intro

This Agreement between Roxanne J Glazier ("You") and Springer Nature ("Springer Nature") consists of your license details and the terms and conditions provided by Springer Nature and Copyright Clearance Center.

[Print](#) [Copy](#)

License Number	4780870657360
License date	Mar 02, 2020
Licensed Content Publisher	Springer Nature
Licensed Content Publication	Nature Cell Biology
Licensed Content Title	Long-term imaging of cellular forces with high precision by elastic resonator interference stress microscopy
Licensed Content Author	Nils M. Kronenberg et al
Licensed Content Date	Jun 19, 2017
Type of Use	Thesis/Dissertation
Requestor type	academic/university or research institute
Format	electronic
Portion	figures/tables/illustrations
Number of figures/tables/illustrations	1
High-res required	no
Will you be translating?	no
Circulation/distribution	1 - 29
Author of this Springer Nature content	no
Title	DNA nanotechnology to map and manipulate podosome forces on fluid interfaces
Institution name	GT/Emory
Expected presentation date	Mar 2020
Portions	3
Requestor Location	Roxanne J Glazier 1515 Dickey Drive

ATLANTA, GA 30322
United States
Attn: Roxanne J Glazier
0.00 USD

Total

[BACK](#)

License Details

This Agreement between Roxanne J Glazier ("You") and Elsevier ("Elsevier") consists of your license details and the terms and conditions provided by Elsevier and Copyright Clearance Center.

[Print](#)[Copy](#)

License Number	4780870567405
License date	Mar 02, 2020
Licensed Content Publisher	Elsevier
Licensed Content Publication	Current Biology
Licensed Content Title	Self-Organized Podosomes Are Dynamic Mechanosensors
Licensed Content Author	Olivier Collin,Sungsoo Na,Farhan Chowdhury,Michael Hong,Myung Eun Shin,Fei Wang,Ning Wang
Licensed Content Date	Sep 9, 2008
Licensed Content Volume	18
Licensed Content Issue	17
Licensed Content Pages	7
Type of Use	reuse in a thesis/dissertation
Portion	figures/tables/illustrations
Number of figures/tables/illustrations	1
Format	electronic
Are you the author of this Elsevier article?	No
Will you be translating?	No
Title	DNA nanotechnology to map and manipulate podosome forces on fluid interfaces
Institution name	GT/Emory
Expected presentation date	Mar 2020
Portions	2
Requestor Location	Roxanne J Glazier 1515 Dickey Drive ATLANTA, GA 30322 United States Attn: Roxanne J Glazier 98-0397604
Publisher Tax ID	98-0397604
Total	0.00 USD

[BACK](#)

Podosome Force Generation Machinery: A Local Balance between Protrusion at the Core and Traction at the Ring



Author: Anaïs Bouissou, Amsha Proag, Nicolas Bourg, et al

Publication: ACS Nano

Publisher: American Chemical Society

Date: Apr 1, 2017

Copyright © 2017, American Chemical Society

PERMISSION/LICENSE IS GRANTED FOR YOUR ORDER AT NO CHARGE

This type of permission/license, instead of the standard Terms & Conditions, is sent to you because no fee is being charged for your order. Please note the following:

- Permission is granted for your request in both print and electronic formats, and translations.
 - If figures and/or tables were requested, they may be adapted or used in part.
 - Please print this page for your records and send a copy of it to your publisher/graduate school.
 - Appropriate credit for the requested material should be given as follows: "Reprinted (adapted) with permission from (COMPLETE REFERENCE CITATION). Copyright (YEAR) American Chemical Society." Insert appropriate information in place of the capitalized words.
 - One-time permission is granted only for the use specified in your request. No additional uses are granted (such as derivative works or other editions). For any other uses, please submit a new request.
- If credit is given to another source for the material you requested, permission must be obtained from that source.

BACK

CLOSE WINDOW

License Details

This Agreement between Roxanne J Glazier ("You") and Springer Nature ("Springer Nature") consists of your license details and the terms and conditions provided by Springer Nature and Copyright Clearance Center.

Print

Copy

License Number	4780860128360
License date	Mar 02, 2020
Licensed Content Publisher	Springer Nature
Licensed Content Publication	Nature Methods
Licensed Content Title	Bayesian localization microscopy reveals nanoscale podosome dynamics
Licensed Content Author	Susan Cox et al
Licensed Content Date	Dec 4, 2011
Type of Use	Thesis/Dissertation
Requestor type	academic/university or research institute
Format	electronic
Portion	figures/tables/illustrations
Number of figures/tables/illustrations	1
High-res required	no
Will you be translating?	no
Circulation/distribution	1 - 29
Author of this Springer Nature content	no
Title	DNA nanotechnology to map and manipulate podosome forces on fluid interfaces
Institution name	GT/Emory
Expected presentation date	Mar 2020
Portions	2F
Requestor Location	Roxanne J Glazier 1515 Dickey Drive ATLANTA, GA 30322 United States Attn: Roxanne J Glazier
Total	0.00 USD

BACK

License Details

This Agreement between Roxanne J Glazier ("You") and Springer Nature ("Springer Nature") consists of your license details and the terms and conditions provided by Springer Nature and Copyright Clearance Center.

[Print](#)[Copy](#)

License Number	4780871369346
License date	Mar 02, 2020
Licensed Content Publisher	Springer Nature
Licensed Content Publication	Springer eBook
Licensed Content Title	Choosing Reporter-Quencher Pairs for Efficient Quenching Through Formation of Intramolecular Dimers
Licensed Content Author	Mary Katherine Johansson
Licensed Content Date	Jan 1, 2006
Type of Use	Thesis/Dissertation
Requestor type	academic/university or research institute
Format	electronic
Portion	figures/tables/illustrations
Number of figures/tables/illustrations	1
Will you be translating?	no
Circulation/distribution	1 - 29
Author of this Springer Nature content	no
Title	DNA nanotechnology to map and manipulate podosome forces on fluid interfaces
Institution name	GT/Emory
Expected presentation date	Mar 2020
Portions	1
Requestor Location	Roxanne J Glazier 1515 Dickey Drive ATLANTA, GA 30322 United States Attn: Roxanne J Glazier
Total	0.00 USD

[BACK](#)

Formation of Supported Bilayers on Silica Substrates

Author: Travers H. Anderson, Younjin Min, Kim L. Weirich, et al

Publication: Langmuir

Publisher: American Chemical Society

Date: Jun 1, 2009

Copyright © 2009, American Chemical Society



PERMISSION/LICENSE IS GRANTED FOR YOUR ORDER AT NO CHARGE

This type of permission/license, instead of the standard Terms & Conditions, is sent to you because no fee is being charged for your order. Please note the following:

- Permission is granted for your request in both print and electronic formats, and translations.
 - If figures and/or tables were requested, they may be adapted or used in part.
 - Please print this page for your records and send a copy of it to your publisher/graduate school.
 - Appropriate credit for the requested material should be given as follows: "Reprinted (adapted) with permission from (COMPLETE REFERENCE CITATION). Copyright (YEAR) American Chemical Society." Insert appropriate information in place of the capitalized words.
 - One-time permission is granted only for the use specified in your request. No additional uses are granted (such as derivative works or other editions). For any other uses, please submit a new request.
- If credit is given to another source for the material you requested, permission must be obtained from that source.

[BACK](#)

[CLOSE WINDOW](#)

Control of Cell Adhesion and Growth with Micropatterned Supported Lipid Membranes

Author: Jay T. Groves, Lara K. Mahal, Carolyn R. Bertozzi

Publication: Langmuir

Publisher: American Chemical Society

Date: Aug 1, 2001

Copyright © 2001, American Chemical Society



PERMISSION/LICENSE IS GRANTED FOR YOUR ORDER AT NO CHARGE

This type of permission/license, instead of the standard Terms & Conditions, is sent to you because no fee is being charged for your order. Please note the following:

- Permission is granted for your request in both print and electronic formats, and translations.
 - If figures and/or tables were requested, they may be adapted or used in part.
 - Please print this page for your records and send a copy of it to your publisher/graduate school.
 - Appropriate credit for the requested material should be given as follows: "Reprinted (adapted) with permission from (COMPLETE REFERENCE CITATION). Copyright (YEAR) American Chemical Society." Insert appropriate information in place of the capitalized words.
 - One-time permission is granted only for the use specified in your request. No additional uses are granted (such as derivative works or other editions). For any other uses, please submit a new request.
- If credit is given to another source for the material you requested, permission must be obtained from that source.

[BACK](#)

[CLOSE WINDOW](#)

License Number 4796540057927

[Printable Details](#)

License date Mar 26, 2020

Licensed Content

Licensed Content Publisher John Wiley and Sons
Licensed Content Publication Advanced Materials
Licensed Content Title Printing via Photolithography on Micropartitioned Fluid Lipid Membranes
Licensed Content Author S. G. Boxer, N. Ulman, J. T. Groves, et al
Licensed Content Date May 22, 2000
Licensed Content Volume 12
Licensed Content Issue 10
Licensed Content Pages 4

Order Details

Type of use Dissertation/Thesis
Requestor type University/Academic
Format Electronic
Portion Figure/table
Number of figures/tables 1
Will you be translating? No

About Your Work

Title of your thesis / dissertation DNA nanotechnology to map and manipulate podosome forces on fluid interfaces
Expected completion date Mar 2020
Expected size (number of pages) 1

Additional Data

Original Wiley figure/table number(s) 3

Requestor Location

Roxanne J Glazier
1515 Dickey Drive

Requestor Location
ATLANTA, GA 30322
United States
Attn: Roxanne J Glazier

Tax Details

Publisher Tax ID EU826007151

Price

Total 0.00 USD



Size-Tunable Organic Nanodot Arrays: A Versatile Platform for Manipulating and Imaging Cells

Author: Fuwei Pi, Pierre Dillard, Ranime Alameddine, et al

Publication: Nano Letters

Publisher: American Chemical Society

Date: Aug 1, 2015

Copyright © 2015, American Chemical Society

PERMISSION/LICENSE IS GRANTED FOR YOUR ORDER AT NO CHARGE

This type of permission/license, instead of the standard Terms & Conditions, is sent to you because no fee is being charged for your order. Please note the following:

- Permission is granted for your request in both print and electronic formats, and translations.
 - If figures and/or tables were requested, they may be adapted or used in part.
 - Please print this page for your records and send a copy of it to your publisher/graduate school.
 - Appropriate credit for the requested material should be given as follows: "Reprinted (adapted) with permission from (COMPLETE REFERENCE CITATION). Copyright (YEAR) American Chemical Society." Insert appropriate information in place of the capitalized words.
 - One-time permission is granted only for the use specified in your request. No additional uses are granted (such as derivative works or other editions). For any other uses, please submit a new request.
- If credit is given to another source for the material you requested, permission must be obtained from that source.

[BACK](#)[CLOSE WINDOW](#)

License date Mar 26, 2020

Licensed Content

Licensed Content Publisher	The American Association for the Advancement of Science
Licensed Content Publication	Science
Licensed Content Title	Restriction of Receptor Movement Alters Cellular Response: Physical Force Sensing by EphA2
Licensed Content Author	Khalid Salaita, Pradeep M. Nair, Rebecca S. Petit, Richard M. Neve, Debopriya Das, Joe W. Gray, Jay T. Groves
Licensed Content Date	Mar 12, 2010
Licensed Content Volume	327
Licensed Content Issue	5971

About Your Work

Title	DNA nanotechnology to map and manipulate podosome forces on fluid interfaces
Institution name	GT/Emory
Expected presentation date	Mar 2020

Requestor Location

	Roxanne J Glazier 1515 Dickey Drive
Requestor Location	ATLANTA, GA 30322 United States Attn: Roxanne J Glazier

Price

Total	0.00 USD
-------	----------

Order Details

Type of Use	Thesis / Dissertation
Requestor type	Scientist/individual at a research institution
Format	Electronic
Portion	Text Excerpt
Number of pages requested	1

Additional Data

Portions	Fig 3A
----------	--------

Tax Details

Ratiometric Tension Probes for Mapping Receptor Forces and Clustering at Intermembrane Junctions



Author: Victor Pui-Yan Ma, Yang Liu, Lori Blanchfield, et al

Publication: Nano Letters

Publisher: American Chemical Society

Date: Jul 1, 2016

Copyright © 2016, American Chemical Society

PERMISSION/LICENSE IS GRANTED FOR YOUR ORDER AT NO CHARGE

This type of permission/license, instead of the standard Terms & Conditions, is sent to you because no fee is being charged for your order. Please note the following:

- Permission is granted for your request in both print and electronic formats, and translations.
 - If figures and/or tables were requested, they may be adapted or used in part.
 - Please print this page for your records and send a copy of it to your publisher/graduate school.
 - Appropriate credit for the requested material should be given as follows: "Reprinted (adapted) with permission from (COMPLETE REFERENCE CITATION). Copyright (YEAR) American Chemical Society." Insert appropriate information in place of the capitalized words.
 - One-time permission is granted only for the use specified in your request. No additional uses are granted (such as derivative works or other editions). For any other uses, please submit a new request.
- If credit is given to another source for the material you requested, permission must be obtained from that source.

[BACK](#)

[CLOSE WINDOW](#)

Your confirmation email will contain your order number for future reference.

License Number 4796550402600

[Printable Details](#)

License date Mar 26, 2020

Licensed Content

Licensed Content Publisher Springer Nature
Licensed Content Publication Nature Immunology
Licensed Content Title Germinal center B cells recognize antigen through a specialized immune synapse architecture
Licensed Content Author Carla R Nowosad et al
Licensed Content Date May 16, 2016

Order Details

Type of Use Thesis/Dissertation
Requestor type academic/university or research institute
Format electronic
Portion figures/tables/illustrations
Number of figures/tables/illustrations 1
High-res required no
Will you be translating? no
Circulation/distribution 1 - 29
Author of this Springer Nature content no

About Your Work

Title DNA nanotechnology to map and manipulate podosome forces on fluid interfaces
Institution name GT/Emory
Expected presentation date Mar 2020

Additional Data

Portions F7

Requestor Location

Roxanne J Glazier
1515 Dickey Drive

Requestor Location ATLANTA, GA 30322
United States
Attn: Roxanne J Glazier

Tax Details

Price

Total 0.00 USD

Effects of Supported Lipid Monolayer Fluidity on the Adhesion of Hematopoietic Progenitor Cell Lines to Fibronectin-Derived Peptide Ligands for $\alpha 5\beta 1$ and $\alpha 4\beta 1$ Integrins



Author: A. Sofia Garcia, Shara M. Dellatore, Phillip B. Messersmith, et al

Publication: Langmuir

Publisher: American Chemical Society

Date: Mar 1, 2009

Copyright © 2009, American Chemical Society

PERMISSION/LICENSE IS GRANTED FOR YOUR ORDER AT NO CHARGE

This type of permission/license, instead of the standard Terms & Conditions, is sent to you because no fee is being charged for your order. Please note the following:

- Permission is granted for your request in both print and electronic formats, and translations.
 - If figures and/or tables were requested, they may be adapted or used in part.
 - Please print this page for your records and send a copy of it to your publisher/graduate school.
 - Appropriate credit for the requested material should be given as follows: "Reprinted (adapted) with permission from (COMPLETE REFERENCE CITATION). Copyright (YEAR) American Chemical Society." Insert appropriate information in place of the capitalized words.
 - One-time permission is granted only for the use specified in your request. No additional uses are granted (such as derivative works or other editions). For any other uses, please submit a new request.
- If credit is given to another source for the material you requested, permission must be obtained from that source.

[BACK](#)[CLOSE WINDOW](#)

License Number 4796570166223

[Printable Details](#)

License date Mar 26, 2020

Licensed Content

Licensed Content Publisher John Wiley and Sons
Licensed Content Publication Advanced Healthcare Materials
Guiding hMSC Adhesion and Differentiation on Supported Lipid Bilayers
Licensed Content Title
Licensed Content Author Gülistan Koçer, Pascal Jonkheijm
Licensed Content Date Nov 28, 2016
Licensed Content Volume 6
Licensed Content Issue 3
Licensed Content Pages 11

Order Details

Type of use Dissertation/Thesis
Requestor type University/Academic
Format Electronic
Portion Figure/table
Number of figures/tables 1
Will you be translating? No

About Your Work

Title of your thesis / dissertation DNA nanotechnology to map and manipulate podosome forces on fluid interfaces
Expected completion date Mar 2020
Expected size (number of pages) 1

Additional Data

Original Wiley figure/table number(s) 2

Requestor Location

Roxanne J Glazier
1515 Dickey Drive
Requestor Location ATLANTA, GA 30322
United States
Attn: Roxanne J Glazier

Tax Details

Publisher Tax ID EU826007151

Price

Total 0.00 USD

Billing Address

Roxanne Glazier
General Delivery
1515 Dickey Drive
Atlanta, GA 30322
United States
+1 (617) 875-9132
roxanne.glazier@emory.edu

PO Number (optional)

N/A

Customer Location

Roxanne Glazier
General Delivery
1515 Dickey Drive
Atlanta, GA 30322
United States

Payment options

Invoice

PENDING ORDER CONFIRMATION**Total Due: 0.00 USD**

Confirmation Number: Pending

[Print Friendly Format](#)

Order Date: 26-Mar-2020

Includes Publisher Terms and Conditions

1. Soft matter**0.00 USD**

Order license ID
ISSN
Type of Use

Pending
1744-6848
Republish in a thesis/dissertation

Publisher
Portion

ROYAL SOCIETY OF CHEMISTRY
Chart/graph/table/figure

[View Details](#)[Print License](#)**2. Soft matter****0.00 USD**

Order license ID
ISSN
Type of Use

Pending
1744-6848
Republish in a thesis/dissertation

Publisher
Portion

ROYAL SOCIETY OF CHEMISTRY
Chart/graph/table/figure

[View Details](#)[Print License](#)**Total Items: 2****Order Total: 0.00 USD****Total Due: 0.00 USD**

License Number 4796581096701

[Printable Details](#)

License date Mar 26, 2020

Licensed Content

Licensed Content Publisher John Wiley and Sons
Licensed Content Publication Advanced Healthcare Materials
Dynamic Cellular Interactions with
Extracellular Matrix Triggered by
Biomechanical Tuning of Low-Rigidity,
Supported Lipid Membranes
Licensed Content Title
Licensed Content Author Nam-Joon Cho, Jay T. Groves, Kabir H.
Biswas, et al
Licensed Content Date Mar 30, 2017
Licensed Content Volume 6
Licensed Content Issue 10
Licensed Content Pages 8

About Your Work

Title of your thesis / dissertation DNA Nanotechnology to Map and
Manipulate Adhesion Forces at Fluid
Interfaces
Expected completion date May 2020
Expected size (number of pages) 300

Requestor Location

Requestor Location Roxanne J Glazier
1515 Dickey Drive
ATLANTA, GA 30322
United States
Attn: Roxanne J Glazier

Price

Total 0.00 USD

Order Details

Type of use Dissertation/Thesis
Requestor type University/Academic
Format Electronic
Portion Figure/table
Number of figures/tables 1
Will you be translating? No

Additional Data

Original Wiley figure/table number(s) F3

Tax Details

Publisher Tax ID EU826007151

Licensed Content

Licensed Content Publisher	Elsevier
Licensed Content Publication	Developmental Cell
Licensed Content Title	Nascent Integrin Adhesions Form on All Matrix Rigidities after Integrin Activation
Licensed Content Author	Rishita Changede,Xiaochun Xu,Felix Margadant,Michael P. Sheetz
Licensed Content Date	7 December 2015
Licensed Content Volume	35
Licensed Content Issue	5
Licensed Content Pages	8
Journal Type	S&T

About Your Work

Title	DNA nanotechnology to map and manipulate adhesion forces at fluid interfaces
Institution name	GT/Emory
Expected presentation date	Mar 2020

Requestor Location

	Roxanne J Glazier 1515 Dickey Drive
Requestor Location	ATLANTA, GA 30322 United States Attn: Roxanne J Glazier

Price

Total	0.00 USD
-------	----------

Order Details

Type of Use	reuse in a thesis/dissertation
Portion	figures/tables/illustrations
Number of figures/tables/illustrations	1
Format	electronic
Are you the author of this Elsevier article?	No
Will you be translating?	No


Additional Data

Portions	2
----------	---

Tax Details

Publisher Tax ID	98-0397604
------------------	------------

License Number 4796780165506

 [Printable Details](#)

License date Mar 26, 2020

Licensed Content

Licensed Content Publisher	Elsevier
Licensed Content Publication	CELL REPORTS
Licensed Content Title	Integrin-Matrix Clusters Form Podosome-like Adhesions in the Absence of Traction Forces Cheng-han Yu,Nisha Bte Mohd Rafiq,Anitha Krishnasamy,Kevin L. Hartman,Gareth E. Jones,Alexander D. Bershadsky,Michael P. Sheetz
Licensed Content Author	Krishnasamy,Kevin L. Hartman,Gareth E. Jones,Alexander D. Bershadsky,Michael P. Sheetz
Licensed Content Date	Dec 12, 2013
Licensed Content Volume	5
Licensed Content Issue	5
Licensed Content Pages	13
Journal Type	HS

Order Details

Type of Use	reuse in a thesis/dissertation
Portion	figures/tables/illustrations
Number of figures/tables/illustrations	2
Format	electronic
Are you the author of this Elsevier article?	No
Will you be translating?	No

About Your Work

Title	DNA nanotechnology to map and manipulate adhesion forces at fluid interfaces
Institution name	GT/Emory
Expected presentation date	Mar 2020

Additional Data

Portions	1,2
----------	-----

Requestor Location

	Roxanne J Glazier 1515 Dickey Drive
Requestor Location	ATLANTA, GA 30322 United States Attn: Roxanne J Glazier

Tax Details

Publisher Tax ID	98-0397604
------------------	------------

Price

Total	0.00 USD
-------	----------

License Number 4796780757552

[Printable Details](#)

License date Mar 26, 2020

Licensed Content

Licensed Content Publisher	Elsevier
Licensed Content Publication	Biophysical Journal
Licensed Content Title	Sustained α -catenin Activation at E-cadherin Junctions in the Absence of Mechanical Force
Licensed Content Author	Kabir H. Biswas, Kevin L. Hartman, Ronen Zaidel-Bar, Jay T. Groves
Licensed Content Date	Sep 6, 2016
Licensed Content Volume	111
Licensed Content Issue	5
Licensed Content Pages	9
Journal Type	S&T

About Your Work

Title	DNA nanotechnology to map and manipulate adhesion forces at fluid interfaces
Institution name	GT/Emory
Expected presentation date	Mar 2020

Requestor Location

	Roxanne J Glazier 1515 Dickey Drive
Requestor Location	ATLANTA, GA 30322 United States Attn: Roxanne J Glazier

Price

Total	0.00 USD
-------	----------

Order Details

Type of Use	reuse in a thesis/dissertation
Portion	figures/tables/illustrations
Number of figures/tables/illustrations	1
Format	electronic
Are you the author of this Elsevier article?	No
Will you be translating?	No

Additional Data

Portions	F4
----------	----

Tax Details

Publisher Tax ID	98-0397604
------------------	------------

Total: 0.00 USD

REFERENCES

1. Groves JT, Mahal LK, Bertozzi CR. Control of cell adhesion and growth with micropatterned supported lipid membranes. *Langmuir : the ACS journal of surfaces and colloids* **17**, 5129-5133 (2001).
2. Kahya N, Schwille P. How Phospholipid-Cholesterol Interactions Modulate Lipid Lateral Diffusion, as Revealed by Fluorescence Correlation Spectroscopy. *Journal of Fluorescence* **16**, 671-678 (2006).
3. Pompe T, *et al.* Friction-Controlled Traction Force in Cell Adhesion. *Biophysical journal* **101**, 1863-1870.
4. Anderson TH, Min Y, Weirich KL, Zeng H, Fygenson D, Israelachvili JN. Formation of Supported Bilayers on Silica Substrates. *Langmuir : the ACS journal of surfaces and colloids* **25**, 6997-7005 (2009).
5. Biswas KH, *et al.* E-cadherin junction formation involves an active kinetic nucleation process. *Proc Natl Acad Sci U S A* **112**, 10932-10937 (2015).
6. Yu C-h, Law JBK, Suryana M, Low HY, Sheetz MP. Early integrin binding to Arg-Gly-Asp peptide activates actin polymerization and contractile movement that stimulates outward translocation. *Proceedings of the National Academy of Sciences* **108**, 20585-20590 (2011).
7. Glazier R, Salaita K. Location, Location, Location: EphB4:Ephrin-B2 Signaling Depends on Its Spatial Arrangement. *Biophysical journal* **115**, 754-756 (2018).
8. Ma VP-Y, Liu Y, Blanchfield L, Su H, Evavold BD, Salaita K. Ratiometric Tension Probes for Mapping Receptor Forces and Clustering at Intermembrane Junctions. *Nano Letters* **16**, 4552-4559 (2016).

9. Yu CH, *et al.* Integrin-matrix clusters form podosome-like adhesions in the absence of traction forces. *Cell reports* **5**, 1456-1468 (2013).
10. Nowosad CR, Spillane KM, Tolar P. Germinal center B cells recognize antigen through a specialized immune synapse architecture. *Nature immunology* **17**, 870-877 (2016).
11. Kung LA, Groves JT, Ulman N, Boxer SG. Printing via photolithography on micropartitioned fluid lipid membranes. *Advanced Materials* **12**, 731-+ (2000).
12. Biswas KH, Hartman KL, Zaidel-Bar R, Groves JT. Sustained alpha-catenin Activation at E-cadherin Junctions in the Absence of Mechanical Force. *Biophysical journal* **111**, 1044-1052 (2016).
13. Plotnikov SV, Pasapera AM, Sabass B, Waterman CM. Force fluctuations within focal adhesions mediate ECM-rigidity sensing to guide directed cell migration. *Cell* **151**, 1513-1527 (2012).
14. Pi F, *et al.* Size-Tunable Organic Nanodot Arrays: A Versatile Platform for Manipulating and Imaging Cells. *Nano Lett* **15**, 5178-5184 (2015).
15. Minner DE, Herring VL, Siegel AP, Kimble-Hill A, Johnson MA, Naumann CA. Iterative layer-by-layer assembly of polymer-tethered multi-bilayers using maleimide-thiol coupling chemistry. *Soft matter* **9**, 9643-9650 (2013).
16. Salaita K, *et al.* Restriction of Receptor Movement Alters Cellular Response: Physical Force Sensing by EphA2. *Science* **327**, 1380-1385 (2010).
17. Ge Y, Lin YH, Lautscham LA, Goldmann WH, Fabry B, Naumann CA. N-cadherin-functionalized polymer-tethered multi-bilayer: a cell surface-mimicking substrate to probe cellular mechanosensitivity. *Soft matter* **12**, 8274-8284 (2016).

18. Humphries JD, Byron A, Humphries MJ. Integrin ligands at a glance. *Journal of Cell Science* **119**, 3901-3903 (2006).
19. Kong F, Garcia AJ, Mould AP, Humphries MJ, Zhu C. Demonstration of catch bonds between an integrin and its ligand. *The Journal of cell biology* **185**, 1275-1284 (2009).
20. Kechagia JZ, Ivaska J, Roca-Cusachs P. Integrins as biomechanical sensors of the microenvironment. *Nature Reviews Molecular Cell Biology* **20**, 457-473 (2019).
21. Brockman JM, *et al.* Mapping the 3D orientation of piconewton integrin traction forces. *Nat Methods* **15**, 115-118 (2018).
22. Kanchanawong P, *et al.* Nanoscale architecture of integrin-based cell adhesions. *Nature* **468**, 580-584 (2010).
23. Murphy DA, Courtneidge SA. The 'ins' and 'outs' of podosomes and invadopodia: characteristics, formation and function. *Nature reviews Molecular cell biology* **12**, 413-426 (2011).
24. Block MR, *et al.* Podosome-type adhesions and focal adhesions, so alike yet so different. *European journal of cell biology* **87**, 491-506 (2008).
25. Takito J, Inoue S, Nakamura M. The Sealing Zone in Osteoclasts: A Self-Organized Structure on the Bone. *International journal of molecular sciences* **19**, (2018).
26. Linder S, Wiesner C. Feel the force: Podosomes in mechanosensing. *Experimental cell research* **343**, 67-72 (2016).

27. Sage PT, *et al.* Antigen Recognition is Facilitated by Invadosome-Like Protrusions Formed by Memory/Effector T Cells. *Journal of Immunology (Baltimore, Md : 1950)* **188**, 3686-3699 (2012).
28. Carman CV, *et al.* Transcellular diapedesis is initiated by invasive podosomes. *Immunity* **26**, 784-797 (2007).
29. Faust JJ, *et al.* An actin-based protrusion originating from a podosome-enriched region initiates macrophage fusion. *Mol Biol Cell* **30**, 2254-2267 (2019).
30. Zhang Y, Ge C, Zhu C, Salaita K. DNA-based digital tension probes reveal integrin forces during early cell adhesion. *Nature communications* **5**, 5167 (2014).
31. Galior K, Liu Y, Yehl K, Vivek S, Salaita K. Titin-based Nanoparticle Tension Sensors Map High-Magnitude Integrin Forces within Focal Adhesions. *Nano letters* **16**, 341-348 (2016).
32. Morimatsu M, Mekhdjian AH, Adhikari AS, Dunn AR. Molecular tension sensors report forces generated by single integrin molecules in living cells. *Nano Lett* **13**, 3985-3989 (2013).
33. Glazier R, Brockman JM, Bartle E, Mattheyses AL, Destaing O, Salaita K. DNA mechanotechnology reveals that integrin receptors apply pN forces in podosomes on fluid substrates. *Nature communications* **10**, 4507 (2019).
34. Liu Y, Galior K, Ma VP, Salaita K. Molecular Tension Probes for Imaging Forces at the Cell Surface. *Accounts of chemical research* **50**, 2915-2924 (2017).
35. Schachtner H, Calaminus SD, Thomas SG, Machesky LM. Podosomes in adhesion, migration, mechanosensing and matrix remodeling. *Cytoskeleton (Hoboken, NJ)* **70**, 572-589 (2013).

36. van den Dries K, Bolomini-Vittori M, Cambi A. Spatiotemporal organization and mechanosensory function of podosomes. *Cell adhesion & migration* **8**, 268-272 (2014).
37. Veillat V, Spuul P, Daubon T, Egana I, Kramer I, Genot E. Podosomes: Multipurpose organelles? *The international journal of biochemistry & cell biology* **65**, 52-60 (2015).
38. David-Pfeuty T, Singer SJ. Altered distributions of the cytoskeletal proteins vinculin and alpha-actinin in cultured fibroblasts transformed by Rous sarcoma virus. *Proc Natl Acad Sci U S A* **77**, 6687-6691 (1980).
39. Tarone G, Cirillo D, Giancotti FG, Comoglio PM, Marchisio PC. Rous sarcoma virus-transformed fibroblasts adhere primarily at discrete protrusions of the ventral membrane called podosomes. *Experimental cell research* **159**, 141-157 (1985).
40. El Azzouzi K, Wiesner C, Linder S. Metalloproteinase MT1-MMP islets act as memory devices for podosome reemergence. *The Journal of cell biology* **213**, 109-125 (2016).
41. Linder S, Aepfelbacher M. Podosomes: adhesion hot-spots of invasive cells. *Trends in cell biology* **13**, 376-385 (2003).
42. Georgess D, Machuca-Gayet I, Blangy A, Jurdic P. Podosome organization drives osteoclast-mediated bone resorption. *Cell adhesion & migration* **8**, 191-204 (2014).
43. Poulter NS, *et al.* Platelet actin nodules are podosome-like structures dependent on Wiskott-Aldrich syndrome protein and ARP2/3 complex. *Nature communications* **6**, 7254-7254 (2015).
44. Joosten B, Willemse M, Fransen J, Cambi A, van den Dries K. Super-Resolution Correlative Light and Electron Microscopy (SR-CLEM) Reveals Novel

Ultrastructural Insights Into Dendritic Cell Podosomes. *Frontiers in immunology* **9**, 1908 (2018).

45. van den Dries K, *et al.* Geometry sensing by dendritic cells dictates spatial organization and PGE(2)-induced dissolution of podosomes. *Cellular and molecular life sciences : CMLS* **69**, 1889-1901 (2012).
46. Shilagardi K, *et al.* Actin-propelled invasive membrane protrusions promote fusogenic protein engagement during cell-cell fusion. *Science* **340**, 359-363 (2013).
47. Sung BH, Weaver A. Cell-cell fusion: a new function for invadosomes. *Curr Biol* **21**, R121-R123 (2011).
48. Eddy RJ, Weidmann MD, Sharma VP, Condeelis JS. Tumor Cell Invadopodia: Invasive Protrusions that Orchestrate Metastasis. *Trends in cell biology* **27**, 595-607 (2017).
49. Hoshino D, *et al.* Exosome secretion is enhanced by invadopodia and drives invasive behavior. *Cell reports* **5**, 1159-1168 (2013).
50. Razidlo GL, *et al.* Targeting Pancreatic Cancer Metastasis by Inhibition of Vav1, a Driver of Tumor Cell Invasion. *Cancer Research* **75**, 2907-2915 (2015).
51. Li Y, *et al.* miR-182 suppresses invadopodia formation and metastasis in non-small cell lung cancer by targeting cortactin gene. *Journal of Experimental & Clinical Cancer Research* **37**, 141 (2018).
52. Buchbinder D, Nugent DJ, Fillipovich AH. Wiskott–Aldrich syndrome: diagnosis, current management, and emerging treatments. *The Application of Clinical Genetics* **7**, 55-66 (2014).

53. Linder S, Nelson D, Weiss M, Aepfelbacher M. Wiskott-Aldrich syndrome protein regulates podosomes in primary human macrophages. *Proc Natl Acad Sci U S A* **96**, 9648-9653 (1999).
54. Calle Y, *et al.* WASp deficiency in mice results in failure to form osteoclast sealing zones and defects in bone resorption. *Blood* **103**, 3552-3561 (2004).
55. Iqbal Z, *et al.* Disruption of the Podosome Adaptor Protein TKS4 (*SH3PXD2B*) Causes the Skeletal Dysplasia, Eye, and Cardiac Abnormalities of Frank-Ter Haar Syndrome. *The American Journal of Human Genetics* **86**, 254-261 (2010).
56. Buschman MD, Bromann PA, Cejudo-Martin P, Wen F, Pass I, Courtneidge SA. The novel adaptor protein Tks4 (*SH3PXD2B*) is required for functional podosome formation. *Mol Biol Cell* **20**, 1302-1311 (2009).
57. Raynaud-Messina B, *et al.* Bone degradation machinery of osteoclasts: An HIV-1 target that contributes to bone loss. *Proc Natl Acad Sci U S A* **115**, E2556-e2565 (2018).
58. Verollet C, *et al.* HIV-1 reprograms the migration of macrophages. *Blood* **125**, 1611-1622 (2015).
59. Gimona M, Buccione R, Courtneidge SA, Linder S. Assembly and biological role of podosomes and invadopodia. *Current Opinion in Cell Biology* **20**, 235-241 (2008).
60. Gawden-Bone C, Zhou Z, King E, Prescott A, Watts C, Lucocq J. Dendritic cell podosomes are protrusive and invade the extracellular matrix using metalloproteinase MMP-14. *Journal of cell science* **123**, 1427-1437 (2010).
61. van den Dries K, *et al.* Dual-color superresolution microscopy reveals nanoscale organization of mechanosensory podosomes. *Mol Biol Cell* **24**, 2112-2123 (2013).

62. Luxenburg C, *et al.* The Architecture of the Adhesive Apparatus of Cultured Osteoclasts: From Podosome Formation to Sealing Zone Assembly. *PLOS ONE* **2**, e179 (2007).
63. Bhuwania R, Cornfine S, Fang Z, Kruger M, Luna EJ, Linder S. Supervillin couples myosin-dependent contractility to podosomes and enables their turnover. *J Cell Sci* **125**, 2300-2314 (2012).
64. van den Dries K, *et al.* Modular actin nano-architecture enables podosome protrusion and mechanosensing. *Nature communications* **10**, 5171 (2019).
65. Bouissou A, *et al.* Podosome Force Generation Machinery: A Local Balance between Protrusion at the Core and Traction at the Ring. *ACS nano* **11**, 4028-4040 (2017).
66. Proag A, *et al.* Working together: spatial synchrony in the force and actin dynamics of podosome first neighbors. *ACS nano* **9**, 3800-3813 (2015).
67. Cox S, *et al.* Bayesian localization microscopy reveals nanoscale podosome dynamics. *Nat Methods* **9**, 195-200 (2011).
68. Kuo S-L, Chen C-L, Pan Y-R, Chiu W-T, Chen H-C. Biogenesis of podosome rosettes through fission. *Scientific Reports* **8**, 524 (2018).
69. Destaing O, Saltel F, Géminard J-C, Jurdic P, Bard F. Podosomes display actin turnover and dynamic self-organization in osteoclasts expressing actin-green fluorescent protein. *Mol Biol Cell* **14**, 407-416 (2003).
70. Meddens MBM, *et al.* Actomyosin-dependent dynamic spatial patterns of cytoskeletal components drive mesoscale podosome organization. *Nature communications* **7**, 13127 (2016).

71. Luxenburg C, Winograd-Katz S, Addadi L, Geiger B. Involvement of actin polymerization in podosome dynamics. *J Cell Sci* **125**, 1666-1672 (2012).
72. Tanaka H, Wang H-H, Thatcher S, Hagiwara H, Takano-Ohmuro H, Kohama K. Electron microscopic examination of podosomes induced by phorbol 12, 13 dibutyrate on the surface of A7r5 cells. *Journal of Pharmacological Sciences* **280**, (2015).
73. Walde M, Monypenny J, Heintzmann R, Jones GE, Cox S. Vinculin binding angle in podosomes revealed by high resolution microscopy. *PloS one* **9**, e88251-e88251 (2014).
74. del Rio A, Perez-Jimenez R, Liu R, Roca-Cusachs P, Fernandez JM, Sheetz MP. Stretching single talin rod molecules activates vinculin binding. *Science* **323**, 638-641 (2009).
75. van den Dries K, *et al.* Interplay between myosin IIA-mediated contractility and actin network integrity orchestrates podosome composition and oscillations. *Nature communications* **4**, 1412 (2013).
76. Labernadie A, *et al.* Protrusion force microscopy reveals oscillatory force generation and mechanosensing activity of human macrophage podosomes. *Nature communications* **5**, 5343 (2014).
77. Labernadie A, Thibault C, Vieu C, Maridonneau-Parini I, Charriere GM. Dynamics of podosome stiffness revealed by atomic force microscopy. *Proc Natl Acad Sci U S A* **107**, 21016-21021 (2010).
78. Rafiq Nisha Bte M, *et al.* Forces and constraints controlling podosome assembly and disassembly. *Philosophical Transactions of the Royal Society B: Biological Sciences* **374**, 20180228 (2019).

79. Collin O, *et al.* Self-organized podosomes are dynamic mechanosensors. *Curr Biol* **18**, 1288-1294 (2008).
80. Kronenberg NM, *et al.* Long-term imaging of cellular forces with high precision by elastic resonator interference stress microscopy. *Nature cell biology* **19**, 864-872 (2017).
81. Tan JL, Tien J, Pirone DM, Gray DS, Bhadriraju K, Chen CS. Cells lying on a bed of microneedles: an approach to isolate mechanical force. *Proc Natl Acad Sci U S A* **100**, 1484-1489 (2003).
82. Kovar DR, Pollard TD. Insertional assembly of actin filament barbed ends in association with formins produces piconewton forces. *Proc Natl Acad Sci U S A* **101**, 14725-14730 (2004).
83. Rafiq NBM, *et al.* Podosome assembly is controlled by the GTPase ARF1 and its nucleotide exchange factor ARNO. *The Journal of cell biology* **216**, 181-197 (2017).
84. Glazier R, Salaita K. Supported lipid bilayer platforms to probe cell mechanobiology. *Biochimica et biophysica acta* **1859**, 1465-1482 (2017).
85. Bennett M, Cantini M, Reboud J, Cooper JM, Roca-Cusachs P, Salmeron-Sanchez M. Molecular clutch drives cell response to surface viscosity. *Proc Natl Acad Sci U S A* **115**, 1192-1197 (2018).
86. Yu C-h, *et al.* Integrin-beta3 clusters recruit clathrin-mediated endocytic machinery in the absence of traction force. *Nature communications* **6**, 8672-8672 (2015).
87. Lakowicz JR. *Principles of fluorescence spectroscopy*. Second edition. New York : Kluwer Academic/Plenum, [1999] ©1999 (1999).

88. BECKER W. Fluorescence lifetime imaging – techniques and applications. *Journal of Microscopy* **247**, 119-136 (2012).
89. Marras SAE, Kramer FR, Tyagi S. Efficiencies of fluorescence resonance energy transfer and contact-mediated quenching in oligonucleotide probes. *Nucleic Acids Res* **30**, e122-e122 (2002).
90. Hughes LD, Rawle RJ, Boxer SG. Choose Your Label Wisely: Water-Soluble Fluorophores Often Interact with Lipid Bilayers. *PLOS ONE* **9**, e87649 (2014).
91. Kasha M. Energy Transfer Mechanisms and the Molecular Exciton Model for Molecular Aggregates. *Radiation Research* **20**, 55-70 (1963).
92. Sillen A, Engelborghs Y. The Correct Use of “Average” Fluorescence Parameters. *Photochemistry and Photobiology* **67**, 475-486 (1998).
93. Johansson MK. Choosing Reporter-Quencher Pairs for Efficient Quenching Through Formation of Intramolecular Dimers. In: *Fluorescent Energy Transfer Nucleic Acid Probes: Designs and Protocols* (ed[^](eds Didenko VV). Humana Press (2006).
94. Wahl M. Modern TCSPC Electronics: Principles and Acquisition Modes. In: *Advanced Photon Counting: Applications, Methods, Instrumentation* (ed[^](eds Kapusta PW, Michael; Erdmann, Rainer). Springer (2015).
95. Changede R, Xu X, Margadant F, Sheetz MP. Nascent Integrin Adhesions Form on All Matrix Rigidities after Integrin Activation. *Developmental cell* **35**, 614-621 (2015).
96. Wang X, Ha T. Defining single molecular forces required to activate integrin and notch signaling. *Science* **340**, 991-994 (2013).

97. Bell G. Models for the specific adhesion of cells to cells. *Science* **200**, 618-627 (1978).
98. Minajeva A, Kulke M, Fernandez JM, Linke WA. Unfolding of titin domains explains the viscoelastic behavior of skeletal myofibrils. *Biophysical journal* **80**, 1442-1451 (2001).
99. Liu C, Montell C. Forcing open TRP channels: Mechanical gating as a unifying activation mechanism. *Biochemical and biophysical research communications* **460**, 22-25 (2015).
100. Gillespie PG, Muller U. Mechanotransduction by hair cells: models, molecules, and mechanisms. *Cell* **139**, 33-44 (2009).
101. Shawky JH, Davidson LA. Tissue mechanics and adhesion during embryo development. *Developmental biology* **401**, 152-164 (2015).
102. Steward AJ, Kelly DJ. Mechanical regulation of mesenchymal stem cell differentiation. *Journal of anatomy* **227**, 717-731 (2015).
103. Takahashi K, Kakimoto Y, Toda K, Naruse K. Mechanobiology in cardiac physiology and diseases. *Journal of cellular and molecular medicine* **17**, 225-232 (2013).
104. Kumar S, Weaver VM. Mechanics, malignancy, and metastasis: the force journey of a tumor cell. *Cancer metastasis reviews* **28**, 113-127 (2009).
105. Wan Z, *et al.* The activation of IgM- or isotype-switched IgG- and IgE-BCR exhibits distinct mechanical force sensitivity and threshold. *eLife* **4**, e06925 (2015).

106. Liu Y, *et al.* DNA-based nanoparticle tension sensors reveal that T-cell receptors transmit defined pN forces to their antigens for enhanced fidelity. *Proc Natl Acad Sci U S A* **113**, 5610-5615 (2016).
107. Chen W, Lou J, Evans EA, Zhu C. Observing force-regulated conformational changes and ligand dissociation from a single integrin on cells. *The Journal of cell biology* **199**, 497-512 (2012).
108. Luo BH, Springer TA. Integrin structures and conformational signaling. *Curr Opin Cell Biol* **18**, 579-586 (2006).
109. Ingber D. Integrins as mechanochemical transducers. *Curr Opin Cell Biol* **3**, 841-848 (1991).
110. Borghi N, *et al.* E-cadherin is under constitutive actomyosin-generated tension that is increased at cell–cell contacts upon externally applied stretch. *Proceedings of the National Academy of Sciences* **109**, 12568 (2012).
111. Leckband DE, de Rooij J. Cadherin adhesion and mechanotransduction. *Annual review of cell and developmental biology* **30**, 291-315 (2014).
112. Murrell M, Oakes PW, Lenz M, Gardel ML. Forcing cells into shape: the mechanics of actomyosin contractility. *Nature reviews Molecular cell biology* **16**, 486-498 (2015).
113. Peskin CS, Odell GM, Oster GF. Cellular motions and thermal fluctuations: the Brownian ratchet. *Biophysical journal* **65**, 316-324 (1993).
114. Sackmann E. How actin/myosin crosstalks guide the adhesion, locomotion and polarization of cells. *Biochimica et biophysica acta* **1853**, 3132-3142 (2015).

115. Lautscham LA, Lin CY, Auernheimer V, Naumann CA, Goldmann WH, Fabry B. Biomembrane-mimicking lipid bilayer system as a mechanically tunable cell substrate. *Biomaterials* **35**, 3198-3207 (2014).
116. Dustin ML. Insights into function of the immunological synapse from studies with supported planar bilayers. *Current topics in microbiology and immunology* **340**, 1-24 (2010).
117. Grakoui A, *et al.* The immunological synapse: a molecular machine controlling T cell activation. *Science* **285**, 221-227 (1999).
118. Brian AA, McConnell HM. Allogeneic stimulation of cytotoxic T cells by supported planar membranes. *Proc Natl Acad Sci U S A* **81**, 6159-6163 (1984).
119. Kalb E, Frey S, Tamm LK. Formation of supported planar bilayers by fusion of vesicles to supported phospholipid monolayers. *Biochimica et biophysica acta* **1103**, 307-316 (1992).
120. Tamm LK, McConnell HM. Supported phospholipid bilayers. *Biophysical journal* **47**, 105-113 (1985).
121. Zwang TJ, Fletcher WR, Lane TJ, Johal MS. Quantification of the layer of hydration of a supported lipid bilayer. *Langmuir : the ACS journal of surfaces and colloids* **26**, 4598-4601 (2010).
122. Mossman KD, Campi G, Groves JT, Dustin ML. Altered TCR signaling from geometrically repatterned immunological synapses. *Science* **310**, 1191-1193 (2005).
123. Yu CH, Groves JT. Engineering supported membranes for cell biology. *Medical & biological engineering & computing* **48**, 955-963 (2010).

124. van Weerd J, Karperien M, Jonkheijm P. Supported Lipid Bilayers for the Generation of Dynamic Cell-Material Interfaces. *Advanced healthcare materials* **4**, 2743-2779 (2015).
125. Rakshit S, Zhang Y, Manibog K, Shafraz O, Sivasankar S. Ideal, catch, and slip bonds in cadherin adhesion. *Proceedings of the National Academy of Sciences* **109**, 18815-18820 (2012).
126. Narui Y, Salaita K. Membrane tethered delta activates notch and reveals a role for spatio-mechanical regulation of the signaling pathway. *Biophysical journal* **105**, 2655-2665 (2013).
127. Sanchez MF, Levi V, Weidemann T, Carrer DC. Agonist mobility on supported lipid bilayers affects Fas mediated death response. *FEBS letters* **589**, 3527-3533 (2015).
128. Huang J, *et al.* The kinetics of two-dimensional TCR and pMHC interactions determine T-cell responsiveness. *Nature* **464**, 932-936 (2010).
129. Care BR, Soula HA. Receptor clustering affects signal transduction at the membrane level in the reaction-limited regime. *Physical review E, Statistical, nonlinear, and soft matter physics* **87**, 012720 (2013).
130. Manz BN, Jackson BL, Petit RS, Dustin ML, Groves J. T-cell triggering thresholds are modulated by the number of antigen within individual T-cell receptor clusters. *Proc Natl Acad Sci U S A* **108**, 9089-9094 (2011).
131. Villard V, *et al.* Synthetic RGD-containing alpha-helical coiled coil peptides promote integrin-dependent cell adhesion. *Journal of peptide science : an official publication of the European Peptide Society* **12**, 206-212 (2006).

132. Edwards LJ, Zarnitsyna VI, Hood JD, Evavold BD, Zhu C. Insights into T cell recognition of antigen: significance of two-dimensional kinetic parameters. *Frontiers in immunology* **3**, 86 (2012).
133. Garcia-Parajo MF, Cambi A, Torreno-Pina JA, Thompson N, Jacobson K. Nanoclustering as a dominant feature of plasma membrane organization. *Journal of Cell Science* **127**, 4995-5005 (2014).
134. Duke T, Graham I. Equilibrium mechanisms of receptor clustering. *Progress in biophysics and molecular biology* **100**, 18-24 (2009).
135. Dustin ML, Groves JT. Receptor signaling clusters in the immune synapse. *Annual review of biophysics* **41**, 543-556 (2012).
136. Selhuber-Unkel C, Lopez-Garcia M, Kessler H, Spatz JP. Cooperativity in adhesion cluster formation during initial cell adhesion. *Biophysical journal* **95**, 5424-5431 (2008).
137. Hartman NC, Nye JA, Groves JT. Cluster size regulates protein sorting in the immunological synapse. *Proceedings of the National Academy of Sciences* **106**, 12729-12734 (2009).
138. Mattheyses AL, Simon SM, Rappoport JZ. Imaging with total internal reflection fluorescence microscopy for the cell biologist. *Journal of Cell Science* **123**, 3621-3628 (2010).
139. Das C, Sheikh KH, Olmsted PD, Connell SD. Nanoscale mechanical probing of supported lipid bilayers with atomic force microscopy. *Physical review E, Statistical, nonlinear, and soft matter physics* **82**, 041920 (2010).
140. Portet T, Dimova R. A New Method for Measuring Edge Tensions and Stability of Lipid Bilayers: Effect of Membrane Composition. *Biophysical journal* **99**, 3264-3273 (2010).

141. Steltenkamp S, Müller MM, Deserno M, Hennessthal C, Steinem C, Janshoff A. Mechanical Properties of Pore-Spanning Lipid Bilayers Probed by Atomic Force Microscopy. *Biophysical journal* **91**, 217-226 (2006).
142. Picas L, Rico F, Scheuring S. Direct Measurement of the Mechanical Properties of Lipid Phases in Supported Bilayers. *Biophysical journal* **102**, L01-L03 (2012).
143. Seitz M, Park CK, Wong JY, Israelachvili JN. Long-Range Interaction Forces between Polymer-Supported Lipid Bilayer Membranes. *Langmuir : the ACS journal of surfaces and colloids* **17**, 4616-4626 (2001).
144. Leckband D, Muller W, Schmitt FJ, Ringsdorf H. Molecular mechanisms determining the strength of receptor-mediated intermembrane adhesion. *Biophysical journal* **69**, 1162-1169 (1995).
145. Wong JY, Kuhl TL, Israelachvili JN, Mullah N, Zalipsky S. Direct measurement of a tethered ligand-receptor interaction potential. *Science* **275**, 820-822 (1997).
146. Natkanski E, Lee WY, Mistry B, Casal A, Molloy JE, Tolar P. B cells use mechanical energy to discriminate antigen affinities. *Science* **340**, 1587-1590 (2013).
147. Vaz WLC, Goodsaid-Zalduondo F, Jacobson K. Lateral diffusion of lipids and proteins in bilayer membranes. *FEBS letters* **174**, 199-207 (1984).
148. Saffman PG. Brownian motion in thin sheets of viscous fluid. *Journal of Fluid Mechanics* **73**, 593-602 (2006).
149. Knight JD, Falke JJ. Single-molecule fluorescence studies of a PH domain: new insights into the membrane docking reaction. *Biophysical journal* **96**, 566-582 (2009).

150. Knight JD, Lerner MG, Marcano-Velazquez JG, Pastor RW, Falke JJ. Single molecule diffusion of membrane-bound proteins: window into lipid contacts and bilayer dynamics. *Biophysical journal* **99**, 2879-2887 (2010).
151. Ziemba BP, Falke JJ. Lateral diffusion of peripheral membrane proteins on supported lipid bilayers is controlled by the additive frictional drags of (1) bound lipids and (2) protein domains penetrating into the bilayer hydrocarbon core. *Chemistry and physics of lipids* **172-173**, 67-77 (2013).
152. Machán R, Hof M. Lipid diffusion in planar membranes investigated by fluorescence correlation spectroscopy. *Biochimica et Biophysica Acta (BBA) - Biomembranes* **1798**, 1377-1391 (2010).
153. Forstner MB, Yee CK, Parikh AN, Groves JT. Lipid lateral mobility and membrane phase structure modulation by protein binding. *Journal of the American Chemical Society* **128**, 15221-15227 (2006).
154. Niemelä PS, *et al.* Membrane Proteins Diffuse as Dynamic Complexes with Lipids. *Journal of the American Chemical Society* **132**, 7574-7575 (2010).
155. Tamm LK. Lateral diffusion and fluorescence microscope studies on a monoclonal antibody specifically bound to supported phospholipid bilayers. *Biochemistry* **27**, 1450-1457 (1988).
156. Nguyen TT, Sly KL, Conboy JC. Comparison of the Energetics of Avidin, Streptavidin, NeutrAvidin, and Anti-Biotin Antibody Binding to Biotinylated Lipid Bilayer Examined by Second-Harmonic Generation. *Analytical Chemistry* **84**, 201-208 (2012).
157. Sako Y, Kusumi A. Compartmentalized structure of the plasma membrane for receptor movements as revealed by a nanometer-level motion analysis. *The Journal of cell biology* **125**, 1251-1264 (1994).

158. Sako Y, Kusumi A. Barriers for lateral diffusion of transferrin receptor in the plasma membrane as characterized by receptor dragging by laser tweezers: fence versus tether. *The Journal of cell biology* **129**, 1559-1574 (1995).
159. Edidin M, Kuo SC, Sheetz MP. Lateral movements of membrane glycoproteins restricted by dynamic cytoplasmic barriers. *Science* **254**, 1379-1382 (1991).
160. Smith A-S, Sengupta K, Goennenwein S, Seifert U, Sackmann E. Force-induced growth of adhesion domains is controlled by receptor mobility. *Proceedings of the National Academy of Sciences* **105**, 6906-6911 (2008).
161. Delanoe-Ayari H, Al Kurdi R, Vallade M, Gulino-Debrac D, Riveline D. Membrane and acto-myosin tension promote clustering of adhesion proteins. *Proc Natl Acad Sci U S A* **101**, 2229-2234 (2004).
162. Marcy Y, Prost J, Carlier M-F, Sykes C. Forces generated during actin-based propulsion: A direct measurement by micromanipulation. *Proc Natl Acad Sci U S A* **101**, 5992-5997 (2004).
163. Footer MJ, Kerssemakers JWJ, Theriot JA, Dogterom M. Direct measurement of force generation by actin filament polymerization using an optical trap. *Proceedings of the National Academy of Sciences* **104**, 2181-2186 (2007).
164. Finer JT, Simmons RM, Spudich JA. Single myosin molecule mechanics: piconewton forces and nanometre steps. *Nature* **368**, 113-119 (1994).
165. Legant WR, Pathak A, Yang MT, Deshpande VS, McMeeking RM, Chen CS. Microfabricated tissue gauges to measure and manipulate forces from 3D microtissues. *Proc Natl Acad Sci U S A* **106**, 10097-10102 (2009).

166. Tabdanov E, *et al.* Micropatterning of TCR and LFA-1 ligands reveals complementary effects on cytoskeleton mechanics in T cells. *Integrative biology : quantitative biosciences from nano to macro* **7**, 1272-1284 (2015).
167. Pyrpassopoulos S, Arpağ G, Feeser EA, Shuman H, Tüzel E, Ostap EM. Force Generation by Membrane-Associated Myosin-I. *Scientific Reports* **6**, 25524 (2016).
168. Hjort Ipsen J, Karlström G, Mourtisen OG, Wennerström H, Zuckermann MJ. Phase equilibria in the phosphatidylcholine-cholesterol system. *Biochimica et Biophysica Acta (BBA) - Biomembranes* **905**, 162-172 (1987).
169. Redondo-Morata L, Giannotti MI, Sanz F. Influence of cholesterol on the phase transition of lipid bilayers: a temperature-controlled force spectroscopy study. *Langmuir : the ACS journal of surfaces and colloids* **28**, 12851-12860 (2012).
170. Loura LMS, Fernandes F, Fernandes AC, Ramalho JPP. Effects of fluorescent probe NBD-PC on the structure, dynamics and phase transition of DPPC. A molecular dynamics and differential scanning calorimetry study. *Biochimica et Biophysica Acta (BBA) - Biomembranes* **1778**, 491-501 (2008).
171. Smith KA, Gale BK, Conboy JC. Micropatterned Fluid Lipid Bilayer Arrays Created Using a Continuous Flow Microspotter. *Analytical Chemistry* **80**, 7980-7987 (2008).
172. Uhl E, Donati A, Reviakine I. Platelet Immobilization on Supported Phospholipid Bilayers for Single Platelet Studies. *Langmuir : the ACS journal of surfaces and colloids* **32**, 8516-8524 (2016).
173. Vafaei S, Tabaei SR, Biswas KH, Groves JT, Cho N-J. Dynamic Cellular Interactions with Extracellular Matrix Triggered by Biomechanical Tuning of Low-Rigidity, Supported Lipid Membranes. *Advanced healthcare materials*, 1700243-n/a (2017).

174. Andreasson-Ochsner M, *et al.* Single cell 3-D platform to study ligand mobility in cell-cell contact. *Lab on a chip* **11**, 2876-2883 (2011).
175. Oliver AE, Parikh AN. Templating membrane assembly, structure, and dynamics using engineered interfaces. *Biochimica et Biophysica Acta (BBA) - Biomembranes* **1798**, 839-850 (2010).
176. Scomparin C, Lecuyer S, Ferreira M, Charitat T, Tinland B. Diffusion in supported lipid bilayers: influence of substrate and preparation technique on the internal dynamics. *The European physical journal E, Soft matter* **28**, 211-220 (2009).
177. Merkel R, Sackmann E, Evans E. Molecular friction and epitactic coupling between monolayers in supported bilayers. *Journal de Physique* **50**, 1535-1555 (1989).
178. Evans E, Sackmann E. Translational and rotational drag coefficients for a disk moving in a liquid membrane associated with a rigid substrate. *Journal of Fluid Mechanics* **194**, 553-561 (1988).
179. Eghiaian F, Rigato A, Scheuring S. Structural, Mechanical, and Dynamical Variability of the Actin Cortex in Living Cells. *Biophysical journal* **108**, 1330-1340 (2015).
180. Han X, *et al.* A self-assembly route for double bilayer lipid membrane formation. *Chemphyschem : a European journal of chemical physics and physical chemistry* **11**, 569-574 (2010).
181. Murray DH, Tamm LK, Kiessling V. Supported double membranes. *Journal of Structural Biology* **168**, 183-189 (2009).
182. Tabaei SR, Jonsson P, Branden M, Hook F. Self-assembly formation of multiple DNA-tethered lipid bilayers. *J Struct Biol* **168**, 200-206 (2009).

183. Zhu Y, Negmi A, Moran-Mirabal J. Multi-Stacked Supported Lipid Bilayer Micropatterning through Polymer Stencil Lift-Off. *Membranes* **5**, 385-398 (2015).
184. Kaizuka Y, Groves JT. Structure and dynamics of supported intermembrane junctions. *Biophysical journal* **86**, 905-912 (2004).
185. Tanaka M, Sackmann E. Polymer-supported membranes as models of the cell surface. *Nature* **437**, 656-663 (2005).
186. Goennenwein S, Tanaka M, Hu B, Moroder L, Sackmann E. Functional Incorporation of Integrins into Solid Supported Membranes on Ultrathin Films of Cellulose: Impact on Adhesion. *Biophysical journal* **85**, 646-655 (2003).
187. Wagner ML, Tamm LK. Tethered polymer-supported planar lipid bilayers for reconstitution of integral membrane proteins: silane-polyethyleneglycol-lipid as a cushion and covalent linker. *Biophysical journal* **79**, 1400-1414 (2000).
188. Diaz AJ, Albertorio F, Daniel S, Cremer PS. Double cushions preserve transmembrane protein mobility in supported bilayer systems. *Langmuir : the ACS journal of surfaces and colloids* **24**, 6820-6826 (2008).
189. Sterling Sarah M, Dawes R, Allgeyer Edward S, Ashworth Sharon L, Neivandt David J. Comparison Actin- and Glass-Supported Phospholipid Bilayer Diffusion Coefficients. *Biophysical journal* **108**, 1946-1953 (2015).
190. Richards MJ, *et al.* Membrane Protein Mobility and Orientation Preserved in Supported Bilayers Created Directly from Cell Plasma Membrane Blebs. *Langmuir : the ACS journal of surfaces and colloids* **32**, 2963-2974 (2016).
191. Lohmüller T, *et al.* Nanopatterning by block copolymer micelle nanolithography and bioinspired applications. *Biointerphases* **6**, MR1-MR12 (2011).

192. Deeg J, *et al.* T Cell Activation is Determined by the Number of Presented Antigens. *Nano Letters* **13**, 5619-5626 (2013).
193. Jackson BL, Groves JT. Scanning probe lithography on fluid lipid membranes. *Journal of the American Chemical Society* **126**, 13878-13879 (2004).
194. Yee CK, Amweg ML, Parikh AN. Membrane Photolithography: Direct Micropatterning and Manipulation of Fluid Phospholipid Membranes in the Aqueous Phase Using Deep-UV Light. *Advanced Materials* **16**, 1184-1189 (2004).
195. Hovis JS, Boxer SG. Patterning and Composition Arrays of Supported Lipid Bilayers by Microcontact Printing. *Langmuir : the ACS journal of surfaces and colloids* **17**, 3400-3405 (2001).
196. Huang RT. Cell adhesion mediated by glycolipids. *Nature* **276**, 624-626 (1978).
197. Shcherbakova DM, Shemetov AA, Kaberniuk AA, Verkhusha VV. Natural Photoreceptors as a Source of Fluorescent Proteins, Biosensors, and Optogenetic Tools. *Annual review of biochemistry* **84**, 519-550 (2015).
198. DeMond AL, Starr T, Dustin ML, Groves JT. Control of Antigen Presentation with a Photoreleasable Agonist Peptide. *Journal of the American Chemical Society* **128**, 15354-15355 (2006).
199. Nakayama K, Tachikawa T, Majima T. Spatial Control of Protein Binding on Lipid Bimembrane Using Photoeliminative Linker. *Langmuir : the ACS journal of surfaces and colloids* **24**, 6425-6428 (2008).
200. Lohmüller T, Triffo S, O'Donoghue GP, Xu Q, Coyle MP, Groves JT. Supported Membranes Embedded with Fixed Arrays of Gold Nanoparticles. *Nano Letters* **11**, 4912-4918 (2011).

201. Groves JT, Ulman N, Boxer SG. Micropatterning fluid lipid bilayers on solid supports. *Science* **275**, 651-653 (1997).
202. Nair PM, Salaita K, Petit RS, Groves JT. Using patterned supported lipid membranes to investigate the role of receptor organization in intercellular signaling. *Nature protocols* **6**, 523-539 (2011).
203. Groves JT, Boxer SG. Electric field-induced concentration gradients in planar supported bilayers. *Biophysical journal* **69**, 1972-1975 (1995).
204. DeMond AL, Mossman KD, Starr T, Dustin ML, Groves JT. T Cell Receptor Microcluster Transport through Molecular Mazes Reveals Mechanism of Translocation. *Biophysical journal* **94**, 3286-3292 (2008).
205. Cremer PS, Boxer SG. Formation and Spreading of Lipid Bilayers on Planar Glass Supports. *The Journal of Physical Chemistry B* **103**, 2554-2559 (1999).
206. Kung LA, Kam L, Hovis JS, Boxer SG. Patterning Hybrid Surfaces of Proteins and Supported Lipid Bilayers. *Langmuir : the ACS journal of surfaces and colloids* **16**, 6773-6776 (2000).
207. Orth RN, Wu M, Holowka DA, Craighead HG, Baird BA. Mast Cell Activation on Patterned Lipid Bilayers of Subcellular Dimensions. *Langmuir : the ACS journal of surfaces and colloids* **19**, 1599-1605 (2003).
208. Jurchenko C, Salaita KS. Lighting Up the Force: Investigating Mechanisms of Mechanotransduction Using Fluorescent Tension Probes. *Molecular and cellular biology* **35**, 2570-2582 (2015).
209. Stabley DR, Jurchenko C, Marshall SS, Salaita KS. Visualizing mechanical tension across membrane receptors with a fluorescent sensor. *Nat Meth* **9**, 64-67 (2012).

210. Liu Y, *et al.* Nanoparticle tension probes patterned at the nanoscale: impact of integrin clustering on force transmission. *Nano Lett* **14**, 5539-5546 (2014).
211. Chang Y, Liu Z, Zhang Y, Galior K, Yang J, Salaita K. A General Approach for Generating Fluorescent Probes to Visualize Piconewton Forces at the Cell Surface. *Journal of the American Chemical Society* **138**, 2901-2904 (2016).
212. Grashoff C, *et al.* Measuring mechanical tension across vinculin reveals regulation of focal adhesion dynamics. *Nature* **466**, 263-266 (2010).
213. Meng F, Suchyna TM, Sachs F. A fluorescence energy transfer-based mechanical stress sensor for specific proteins in situ. *The FEBS journal* **275**, 3072-3087 (2008).
214. Balaban NQ, *et al.* Force and focal adhesion assembly: a close relationship studied using elastic micropatterned substrates. *Nature cell biology* **3**, 466-472 (2001).
215. Roca-Cusachs P, Gauthier NC, Del Rio A, Sheetz MP. Clustering of alpha(5)beta(1) integrins determines adhesion strength whereas alpha(v)beta(3) and talin enable mechanotransduction. *Proc Natl Acad Sci U S A* **106**, 16245-16250 (2009).
216. Li F, Redick SD, Erickson HP, Moy VT. Force measurements of the alpha5beta1 integrin-fibronectin interaction. *Biophysical journal* **84**, 1252-1262 (2003).
217. Baumgartner W, *et al.* Cadherin interaction probed by atomic force microscopy. *Proc Natl Acad Sci U S A* **97**, 4005-4010 (2000).
218. Moore SW, Roca-Cusachs P, Sheetz MP. Stretchy proteins on stretchy substrates: the important elements of integrin-mediated rigidity sensing. *Developmental cell* **19**, 194-206 (2010).

219. Engler AJ, Sen S, Sweeney HL, Discher DE. Matrix elasticity directs stem cell lineage specification. *Cell* **126**, 677-689 (2006).
220. Balgude AP, Yu X, Szymanski A, Bellamkonda RV. Agarose gel stiffness determines rate of DRG neurite extension in 3D cultures. *Biomaterials* **22**, 1077-1084 (2001).
221. Elosegui-Artola A, *et al.* Mechanical regulation of a molecular clutch defines force transmission and transduction in response to matrix rigidity. *Nature cell biology* **18**, 540-548 (2016).
222. Kourouklis AP, Lerum RV, Bermudez H. Cell adhesion mechanisms on laterally mobile polymer films. *Biomaterials* **35**, 4827-4834 (2014).
223. Garcia AS, Dellatore SM, Messersmith PB, Miller WM. Effects of supported lipid monolayer fluidity on the adhesion of hematopoietic progenitor cell lines to fibronectin-derived peptide ligands for alpha5beta1 and alpha4beta1 integrins. *Langmuir : the ACS journal of surfaces and colloids* **25**, 2994-3002 (2009).
224. Koçer G, Jonkheijm P. Guiding hMSC Adhesion and Differentiation on Supported Lipid Bilayers. *Advanced healthcare materials* **6**, 1600862-n/a (2017).
225. Wong DSH, *et al.* Magnetically Tuning Tether Mobility of Integrin Ligand Regulates Adhesion, Spreading, and Differentiation of Stem Cells. *Nano Letters* **17**, 1685-1695 (2017).
226. Attwood SJ, *et al.* Adhesive ligand tether length affects the size and length of focal adhesions and influences cell spreading and attachment. *Scientific Reports* **6**, 34334 (2016).
227. Choi CK, Vicente-Manzanares M, Zareno J, Whitmore LA, Mogilner A, Horwitz AR. Actin and alpha-actinin orchestrate the assembly and maturation of nascent

- adhesions in a myosin II motor-independent manner. *Nature cell biology* **10**, 1039-1050 (2008).
228. Iskratsch T, *et al.* FHOD1 is needed for directed Forces and Adhesion Maturation during Cell Spreading and Migration. *Developmental cell* **27**, 545-559 (2013).
 229. Ganz A, *et al.* Traction forces exerted through N-cadherin contacts. *Biology of the cell / under the auspices of the European Cell Biology Organization* **98**, 721-730 (2006).
 230. Fenz SF, Merkel R, Sengupta K. Diffusion and intermembrane distance: case study of avidin and E-cadherin mediated adhesion. *Langmuir : the ACS journal of surfaces and colloids* **25**, 1074-1085 (2008).
 231. Puech PH, Feracci H, Brochard-Wyart F. Adhesion between Giant Vesicles and Supported Bilayers Decorated with Chelated E-Cadherin Fragments. *Langmuir : the ACS journal of surfaces and colloids* **20**, 9763-9768 (2004).
 232. Perez TD, Nelson WJ, Boxer SG, Kam L. E-Cadherin Tethered to Micropatterned Supported Lipid Bilayers as a Model for Cell Adhesion. *Langmuir : the ACS journal of surfaces and colloids* **21**, 11963-11968 (2005).
 233. Paszek MJ, *et al.* The cancer glycocalyx mechanically primes integrin-mediated growth and survival. *Nature* **511**, 319-325 (2014).
 234. Paszek MJ, Boettiger D, Weaver VM, Hammer DA. Integrin Clustering Is Driven by Mechanical Resistance from the Glycocalyx and the Substrate. *PLOS Computational Biology* **5**, e1000604 (2009).
 235. Xu GK, Qian J, Hu J. The glycocalyx promotes cooperative binding and clustering of adhesion receptors. *Soft matter* **12**, 4572-4583 (2016).

236. Dustin ML, Cooper JA. The immunological synapse and the actin cytoskeleton: molecular hardware for T cell signaling. *Nature immunology* **1**, 23-29 (2000).
237. Afanasyenkau D, Offenhäusser A. Positively Charged Supported Lipid Bilayers as a Biomimetic Platform for Neuronal Cell Culture. *Langmuir : the ACS journal of surfaces and colloids* **28**, 13387-13394 (2012).
238. Moller I, Seeger S. Solid supported lipid bilayers from artificial and natural lipid mixtures - long-term stable, homogeneous and reproducible. *Journal of Materials Chemistry B* **3**, 6046-6056 (2015).
239. Baranov M, Ter Beest M, Reinieren-Beeren I, Cambi A, Figdor CG, van den Bogaart G. Podosomes of dendritic cells facilitate antigen sampling. *J Cell Sci* **127**, 1052-1064 (2014).
240. Hurst IR, Zuo J, Jiang J, Holliday LS. Actin-related protein 2/3 complex is required for actin ring formation. *Journal of bone and mineral research : the official journal of the American Society for Bone and Mineral Research* **19**, 499-506 (2004).
241. Mandal S, Johnson KR, Wheelock MJ. TGF-beta induces formation of F-actin cores and matrix degradation in human breast cancer cells via distinct signaling pathways. *Experimental cell research* **314**, 3478-3493 (2008).
242. Zhou DW, Lee TT, Weng S, Fu J, García AJ, Weaver VM. Effects of substrate stiffness and actomyosin contractility on coupling between force transmission and vinculin–paxillin recruitment at single focal adhesions. *Mol Biol Cell* **28**, 1901-1911 (2017).
243. Proag A, Bouissou A, Vieu C, Maridonneau-Parini I, Poincloux R. Evaluation of the force and spatial dynamics of macrophage podosomes by multi-particle tracking. *Methods (San Diego, Calif)* **94**, 75-84 (2016).

244. Gupta M, Doss B, Lim CT, Voituriez R, Ladoux B. Single cell rigidity sensing: A complex relationship between focal adhesion dynamics and large-scale actin cytoskeleton remodeling. *Cell adhesion & migration* **10**, 554-567 (2016).
245. Zhang Y, *et al.* Platelet integrins exhibit anisotropic mechanosensing and harness piconewton forces to mediate platelet aggregation. *Proc Natl Acad Sci U S A* **115**, 325-330 (2018).
246. Plotnikov SV, Sabass B, Schwarz US, Waterman CM. High-Resolution Traction Force Microscopy. *Methods in cell biology* **123**, 367-394 (2014).
247. Liu Z, *et al.* Mechanical tugging force regulates the size of cell–cell junctions. *Proceedings of the National Academy of Sciences* **107**, 9944 (2010).
248. Kedziora KM, Isogai T, Jalink K, Innocenti M. Invadosomes - shaping actin networks to follow mechanical cues. *Frontiers in bioscience (Landmark edition)* **21**, 1092-1117 (2016).
249. Revach O-Y, Weiner A, Rechav K, Sabanay I, Livne A, Geiger B. Mechanical interplay between invadopodia and the nucleus in cultured cancer cells. *Scientific Reports* **5**, 9466 (2015).
250. Hu S, *et al.* Podosome rings generate forces that drive saltatory osteoclast migration. *Mol Biol Cell* **22**, 3120-3126 (2011).
251. Evans E, Needham D. Physical properties of surfactant bilayer membranes: thermal transitions, elasticity, rigidity, cohesion and colloidal interactions. *The Journal of Physical Chemistry* **91**, 4219-4228 (1987).
252. Boulbitch A. *Deflection of a cell membrane under application of local force* (1998).

253. Ma R, *et al.* DNA probes that store mechanical information reveal transient piconewton forces applied by T cells. *Proceedings of the National Academy of Sciences*, 201904034 (2019).
254. Ma VP-Y, Salaita K. DNA Nanotechnology as an Emerging Tool to Study Mechanotransduction in Living Systems. *Small* **15**, 1900961 (2019).
255. Maheshwari G, Brown G, Lauffenburger DA, Wells A, Griffith LG. Cell adhesion and motility depend on nanoscale RGD clustering. *J Cell Sci* **113** (Pt **10**), 1677-1686 (2000).
256. Karimi F, O'Connor AJ, Qiao GG, Heath DE. Integrin Clustering Matters: A Review of Biomaterials Functionalized with Multivalent Integrin-Binding Ligands to Improve Cell Adhesion, Migration, Differentiation, Angiogenesis, and Biomedical Device Integration. *Advanced healthcare materials* **7**, e1701324 (2018).
257. Walsh AJ, Sharick JT, Skala MC, Beier HT. Temporal binning of time-correlated single photon counting data improves exponential decay fits and imaging speed. *Biomedical optics express* **7**, 1385-1399 (2016).
258. Digman MA, Caiolfa VR, Zamai M, Gratton E. The phasor approach to fluorescence lifetime imaging analysis. *Biophysical journal* **94**, L14-16 (2008).
259. Iqbal A, *et al.* Orientation dependence in fluorescent energy transfer between Cy3 and Cy5 terminally attached to double-stranded nucleic acids. *Proc Natl Acad Sci U S A* **105**, 11176-11181 (2008).
260. Bubb MR, Spector I, Beyer BB, Fosen KM. Effects of jasplakinolide on the kinetics of actin polymerization. An explanation for certain in vivo observations. *The Journal of biological chemistry* **275**, 5163-5170 (2000).
261. Lee BS. Myosins in Osteoclast Formation and Function. *Biomolecules* **8**, (2018).

262. Pernier J, *et al.* A new actin depolymerase: a catch bond Myosin 1 motor. *bioRxiv*, 375923 (2018).
263. Zhang Y, *et al.* Tail domains of myosin-1e regulate phosphatidylinositol signaling and F-actin polymerization at the ventral layer of podosomes. *Mol Biol Cell*, mbcE18060398 (2019).
264. Pourfarhangi KE, Bergman A, Gligorijevic B. ECM Cross-Linking Regulates Invadopodia Dynamics. *Biophysical journal* **114**, 1455-1466 (2018).
265. Groves JT, Dustin ML. Supported planar bilayers in studies on immune cell adhesion and communication. *Journal of immunological methods* **278**, 19-32 (2003).
266. Dervaux J, Limat L. Contact lines on soft solids with uniform surface tension: analytical solutions and double transition for increasing deformability. *Proceedings of the Royal Society A: Mathematical, Physical and Engineering Science* **471**, (2015).
267. Swift LM, Asfour H, Posnack NG, Arutunyan A, Kay MW, Sarvazyan N. Properties of blebbistatin for cardiac optical mapping and other imaging applications. *Pflugers Archiv : European journal of physiology* **464**, 503-512 (2012).
268. Axelrod D. Carbocyanine dye orientation in red cell membrane studied by microscopic fluorescence polarization. *Biophysical journal* **26**, 557-573 (1979).
269. Vacklin HP, Tiberg F, Thomas RK. Formation of supported phospholipid bilayers via co-adsorption with beta-D-dodecyl maltoside. *Biochimica et biophysica acta* **1668**, 17-24 (2005).

270. Martino F, Perestrelo AR, Vinarsky V, Pagliari S, Forte G. Cellular Mechanotransduction: From Tension to Function. *Frontiers in physiology* **9**, 824 (2018).
271. Lam WA, *et al.* Mechanics and contraction dynamics of single platelets and implications for clot stiffening. *Nat Mater* **10**, 61-66 (2011).
272. Upadhyaya A. Mechanosensing in the immune response. *Seminars in Cell & Developmental Biology* **71**, 137-145 (2017).
273. Style RW, *et al.* Traction force microscopy in physics and biology. *Soft matter* **10**, 4047-4055 (2014).
274. Ricart Brendon G, Yang Michael T, Hunter Christopher A, Chen Christopher S, Hammer Daniel A. Measuring Traction Forces of Motile Dendritic Cells on Micropost Arrays. *Biophysical journal* **101**, 2620-2628 (2011).
275. Blanchard AT, Salaita K. Emerging uses of DNA mechanical devices. *Science* **365**, 1080-1081 (2019).
276. Woodside MT, Behnke-Parks WM, Larizadeh K, Travers K, Herschlag D, Block SM. Nanomechanical measurements of the sequence-dependent folding landscapes of single nucleic acid hairpins. *Proceedings of the National Academy of Sciences* **103**, 6190 (2006).
277. Blakely BL, *et al.* A DNA-based molecular probe for optically reporting cellular traction forces. *Nat Methods* **11**, 1229-1232 (2014).
278. Chaudhuri O, *et al.* Hydrogels with tunable stress relaxation regulate stem cell fate and activity. *Nat Mater* **15**, 326-334 (2016).

279. Zhao B, *et al.* Quantifying Tensile Forces at Cell–Cell Junctions with a DNA-based Fluorescent Probe. *bioRxiv*, 2020.2001.2007.897249 (2020).
280. Tolar P, Spillane KM. Force generation in B-cell synapses: mechanisms coupling B-cell receptor binding to antigen internalization and affinity discrimination. *Advances in immunology* **123**, 69-100 (2014).
281. Merindol R, Delechiave G, Heinen L, Catalani LH, Walther A. Modular Design of Programmable Mechanofluorescent DNA Hydrogels. *Nature communications* **10**, 528 (2019).
282. Kilin V, Glushonkov O, Herdly L, Klymchenko A, Richert L, Mely Y. Fluorescence lifetime imaging of membrane lipid order with a ratiometric fluorescent probe. *Biophysical journal* **108**, 2521-2531 (2015).
283. Wang Y-L. Noise-induced systematic errors in ratio imaging: serious artefacts and correction with multi-resolution denoising. *Journal of microscopy* **228**, 123-131 (2007).
284. Ranjit S, Gurunathan K, Levitus M. Photophysics of Backbone Fluorescent DNA Modifications: Reducing Uncertainties in FRET. *The Journal of Physical Chemistry B* **113**, 7861-7866 (2009).
285. Wang L, Gaigalas AK, Blasic J, Holden MJ, Gallagher DT, Pires R. Fluorescence resonance energy transfer between donor-acceptor pair on two oligonucleotides hybridized adjacently to DNA template. *Biopolymers* **72**, 401-412 (2003).
286. Algar WR, Hildebrandt N, Vogel SS, Medintz IL. FRET as a biomolecular research tool - understanding its potential while avoiding pitfalls. *Nat Methods* **16**, 815-829 (2019).

287. Ko J, Oh J, Ahmed MS, Carlson JCT, Weissleder R. Ultra-fast cycling for multiplexed cellular fluorescence imaging. *Angew Chem Int Ed Engl*, 10.1002/anie.201915153 (2020).
288. Eisfeld A, Briggs JS. The J- and H-bands of organic dye aggregates. *Chemical Physics* **324**, 376-384 (2006).
289. Di Fiori N, Meller A. The Effect of dye-dye interactions on the spatial resolution of single-molecule FRET measurements in nucleic acids. *Biophysical journal* **98**, 2265-2272 (2010).
290. Leontis N, Kwok W, Newman J. Stability and structure of three-way DNA junctions containing unpaired nucleotides. *Nucleic Acids Res* **19**, 759-766 (1991).
291. Welch JB, Duckett DR, Lilley DM. Structures of bulged three-way DNA junctions. *Nucleic Acids Res* **21**, 4548-4555 (1993).
292. Johansson MK. Choosing reporter-quencher pairs for efficient quenching through formation of intramolecular dimers. *Methods Mol Biol* **335**, 17-29 (2006).
293. Gopich IV, Szabo A. Theory of the energy transfer efficiency and fluorescence lifetime distribution in single-molecule FRET. *Proc Natl Acad Sci U S A* **109**, 7747-7752 (2012).
294. Cost A-L, Khalaji S, Grashoff C. Genetically Encoded FRET-Based Tension Sensors. *Current Protocols in Cell Biology* **83**, e85 (2019).
295. Valdes-Aguilera O, Neckers DC. Aggregation phenomena in xanthene dyes. *Accounts of chemical research* **22**, 171-177 (1989).

296. Woźniak AK, Schröder GF, Grubmüller H, Seidel CAM, Oesterhelt F. Single-molecule FRET measures bends and kinks in DNA. *Proceedings of the National Academy of Sciences* **105**, 18337 (2008).
297. Qu P, Chen X, Zhou X, Li X, Zhao X. Fluorescence quenching of TMR by guanosine in oligonucleotides. *Science in China Series B: Chemistry* **52**, 1653-1659 (2009).
298. von Hippel PH, Johnson NP, Marcus AH. Fifty years of DNA "breathing": Reflections on old and new approaches. *Biopolymers* **99**, 923-954 (2013).
299. Fišerová E, Kubala M. Mean fluorescence lifetime and its error. *Journal of Luminescence* **132**, 2059-2064 (2012).
300. Melinger JS, *et al.* FRET from Multiple Pathways in Fluorophore-Labeled DNA. *ACS Photonics* **3**, 659-669 (2016).
301. Szabó Á, *et al.* The Effect of Fluorophore Conjugation on Antibody Affinity and the Photophysical Properties of Dyes. *Biophysical journal* **114**, 688-700 (2018).
302. Roy R, Hohng S, Ha T. A practical guide to single-molecule FRET. *Nat Methods* **5**, 507-516 (2008).
303. Smoligovets A, Smith A, Wu H-J, Petit R, Groves J. Characterization of dynamic actin associations with T-cell receptor microclusters in primary T cells. *Journal of cell science* **125**, 735-742 (2012).
304. Pan K, Boulais E, Yang L, Bathe M. Structure-based model for light-harvesting properties of nucleic acid nanostructures. *Nucleic Acids Res* **42**, 2159-2170 (2014).

305. Buckhout-White S, *et al.* Assembling programmable FRET-based photonic networks using designer DNA scaffolds. *Nature communications* **5**, 5615 (2014).
306. Pehlivan ZS, Torabfam M, Kurt H, Ow-Yang C, Hildebrandt N, Yüce M. Aptamer and nanomaterial based FRET biosensors: a review on recent advances (2014-2019). *Mikrochim Acta* **186**, 563-563 (2019).
307. Zadeh JN, *et al.* NUPACK: Analysis and design of nucleic acid systems. *Journal of Computational Chemistry* **32**, 170-173 (2011).
308. Reid YS, D; Riss, T; and Minor, L. Assay Guidance Manual: Authentication of Human Cell Lines by STR DNA Profiling. (ed[^](eds editors SGGBKea). Eli Lilly & Company and National Center for Advancing Translational Sciences (2013).
309. Groves JT, Boxer SG. Micropattern Formation in Supported Lipid Membranes. *Accounts of chemical research* **35**, 149-157 (2002).
310. Mossman K, Groves J. Micropatterned supported membranes as tools for quantitative studies of the immunological synapse. *Chemical Society reviews* **36**, 46-54 (2007).
311. Danhier F, Le Breton A, Préat V. RGD-Based Strategies To Target Alpha(v) Beta(3) Integrin in Cancer Therapy and Diagnosis. *Molecular Pharmaceutics* **9**, 2961-2973 (2012).
312. Lessey-Morillon EC, *et al.* The RhoA Guanine Nucleotide Exchange Factor, LARG, Mediates ICAM-1–Dependent Mechanotransduction in Endothelial Cells To Stimulate Transendothelial Migration. *The Journal of Immunology* **192**, 3390-3398 (2014).
313. Ferrari R, *et al.* MT1-MMP directs force-producing proteolytic contacts that drive tumor cell invasion. *Nature communications* **10**, 4886 (2019).

314. Blanchard ATC, D.; Brockman, J; Mattheyses, A.L.; Salaita, K. Superresolution Traction Force Mapping with Structured Illumination Molecular Force Microscopy. (ed[^](eds) (2020).
315. Branch KM, Hoshino D, Weaver AM. Adhesion rings surround invadopodia and promote maturation. *Biology Open* **1**, 711-722 (2012).
316. Gimona M, Buccione R. Adhesions that mediate invasion. *The international journal of biochemistry & cell biology* **38**, 1875-1892 (2006).
317. Davenport A, *et al.* Chimeric antigen receptor T cells form nonclassical and potent immune synapses driving rapid cytotoxicity. *Proceedings of the National Academy of Sciences* **115**, 201716266 (2018).
318. Benninger RKP, Piston DW. Two-photon excitation microscopy for the study of living cells and tissues. *Current protocols in cell biology* **Chapter 4**, Unit-4.11.24 (2013).
319. de Gennes P-G. Maximum pull out force on DNA hybrids. *Comptes Rendus de l'Académie des Sciences - Series IV - Physics* **2**, 1505-1508 (2001).
320. Hatch K, Danilowicz C, Coljee V, Prentiss M. Demonstration that the shear force required to separate short double-stranded DNA does not increase significantly with sequence length for sequences longer than 25 base pairs. *Physical review E, Statistical, nonlinear, and soft matter physics* **78**, 011920 (2008).
321. Holoubek A, *et al.* Monitoring of nucleophosmin oligomerization in live cells. *Methods and Applications in Fluorescence* **6**, 035016 (2018).

322. Anthony NR, Mehta AK, Lynn DG, Berland KM. Mapping amyloid-beta(16-22) nucleation pathways using fluorescence lifetime imaging microscopy. *Soft matter* **10**, 4162-4172 (2014).
323. Ostašov P, Sýkora J, Brejchová J, Olžýňská A, Hof M, Svoboda P. FLIM studies of 22- and 25-NBD-cholesterol in living HEK293 cells: Plasma membrane change induced by cholesterol depletion. *Chemistry and physics of lipids* **167-168**, 62-69 (2013).
324. Oreopoulos J, Yip CM. Probing membrane order and topography in supported lipid bilayers by combined polarized total internal reflection fluorescence-atomic force microscopy. *Biophysical journal* **96**, 1970-1984 (2009).